Skolkovo Institute of Science and Technology

VOID SPACE EVOLUTION AND ORGANIC MATTER TRANSFORMATION OF BAZHENOV FORMATION ROCKS DURING HIGH TEMPERATURE TREATMENT

Doctoral Thesis

by

TAGIR KARAMOV

DOCTORAL PROGRAM IN PETROLEUM ENGINEERING

Supervisor
Professor Mikhail Spasennykh

Co-supervisor
Professor Yuri Popov

Moscow - 2022

I hereby declare that the work presented in this thesis was carried out by myself at Skolkovo Institute of Science and Technology, Moscow, except where due acknowledgement is made, and has not been submitted for any other degree.

Tagir Karamov

Professor Mikhail Spasennykh

Abstract

Progressive depletion of conventional oil and gas reserves forces scientists to look for new hydrocarbon sources and improve recovery technologies. One of the most promising objects is organic-rich shales. However, no technology exists with proven efficiency for hydrocarbon recovery from such reservoirs. The most advanced methodologies are based on high-temperature treatment, which promotes the simultaneous conversion of solid organic matter into hydrocarbons and the production of existing hydrocarbons. High-temperature processing causes alterations in the mineral matrix and organic matter, nevertheless the knowledge on alterations in shales are limited, and require in-depth investigation. The goal of the thesis is evaluation and identification of patterns of void space evolution and organic matter transformation during high-temperature treatment of organic-rich shales on the example of Bazhenov Formation rocks.

The study is based on a comparison of source rocks before and after thermal treatment, including in-situ high-pressure air injection using combustion tube technique, pyrolysis in mini-reactors and pyrolysis cells of Rock Eval and pyro-GC-TOFMS. Two principal shale components, mineral matrix and organic matter, were studied in four lithotypes of Bazhenov Formation shales during the treatments. Special attention was given to microstructural transformations of organic matter. A wide variety of advanced lithological, geochemical, and petrophysical methods helped to investigate mineral composition alterations, organic matter transformations, and accompanying pore space evolution. Lithological methods included petrology, scanning electron microscopy, broad ion beam polishing, energy-dispersive X-Ray spectroscopy, X-Ray powder diffraction, and micro-computer tomography. Geochemical methods were pyrolysis, two-dimensional gas chromatography with time-of-flight mass spectrometry, and isotope ratio mass spectrometry. The main petrophysical method was thermal property profiling based on optical scanning technique.

The results of the study show significant alterations in the composition and microstructure of shales, which affected the pore space evolution during the treatment. All the components of the mineral matrix were transformed. A specific combination of mineral components in a rock (lithotype) leads to particular processes, which can be beneficial or unfavorable for the void space. Detailed investigation of the organic matter showed that microstructural evolution of organic matter is closely associated with thermal maturation and its development related to treatment temperature, duration, and rock fabric. Outcomes of the study imply an increase in the prediction accuracy of high-temperature based technology simulation and the technologies application efficiency. The gained knowledge will help in the creation of advanced technologies for effective hydrocarbon recovery from organic-rich shales.

Publications

Peer-Reviewed Articles in International Scientific Journals

1. Kovaleva, L., Zinnatullin, R., Musin, A., Kireev, V., **Karamov, T.**, Spasennykh, M. Investigation of source rock heating and structural changes in the electromagnetic fields using experimental and mathematical modeling (2021) Minerals, 11 (9). DOI: 10.3390/min11090991 (Scopus Q2, SJR Q2)
2. Bogdanovich, N., Kozlova, E., **Karamov, T.** Lithological and geochemical heterogeneity of the organo-mineral matrix in carbonate-rich shales (2021) Geosciences (Switzerland), 11 (7). DOI: 10.3390/geosciences11070295 (Scopus Q1, SJR Q2)
3. Leushina, E., Bulatov, T., Kozlova, E., Panchenko, I., Voropaev, A., **Karamov, T.**, Yermakov, Y., Bogdanovich, N., Spasennykh, M. Upper jurassic–lower cretaceous source rocks in the north of western siberia: Comprehensive geochemical characterization and reconstruction of paleo-sedimentation conditions (2021) Geosciences (Switzerland), 11 (8). DOI: 10.3390/geosciences11080320 (Scopus Q1, SJR Q2)
4. Mukhametdinova, A., **Karamov, T.**, Bogdanovich, N., Borisenko, S., Rudakovskaya, S., Cheremisin, A. Wettability of organic-rich source rocks: Case study on Bazhenov Formation (Abalak-Bazhenov group) (2020) Advances in Geosciences, 54, pp. 195-204. DOI: 10.5194/adgeo-54-195-2020 (Scopus Q3, SJR Q2)
5. Mukhametdinova, A., Mikhailova, P., Kozlova, E., **Karamov, T.**, Baluev, A., Cheremisin, A. Effect of thermal exposure on oil shale saturation and reservoir properties (2020) Applied Sciences (Switzerland), 10 (24), pp. 1-24. DOI: 10.3390/app10249065 (Scopus Q2, SJR Q2)
6. Idrisova, E., Gabitov, R., **Karamov, T.**, Voropaev, A., Liu, M.-C., Bogdanovich, N., Spasennykh, M. Pyrite morphology and δ34S as indicators of deposition environment in organic-rich shales (2021) Geosciences (Switzerland), 11 (9). DOI: 10.3390/geosciences11090355 (Scopus Q1, SJR Q2)
7. Mukhametdinova, A., Kazak, A., **Karamov, T.**, Bogdanovich, N., Serkin, M., Melekhin, S., Cheremisin, A. Reservoir properties of low-permeable carbonate rocks: Experimental features (2020) Energies, 13 (9). DOI: 10.3390/en13092233 (Scopus Q1, SJR Q2)

Patent

Popov E., **Karamov T.**, Popov Yu., Spasennykh M., Kozlova E., 2020. Method for determining total content of organic matter in rocks of shale strata enriched with hydrocarbons (versions). Russian patent RU2720582C1.

Conferences/Conference proceedings

1. **Karamov T.**, Leushina E., Kozlova E., Bulatov T., Spasennykh M. Development of Organic Matter Porosity During Thermal Maturation: Study on the Example of the Bazhenov Formation Source Rocks (2021), Conference Proceedings, 30th International Meeting on Organic Geochemistry (IMOG 2021), Sep 2021, Volume 2021, p.1 – 2

   DOI: 10.3997/2214-4609.202134225
2. **Karamov, T.**, Leushina, E., Kozlova, E., Bulatov, T., Spasennykh, M. Void Space Formation in the Bazhenov Formation Kerogen during Isothermal Treament in an Open System (2021) EAGE/SPE Workshop on Shale Science 2021: New Challenges.

   DOI: 10.3997/2214-4609.202151024
3. **Karamov, T.**, Mukhametdinova, A., Bogdanovich, N., Plotnikov, V., Khakimova, Z. Pore structure investigation of upper devonian organic-rich shales within the verkhnekamsk depression (2019) International Multidisciplinary Scientific GeoConference Surveying Geology and Mining Ecology Management, SGEM, 19 (1.2), pp. 1045-1052.

   DOI: 10.5593/sgem2019/1.2/S06.133
4. Mukhametdinova, A., **Karamov, T.**, Bogdanovich, N., Cheremisin, A., Plotnikov, V. Complex characterization of organic-rich carbonate shales saturation (2019) International Multidisciplinary Scientific GeoConference Surveying Geology and Mining Ecology Management, SGEM, 19 (1.2), pp. 719-726.

   DOI: 10.5593/sgem2019/1.2/S06.091
5. **Karamov, T.**, Bogdanovich, N., Mukhametdinova, A., Kozionov, A., Kozionov, E., Kozlova, E., Plotnikov, V. Pore space analysis of domanic formation rocks (2019) EAGE/SPE Workshop on Shale Science 2019 - Shale Sciences: Theory and Practice.

   DOI: 10.3997/2214-4609.201900479

Acknowledgements

I would like to thank all the people who I faced during my PhD journey.

I would also like to extend my deepest gratitude to my supervisor Mikhail Spasennykh for the opportunity to work in an incredible scientific atmosphere filled with enthusiasm and support.

I'm deeply indebted to my co-supervisor Yuri Popov, who inoculates a world-level scientific literacy and strong scientific discipline.

I am grateful to Evgeniy Popov for his consistency and patience during the experiment planning and realization with his outstanding laboratory engineers.

Many thanks to the Advanced Imaging Core Facility staff, especially to Head of the laboratory Yaroslava Shakhova, who gave me the possibility to learn from the world-leading experts in electron microscopy.

I'd like to acknowledge the guidance of Natalia Bogdanovich throughout PhD study and the initiation into scientific project activities.

Special thanks go to my colleges in the lab: Aliya Mukhametdinova, Elizaveta Idrisova, Elena Kozlova, Evgenia Leushina for their continuous help, expertise, discussions and assistance.

And, I would like to express my sincere gratitude to my family for infinite support and endless trust.

Table of Contents

List of Abbreviations

BF – Bazhenov Formation

OM – organic matter

HC – hydrocarbons

SEM – Scanning electron microscope

XRD – X-Ray diffraction

EDS – Energy-dispersive X-ray spectroscopy

CT – computed tomography

GCxGC-TOFMS – two-dimensional gas chromatography with time-of-flight mass spectrometer

BIB – broad ion beam

TOC – Total organic carbon content, wt. %

HI – hydrogen index, mg HC/g TOC

OI – oxygen index, mg CO_2/g TOC

Corg – total organic carbon content, wt. %

ECD – equivalent circular diameter

List of Figures

List of Tables

Chapter 1. Introduction

Global growth of energy demand and progressive depletion of conventional hydrocarbon reservoirs have created a necessity for new oil and gas sources [1–4]. Organic-rich shales (or oil shales) are considered as one of the richest unconventional reservoir, which contains both liquid hydrocarbons and solid insoluble organic matter. Insoluble organic matter is represented by kerogen, which can be transformed into petroleum-like hydrocarbons through heating [2]. Enormous reserves of organic-rich shales, around 35% of the world's reserves [3], make them economically reasonable [4]. However, there are numerous challenges regarding the production and extraction of hydrocarbons from such reservoirs. These challenges are connected with extremely low porosity and permeability on the one side, and with a presence of a significant amount of potentially recoverable organic matter – kerogen on the other side. Currently, there are no technologies exist with proven efficiency in hydrocarbon production from these types of reservoirs [5]. Nonetheless, the most promising techniques are based on high-temperature treatment processes. The main advantage of these processes is a simultaneous conversion of solid organic matter into hydrocarbons and the production of existing hydrocarbons with an effect on the porosity[6–8]. There is a variety of high-temperature based techniques: high-pressure air injection, in-situ combustion, electrical heating, thermogas, and many others [9,10].

It is known from the literature that the application of high-temperature based techniques in shales promotes alterations in the rock texture and structure [11–15]. Several reports showed a porosity increase as a result of heating, estimated with different modifications of the computed tomography (CT) technique. Using normal micro-CT [7], in-situ micro-CT and synchrotron based in-situ micro-CT [12,15,16] the authors demonstrated a porosity increasein organic-rich shales, which they mainly attributed to fracturing. Fractures are considered as a result of organic matter transformation with further hydrocarbons expulsion during the experiment. Detailed morphological transformations in the organic matter during thermal treatment are less studied. The studies report porosity development with thermal maturation degree increase across natural maturation level variation, and there is a lack of clear experimental confirmation organic porosity development during artificial thermal maturation. Even fewer data exist on mineral matrix behavior and associated porosity formation during high-temperature treatment of shales. Based on main gaps in knowledge on organic-rich shales components behavior during high-temperature treatment the thesis was designed, aims and objectives were formulated.

The thesis is devoted to the investigation of pore space evolution and organic matter microstructural transformation of Bazhenov Formation shales during high-temperature treatment. Bazhenov Formation (BF) organic-rich shales are considered as main source rock in the West

Siberian petroleum basin, one of the largest source rock formations in the World, and one of the most perspective unconventional reservoirs [4,17,18]. The study is based on a series of high-temperature experiments on four representative BF rock types (lithotypes).

The study is based on a comparison of source rocks before and after thermal treatment, including in-situ high-pressure air injection using combustion tube technique, pyrolysis in mini-reactors, and pyrolysis cells of Rock-Eval and pyro-GC-TOFMS. The experiments showed a direct association of void space formation during high-temperature treatment in shales with both mineral matrix alterations (composition and structure) and organic matter micromorphological transformations. Alterations of the mineral matrix were investigated in detail and chemical reactions behind these alterations were proposed. Due to the fact that organic matter is very sensitive to thermal treatment, hence focused separate experiments are needed. The experiments in closed and open systems aided to establish key factors controlling organic porosity development and propose organic porosity classification. As a key result of the study, comprehensive conceptual schemes of shales alterations and pore space evolution were suggested. It is shown that alterations in the mineral matrix and organic matter lead to the reduction of thermal conductivity and isotope composition shifting. On the basis of suggested schemes recommendations regarding lithotype selection for effective technology application are given.

Results of the study are intended to increase the prediction accuracy of high-temperature based technology simulations and technologies application efficiency. The recommendations allow to reasonably choose the most appropriate intervals/lithotypes for technology application. Consideration of the full range of chemical processes including mineral matrix and thermal conductivity reduction during the high-temperature treatment modeling will increase the quality and prediction power of models. Understanding of chemical processes associated with mineral matrix will facilitate correct equipment material choice for the technology. The most perspective rock types are recommended for the high-temperature treatment, which should be a basis during interval selection during technology planning. Ultimately, the gained knowledge brings the creation an effective technology for effective hydrocarbon recovery technology from organic-rich shales closer.

Aims and objectives of the research

The main aim of the thesis is evaluation and patterns recognition of void space evolution and organic matter transformation during high temperature treatment of Bazhenov Formation rocks.

To achieve the stated aim following objective has been accomplished:

Perform a comprehensive literature review of the state of the art: geology of Bazhenov Formation, existed thermal-based technologies, and data on alterations of mineral matrix and organic matter.

Establish and choose the most common lithotypes in Bazhenov Formation through the study of lithological, petrophysical, and geochemical properties of Bazhenov Formation in their natural states, such as mineral composition, porosity, and organic matter.

Plan and conduct a high-temperature experiment on Bazhenov Formation rocks aimed at evaluation of mineral matrix and organic matter.

Study lithological, petrophysical, and geochemical of Bazhenov Formation rock properties after the high-temperature treatment.

Comparative analysis of the results changes occurred in different lithotypes. Distinguishing the most promising lithotypes for treatment. Creation of the conceptual scheme of the alterations.

The thesis structure is organized in the following manner.

Chapter 2 gives a background for the study (literature review), including Bazhenov Formation geology, existing thermal-based technologies, and alteration of mineral matrix and organic matter.

Chapter 3 is devoted to the study of Bazhenov Formation lithology aimed to establish and choose the most representative and important lithotypes for the physical experiments.

Chapter 4 describes the main results of laboratory experimental modeling of the mineral matrix alteration and void space evolution processes during high-temperature treatment in a combustion tube and investigation of samples before and after the experiment.

Chapter 5 gives a detailed characterization of organic microstructure in its natural conditions and alterations during thermal treatment.

Chapter 6 is dedicated to the analysis of the results from the point of view of perspectivity and effectiveness of the high temperature treatment technology. Comprehensive conceptual schemes of shales alteration are proposed.

Chapter 7 gives summary, conclusions and recommendations of the study.

Chapter 2. State of the art

2.1. Geological Background

General information

Bazhenov Formation (BF) is a key source rock in the West Siberian sedimentary basin and one of the principal unconventional reservoirs in the Russian Federation and in the World [18,19]. BF rocks are represented by organic-rich siliceous, carbonate and argillaceous mudstones, which correspond to Upper Jurassic – Lower Cretaceous sequences [20]. Bazhenov Formation rocks are often considered as shales due to noticeable fissility along bedding plane and fine grained texture [20,21]. The BF and the stratigraphic equivalents occupy most of the West Siberian sedimentary basin and occur on the area of more than one million square kilometers (Figure 2.1.1) at a depth of 2 500 – 3 000 m with average thickness variations in the range of 20-40 m [18,22]. Deposition of the sediments took place in the deep marine environment in the anoxic conditions that were favorable for organic matter accumulation and preservation. Total organic carbon (TOC) in the rocks lies in a range of 0.1-25% with an average value of 5-10%. The organic matter mostly is derived from bacterial and plankton material and related to the kerogen II type. Maturity ranges from immature to the end of the oil window along the basin [18,23–25]. According to the EIA report (2015) Bazhenov Formation contains enormous resources – 1.24 billion barrels of oil in-place, the majority of which are classified as shale oil [4].

Stratigraphy

Bazhenov Formation is Volgian-early Berriasian aged (latest Jurassic–earliest Cretaceous) organic-rich shales, deposited in a deep-water marine anoxic condition in the entire area of West Siberian sedimentary basin [18,22].

On the marginal zones of the West Siberian basin BF is gradually replaced by thicker nearshore shales depleted in the organic matter and considered as a stratigraphic equivalent of the BF (Figure 2.1.1) [26].

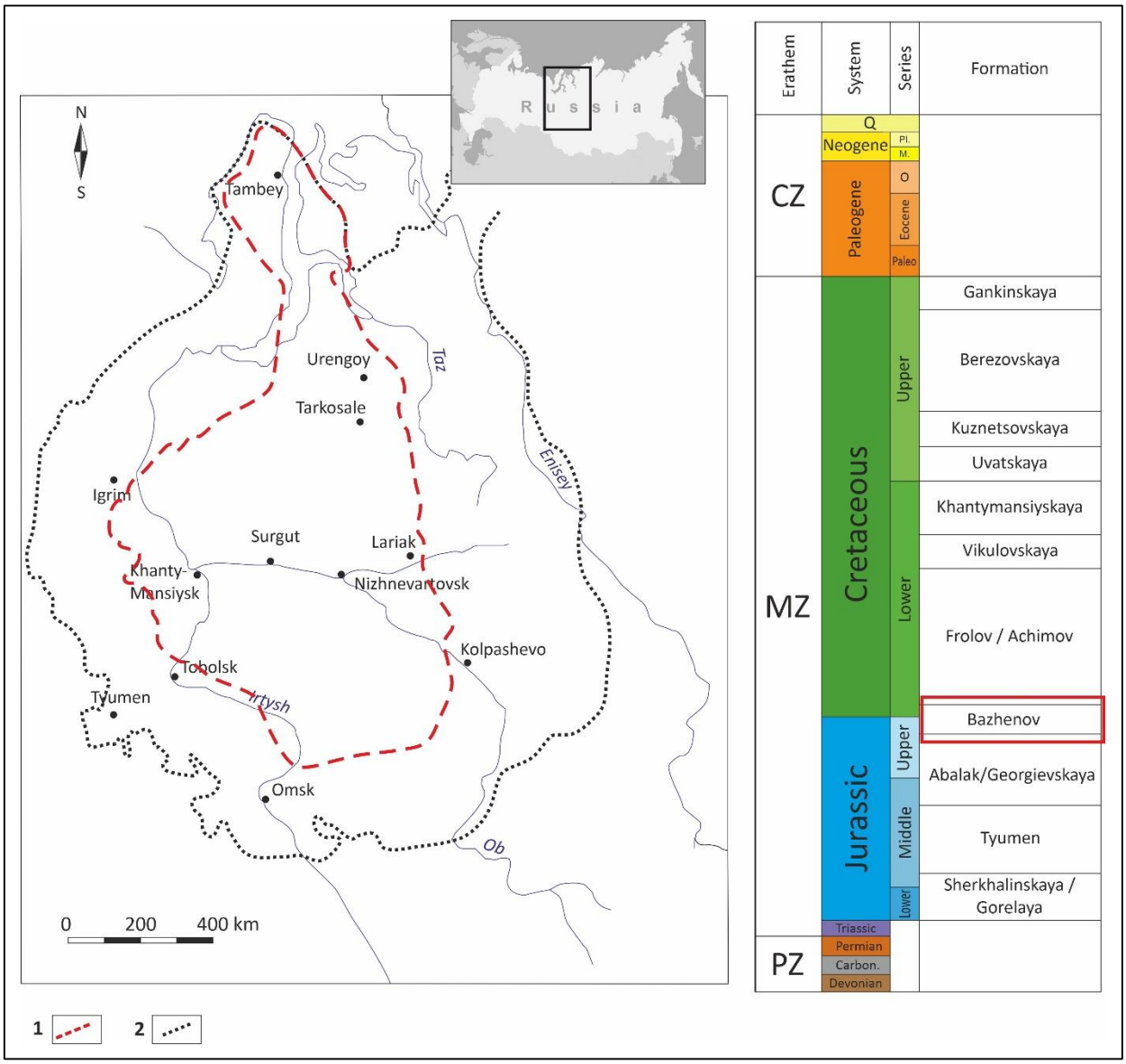

Figure 2.1.1. The location of the Bazhenov Formation with stratigraphic equivalents (left) and generalized stratigraphic column (right) (modified after Panchenko et al., 2016 and Ulmishek, 2003).
1 – boundary of Bazhenov Formation; 2 – boundary of Bazhenov Formation stratigraphical equivalents.

Bazhenov Formation sediments overlay Georgiev horizon (horizon here means formation with stratigraphic equivalents within the sedimentary basin), which is represented by argillite dominated deposits such as Georgiev, Abalak, Nurmian, Vasyugan formations (Figure 2.1.1) within different basin areas [18,28]. The BF mudstones underlay Neocomian clastic edges (clinoforms) of Megion, Vartov, and Achimov formations, and, in some areas, by argillaceous rocks of Akh, Kulomzin, or Frolov formations (Figure 2.1.1).

Tectonic development

Tectonic development of BF is closely associated with the whole West Siberian basin evolution. The West Siberian basin is a Mesozoic-Tertiary sedimentary strata superposed on the Triassic rift system. The multi-aged basement of the basin is complex and consists of different terranes coalesced during the Hercynian stage of oceanic basins enclosure, and collision of the Siberian and Kazakhstan continents with the Russian craton (Figure 2.1.2A). The basement includes foldbelts (Ural foldbelt on the western margin of the basin), massifs (Uvat massif, which is maybe either continuation of the Kazahstan continent or a separate microcontinent; Mezhov massif and other smaller ones), portion of the Siberian platform which form the eastern margin of the basement of the West Siberian basin, and folded region on the east-south Altay-Sayan (Figure 2.1.2A). [29,30]

The principal stage prior to sediment cover deposition is rifting occurred in the basement during the Early Triassic time. Rifts partially determined the structure of Jurassic-Cretaceous strata. The largest rift is the Koltogor-Urengoy rift (Figure 2.1.2A), which extends from the south to the north onshore (1 800 km), and northward continuously offshore to the Kara Sea. The deposition of the sediment cover of the West Siberian basin commenced in the Middle Triassic time [31]. The deposition occurred gradually from the northern part at the Bajocian time, expanding southward, reaching the present-day basin boundary. During the Lower and Middle Jurassic times, clastic continental and marine sediments covered the basement (Tyumen Formation). In the Callovian period, broad transgression took place in the entire basin area. During the Callovian-Kimmeridgian time nearshore sandstones and shales were deposited (Vasyugan Formation, Abalak Formation) [32].

In the Volgian-early Berriasian time, a deep depression developed across the entire basin area (more than 1 million km^2), characterized by deep-water anoxic conditions. The sea depth was in the range of 300-700 m, according to different authors [33,34]. During this period organic-rich shales of the Bazhenov Formation were deposited in a deep-water anoxic central basin. Thicker nearshore, organic matter depleted shales with sandstones were deposited in the marginal zones of the basin (Figure 2.1.2B) [26].

The Bazhenov deep water basin was gradually filled by Neocomian clastic wedges (cliniforms) with westward propagation (e.g., Achimov Formation). However, there were small inherited deep-water zones at the western boundary of the West Siberian basin, where sedimentation of shales occurred (Frolov, Akh formations) [18].

Further development of the West Siberian basin continued with the shallow marine sedimentation in the Aptian, Albian, and Cenomanian times. Turonian time is characterized by a

regional transgression across the entire basin territory. Marine clastic sedimentation lasted until the end of the middle Eocene. A new stage of basin development started in the late Eocene and continued to the Tertiary period. The shifting of the depocenter, initially located in the northern part of the basin through Mesozoic time to the southern part, took place, which resulted in the Eocene-Pliocene clastic continental sedimentation. This shifting was followed by uplift on the northern part of the basin in the Oligocene period, erosion continued until the middle Pliocene time. The uplift was associated with west-east compressional stress, which resulted in a structural growth of linear arches in Mesozoic sediments [18,35]. The present-day Jurassic-Cretaceous strata of the West Siberian basin represents a gentle depression, where sedimentary strata superposed on the Early Triassic rifts and Paleozoic structures. The marginal areas of the basin are monoclonal structures, that are slightly tilted basinward. The Bazhenov Formation structure (which is the top part of the Upper Jurassic sequence and regional seismic reflector) is quite gentle, and the surface slightly dips from the boundaries to the depth of 2.5-3 km in the south and center of the basin, and up to 4-4.5 km in the deepest northern areas [36]. Jurassic-Cretaceous strata is gently deformed into monoclines, arches, and depressions (Figure 2.1.2C). The structure of Jurassic strata is mostly related to the filling of the pre-Jurassic topography.

Lithology (composition)

BF rocks are composed of four principal components: siliceous minerals (quartz or amorphous silica), carbonate minerals (calcite, dolomite, rarely siderite), clay minerals (predominantly illite, kaolinite), and organic matter, also sulfides (pyrite) are widely present in the rocks. These components are occurred in various proportions and commonly form combinations of two or more. Depending on the structure and texture of the components, different lithotypes (rock types) may be determined.

Note on the rock classification (lithotype nomenclature)

There are plenty of classification schemes for BF rocks. The most common schemes are based on the composition (prevailing component). Postnikov et al. [37,38] used classical Shvanovs' classification, which suggests using several words (component term) for rock designating in the order of component increasing. The alternative classification was proposed by Kontorovich [20], which is quite similar but suggests establishing four groups of lithotypes: silicates, mudstones, carbonates, and mixtites. There are recent classifications proposed by Nemova [39] and Gavrilov [40], which are identical to mentioned ones and do not add new ideas. These classifications do not consider one of the main lithological characteristics of a rock – texture, which is an essential aspect to separate fine-grained organic-rich rocks from other classes with similar composition.

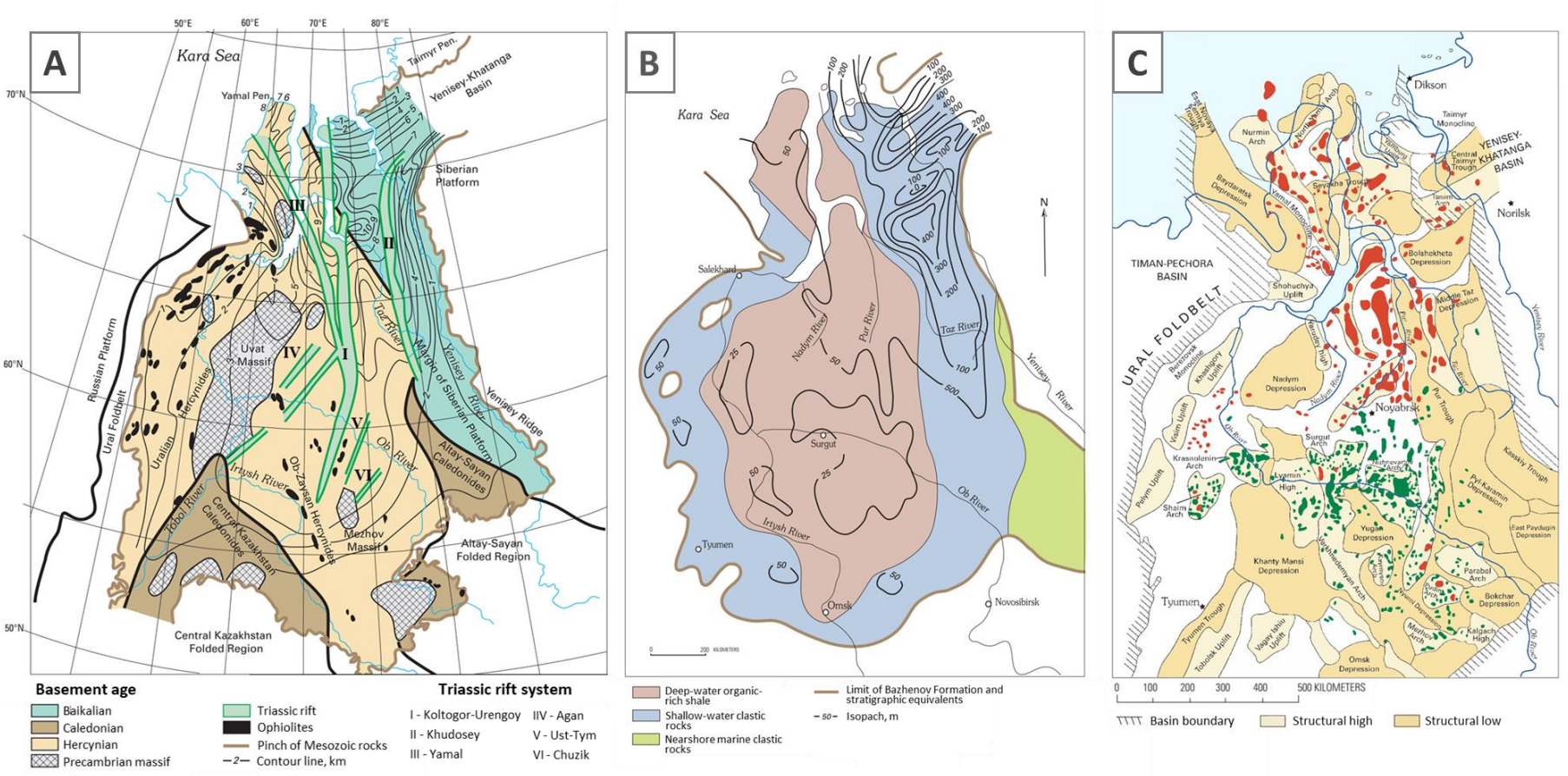

Figure 2.1.2. A – Basement tectonic map of West Siberian basin, B – Lithofacies map of Bazhenov Formation and stratigraphic equivalents, C – tectonic map of West Siberian basin (modified form Ulmishek, 2003 [18])

The author of the thesis suggests using classification for fine-grained sedimentary rocks proposed by Lazar et al. [21], which include both composition and texture of a rock, and may encompass most of the rock heterogeneity. The classification implies to designate rocks with >75% of grains with the size of <62.5 μm as "mudstone" (Figure 2.1.3A), and use a ternary diagram (Figure 2.1.3B) based on the principal components for compositional characteristics. Hereinafter Lazars' classification is used.

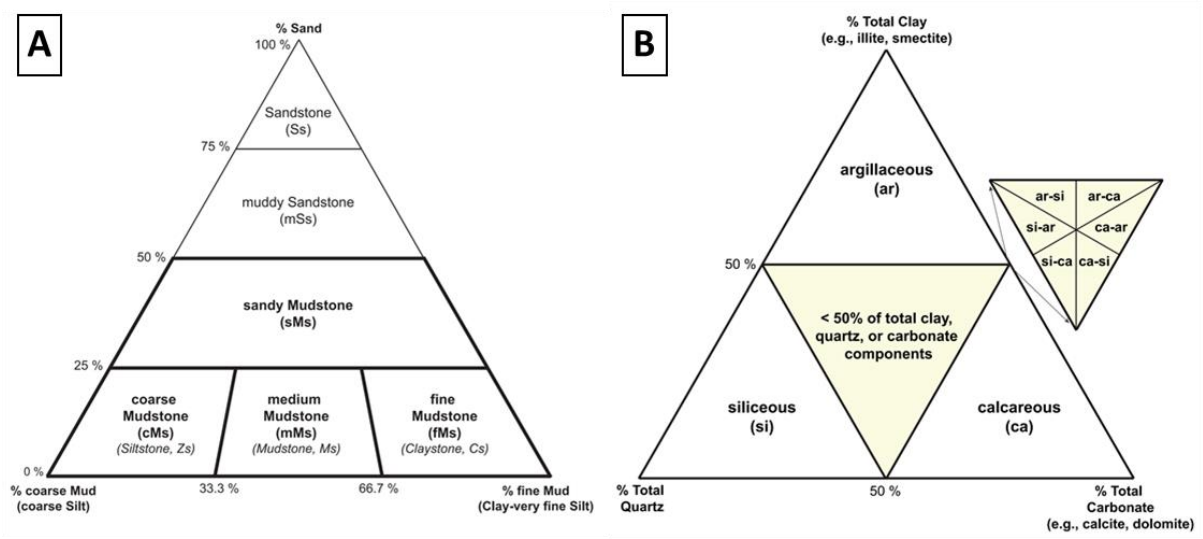

Figure 2.1.3. Nomenclature for fine-grained sedimentary rocks: A – texture (grain size), B – composition [21].

Bazhenov Formation rock composition (lithotypes)

Bazhenov Formation rocks are represented by different varieties of siliceous, argillaceous, and carbonate mudstones enriched with OM [23]. The most common lithologies are siliceous mudstones, carbonate mudstones, siliceous-argillaceous-mudstone, and carbonate-argillaceous mudstone [23,39,41]. All the lithotypes contain more than 1% of organic matter and may be considered as organic-rich [42,43].

Siliceous mudstones (organic-rich). The lithotype is composed of >50% of silica (quartz). Depending on the structure and texture may be distinguished different variations, the most important is radiolarian mudstone, which is often characterized by a porosity value up to 10%, and considered as a reservoir. Different variations with clay minerals, calcite, dolomite are possible.

Carbonate (calcareous/dolomite) mudstones (organic-rich). The lithotype is composed of more than 50% of carbonate minerals (calcareous, dolomite, rarely siderite). Different types may be distinguished depending on the structure, where apporadiolarian (formed due to

carbonatization of radiolarite) mudstone is often considered as a reservoir. Also, variations with silica and clay minerals are widespread.

Siliceous-argillaceous-mudstone (organic-rich). One of the most common lithotypes in the Bazhenov Formation sequence. The composition is dominated by siliceous and clay minerals. The lithology is often characterized by a maximum amount of organic matter (organic carbon).

Carbonate-argillaceous mudstone (organic-rich). The less common, nevertheless widely described lithotype with carbonate (normally calcareous) and clay minerals dominance. Components may both be mixed in each other, or carbonate component may form well-defined micro lenses and inclusions.

Argillaceous mudstones (clay minerals >50%) normally do not present in BF rocks. However, they are major lithology in overlain and underlain shale formations (Frolov and Abalak formations accordingly). Terrigenous particles (sand, silt) also may be present in BF rocks; however, they are not regular and do not exceed 1-3%. Another component is pyrite, which is important from the point of view for void space [44] and deposition environment analysis. There are no well explained and proven scheme of lithotype distribution in the Bazhenov Formation, however, local patterns for some areas are well understood [22,27,45].

2.2. Shale recovery technologies based on high temperature treatment

High heterogeneity, low porosity, and permeability make conventional technologies inapplicable for organic-rich shales. Only several approaches may be used to recover hydrocarbons from such types of rocks: hydraulic fracturing and thermal treatment technologies. Hydraulic fracturing may be quite effective for shale oil and gas extraction, but it requires significant volumes of water. This procedure can cause water pollution and other potential ecological hazards. Many formations in the world contain a significant amount of HC in the form of kerogen, and hydraulic fracturing will be futile in terms of kerogen potential transformation into HC. Thermal treatment is a technology that can be effective in conversing kerogen into the gaseous and liquid hydrocarbons with its further extraction [46–48]. Organic-rich shales (oil shales) may be developed with various techniques based on thermal effect (high-temperature treatment) [5,46]. The heating of black shales is an approach that will help to achieve two fundamental goals: extract existing light oil from micro- and nano- pores, and convert solid OM (kerogen) into liquid hydrocarbons with further production. There is no technology with proven efficiency for organic-rich shale development, especially for Bazhenov Formation shales, however, high-temperature techniques are the most promising. In this section, thermal-based technologies aimed at shales recovery are briefly discussed.

1. "ElectroFrac" technology (ExxonMobil Corporation).

The technology is designed to heat organic-rich shales in the subsurface (in-situ) conditions using electricity, which is conducted through the special conductive material (resistive heating element), that fills initially induced fractures. Then the heat goes to the formation and continuously converts kerogen into liquid-like hydrocarbons, which may be further produced by conventional way [49]. The conceptual scheme is shown in Figure 2.2.1A. The temperature range is quite wide and may reach 1200°C [50]. Experimental pilot project showed promising results – production from such fractures lasting several months [51,52].

2. Radio Frequency heating technologies

There are a number of techniques based on the radio frequency (microwave) heating of organic-rich shales, which has advantages over conventional heating, including rapid energy deposition, selectivity, better control, lower thermal gradients [49]. One of the examples is Raytheons' "Radio Frequency / Critical Fluid Technology", which represents a combination of radio frequency and critical liquid driving techniques. Radio frequency transmitters are located in the well within the shale formation interval and heat the shale (Figure 2.2.1B). The heating results in micro fracturing, and transformation of organic matter into liquid-like and gaseous

hydrocarbons. Hydrocarbons are extracted and driven by injecting critical carbon dioxide. Afterward, CO_2 is separated and may be used again. [53] suggested the technique of microwave heating of oil shale based on the absorbents injection, that uses separate wells for heating and production (Figure 2.2.1C).

3. "In-situ Conversion Process" (ICP) technology (Shell Oil Company).

ICP technology implies in-situ electric heaters to convert solid OM into mobile hydrocarbons. The heaters continuously and slowly heat a shale up to the temperatures of 650-700°C (Figure 2.2.1D). This leads to the kerogen transformation into hydrocarbons, which may be produced by conventional methods. According to literature data technology result in 1/3 of gas and 2/3 of light oil. The main advantage is fewer steps are needed to get liquid hydrocarbons [49,52,54].

4. "Conduction, Convection and Reflux process" (CCR) technology (American Shale Oil).

AMSO has introduced a process for in-situ oil shale retorting, which involves conventional proven drilling and completion technologies coupled with a formation heating strategy. Heat is delivered to a shale formation by two horizontal wells so that heater well is below the production well (Figure 2.2.1E). Wells are located near the shale bed basement. The process is based on thermal fracturing, convection, and refluxing, which allow enhancing heat distribution [49]. Kerogen conversion into the hydrocarbons is followed by light products rise and reflux, whereas associated gases serve as fuel for the heater [52].

5. "Chevron's Technology for the Recovery and Upgrading of Oil from Shale" (CRUSH) technology (Chevron).

CRUSH technology is based on the high-temperature carbon dioxide injection into the formation to convert solid organic matter into liquid hydrocarbons. The technology implies drilling two vertical wells and inducing horizontal fractures by carbon dioxide injection (Figure 2.2.1F).

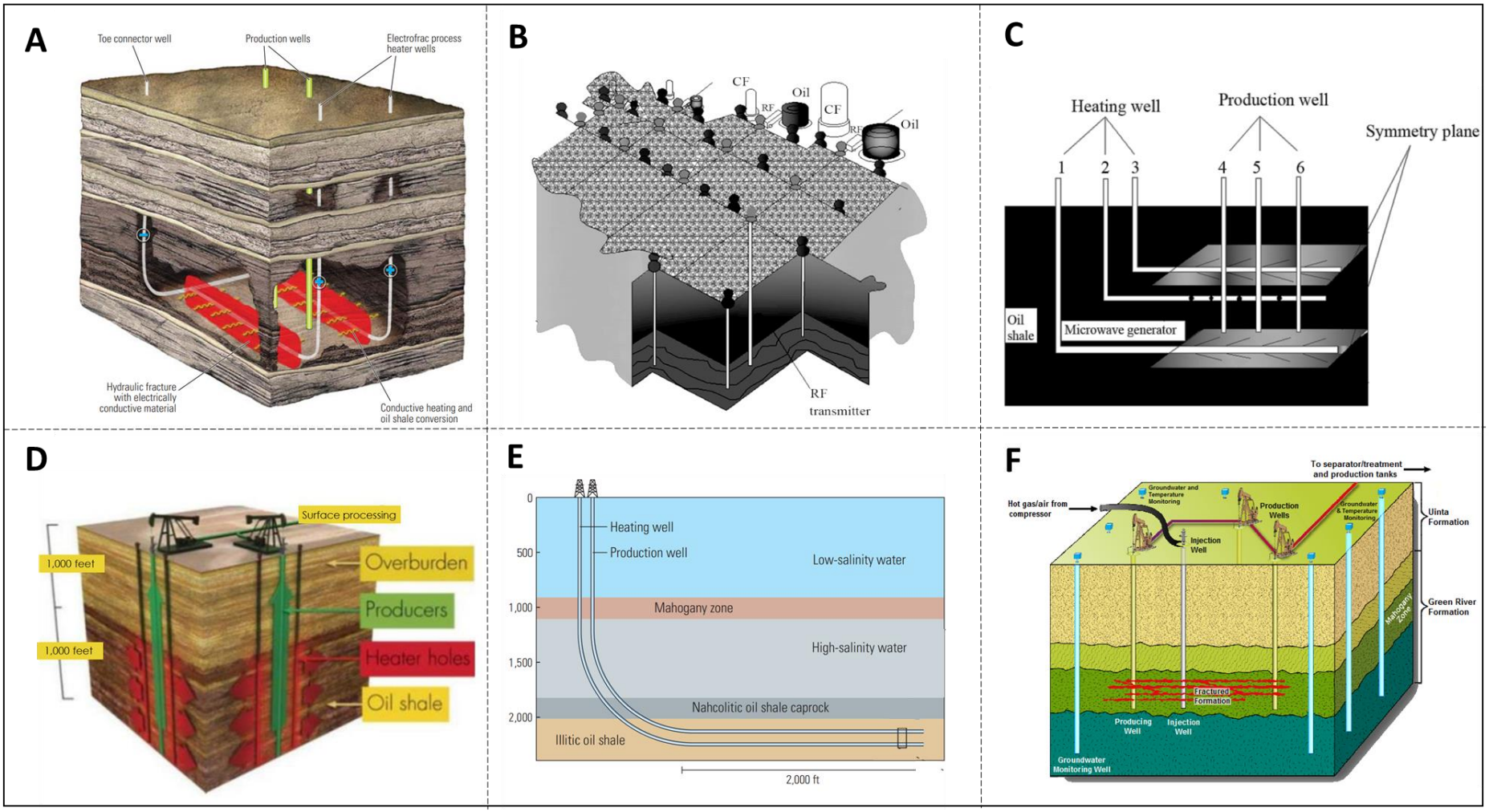

Figure 2.2.1. Schematic representation of high-temperature treatment technologies. A – “ElectroFrac” technology [49]; B – “Radio Frequency / Critical Fluid Technology” technology [53]; C – microwave heating technology [53]; D – “In-situ Conversion Process” technology [55], E – “Conduction, Convection and Reflux process” technology [52]; F – “Chevron's Technology for the Recovery and Upgrading of Oil from Shale” technology [49].

After additional pressure is added for active gas circulation within the fractured area, which allows to rubblize production zone. Additional explosives may help to increase rubblization. The exhausted carbon dioxide is redirected to the gas generator, reheated, and recycled [49,56]. The gases are generated through the combustion of remaining OM in depleted zones to process further intervals. Generated hydrocarbons are produced in conventional vertical wells. [49,56].

6. Thermogas (RITEK Oil Company, Russia)

RITEK proposed "Thermogas" technology for Bazhenov Formation, which is based on air and water injection into the formation (Figure 2.2.2) [57]. The area of oxidation chemical processes is controlled by the injection rate and the proportion of air and water. The technology represents a variation of the high-pressure air injection (HPAI) approach, initially proposed by Sheinman A.B. and Dubrovay K.K. in the 1930s.

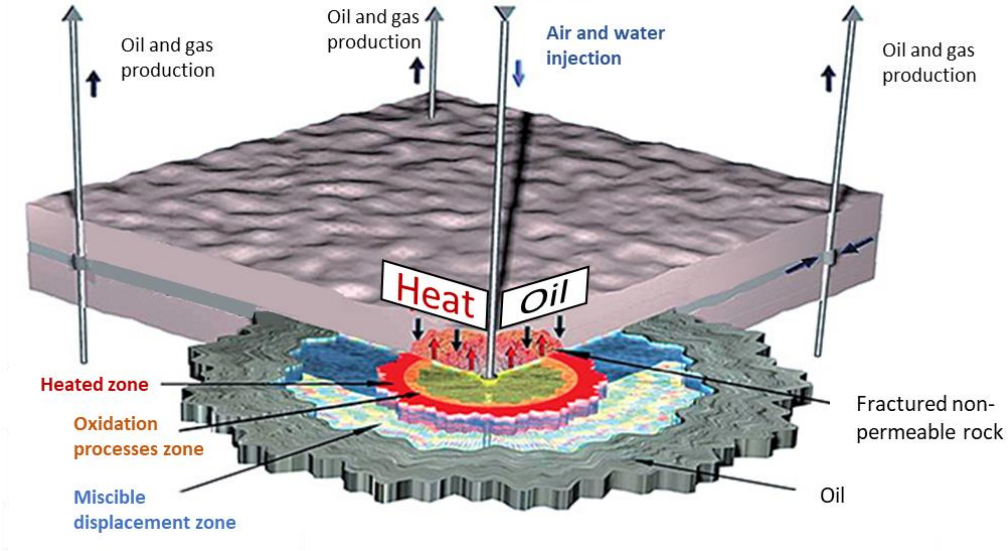

Figure 2.2.2. Schematic representation of "Thermogas" technology [58]

The approach implies injection of air into a reservoir with the initiation of the oxidation process, which displace hydrocarbons to the production wells. The key driving factors of HPAI are increased mobility ratio, vaporization of oil, steam, and flue gases [59]. The application of the air injection in shale reservoirs for kerogen *in situ* conversion into hydrocarbons is described by Johnson and Crawford [60]. It is suggested that kerogen conversion may be cost-effective in case of sufficient permeability of strata, and, to achieve that, fractures in shales should be created. The air initiates ignition of kerogen and propagation of combustion front, which causes the generation and displacement of synthetic hydrocarbons. RITEK company has several cases of successful thermoses applications [58] on the Sredme-Nazymskoe oil field. It was reported that treatment resulted in reservoir pressure increase, oil production growth, and increasing of hydrocarbon gases proportion in the product. The latter means that kerogen is the main fuel for oxidation processes.

Oil and gas companies have already presented a wide variety of thermal-based organic-rich recovery technologies, and some techniques are still at the early development stage. Despite a diversity of the techniques, all of them are similar in their basics and suggest thermal exposure normally in the range of 200-900°C. For now, there is a gap in the literature on their effect concerning pore space evolution, mineral composition alteration, and rock fabric (structure and texture).

2.3. Alterations of mineral matrix and organic matter during thermal treatment

The heating of the shales leads to changes in the structure, mineral composition, and physical properties [61]. Details of the alterations during heating are poorly known; only rock structure and OM decomposition process have been analyzed to some extent by several authors [46–48,61,62]. Understanding these alterations is crucial for the effective implementation of the technology and further oil and gas recovery.

One of the first experiments aimed to investigate shale alterations during heating was performed by Tisot [63] in 1967. Seven samples from the Green River Fm with different OM content were collected and heated under controlled conditions up to 815°C in stress-free conditions (Figure 2.3.1). Physical properties were evaluated before and after heating. The main results are decomposition of OM continued up to 400°C, porosity and permeability increase with temperature rise, new fractures along lamination appeared after heating, weight loss is associated with OM decomposition.

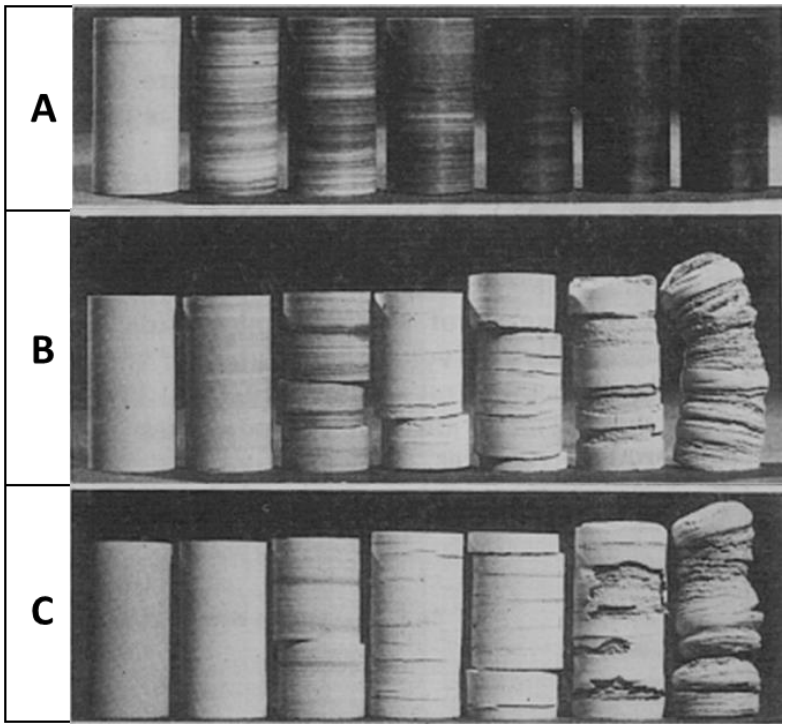

Figure 2.3.1. Structural alterations of samples before and after experiment [63].

A - raw samples; B - samples heated to 400°C; C - samples heated to 815°C.

Prats conducted a similar experiment on Green River Oil Shales [62] with the aim to estimate thermal properties changes during heating. Four sets of samples were collected from different locations of the Green River Formation with different TOC. Thermal conductivity was measured with the transient line heat-source (probe) method. Samples were heated in the special oven. Prats et al. [62] showed that the thermal conductivity decreases (up to 30%) as the

temperature increases. He concluded that the thermal conductivity of organic-rich shales is affected by the degree of kerogen conversion into fluid products; the fraction of converted kerogen is controlled by temperature history.

Decades later similar experiment was performed in Salt Lake City by Tiwari [7].Three samples from Green River Fm with different TOC were collected for the investigation and split into three parts. The samples were subjected to pyrolysis at different temperatures: 350 ºC, 425 ºC, and 500 ºC in the N2 atmosphere for 24 hours. After heating the weight of all samples has fallen according to initial TOC content: higher TOC - larger the weight loss. Moreover, samples characterized with high TOC content were destroyed after temperature treatment. All samples were investigated with the micro-CT method. The authors demonstrated that new pores and fractures are associated with OM veins and lenses. Figure 2.3.2 shows the sample after 425°C temperature. The sample contained around 20% of TOC, after heating a major part of OM was decomposed, and a new pore space was formed. The generated void space is patchy and consistent with the initial OM distribution along laminas. The authors concluded that heating of the samples with high TOC content leads to generating a new void space, and the distribution of these voids is strongly controlled by OM distribution.

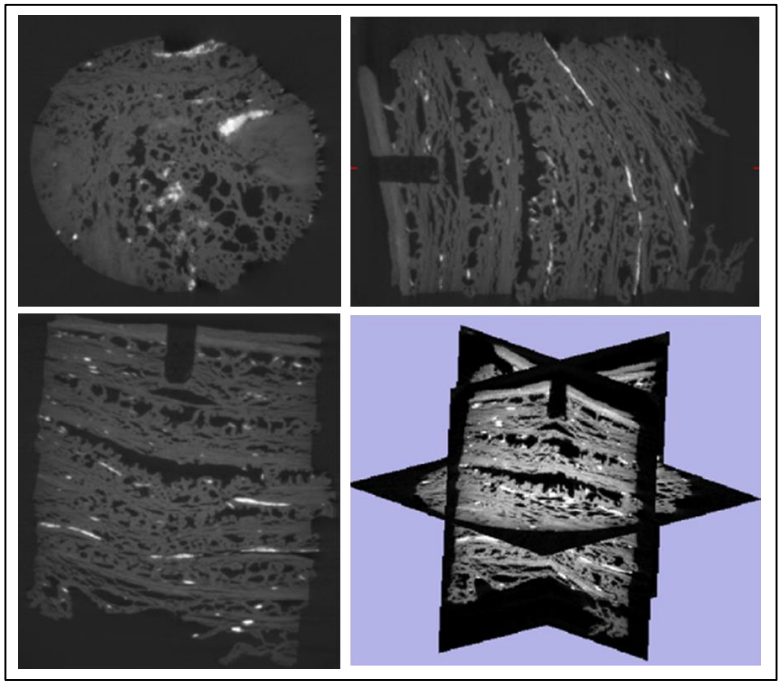

Figure 2.3.2. Sample structure after heating up 425°C [7].

An identical experiment was accomplished by Jing Zhao et al. [64] for Daqing and Yan'an oil shales samples with different TOC content and structure. The samples were heated up to the temperatures of 100°C, 200°C, 300°C, 400°C, 500°C, 600°C in the pyrolysis reactor. At the temperature of 200 °C new fractures started to form with the beginning OM destruction (Figure 2.3.3).

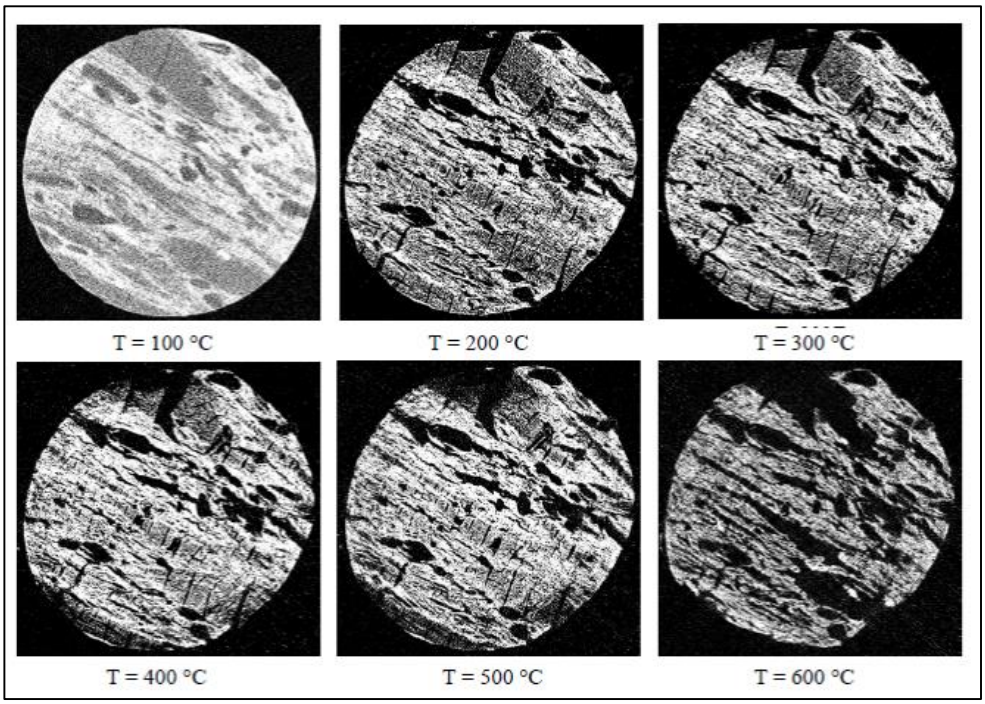

Figure 2.3.3. Micro-CT images of the sample during heating. [64]

The main issue of most experiments is repeated cycles of cooling and heating of the samples: they are cooled to room temperature to make a micro-CT scan, then heating continues. Kobchenko et al. (2011) [15] and Saif et al. (2016) [14] overcame this problem by time-resolved X-Ray synchrotron tomography. Kobchenko with coauthors [15,16] performed time-resolved X-ray synchrotron tomography imaging of the sample during heating (temperature was increased from 60° to 400°C) of Green River Fm shales. At the temperature of about 350 °C, fractures along the bedding started to form in conformity with the previous experiments. Authors argue that new cracks that occurred at 350°C were associated with significant mass loss and release of light hydrocarbons generated by the decomposition of OM. Kerogen density varies in the range of 1.25-1.35 g/cm3 [5, 6], whereas hydrocarbons density generally is lower and lies between 0.5 g/cm3 and 1.2 g/cm3. Considering that kerogen forms relatively enclosed layers and inclusions, and that the total mass will not change during conversion (law of mass conservation), it might be suggested that the volume of generated hydrocarbons will be higher. So, increasing of volume leads to the increasing internal pressure build-up, which results in fracture formation. However, there are no data on pressure break point value during kerogen conversion in the literature because it is challenging task to measure this pressure. Decomposition of kerogen caused an internal pressure build-up enough to generate fractures in the sample.

Saif et al. (2016) [14] used 4D X-Ray synchrotron microtomography with simultaneous heating of immature Green River shale samples in vacuum conditions. They observed a dramatic increase of porosity at 400°C with a resulting total porosity of 22%, whereas pores were not

resolved at a lower temperature. Further heating led to a porosity increase up to 25%. A bit different experiment was performed by Saif et al. (2017) [13] to investigate Green River shale samples before and after pyrolysis (500°C) with the FIB-SEM method. The researchers found dominance of nanopores with total porosity of about 5% before heating and prevalence of 1-2 μm pores with total porosity of 18% after the heating.

Popov et al. [65] using micro-CT demonstrated an increase of porosity from 1% to 32% resulting from the Bazhenov Formation shales treatment at 450°C in the HPAI experiment in the combustion tube. At the same time, Bondarenko with colleagues [66] reported increasing porosity up to 20-30% at temperatures of 460-470°C resulting from HPAI laboratory experiment in combustion tube, porosity was measured with porosimetry method. In contrast, Mukhametdinova [67] emphasized that combustion may result in a porosity increase of up to 9%. It is essential to mention that the authors do not differentiate pores and fractures, as well as they do not specify components of the rock that became porous.

Often high-temperature treatment techniques include oxidation processes (e.g., high-pressure air injection [59]). There is a gap in the literature on investigating mineral matrix alterations during oxidation. The majority of papers are devoted to void space evaluation through pyrolysis, which represents heating in inert conditions. There are only a few studies concerning the alteration of a mineral matrix in shales during oxidative processes. Chen et al. (2017) [68] reported the results of oxidation treatment of Lower Silurian Longmaxi shale samples with H_2O_2 (15wt%). The authors showed dissolution of carbonates, reduction of inorganic minerals containing ferrous iron (e.g., pyrite and chlorite), and removing of OM. Wei Chen et al. [69] demonstrated that heating of shale samples wit air (both low and high-temperature combustion) resulted in increasing void space due to OM oxidation and rocks decarbonization (decomposition of $CaCO_3$). Sun et al. (2014) [71] observed a decomposition of inorganic minerals such as pyrite and calcite during oxidation but did not consider associated microstructural changes. The main issue of the discussed articles is an absence of void space examination and a narrow collection of samples. However, they may serve as a starting point. Sun with colleges [75] showed that transformation pyrite is possible, which potentially might cause dissolution of carbonates. Investigation of water air wet oxidation by Kaldas et al. [76] demonstrated conversion of 91% total organic carbon content at 175°C after 3 hours. In turn, Basu et al. [77] demonstrated that combustion of shales in the temperature range of 200-1400°C might be divided into five stages according carbon released during the process: at 200°C realizing of carbon trapped in pores (hydrocarbons), at 400-700°C realizing of carbon associated with clay minerals, at 500-800°C realizing form carbonate minerals, 800-1000°C realizing of carbon associated with the silicate minerals. 1200-1400°C processes associated with graphitized carbon. Chen et al. suggested that

decomposition of minerals and porosity increasing might occur during organic matter oxidation at high temperature combustion [46,78].

The most sensitive component of oil shale to heating is organic matter. Only few works are devoted to investigation of microstructure in organic matter during thermal maturation [72–74]. Wu et al. (2015) [74] stated the positive correlation of artificial maturity with organic matter (OM) porosity using SEM imaging and pyrolysis. Ko et al. (2016) [73] found from heating experiments formation of nanometer-sized organic pores at gas generation stage. Cavelan et al. (2020) [72] noted that artificial OM degradation leads to evolution of OM texture from smooth non-porous to granular porous at gas generation stage. However, the results of these works are under discussion – the authors imaged random OM inclusions during the treatment [72,73], or the obtained artificial organic pores significantly differ from the naturally occurred [74].

Alterations of mineral matrix and organic matter during thermal treatment are superficially studied. In many recent papers, researchers confirmed that fractures appear in organic-rich shales during heating. However, the studies are limited by low resolution, neglection of pore formation, and often do not specify components that became porous. A few articles devoted to the organic matter structure show that a formation of pore space in OM is possible. There are significant uncertainties with a void space in a mineral matrix and organic matter, which is formed during thermal treatment. Composition of shales is quite diverse and can vary significantly even within the Bazhenov Formation in term of mineral composition (carbonaceous, siliceous, and argillaceous), organic matter content (TOC content lies in wide range of 0.1-25%). EOR simulation studies do not consider mentioned diversity and different behavior of the components during the treatment, porosity and thermal conductivity are considered as constant values [79], which results in numerous biases. As well as a real application of thermal EOR in shales neglect mentioned factors [58]. However high-temperature treatment might cause different chemical and physical processes in a subsurface, which are not controlled or even understood well. These processes are related to crucial aspects of hydrocarbon production and technology application such as filtration pathways, physical (e.g. thermal conductivity) and chemical properties (gases, fluids etc.). All of these directly indicates, that understanding of these alterations is essential knowledge for accurate EOR processes simulation, effective interval selection and technology application.

2.4. Summary

Bazhenov Formation (BF) is a major source rock in the West Siberian petroleum basin and one of the principal unconventional reservoirs in the Russian Federation and in the World. BF rocks correspond to Upper Jurassic – Lower Cretaceous age and are composed of siliceous, carbonate, and argillaceous mudstones. Total organic carbon varies in a range of 0.1-25% with an average value of 5-10%. The organic matter is related to the kerogen II type. Maturity ranges from immature to the end of the oil window along the basin. Bazhenov Formation reservoir contains huge resources – 1.24 billion barrels of oil in-place, the majority of which are classified as shale oil.

Oil companies already propose many technology concepts to recover shale oil from black shales. The most promising ones are based on high-temperature impact. However, there is no technology with proven efficiency. The application of these techniques is associated with many uncertainties concerned void space, mineral matrix, and organic matter.

Most articles dedicated to the thermal treatment of shales focus on the investigation of void space during pyrolysis neglecting the fundamental reasons behind porosity increase. The studies are lack of differentiation of formed void space to fractures and pores and often do not specify components that became porous. A few articles devoted to alterations of a mineral matrix do not call attention to the microstructural changes during heating. Organic-rich shales are characterized by variable mineral composition even within one formation (variations of carbonate, siliceous, and clay minerals). Therefore, it is necessary to investigate the high-temperature effect differentially for different rock types. There are still many open questions around the alterations in shales during heating, and a certain need for investigation exists. The thesis is intended to expand knowledge on the behavior of different shale lithotypes during high-temperature treatment on the example of Bazhenov Formation shales. Particularly, alterations of a key shale components in terms of microstructure, chemical composition, and physical properties with a focus on pore space during high-temperature treatment.

Chapter 3. Lithological characterization of the Bazhenov Formation shales

3.1. Motivation

Lithological studies are the fundamental part of any reservoir or source rock characterization. Lithology determines a rock type (lithotype) with a particular mineralogy, texture, fabric, and pore structure. These characteristics are directly related to the physical and chemical properties of the rock, which, in turn, determine most aspects of upstream processes: using a particular bit during the drilling; the response of the well logging/petrophysical tool used to measure formation characteristics; the application of a particular EOR/IOR technique, or direction of oil and gas exploration and prospecting surveys.

The main goal of the chapter is to perform complex lithological studies of BF mudstones before high-temperature treatment. Complex characterization aids to justify the selection of particular lithotypes for the experiments and further detailed OM investigations. Since the literature review showed a wide variety of Bazhenov Formation shale rock types, it is essential to carefully perform complex characterization of available samples with further classification. For this purpose, samples were selected from two wells, located in the different areas of the West Siberian petroleum basin (Figure 3.2.1). One of the wells is located in the high north of the West Petroleum basin near the Arctic shelf region, where the lithology of the Bazhenov Formation is poorly known.

3.2. Materials and methods

Materials

According to the literature, in the northern West Siberia regions, Bazhenov Formation shales and stratigraphic equivalents are represented by bituminous argillite-like shales [80], bituminous and non-bituminous argillites [81,82] with total organic carbon content up to 5-10% [83,84]. The deposition environment is consistent with the BF within the central part of the basin, deep-water marine environment with anoxic conditions during the Upper Jurassic transgression maximum [80,81,85]. The absolute majority of publications related to the Bazhenov Formation of the West Siberia northern regions deal with the basin level lithology and geochemistry, and ignore the detailed lithological structure of the formation. Apart from the main aim of the chapter, this study fills the gap in the lithology of the BF section in the northern part of the West Siberian basin. Concerning the second well, the area is well studied, and the detailed lithological structure of the section is given by a number of authors [27,39,86]. The main rock types are siliceous mudstones

and carbonate mudstones with clay content variations. Generally, it is a good representation of a typical section of BF.

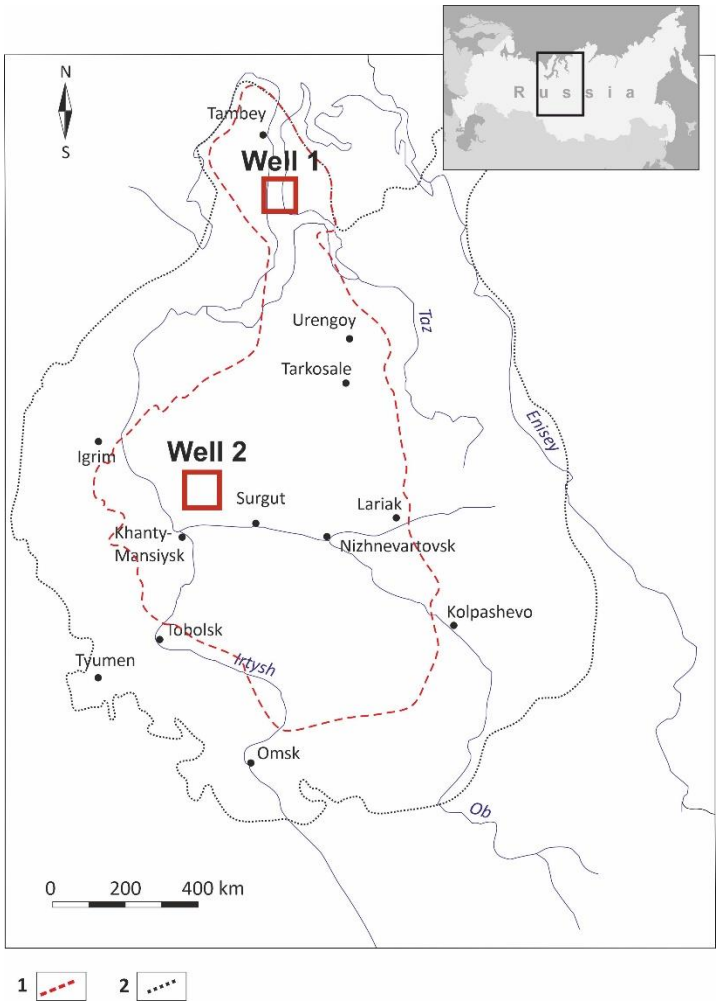

Figure 3.2.1. Location of the selected wells for the study.

Methods

Optical polarizing microscopy.

Thin 20×20 mm sections with a thickness of 10–20 μm were prepared to analyze rock texture, fabric, and mineral composition. The thin sections were investigated by the optical polarizing (petrographic) microscope AxioScope 5 (Carl Zeiss). Typically, the thickness of the specimens should be around 30 μm, however, BF mudrocks are significantly enriched with organic matter, that "hides" textural and mineralogical features, thinning helps to overcome this effect [87].

Powder X-ray diffraction

The average bulk quantitative mineralogical composition was obtained using an X-Ray Diffraction powder analysis technique with the Huber G670 instrument (transmission geometry,

linear PSD detector, Co tube Kα1=1.78892 Å, 1200 W). The analysis was performed on the powder probes of 50-100 mg.

Scanning Electron Microscopy

Scanning Electron Microscopy (SEM) is a major technique used for an investigation of rock structure at a micrometer and nanometer scale. We used Thermo Fisher Scientific Quattro ESEM on small (3-5 mm) rock samples. Samples were coated with gold (up to 20 nm thick) to discharge the samples during the scanning. Scanning involved secondary electrons (SE) and backscattered electrons (BSE), magnification x500-x200000, acceleration voltage 10–15 kV, and working distance 9–11 mm.

Programmed pyrolysis

Geochemical characterization of BF rocks was performed with HAWK Resource Workstation (Wildcat Technologies, USA) using standard Rock-Eval pyrolysis program technique [88,89]. For the analysis, a small powder probe was prepared from each sample (~200 mg). Main pyrolitical parameters were determined, such as S1, S2, S3, temperature Tmax (°C), TOC (wt.%), hydrogen index (HI, mg HC/g TOC), and oxygen index (OI, mg CO_2/g TOC).

Thermal core logging

The thermal core logging technique is based on the optical scanning instrument application and provides a continuous non-contact measurement of thermal conductivity and volumetric heat capacity on full-diameter cores, core samples, core plugs, broken cores, and other types of rock samples. The technique allows obtaining a wide set of thermal properties profiles: principal values of thermal conductivity tensor parallel ($\lambda\parallel$) and perpendicular ($\lambda\perp$) to bedding with ~1 mm spatial resolution, volumetric heat capacity (VHC), thermal anisotropy coefficient K defined as $\lambda\parallel/\ \lambda\perp$, and thermal heterogeneity factor b (defined by the ratio of difference between the maximum and minimum values to the mean value of thermal conductivity as $b = (\lambda_{max} - \lambda_{min})/\ \lambda_{avg}$). The accuracy and precision of the measured thermal conductivity are ±2% and ±1.5% respectively [90]. The technique is recognized, tested, and included in ISRM suggested methods for determining the thermal properties of rocks [90].

For the comprehensive investigation of TOC distribution over the BF depth, the method for oil shale total organic carbon profiling from thermal conductivity logging was developed and patented [91]. The method implies conversion of the thermal conductivity profile into total organic carbon content profile through several operations, which include recording of thermal conductivity (parallel to bedding component) profile with adjusted spatial resolution, sampling for pyrolysis analysis, determination of mineral matrix thermal conductivity, establishing a coupling coefficient

between thermal conductivity and total organic carbon content obtained by pyrolysis, and, finally, calculation of continuous TOC profile. The method is based on the significant thermal conductivity difference of mineral matrix (2.5-3.1 W/(m K)) and organic matter (0.2-0.4 W/(m K)) [90]. Since the thermal conductivity of mineral matrix varies in a narrow range, thermal conductivity of organic-rich mudrock is determined by variations of organic matter content.

Isotope Ratio Mass Spectrometry analyses

Sulfur isotope composition and bulk content were determined by isotope ratio mass spectrometry using an EA-IRMS system, consisting of an isotope ratio mass spectrometer IRMS Delta V plus (Thermo Fisher Scientific) connected to an Elemental Analyzer Thermo Scientific Flash 2000 (Thermo Fisher Scientific). The system provides combustion of total sulfur from the sample in SO_2 gas at 1020°C, with subsequent measurement of isotope composition. The reference materials used for calibration were: Sulfate NBS 127 $\delta^{34}S$: +21.3‰, Methionine $\delta^{34}S$: +9.3‰, and 4,4-Diaminodiphenyl sulfone $\delta^{34}S$: +6.0‰. $\delta^{34}S$ values are reported relative to Vienna Canyon Diablo troilite (V-CDT).

3.3. Results

Well 1. Northern part of West Siberian petroleum basin

The well 1 is located in the northern part of West Siberia, which is one of the most underexplored areas in the basin. Hence, the very first step of the study is a stratigraphic tie for the section, despite the initial information of its belonging to BF formation. In accordance with the regional stratigraphic scheme [28], the section belongs to the upper part of the Golchikha Formation, which total thickness may reach 950 m. The studied interval is less than 20 m, the rocks within the interval have certain similarities with the Bazhenov-Abalak complex of the central part of West Siberia in its composition and textural-structural features. Micropaleontological and palynological analyses were performed for substantiating the deposits age and refining the stratigraphic boundaries.

Stratigraphy

The deposits are impoverished of paleobiota, the solitary shells found are characterized by poor integrity and significant pyritization. Most parts of the finds fall into the lower part of the section. Notwithstanding, shells of radiolarian and foraminifers (Figure 3.3.1) in conjunction with palynoforms (spores, pollen, dinocysts, prasinophytes) provided the possibility to determine the stratigraphic identity of the deposits resolutely enough. In particular, the age of the bottom part of the section corresponds to the Later Kimmeridgian. It is confirmed by the remains of dinosysts, which are characteristic paleobiota of Georgiev Formation (Horizon) deposits (Figure 3.3.5). In the upper part of the section, shells of radiolarians and foraminifers are found (Figure 3.3.1, Figure 3.3.5), which corresponds to the Tithonian Age. In addition, the so-called “prasinophytic palynofacies” was found, which is characteristic of Bazhenov Formation deposits. The fauna and phytofossils of the upper part of the section belong to the Berriasian, Early Valanginian ages. However, in this case, impoverishment of fossils and poor preservation made it impossible to reliably determine the upper boundary of the Bazhenov Formation (i.e., the Tithonian/Berriasian boundary), that is why it was marked conditionally (Figure 3.3.5). The age of the deposits and stratigraphic subdivisions are presented in Figure 3.3.5.

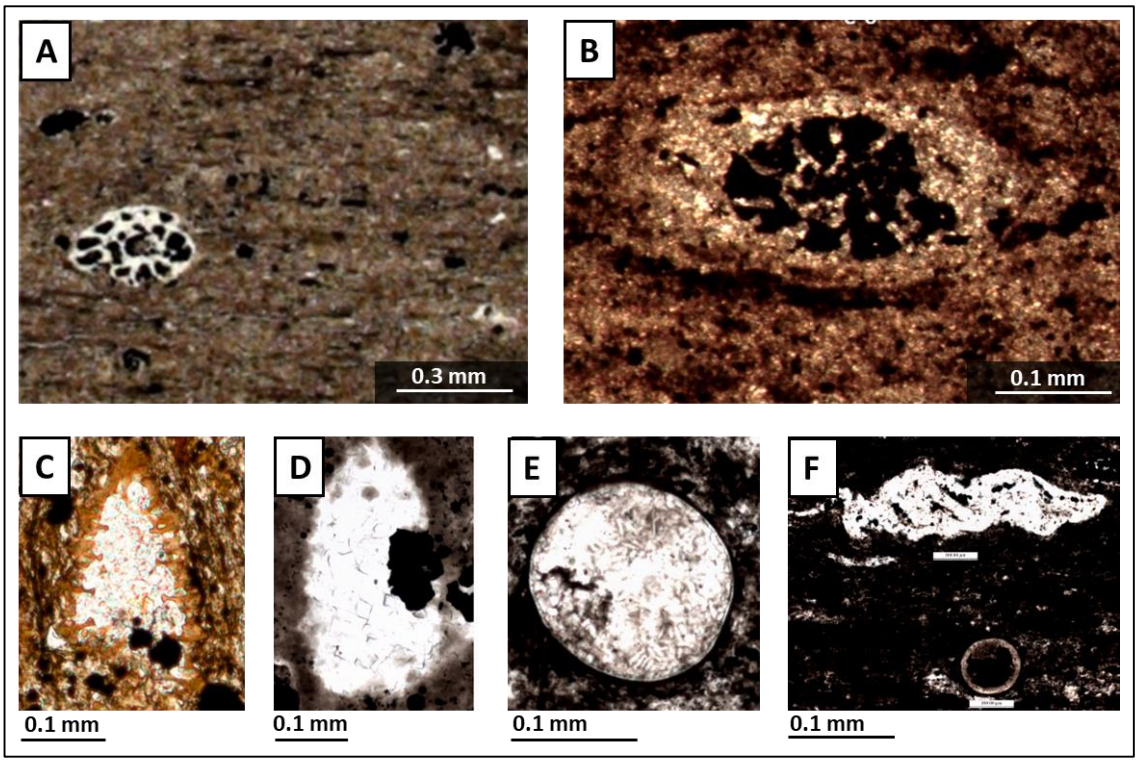

Figure 3.3.1. Examples of foraminifera (A, B) and radiolaria (C-F) relicts in thin sections.

(A, B – shells of foraminifera (*Recurvoides sp.*); C, D – radiolarian fragments cross-sections (*Parvicingula cf.sp. chabakovi* and *Lithocampe? sp. aff. St. oblongata (Rust)*), E – fragment of a radiolarian nucleus, F – the upper particle is a mollusk shell, the lower particle is a fragment of a radiolarian nucleus).

Lithology and deposition environment

Two main groups of rock types are identified: siliceous-argillaceous and carbonate mudstones. Each group is characterized by a certain assemblage of lithotypes that are differentiated on the basis of rock fabric, structural and textural characteristics, organic matter content, and mineral composition.

Group of siliceous-argillaceous mudstones. Rocks of this group are relatively uniform in mineral composition, they are dominantly composed of clay minerals (by XRD data, their average volume fraction is 42%) and the siliceous component (38% on the average). Also, some feldspars (up to 10%), pyrite (in a finely dispersed form, in a form of framboids and pseudomorphs over organic detritus, up to 8%), and in some cases carbonates (up to 3%, dolomite, less frequently calcite, in most cases carbonates are diagenetic in origin) are present in the rock. The lithotypes of the group are represented by fine-grained rocks and may be considered as mudstones according to the classification proposed by Lazar et al. [21]. The group is represented by four lithotypes that differ in rock fabric and total organic carbon content, which provides insight into the amount of organic matter (OM) in the rock.

- *Argillaceous-siliceous massive mudstone with bioturbation:* rocks are characterized by the presence of trace fossils, often pyritized. Average TOC content is 2.2% (max. 3.8%, min. 5%) (Figure 3.3.2A).
- *Argillaceous-siliceous organic-rich mudstone:* rocks without expressed lamination at the micro- and macro- levels. Average TOC content is 4.8% (max. 7.8%, min. 2.3%) (Figure 3.3.2B).
- *Argillaceous-siliceous organic-rich mudstone with microscale planar lamination:* distinctive characteristic is strongly pronounced thin lamination that may be diagnosed under the microscope only and is caused by the lamina-by-lamina distribution of organic matter, clay minerals, and siliceous component. Average TOC content is 7.6% (max. 12%, min. 3%) (Figure 3.3.2C).
- *Argillaceous-siliceous laminated mudstone with bioturbation:* rocks are characterized by rhythmic horizontal lamination caused by the presence of darker (enriched in OM) and light (lean in OM) zones with trace fossils. Average TOC content is 1.9% (max. 4.3%, min. 0.9%) (Figure 3.3.2D).

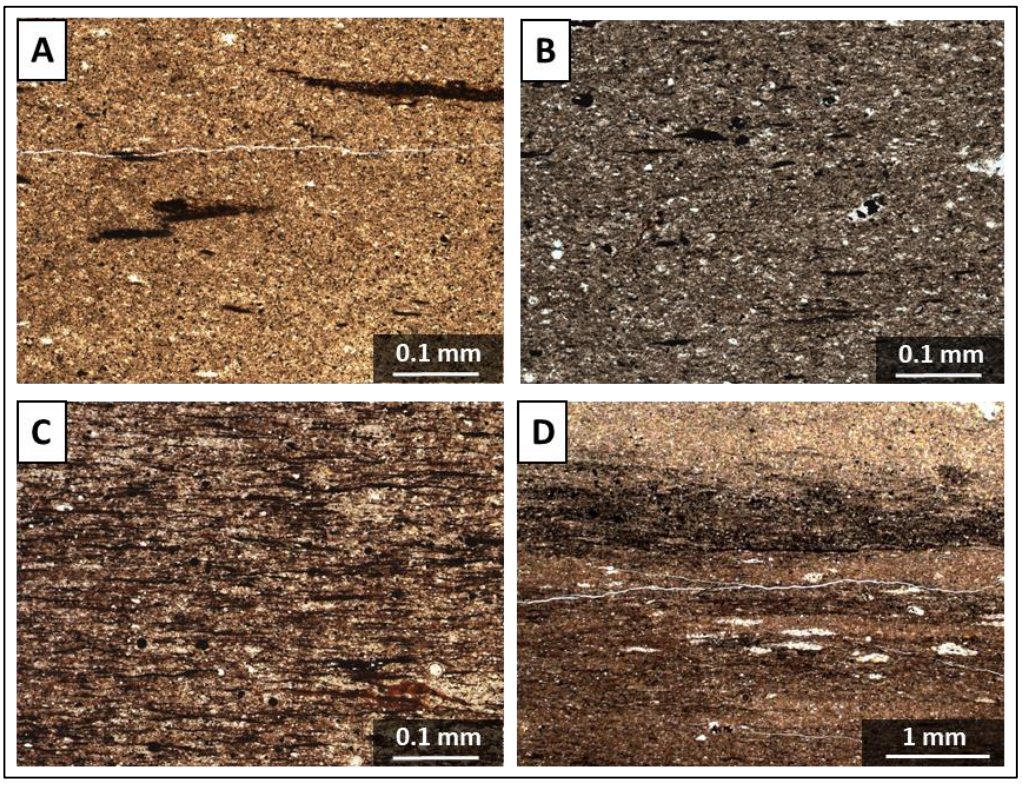

Figure 3.3.2. Thin-section microphotographs of siliceous-argillaceous mudstones: A - argillaceous-siliceous massive mudstone with bioturbation, B - argillaceous-siliceous organic-rich mudstone, C - argillaceous-siliceous organic-rich mudstone with microscale planar lamination, D - Argillaceous-siliceous laminated mudstone with bioturbation.

Group of carbonate rocks. Rocks are composed mainly of fine-grained (<20 μm) carbonate minerals: calcite, dolomite and siderite, the content of carbonates are in the range of 70-85%. The siliceous component is present in an amount of 7-16%, while clay minerals and feldspars play a minor role in a mineralogical composition (up to 5%), pyrite in various forms is observed (up to 3%). Detected are solitary poorly preserved (destruction, pyritization) relicts of mollusks and radiolarians shells are detected. TOC content is less than 2%. Three lithotypes are distinguished, which differ in rock fabric and mineral composition.

- *Dolomitic-siliceous fine-grained siderite:* rock is composed of crystalline siderite by 42% and of dolomite by 35%; siliceous fine-crystalline and cryptocrystalline mass are rated at about 16% (Figure 3.3.3A). Clay minerals and pyrite account for 7%.
- *Siliceous fine-grained limestone:* rock is represented by two varieties – fine-crystalline and microcrystalline ones. The main component is calcite – 75%, the siliceous component is present in the cryptocrystalline form in a lesser amount – 12% (Figure 3.3.3B).

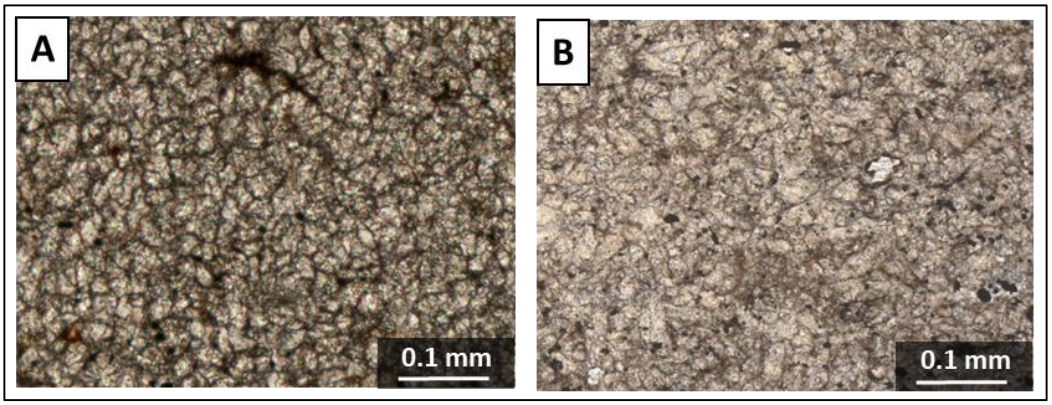

Figure 3.3.3. Thin-section microphotographs of carbonate lithotypes: A - dolomitic-siliceous fine-grained siderite, B - siliceous fine-grained limestone.

The lower part of the section is the age equivalent of the Georgievskiy Formation and it is represented by massive argillaceous rocks, often with trace fossils. Two thin interlayers of siliceous-dolomitic (~20 cm) secondary siderite and fine-crystalline siliceous limestone (~30 cm), probably, developed over rocks of siliceous-argillaceous composition. TOC content in the rock mass is rather stable and is within the range of 1.5% to 3.9% with an average value of 2.2%, organic matter contains kerogen of mixed type II-III (Figure 3.3.5). Uniform argillite dominated mineral composition, bioturbation, low amount of detritus and mixed-composition OM indicate that the deposits were formed in a quiet hydrodynamic environment at some distance from a provenance area, in the presence of oxygen in the near-bottom water layer, which favored the life of burrowing organisms and made it not possible for OM to preserve in full measure.

Based on lithology and TOC content, eight members within BF were distinguished. The members are different in TOC, texture, and structure. Organic matter corresponds to II and III types (Figure 3.3.5). The main part of the section is composed of argillaceous-siliceous rocks (Figure 3.3.5) with a relatively stable mineral composition, differing textural features, and TOC content. The deposits are characterized by laminated, thinly-laminated and microlaminated textures that are manifested on different scales. TOC content varies within the range of 1-12% with an average value of 5%. The transition interval of the Georgievskiy Formation into the Bazhenov Formation is characterized by a gradual increase of TOC and the appearance of thin lamination in the first member (Figure 3.3.5). This is a result of the formation of conditions favorable for OM accumulation and burial with a simultaneous increase in bioproductivity. The first member is composed of argillaceous-siliceous organic-rich mudstone with microscale planar lamination, which is characterized by highly pronounces microlamination, which is caused by the lamina-by-lamina distribution of OM in the form of wisps and lenticules that are identifiable under a microscope only. At the same time, the member is characterized by the highest amount of pyrite, in individual cases fraction of pyrite reaches 13%. The scanning electron microscope investigation demonstrated the dominance of framboidal pyrite, which is closely associated with OM: organic matter envelops pyrite crystals and may fill the space between the crystals (Figure 3.3.3A), which indicates their conjoint formation. Organic matter contains kerogen of type II. The dominance of type II kerogen and framboidal pyrite, microlaminated fabric and argillaceous-siliceous composition are evidential of the developing deep-water anaerobic environments with sulfuric contamination, that favored OM accumulation and preservation. Members 2 and 3 are similar to member 1 in many aspects. Member 2 is characterized mainly by a lower OM content (TOC = 3.4÷6.7%, average 4.7%). Member 3 is analogous to the first one, is characterized by highly pronounced microlaminated texture and the highest OM content in the section (TOC = 6.4÷11.6%, average 8.8%), OM contains kerogen of type II. The formation of rocks took place in deep-water anaerobic environments, though probably with episodic oxygen income. Member 4 differs from all the above-described ones by poorly pronounced laminated texture. It is composed of argillaceous-siliceous massive mudstone with bioturbation. OM is presented in finely dispersed form; OM content is not very high (TOC = 1.4÷7.3%, average 4.3%), kerogen belongs to a mixed type (II and III, Figure 3.3.5). Individual fragments of quartz and feldspar silt-sized clasts, bioturbation marks were observed. These are evidenced in the formation of rocks in relative vicinity to the provenance area, nonetheless, anaerobic conditions and sulfuric contamination existed to some extent. Members 5 and 7 are close in their properties to members 1 and 3, organic carbon content is 4÷8.7% with an average of 7.1% and 6.3÷9.5% with an average of 7.6%, respectively. Organic matter is represented with kerogen of mainly type II. An absence of clastic

material and increased values of TOC content are evidential of a deep-water anaerobic depositional environment. Members 6 and 8 are characterized by macroscopic lamination caused by the rhythmic alternation of dark (enriched with OM) and light-colored (lean in OM) interlayer. The OM is represented by mixed type kerogen. TOC content is non-uniform and varies within the range of 0.5÷4.3% with an average of 2%. Macroscopic lamination is a result of the changeability of redox conditions caused by sea level fluctuations, which probably entailed income of oxygen with breach of anaerobic conditions and sulfuric contamination.

According to Kontorovich et al. [92] in the Volgian time the study area was occupied by a deep-sea (200-400 m), which resulted in siliceous-argillaceous mudstones with thin-laminated fabric. However, the section is characterized by significant variations of TOC content, presence of both macrolaminated and massive mudstones, presence of silty material, and bioturbations, that altogether being evidential of variability of redox conditions. Zakharov et al. in [82] suggest that the Bazhenov sea in the Upper Jurassic – Lower Cretaceous time was connected with the Arctic Basin by a strait located in the territory of the present-day Yamal Peninsula. It is supposed that a barrier existed on the bottom of the strait, that controlled the ingress of arctic waters enriched with oxygen into the Bazhenov sea. During periods of low sea level and high position of the barrier, communication of water masses was hampered, and anoxia was formed in near-bottom waters and at the sediment-water interface, which favorably affected the organic matter accumulation and preservation. A sea level rise and lowering of the threshold lead to arctic water inflow enriched with the oxygen Bazhenov sea, flourishing of life-activity of filter-feeding organisms consuming organic matter and forming sub-oxidizing depositional environments that encumbered organic matter accumulation and burial. The investigated well is located close to the paleobarrier, and we suggest variations in TOC contents, quality of organic matter, presence of laminated and massive structures, the appearance of silty material, and bioturbations caused by the vertical position of the paleobarrier, which controlled influx of arctic water masses with oxygen. The members 4, 6, 8 with relatively low TOC content, presence of bioturbation, and silty material were most probably formed in periods of high sea level (low position of the barrier) and ingress of arctic waters saturated with oxygen. In these same periods, ingress of humic organic matter took place that was associated with activation of underwater currents connected with the clastic source area. Currents brought silty material, aeration of the sediment favored life activity of burrowing organisms. While the formation of members 1-3, 5, 7 is associated with a lower sea level and a higher position of the barrier, and, as a consequence, hampered water exchange. During this period, the accumulation of maximum amounts of marine organic matter took place. Leushina et al. [93] demonstrated geochemical observations on the same well, that confirm given conclusions, the authors using specific elemental ratios came to similar conclusions.

Sulfur isotope composition

Mass spectrometry analysis (IRMS) allowed to evaluate bulk $\delta^{34}S$ in the samples (Figure 3.3.5). The values of $\delta^{34}SCDT$ vary from −37.3 to +4.2‰, although most of the sulfur is isotopically light (i.e., $-37.3 \leq \delta^{34}SCDT \leq -18.6$‰). Only within three samples $\delta^{34}SCDT$ exceeds −18‰: −7.8‰ (member 5); −4.4‰ (member 6); and +4.2‰ (member 8). The results are shown in the [94]. The main host of sulfur in the mudstones is pyrite. The variations of sulfur isotope composition are caused by the form of pyrite aggregates, which are variously sized framboids and individual crystals. The specific aggregates of pyrite correspond to a particular redox setting in the basin. The abundance of small framboids (up to 10 μm) suggests that sedimentation occurred in the anoxia dominated conditions with the presence of hydrogen sulfide above sediment-water boundary or in the upper layer of sediments with an excess of marine sulfate. These conditions are also favorable for the organic matter accumulation and preservation. This assumption is in good correspondence with the SEM observations of OM within framboids. Larger framboids and individual pyrite crystals (>10 μm) are evidence of suboxic accumulation conditions, and considered as a secondary mineral, formed during diagenesis. These assumptions correspond well to the observations based on the lithology and TOC content.

Void space

Investigation of mudstones with scanning electronic microscope demonstrated that there are different morphological types of voids, which are intercrystalline and intracrystalline space in clay minerals. The size of voids varies from first micrometers up to 10-20 μm. The most typical pores are inter-layer, inter-aggregate slit-pores in the clay minerals (Figure 3.3.4). Horizontal dominated orientation of clay minerals (microlamination) considerably influences anisotropy of poroperm properties. Space filled with kerogen also may be considered as potential void space, resulting from thermal EOR techniques application.

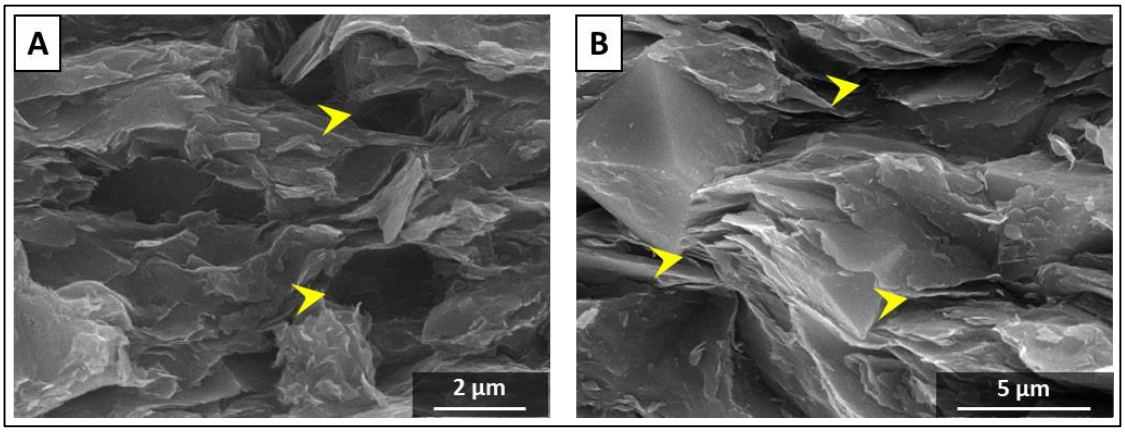

Figure 3.3.4. Void space in siliceous-argillaceous mudstones. A – isometric intercrystalline pores, B – elongated inter-aggregate voids in clay minerals.

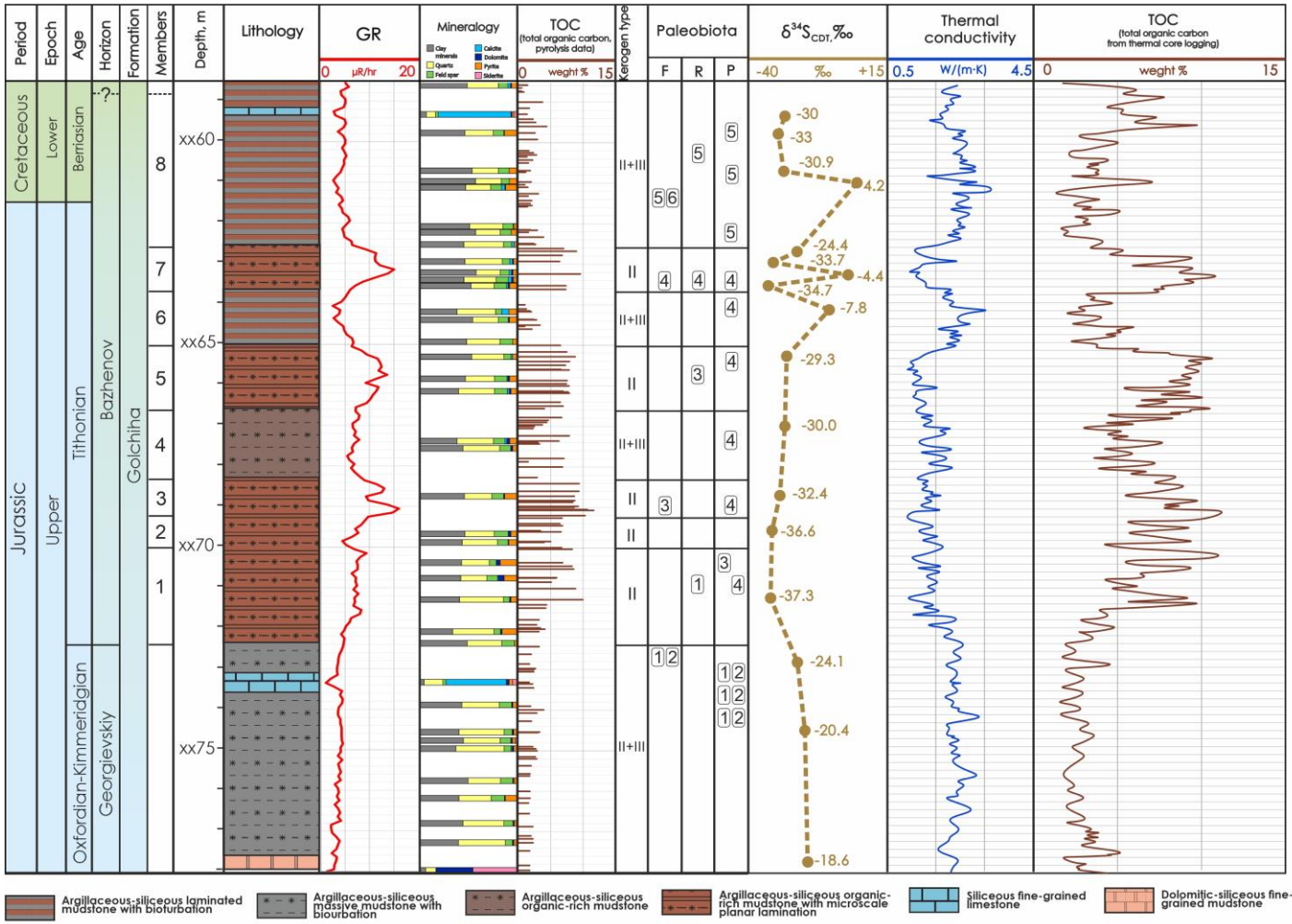

Figure 3.3.5. Summarized well 1 section column of the studied interval.

(Paleobiota. F – foraminifera:*1 - Lenticulina cf. Gerkei Dain, 2- Trochammina ex.gr. kumaensis Levina, 3 -Spiroplectammina cf. vicinalis Dain, 4 - Evolutinella cf. emeljanzevi (Schleifer), 5 - Lenticulina gigantella Rom., 6 - Trochammina cf. polymera Dubrovskaya,* ***R – radiolaria:*** *1 -Parvicingula cf. Multipora, 2- Dictyomitra? cf. sp. ex gr. multicostata Zittel, 3 - Parvicingula ? sp., 4 - Cenosphaera? sp., 5 - Gen. sp. Indet,* ***P – palinomorphs:*** *1 - Disaccites-Classopollis-Sciadopityspollenites, 2- Prolixosphaeridium-Valensiella- Cassiculosphaeridia, 3 - Botryococcus spp., 4 - «prasinophyte palynofacie», 5 - Dingodinium spp.-Cleistosphaeridium spp.-Sentusidinium spp.)*

Well 2. Central part of West Siberian petroleum basin

The second well is located in the central part of the West Siberian petroleum basin. Bazhenov Formation at the central part is the most studied in many aspects, including stratigraphy, lithology and geochemistry by a number of authors [20,27,39]. Regional correlation allowed to distinguish Bazehnov Formation, and there is no essential need for detailed stratigraphic investigations. The focus is made on the lithological variety of the BF in that part of the basin.

Lithology

The rocks are represented predominantly by mudstones, which differ in composition, structure and texture. Distinct differences in mineral composition and rock fabric allowed to distinguish 6 lithotypes (Figure 3.3.6), which form 4 members in the studied interval (Figure 3.3.7).

- *Siliceous-argillaceous organic-rich mudstone.* The rock is composed predominantly of fine-grained quartz (50-65 volume %) and clay minerals (20-35 volume %) with an average TOC content of 12 weight %. The rock is characterized by laminated OM and clay minerals distribution, which causes thin-laminated rock fabric (Figure 3.3.6A).
- *Argillaceous-siliceous mudstone.* The mudstone is composed of clay minerals (65-70%) and quartz (25-30%), an average TOC content is around 3%. The rock is characterized by indistinct lamination (Figure 3.3.6B). The lithotype is common for the Abalak Formation, and is not observed in Bazhenov Formation interval.
- *Siliceous mudstone (radiolarite).* The rock consists of quartz (90-95%) and it is characterized by radiolarian relicts and a minor amount of clay minerals. Organic matter is distributed in a patchy manner; the average TOC content is approximately 4.5%. A void space was observed in the lithotypes, represented by intercrystalline pores, porosity varies in the range of 2-5% (Figure 3.3.6C).
- *Aporadiolarian siliceous crystalline dolomite.* The lithotype represents medium-to-fine grained dolomite dominated radiolarite (crystals 50-100 μm in size, 85-90%) with fine-grained quartz (up to 10-15%). Initial siliceous radiolarian material is considered to be replaced by dolomite during diagenesis. Quartz represents fine (10-15 μm) idiomorphic crystals, which partially occupy the surface of dolomite crystals. Organic matter has a patchy distribution, an average TOC content is 3%. The rock is characterized by the porosity of 3-8% (Figure 3.3.6D).

- *Calcareous mudstone.* The mudstone is predominantly composed of fine-grained calcite (60-95%), with a minor amount of dolomite (up to 20%) and quartz (up to 10%). The rock is depleted in organic matter and TOC content does not exceed 2-5% (Figure 3.3.6E).
- *Argillaceous-calcareous organic-rich mudstone.* The lithotype represents a mixture of calcite and clay minerals. Calcite is presented in the form of distinct laminas and lenses in the clay minerals matrix, or there is thin interlayering of clay and calcite components. Bulk mineral composition varies, the major part of the rock is represented by clay minerals (up to 50-70%), calcite occupies a smaller part of a rock (30-50%). The mudstone is enriched with organic matter, which is presented in the form of thin laminas, lenses, and inclusions. An average TOC content is approximately 12% (Figure 3.3.6F).

Based on lithotype order and succession, 4 members were distinguished within BF interval. The members generally represent repeating cycles of sedimentation. There are two pairs of members, first and second, third and fourth. The members within a pair are quite similar in terms of composition, lithotypes succession, and thickness. The basement of the first and second members is composed of argillaceous-calcareous and calcareous mudstones; which are overlain by the siliceous and siliceous-argillaceous mudstones. Intervals of siliceous mudstones are characterized by depleted TOC content and increased porosity. The third and fourth members are represented by the mixed rocks: interlayering of siliceous-argillaceous and argillaceous-calcareous mudstones in the lower part, and the dominance of argillaceous-calcareous mudstones in the upper part.

The formation of the BF rocks is related to the deep marine anoxic environment, which varied in degree of anoxia, presence of local deep water streams and bioproductivity during Tithonian and Berriasian time [27,41,82]. These variations resulted in fluctuations of TOC content and lithotype variability. Radiolarian dominated lithotypes are considered to be formed during the significant increase of radiolarian bioproductivity. Lenses, inclusions, sometimes the presence of single radiolarians are the result of water movement activation during sedimentation. In contrast, most of the carbonates have a secondary (diagenetic) origin, except rare coccolithophorid layers and mollusk relicts [95]. Carbonatization of radiolarites occurred due to the presence of void space and the ability of these rocks to filtrate the water solutions. This process resulted in the formation of apporadiolarian dolomite/limestone. The source of magnesium potentially might be algae, or clay minerals, which lose their magnesium during diagenesis. The combination of these processes led to a wide variety of rock types in the Bazhenov Formation shales.

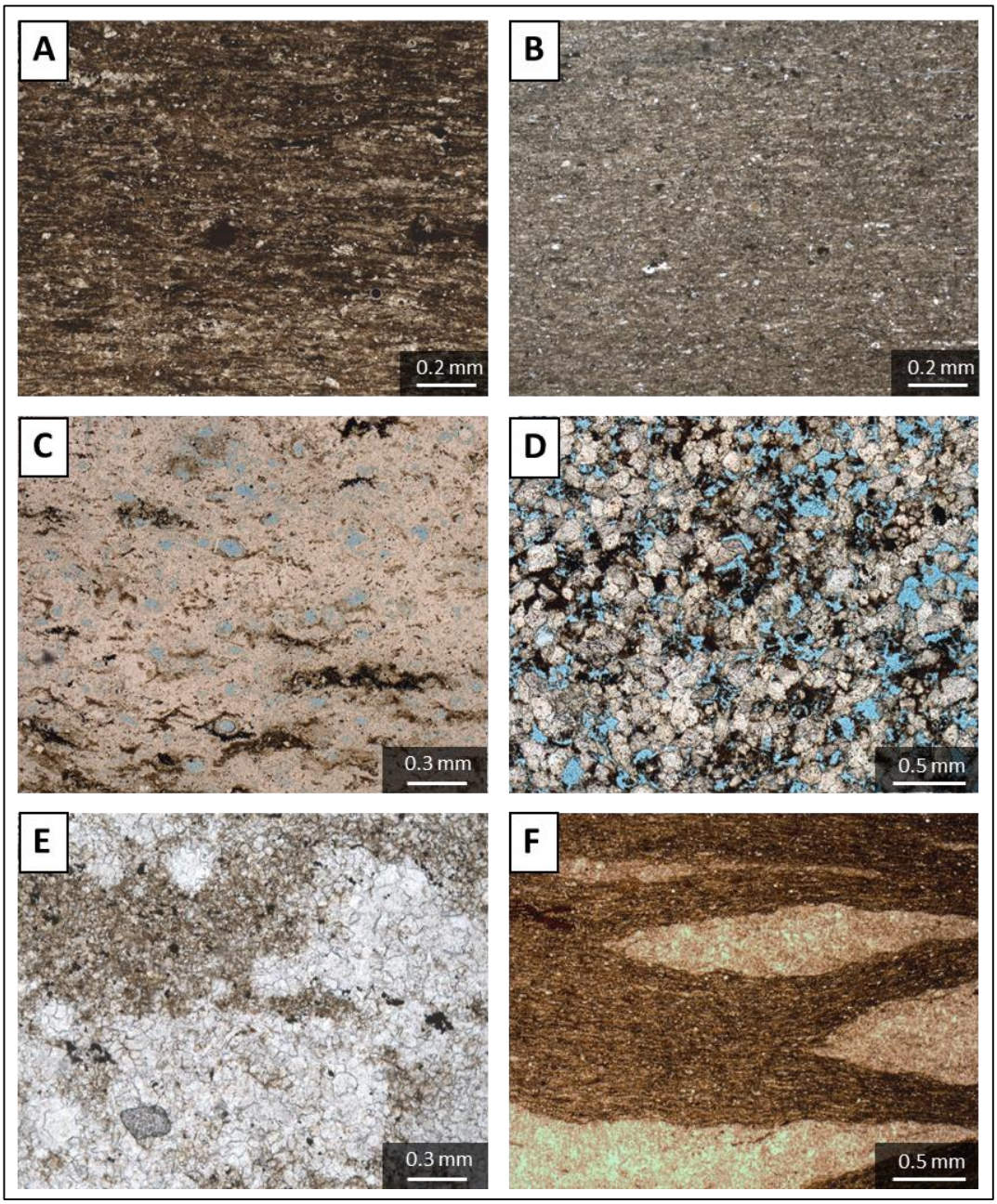

Figure 3.3.6. Thin section microphotographs of the main lithotypes.

A – siliceous-argillaceous organic-rich mudstone; B – argillaceous-siliceous mudstone; C – siliceous mudstone (radiolarite); D – aporadiolarian siliceous crystalline dolomite; E – calcareous mudstone; F – argillaceous-calcareous organic-rich mudstone.

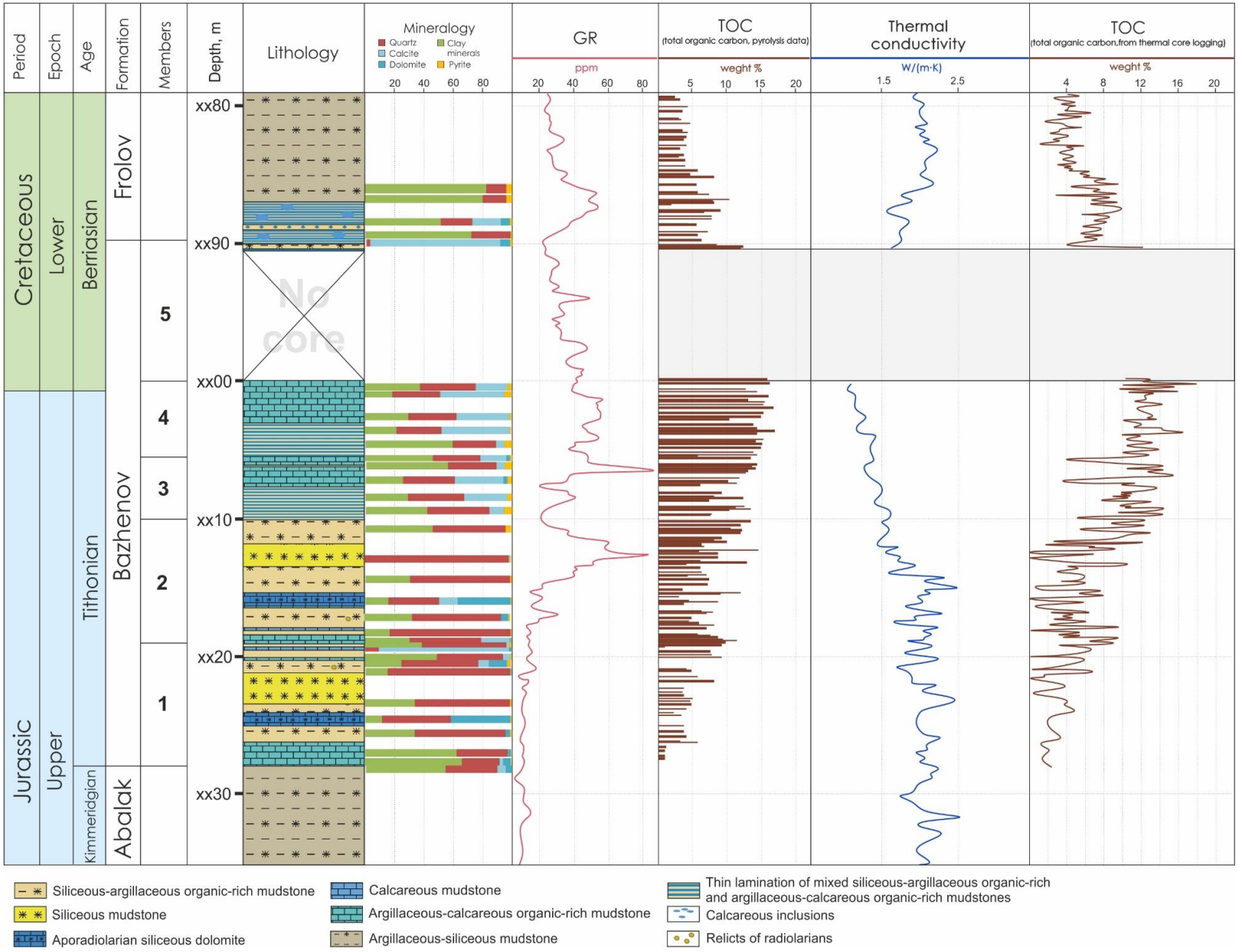

Figure 3.3.7. Summarized well 2 section of the studied interval.

Void space

Across studied BF interval only two lithotypes are characterized with a systematic porosity, and both are associated with radiolarian relict enrichment: siliceous mudstone (radiolarite) and aporadiolarian siliceous crystalline dolomite. Porosity in siliceous mudstone (radiolarite) is in the range of 2-5%, in aporadiolarian siliceous crystalline dolomite porosity is considerably higher and in the range of 3-8%, in some local areas may exceed 10%. In both cases, pore space is concentrated in the intercrystalline space. The size of individual pores is comparable for both rock types and varies from 0.01 mm to 0.3 mm, however, the major part of pores is approximately 0.05-0.1 mm in size (Figure 3.3.6C and D).

A different type of porosity is related to organic matter (kerogen). Pores in the organic matter are not systematic and have the size of nano- and micrometers order (Figure 3.3.8). However, there are examples in the literature, where organic porosity may cause porosity higher than 5% and be characterized by the size of first micrometers [96]. Organic porosity is common for the OM enriched lithotypes, such as argillaceous-calcareous and siliceous-argillaceous organic-rich mudstones. OM pores are often considered as a result of thermal maturation [97], and it would be a reasonable suggestion that high temperature based EOR techniques will significantly affect the OM porosity and structure. The occurrence of a such porosity types of in shales is still the object of debate, and there is a certain need for deeper study. Chapter 5 addresses this issue and reveals important aspects of organic porosity across natural thermal maturation gradient and its formation during artificial maturation (thermal treatment).

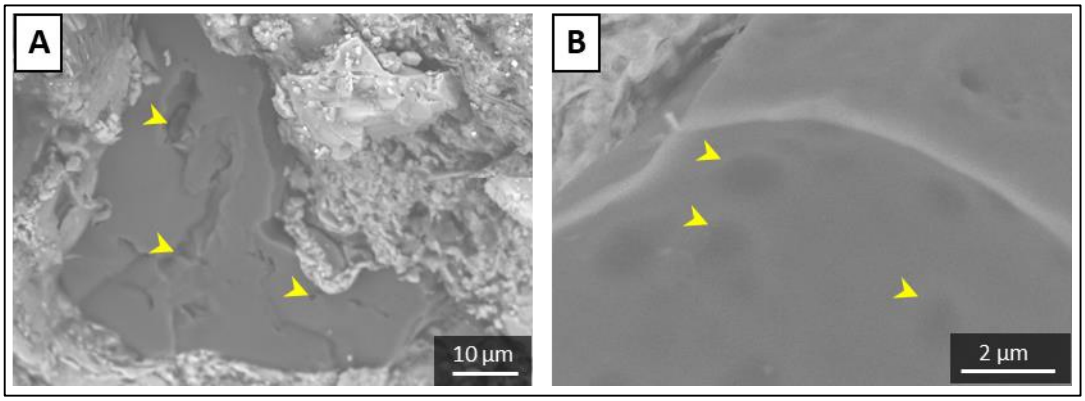

Figure 3.3.8. Single pores in organic matter.

3.4. Summary

Complex lithological characterization of the BF interval in two wells has been performed. The Bazhenov shales in the northern part of the West Siberian petroleum basin are characterized by relatively stable mineralogical composition, however, certain differences in rock fabric, texture, structure and TOC content are observed. The major rock type is argillaceous-siliceous mudstone, which is subdivided into several lithotypes according to mentioned differences in rock fabric, texture, structure, and TOC content. Carbonate rocks form rare thin layers and are represented by fine-grained limestone and siderite. In contrast, the Bazhenov Formation shales in the central part of the West Siberian petroleum basin are variable in mineral composition, they contain siliceous, carbonate and clay components. Based on the combination of the components and their structural relationships the following lithotypes have been distinguished: siliceous mudstones, siliceous-argillaceous organic-rich mudstones, apporadiolarian siliceous dolomite, calcareous mudstone, argillaceous-siliceous mudstone, and argillaceous-calcareous organic-rich mudstone.

The following lithotypes encompass the main variability of BF lithology in term of mineralogical composition, porosity, and organic matter content: siliceous mudstone, aporadiolarian siliceous dolomite, argillaceous-siliceous organic-rich mudstone, and calcareous-argillaceous organic-rich mudstone.

Chapter 4. Experimental modeling of the mineral matrix alteration and void space evolution during high temperature treatment

4.1. Motivation

High-temperature based EOR techniques are promising for effective shale recovery due to two key processes: displacement of existing hydrocarbons and transformation of solid organic matter into liquid hydrocarbons. These processes are strongly associated with void space evolution during thermal treatment. Void space is an essential proxy for the hydrocarbons filtration during recovery. However, there are still many questions concerning driving factors for pore space evolution, mineral matrix alterations, and microstructural OM transformation during the treatment. Shedding the light on those issues permit reasonably select shale intervals for technology application, improve computational simulation of high-temperature EOR processes due to understanding of exact alteration of the mineral matrix and OM, and to predict pore space evolution during technologies application.

This chapter is devoted to the investigation of the pore space evolution, alterations in the mineral matrix (structure and phase composition) and accompanying chemical and physical properties during the high temperature treatment. Prepared sample collection encompasses a wide variety of Bazhenov Formation lithology. High-temperature treatment experiment was performed in the laboratory combustion tube, which represents a physical model of the high-pressure injection process. The temperatures of the treatment are in the range of 109 – 919°C. Alterations of void space and mineral matrix were examined with set of lithological, geochemical and petrophysical methods. Obtained results revealed mineral matrix transformations and the evolution of void space during the high-temperature treatment.

4.2. Samples

Samples were prepared after detailed lithological studies of Bazhenov shales, described in the previous chapter. Sample collection for the experiment include 4 different lithotypes, which vary in mineral composition, rock fabric, texture, structure, amount of OM and porosity. These lithotypes may be considered as a representative collection of the BF. Prepared lithotypes encompasses the major mineral component variations of the Bazhenov Formation shales: carbnonate, siliceous and clay components. These lithotypes are siliceous mudstone, aporadiolarian siliceous dolomites, argillaceous-siliceous organic-rich mudstone, calcareous-argillaceous organic-rich mudstone. Two of them, siliceous mudstone and aporadiolarian siliceous dolomites are considered as a reservoir rock types and are characterized by presence of porosity.

Two others are source rock lithotypes, they contain significant amount of organic matter. Representative sample (i.e. includes all the inherent heterogeneities) was prepared for each lithotype with the size of 5x5x10 cm.

4.3. Experiment design

To study pore space evolution and mineral matrix alterations in Bazhenov shales a laboratory experiment in the combustion tube was performed. The experiment represents a physical laboratory model of *in-situ* high-pressure air injection. The combustion tube diameter is 100 mm, the tube consists of 33 zones, each zone is 50 mm in length. Each zone is equipped by external heaters and thermocouples to record temperature one the wall surface and in the center of the tube. Heat losses are reduced by the thermal insulation.

To achive the aim of the experiment each lithotype sample was divided into four parts (subsamples), as a result sixteen subsmples were prepared (4 lithotypes x 4 subsamples). Three subsamples (out of four) of each lithotype were packed into the three specific zones of the tube, and one served as a reference, unexposed, sample. In total, 12 subsamples were packed in the tube, 4 served as references. Samples were loaded at different zones of the tube to touch the specific areas of expected position of the combustion front: behind the combustion front (zone 11, A in Figure 4.3.1), ahead of the front (zone 24, C in Figure 4.3.1), and approximately on the front/slightly ahead (zone 18, B in Figure 4.3.1) Table 4.3.1 provides the list of the subsamples prepared for the experiment. Major space of the tube was filled by disintegrated core of Bazhenov shales (0.1–1 mm fraction) without additional saturation. The first and the last sections were loaded by the siliceous sand to prevent small particles ingress into the system of liquid analysis. The simplified scheme of the combustion tube with the loaded subsamples is shown in Figure 4.3.1.

Table 4.3.1. List of the samples for the experiment.

Lithotype	**Sample ID**	**Zone in combustion tube**
Siliceous mudstone	1O	Reference (not packed)
	1C	24
	1B	18
	1A	11
Aporadiolarian siliceous dolomites	2O	Reference (not packed)
	2C	24
	2B	18

	2A	11
Argillaceous-siliceous organic-rich mudstone	3O	Reference (not packed)
	3C	24
	3B	18
	3A	11
Calcareous-argillaceous organic-rich mudstone	4O	Reference (not packed)
	4C	24
	4B	18
	4A	11

Combustion tube, packed with the samples and disintegrated core (porosity ~30%), was pressurized by helium up to formation pressure (31MPa) and the temperature was increased up to 100°C (formation temperature). The system for liquid and gaseous products collection was connected to the tube outlet, however, since analysis of fluids is beyond of the key aim and objectives of the study, they are not discussed. Four zones of combustion tube were preheated to 200°C to accelerate the ignition and to start the high-temperature oxidation. The experiment was performed according to following steps.

1. Injection of helium gas to build up the pressure up to the formation pressure ~31 MPa with simultaneous temperature increase up to the ~100°C.
2. Heating of the 1-4 zones up to 200°C during helium injection (flux is 40 $m^3/(m^2 \cdot h)$).
3. Injection of air for combustion initialization (flux is 40 $m^3/(m^2 \cdot h)$). The regime was close to the adiabatic and controlled by programmed heaters. Each 30 minute fluids and gases were sampled from the outlet.
4. After the combustion front reached 16th zone, injection of air was terminated, injection of nitrogen started.
5. After the disappearing of combustion gases nitrogen injection was stopped. Samples were retrieved and prepared for the studies.

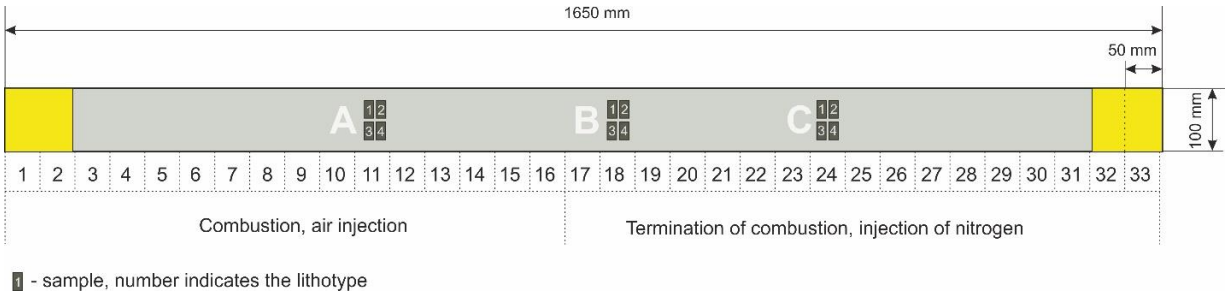

Figure 4.3.1. The scheme of the combustion tube with the packed samples.

4.4. Methods

Optical polarized microscopy

The method is described in the "Chapter 3. Lithological characterization of the Bazhenov Formation shales"**.** From each subsample a thin-section was prepared and studied.

Scanning Electron microscopy

Scanning Electron Microscopy (SEM) is a major method that allows to effectively investigate porosity at micro- and nanoscale [96,98]. Prepared probes were imaged using a Thermo Fisher Scientific I Quattro S SEM instrument equipped with secondary electron (SE) detector for pore investigation (5-10 kV, working distance 9-10 mm) and backscattered electron (BSE) detector for mineralogical heterogeneity investigation based on phase density contrast. An integrated EDS instrument (Quantax, Bruker, USA) helped to perform semi-quantitative elemental analysis in one point (point analysis) and across area (mapping).

X-ray powder diffraction

X-ray powder diffraction allows to perform semi-quantitative analysis of mineral composition. For detailed investigation of mineral matrix alterations during thermal treatment and uncertainty reduction two X-ray powder diffraction geometries were used: reflection geometry (Bregg-Brentanto) and transmission geometry (Debye-Scherrer). Reflection geometry was applied using Bruker D8 ADVANCE (Germany). The instrument is equipped with energy dispersive detector LYNXEYE XE, includes two copper X-ray tubes (Ka1=1.54051 Å, Ka2=1.54433 Å, max power 1600 W). For transmission geometry Huber G670 was used. The diffractometer is equipped with linear PSD detector, cobalt X-ray tube (Ka1=1.78892 Å, , max power 1200 W).

Micro-CT imaging

Investigation samples 3D microstructure was carried out with micro-computed tomography (micro-CT) by GE Phoenix CT System v|tome|×L240. The system is equipped with 180 kV nanofocus X-ray tubes and a 2048 × 2048 pixel^2 on 14-bit GE DXR-250 flat panel detector. The accelerating voltage and the beam current of X-ray tube was 70–200 kV and 140–580 µA, respectively. The number of projections was 2400. Raw data were acquired by the GE datos|x software, Reconstruction and further processing of data was made in GE datos|x and PerGeos software.

For the micro-CT imaging, the cylindrical specimens with 3 mm diameter and 3 mm height were dry cut using a low-speed diamond drilling bit. The same volume was scanned with the voxel size of 2.6 µm.

Thermal property profiling (thermal conductivity profiling)

The method is described in the “Chapter 3. Lithological characterization of the Bazhenov Formation shales”**.** However, unlike previous chapter, the measurements were performed on individual samples. All the samples were measured; each sample were measured three times for uncertainty reduction.

Programmed pyrolysis

The method is described in the “Chapter 3. Lithological characterization of the Bazhenov Formation shales”**.**

Isotope Ratio Mass Spectrometry analyses

The method is described in the “Chapter 3. Lithological characterization of the Bazhenov Formation shales”**.**

4.5. Results

The experiment was conducted as it was planned, the experiment duration was approximately 48 hours. Scheme of the experiment is given in Figure 4.5.1. The experiment temperatures were in the range of 109 – 919°C. The packed subsamples were in the planned intervals/zones. According to Bondarenko [99] four intervals can be distinguished after the experiment: burned, combustion front, transition interval, and the interval of kerogen pyrolysis and products displacement. Burned interval is characterized by converted and displaced OM. Combustion front is an active reaction zone of OM oxidation/burning. Transitional interval is considered as an interval of kerogen decomposition due to pyrolysis and hydropyrolysis.

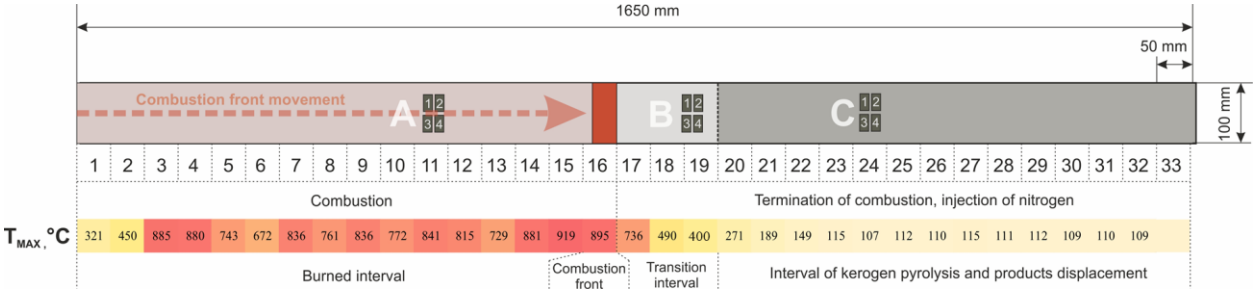

Figure 4.5.1. Resulting scheme of the experiment, differentiation of the tube into main intervals. Arrow indicates combustion path.

The following sections contain results and observations made by described methods. The mechanisms and processes behind the results are considered in Chapter 6.

4.5.1. Photographs of the samples

Photographs obtained by the optical microscope are given in Figure 4.5.2. The general trend observed from the photographs is lightening of the samples with temperature increase and the reddish color of the samples after the combustion front. On the two samples 2B and 4B boundary of combustion was observed, which indicates the combustion front propagation into solid samples. Reddish particles and whisps were observed in the samples after the combustion front propogtion (841ºC).

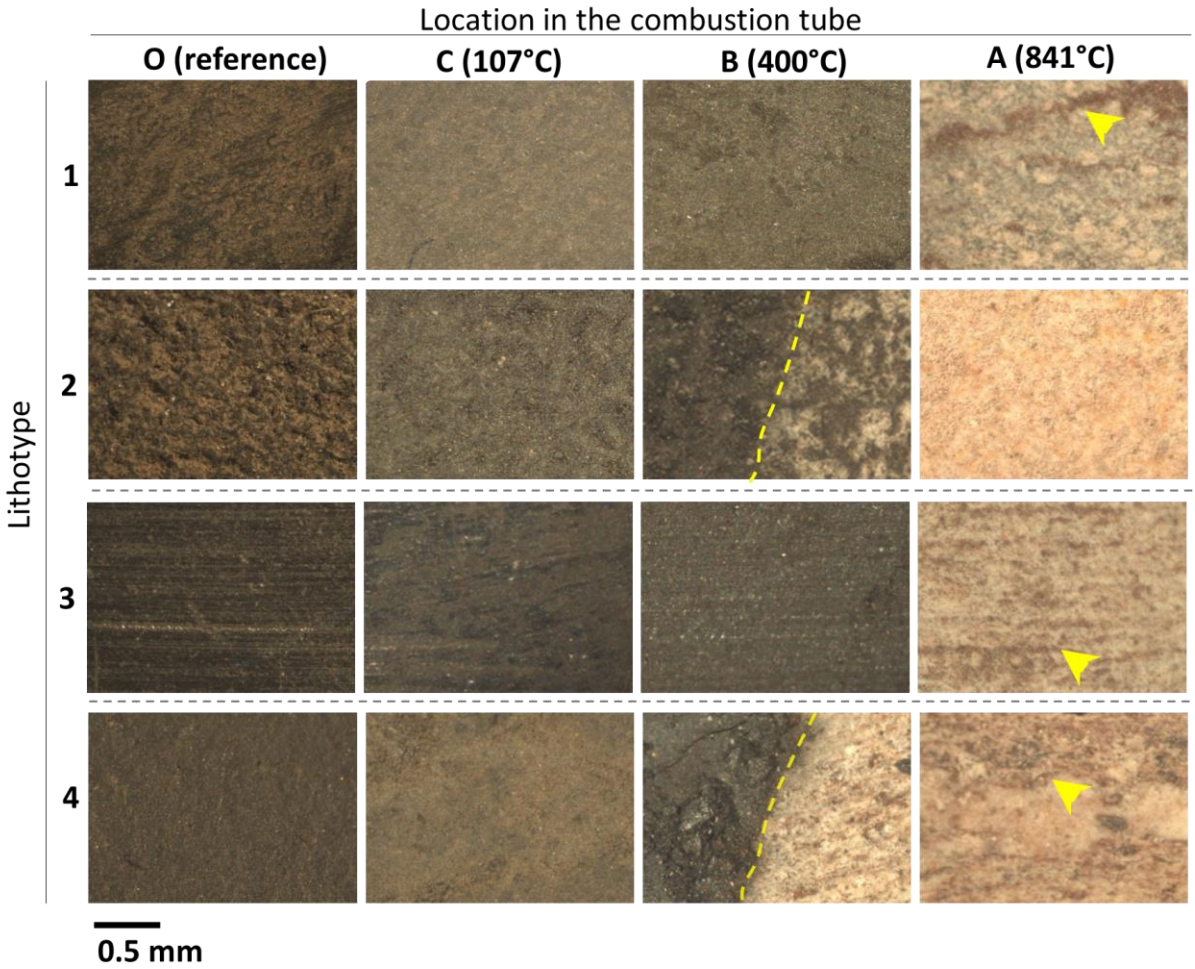

Figure 4.5.2. Photographs of the subsamples. Dashed line – boundary of the combustion. Arrows indicate reddish particles.

4.5.2. Polarizing optical microscopy

Microphotographs of thin-sections obtained with polarizing microscopy are shown in Figure 4.5.3 and Figure 4.5.4. The general trend for all samples is a decrease in the amount of organic matter in the samples with increasing temperature. However, accurate evaluation of OM content is not possible from the thin-section due dispersed structure and mixing with fine-grained minerals. Decreasing of the OM is expressed in lighting of the samples. It is become noticeable at the B section; whereas at the C it is not obvious.

The second general trend is formation of reddish component, which has been observed in reflected light. These components are common for all the lithotypes, however, clay-rich, OM-rich and pyrite-rich lithotypes are characterized by larger amount of reddish component (lihtotypes 3 and 4).

Despite similarity of changes observed with optical microscopy along the different lithotypes, there are certain aspect in each specific lithotype.

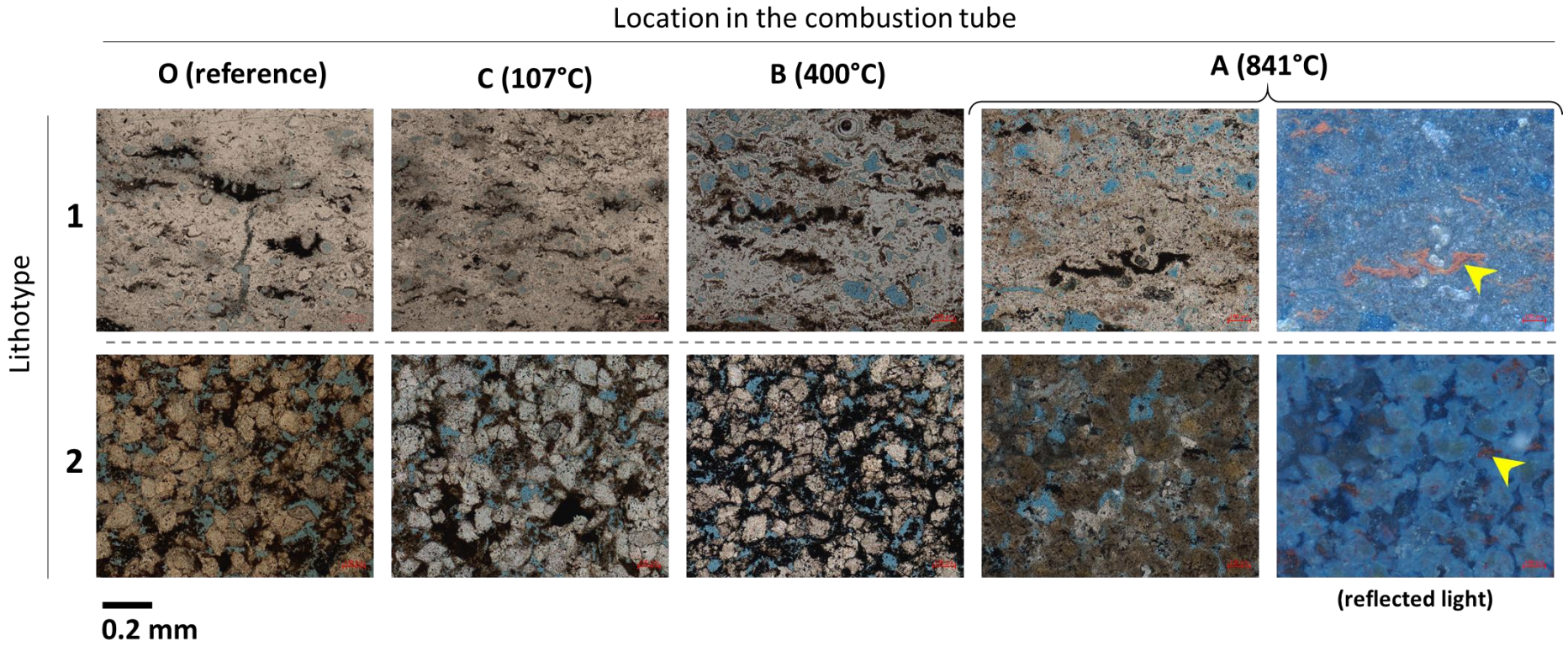

Figure 4.5.3. Microphotographs of lithotype 1 and lithotype 2 subsamples.

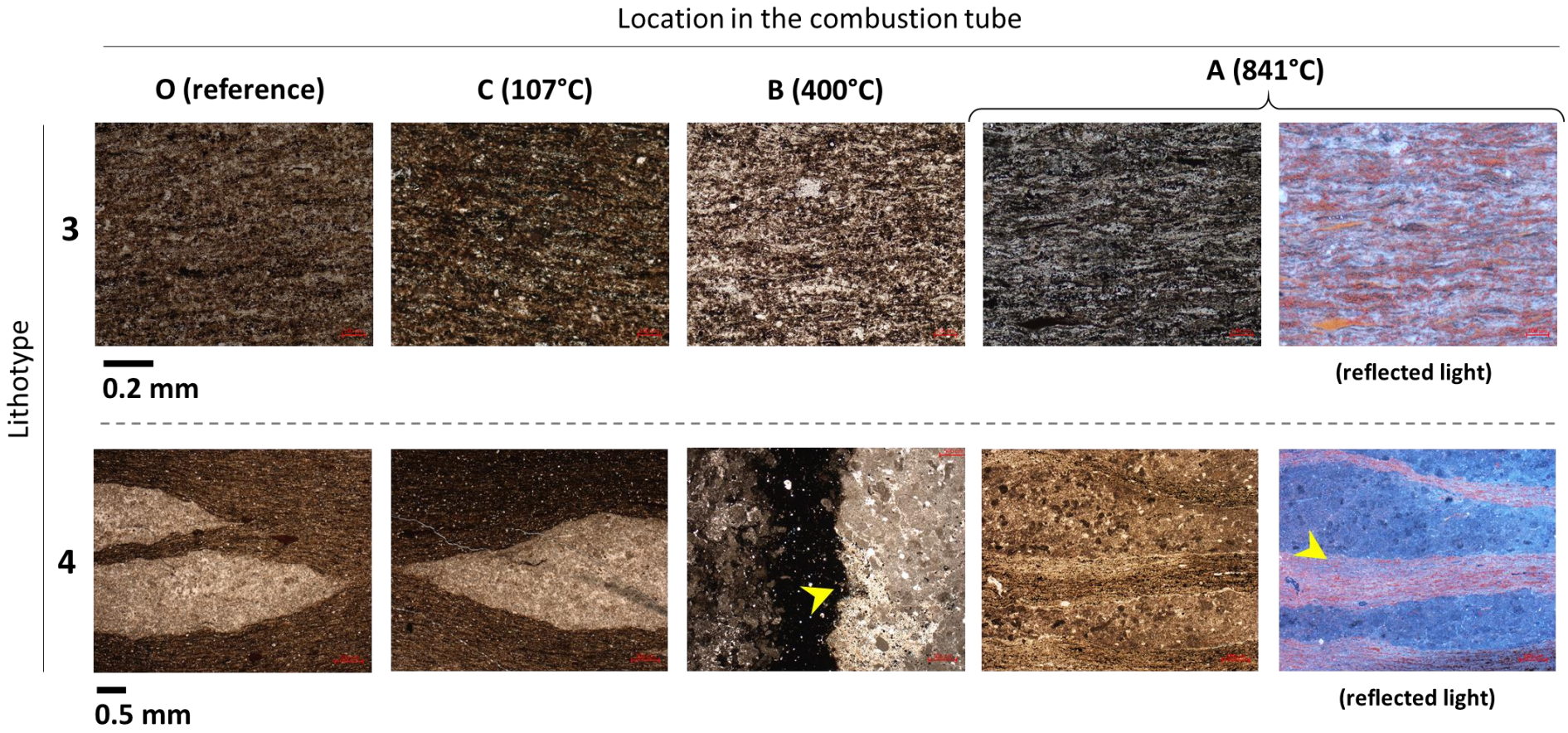

Figure 4.5.4. Microphotographs of lithotype 3 and lithotype 4 subsamples.

Lithotype 1. Siliceous mudstone. The lithotype is composed of quartz. There are minor changes in the subsamples 1B and 1C, predominantly decreased OM content. Subsample 1A is characterized by the presence of reddish component (Figure 4.5.3). The lithotype is characterized by relatively high porosity, up to 10-15%. Slight porosity increase was observed (up to 1-2%) in 1A and 1B, caused by transformation and evacuation of OM.

Lithotype 2. Aporadiolarian siliceous dolomites. The lithotype is characterized by the dominance of both dolomite and quartz. Temperature increasing is accompanied by porosity increase from 5% to 5-7% due to transformation and displacement of OM. Mineral matrix is darkening with temperature increase, which indicates appearance of micritic fabric of the grains (Figure 4.5.3). Also appearance of reddish component was observed in a low amount.

Lithotype 3. Argillaceous-siliceous organic-rich mudstone. The lithotype is composed of clay minerals and silicones component (quartz) with significant amount of OM (TOC is 11.5%). Temperature increase lead to the significant lightening of the sample, which is a result of transformation and displacement of initial high amount of OM during heating. The lithotype is rich in reddish component after the combustion front propagation (3A).

Lithotype 4. Calcareous-argillaceous organic-rich mudstone. The lithotype is characterized by a mixed mineral composition of clay, quartz and carbonates (calcite and dolomite) minerals. Decreasing of OM content was observed with temperature increase. The subsample after the combustion front propagation (4A) is characterized by the formation of reddish component in the clay rich laminas, whereas carbonate lenses are free of these reddish component. In the subsample 4B “micro” combustion front was observed (Figure 4.5.4 section B, Figure 4.5.5).

Figure 4.5.5 demonstrates panoramic microphotograph of the subsample 4B (located close to the combustion front). The black elongated strip was distinguished across the section with the width of 3-8 mm. One side of the rock looks normal with OM and without any reddish inclusions. The other side is light due to OM removal, and characterized by the presence of reddish component. The black strip is considered as a micro- combustion front.

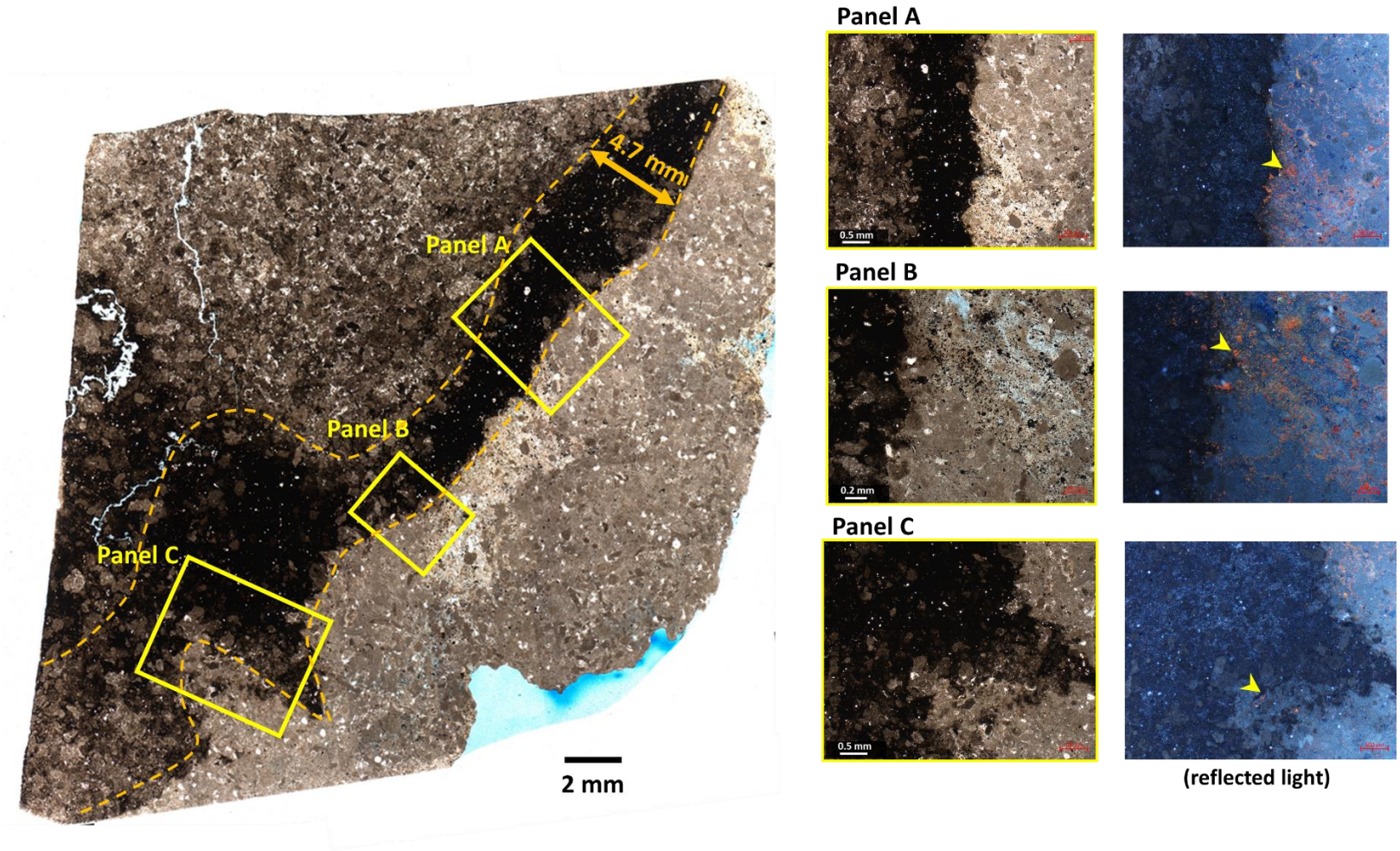

Figure 4.5.5. Panoramic view of lithotype 4 from the section B (located close to the combustion front). Dashed line – "micro-" combustion front. Left side of the sample is not altered. The right part became lighter, it is characterized by single pores, absence of OM and reddish component presence.

4.5.3. SEM imaging and EDS analysis

SEM analysis of broken surfaces made possible to investigate the microstructure of subsamples with simultaneous analysis of chemical composition with integrated EDS instrument. The results are given bellow according the lithotypes.

Lithotype 1. Siliceous mudstone

The lithotype 1 at its initial state (reference subsample 1O) is characterized by the dominance of idiomorphic quartz crystals, which often form porous structures sometimes characterized by inherited radiolarian relict structures (Figure 4.5.6A). The size of pores are in the range of 1-100 μm. Organic matter is rare and usually present in the form of inclusions with the size up to 15 μm (Figure 4.5.6B). Pyrite presences in the form of framboids predominantly, formed by cubic/octahedral crystals in most cases.

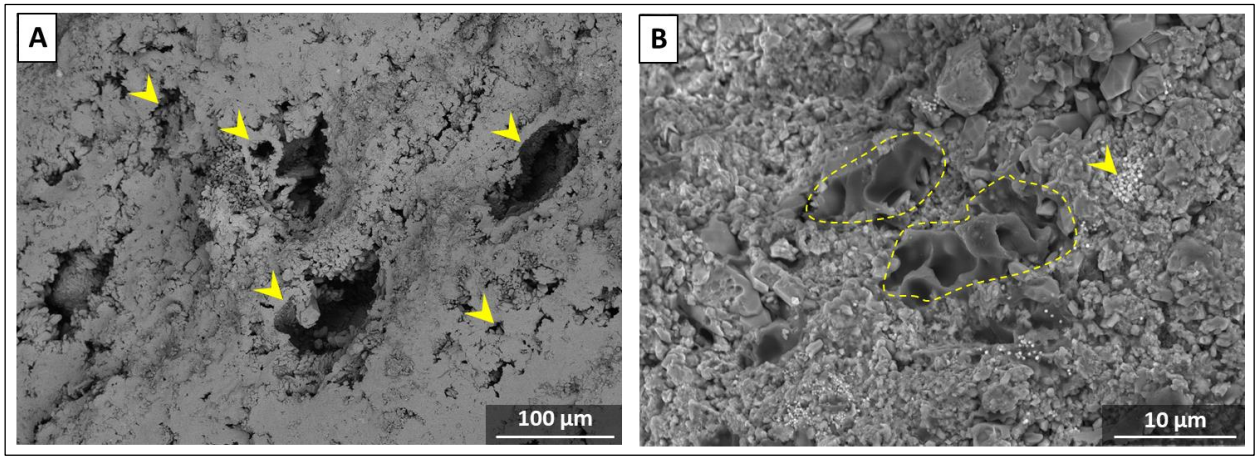

Figure 4.5.6. SEM images of Lithotype 1, subsample 1O (referance). A – pore space formed by idiomorphic quartz crystals, sometimes characterized by inherited radiolarian relict structures. B – organic matter with inherited structure (dashed line), arrow indicates pyrite framboids with cubic/octahedral crystals.

The temperatures of 107°C and 400°C did not cause to any significant changes in the minerals morphology and composition in the lithotype (Figure 4.5.7). The texture and the structure of all the components were preserved, except OM, which were not observed.

The temperature 841°C lead to changes in iron sulfide (pyrite) morphology and the composition. Pyrite in its initial state was not observed, only iron oxide (hematite), which occupies the space initially filled by pyrite framboids. Significant amount of iron oxide (hematite Fe_2O_3, Figure 4.5.8A), is the reason of reddish color of samples after the treatment. The morphology of hematite is variable and represents a dendritic structure within the framboid relicts (Figure 4.5.8A, Figure 4.5.9). There is minor amount of other newly formed phases, such as elemental iron, magnesium sulfide, calcium sulfide (Figure 4.5.8 and Figure 4.5.10). The individual size of these

crystals do not exceed 10 μm, however they may form aggregates with the size up to 50 μm. The minor components fill existing pore space and complicate the void space. Furthermore, the minor components make the matrix behavior less predictable due to their high reactivity (Figure 4.5.9).

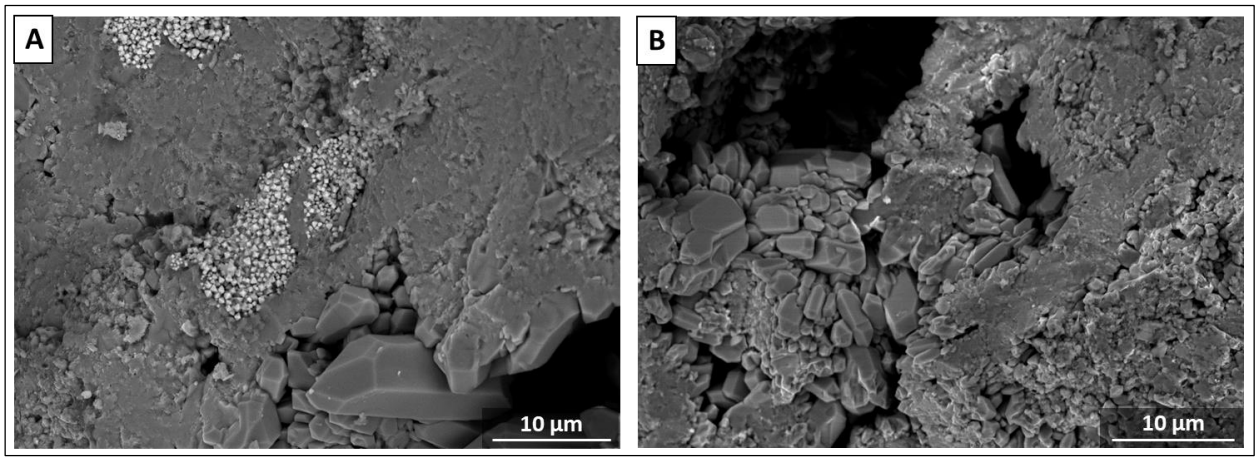

Figure 4.5.7. SEM images of Lithotype 1. A – subsample 1C (107°C), B – subsample 1B (400°C). No alterations observed compared to reference sample.

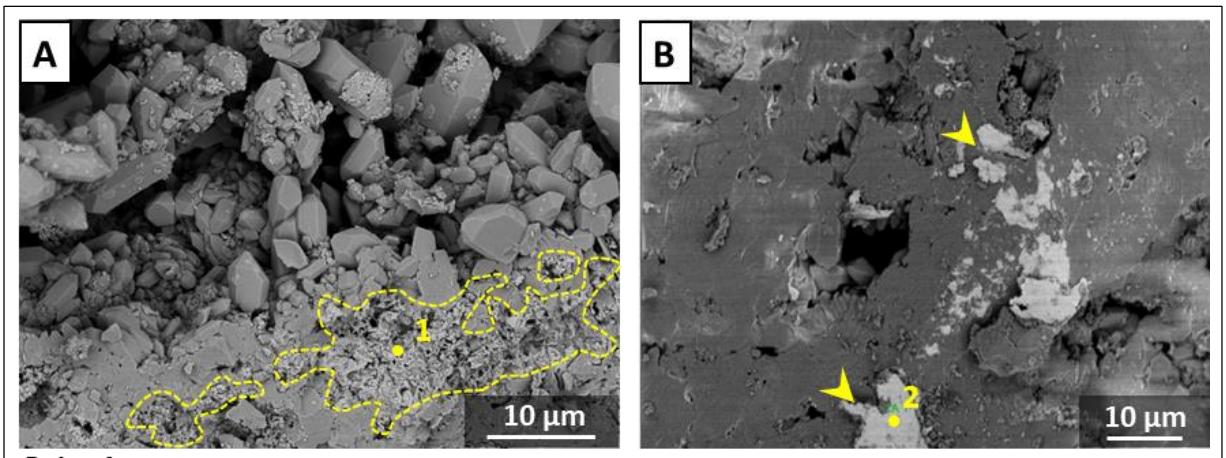

Point 1

Element	At. No.	Netto	Mass [%]	Mass Norm. [%]	Atom [%]
Oxygen	8	16358	37.30	37.30	62.83
Iron	26	10731	54.13	54.13	26.12
Carbon	6	858	2.34	2.34	5.25
Silicon	14	659	2.90	2.90	2.78
Sulfur	16	620	2.52	2.52	2.12
Magnesium	12	416	0.81	0.81	0.90
		Sum	**100.00**	**100.00**	**100.00**

Point 2

Element	At. No.	Netto	Mass [%]	Mass Norm. [%]	Atom [%]
Iron	26	11771	88.37	88.37	69.00
Oxygen	8	1196	4.79	4.79	13.05
Carbon	6	717	3.52	3.52	12.79
Silicon	14	628	3.32	3.32	5.16
		Sum	**100.00**	**100.00**	**100.00**

Figure 4.5.8. SEM images and EDS point analysis in subsample 1A (after 841°C). A – example of iron oxide (hematite). B –elementary iron.

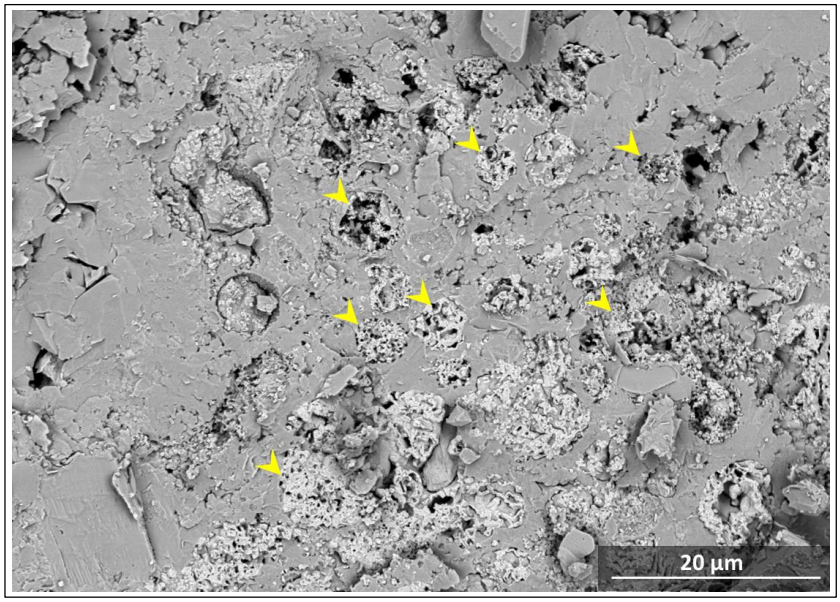

Figure 4.5.9. Newly formed iron oxide (hematite) in subsample 1A (after 841°C). Hematite is located within the round structures, which initially were occupied by pyrite framboids.

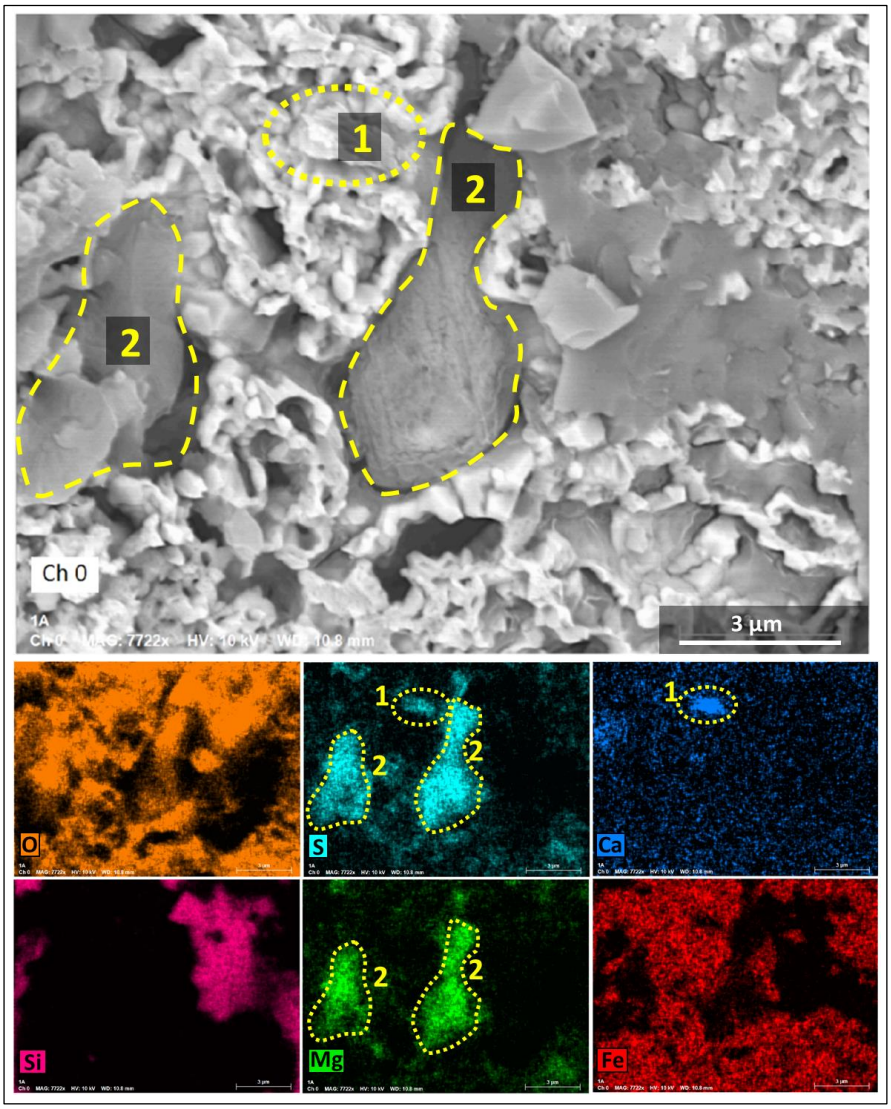

Figure 4.5.10. Results of EDS mapping in subsample 1A (after 841°C). 1 – concentration of Ca and S in one grain, which indicate formation of calcium sulfide, 2 – concentration of Mg and S in one area – magnesium sulfide. Most of the outer space is occupied by hematite (iron oxide).

Lithotype 2. Aporadiolarian siliceous dolomite

The lithotype 2 is composed of idiomorphic dolomite crystals with a size 30-100 μm and relatively small 1-15 μm quartz grains, which fill the space between the dolomite particles (Figure 4.5.11A). Surface of dolomite crystals is smooth, continuous and solid (Figure 4.5.11B).

SEM and EDS analysis of the subsamples showed that the temperatures of 107°C (Figure 13A, B). After 490°C heterogeneities on the dolomite crystals were observed, which may indicate beginning of the decomposition (Figure 4.5.12C,D).

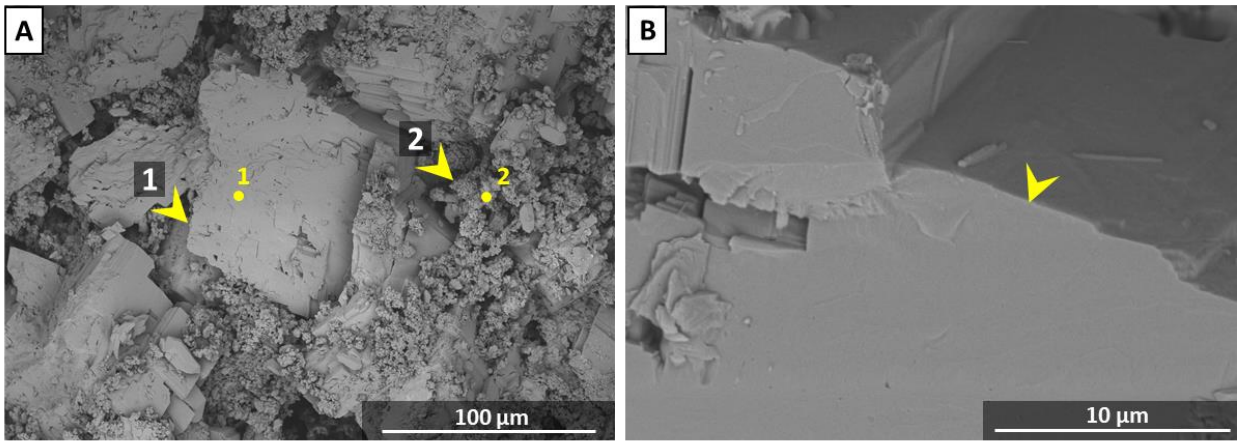

Point 1

Element	At. No.	Netto	Mass [%]	Mass Norm. [%]	Atom [%]
Oxygen	8	79346	26.20	62.42	61.83
Carbon	6	24928	9.52	22.69	29.93
Magnesium	12	27309	3.73	8.90	5.80
Calcium	20	4760	2.36	5.62	2.22
Silicon	14	800	0.16	0.38	0.21
Gold	79	6391	0.00	0.00	0.00
		Sum	**41.98**	**100.00**	**100.00**

Point 2

Element	At. No.	Netto	Mass [%]	Mass Norm. [%]	Atom [%]
Oxygen	8	20372	55.64	60.98	66.56
Silicon	14	17441	25.55	28.00	17.41
Carbon	6	1602	10.06	11.02	16.03
Gold	79	849	0.00	0.00	0.00
		Sum	**91.25**	**100.00**	**100.00**

Figure 4.5.11. SEM images and EDS analysis results in a two points of subsample 2O (reference sample). A – small quartz grains fill the space between dolomite crystals. B – smooth surface of dolomite crystals.

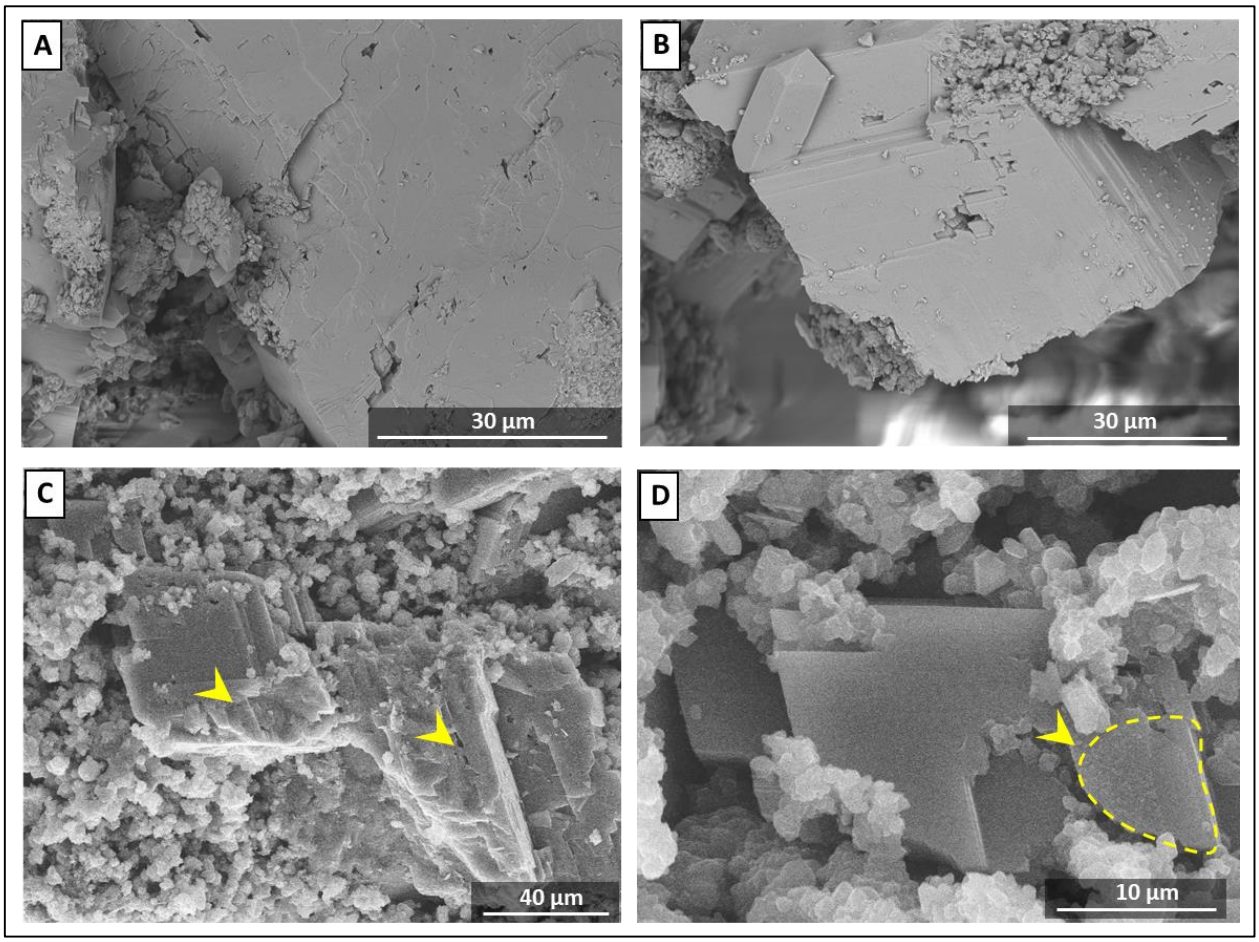

Figure 4.5.12. SEM images of subsamples 2C (107°C) (A,B) and 2B (490°C) (C,D). A, B – No alterations observed. C, D – heterogeneities on dolomite crystals after 400°C.

The exposure of 841°C resulted to the significant alterations in the microstructure and composition of a rock. Initially continuous and smooth dolomite crystals became rough, and composed of smaller, nanosized crystals. However initial geometry of crystals remained recognized (Figure 4.5.13, Figure 4.5.14). Despite similar bulk chemical composition particular proportions of Ca, Mg, O and C has been altered and new element - sulfur was observed, which indicate new mineral formation (Figure 4.5.13). Quartz still present in the same form. Hematite (iron oxide) ubiquitously found in the sample (Figure 4.5.13).

The thermal exposure has led to formation of two microstructural patterns (Figure 4.5.14). In the first case new nanoscale crystals are covered with the “crust”, which is represented by elongated needle-like minerals (Figure 4.5.14A). In the second case crystals are porous (Figure 4.5.14B), the pores are up to 1 µm in size.

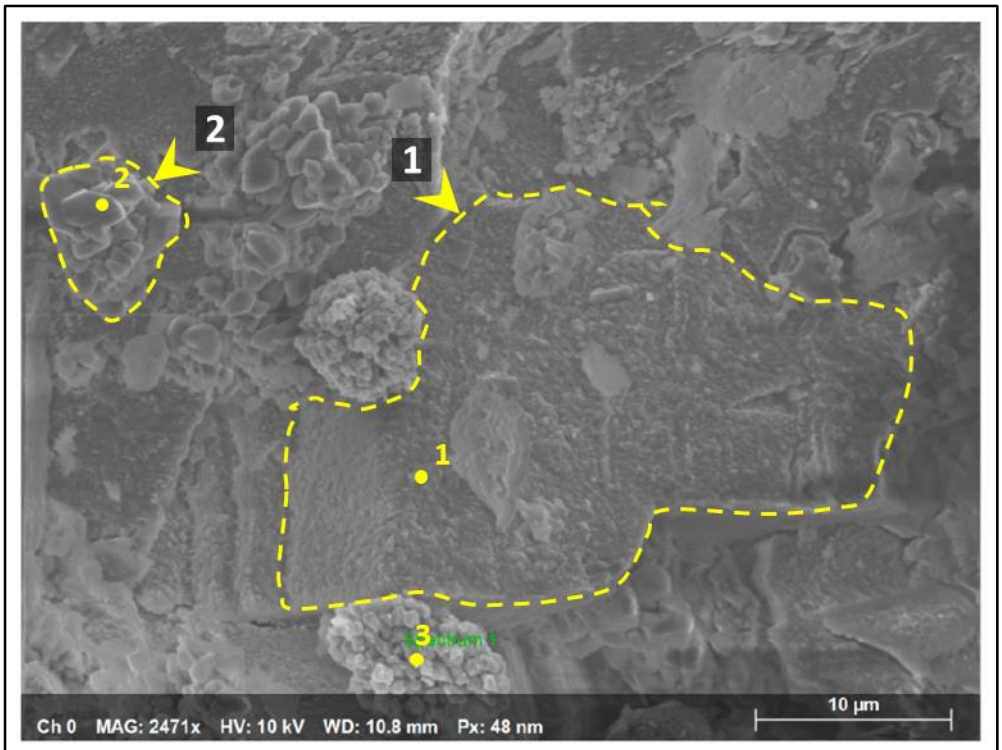

Point 1

Element	At. No.	Netto	Mass [%]	Mass Norm. [%]	Atom [%]
Oxygen	8	47482	56.73	56.73	68.47
Magnesium	12	25405	12.82	12.82	10.18
Carbon	6	1832	3.92	3.92	6.30
Calcium	20	8993	12.50	12.50	6.02
Silicon	14	11772	6.65	6.65	4.57
Sulfur	16	10656	7.39	7.39	4.45
		Sum	**100.00**	**100.00**	**100.00**

Point 2

Element	At. No.	Netto	Mass [%]	Mass Norm. [%]	Atom [%]
Oxygen	8	21082	53.14	53.14	61.88
Silicon	14	30402	38.93	38.93	25.82
Carbon	6	1167	7.93	7.93	12.30
		Sum	**100.00**	**100.00**	**100.00**

Point 3

Element	At. No.	Netto	Mass [%]	Mass Norm. [%]	Atom [%]
Oxygen	8	25523	49.59	49.59	70.40
Iron	26	1895	40.29	40.29	16.38
Carbon	6	1157	4.29	4.29	8.11
Sodium	11	1733	3.27	3.27	3.23
Silicon	14	1250	1.73	1.73	1.40
Calcium	20	265	0.83	0.83	0.47
		Sum	**100.00**	**100.00**	**100.00**

Figure 4.5.13. SEM images and EDS analysis results of subsample 2A (841°C). Significant microstructural and chemical alterations in idiomorphic crystals.

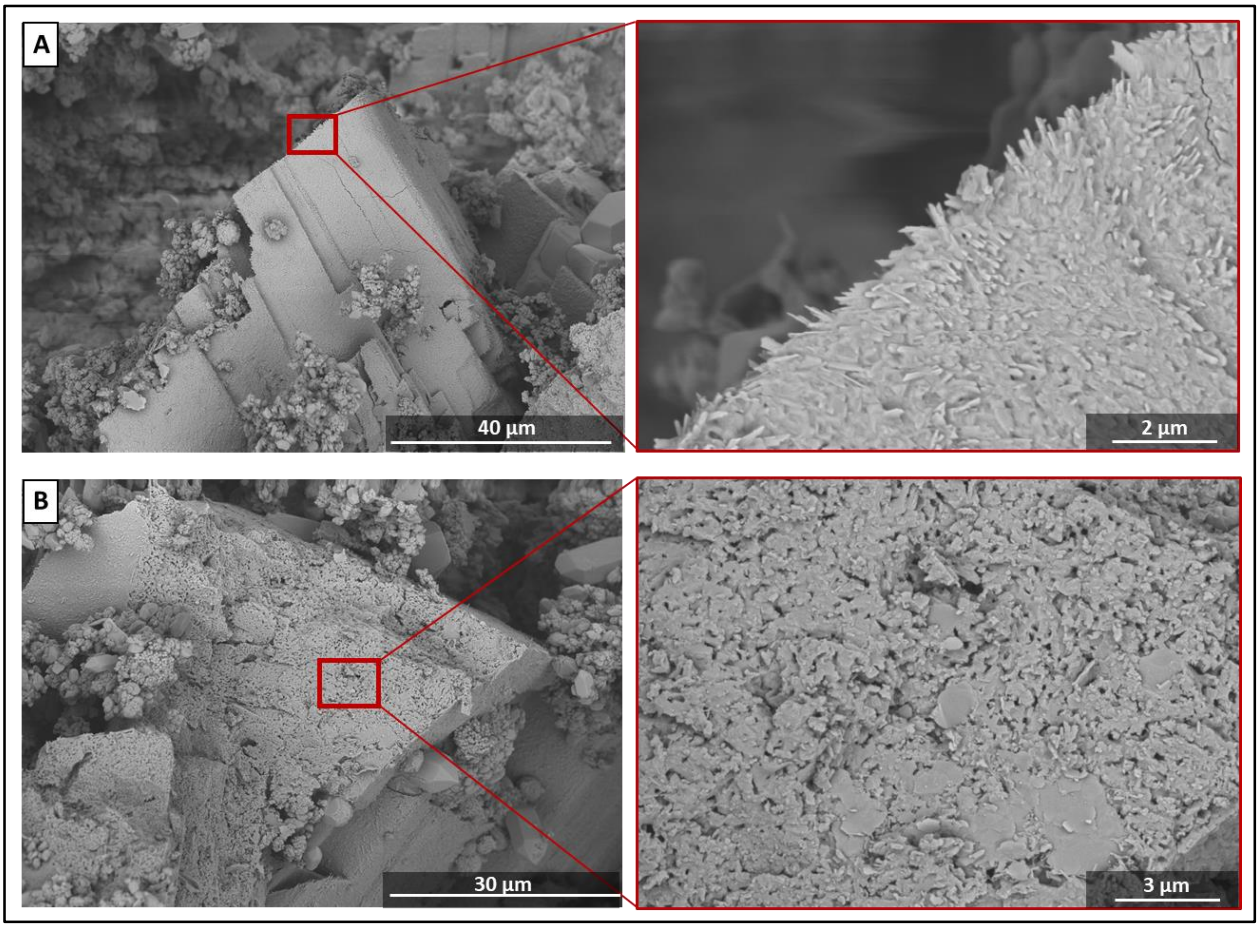

Figure 4.5.14. Two types of microstructural patterns in subsample 2A (841°C), observed on the idiomorphic crystals, initially represented by dolomite. A – elongated needle-like nanocrystals, B – porous clotty microstructure, formed by isometric nanocrystals.

EDS analysis showed prevailing of Ca, Si and O within some grains, which may indicate presence of wollastonite CaSiO (Figure 4.5.15A). Ca, S and O are often observed together (Figure 4.5.15B) or as a part of aggregate (Figure 4.5.15A), which is signature of anhydrite. In some cases, only Ca and O are found together (Figure 4.5.15C), that reveals calcium oxide presence. EDS mapping showed separate location of Mg and Ca in the aggregates (Figure 4.5.15D), that observation suggests existence of such compounds as CaO, MgO and $CaCO_3$.

EDS mapping allowed to analyze chemical composition of two observed microstructural patterns (Figure 4.5.16). The “crust” appears to be composed of anhydrite (Ca, S and O in the same grains) with MgS in some areas. The inner part is represented by the Ca, Mg, C and O. The prevalence of such elements indicates the presence of compounds such as $CaCO_3$, MgO and CaO.

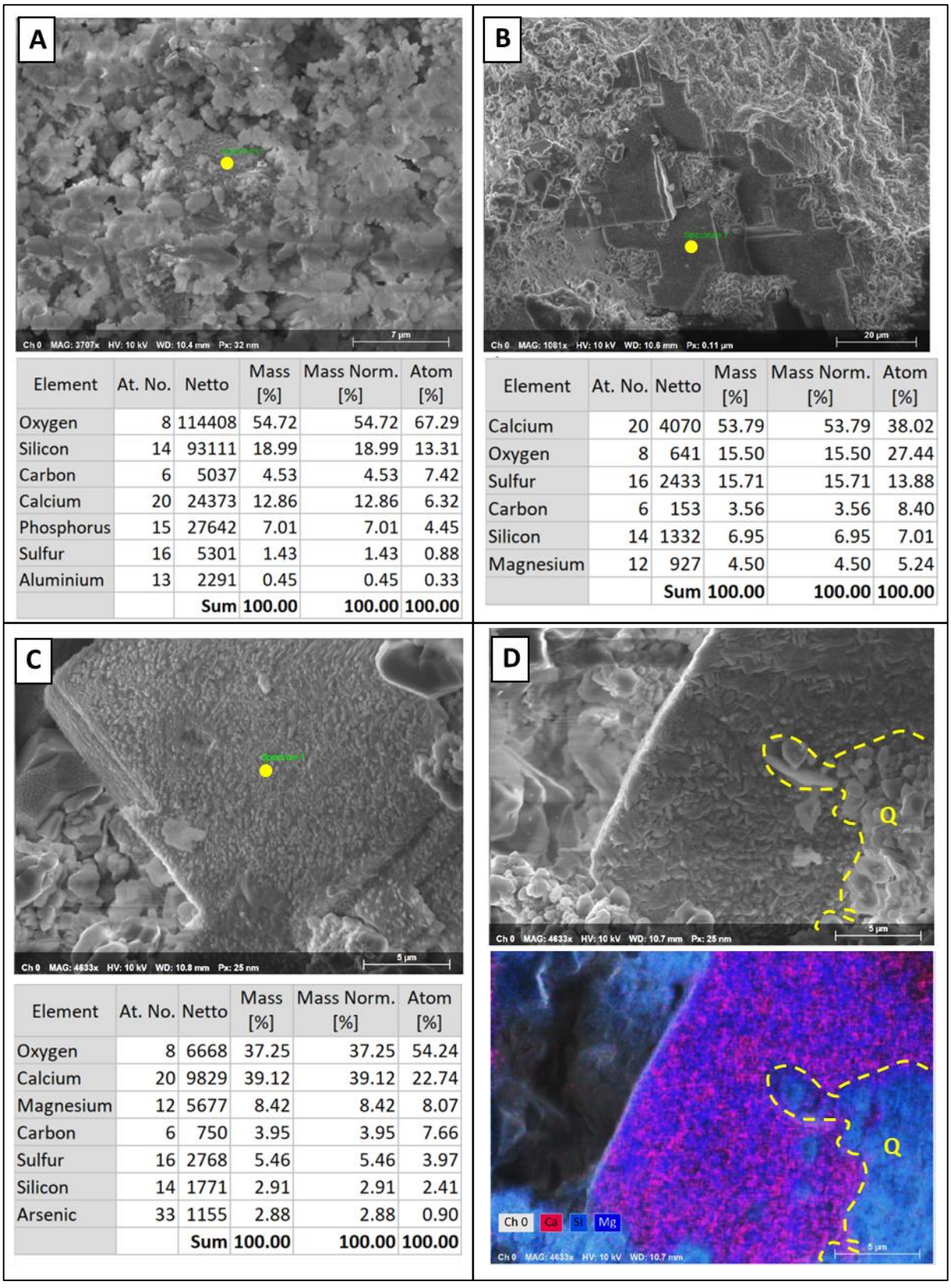

Element	At. No.	Netto	Mass [%]	Mass Norm. [%]	Atom [%]
Oxygen	8	114408	54.72	54.72	67.29
Silicon	14	93111	18.99	18.99	13.31
Carbon	6	5037	4.53	4.53	7.42
Calcium	20	24373	12.86	12.86	6.32
Phosphorus	15	27642	7.01	7.01	4.45
Sulfur	16	5301	1.43	1.43	0.88
Aluminium	13	2291	0.45	0.45	0.33
		Sum	**100.00**	**100.00**	**100.00**

Element	At. No.	Netto	Mass [%]	Mass Norm. [%]	Atom [%]
Calcium	20	4070	53.79	53.79	38.02
Oxygen	8	641	15.50	15.50	27.44
Sulfur	16	2433	15.71	15.71	13.88
Carbon	6	153	3.56	3.56	8.40
Silicon	14	1332	6.95	6.95	7.01
Magnesium	12	927	4.50	4.50	5.24
		Sum	**100.00**	**100.00**	**100.00**

Element	At. No.	Netto	Mass [%]	Mass Norm. [%]	Atom [%]
Oxygen	8	6668	37.25	37.25	54.24
Calcium	20	9829	39.12	39.12	22.74
Magnesium	12	5677	8.42	8.42	8.07
Carbon	6	750	3.95	3.95	7.66
Sulfur	16	2768	5.46	5.46	3.97
Silicon	14	1771	2.91	2.91	2.41
Arsenic	33	1155	2.88	2.88	0.90
		Sum	**100.00**	**100.00**	**100.00**

Figure 4.5.15. Results of EDS analysis and mappinng of subsample 2A. A – domination of Ca, Si and O in one crystal (wollastonite), B –Ca, S and O in one single crystal (anhydrite), C – dominance of Ca and O in one point, aggregate with the dominance of CaO, D – EDS mapping of an aggregate of nanocrystals, Mg and Ca are located separatly and correspond to a different compounds such as MgO, CaO, and $CaCO_3$. Q – quartz.

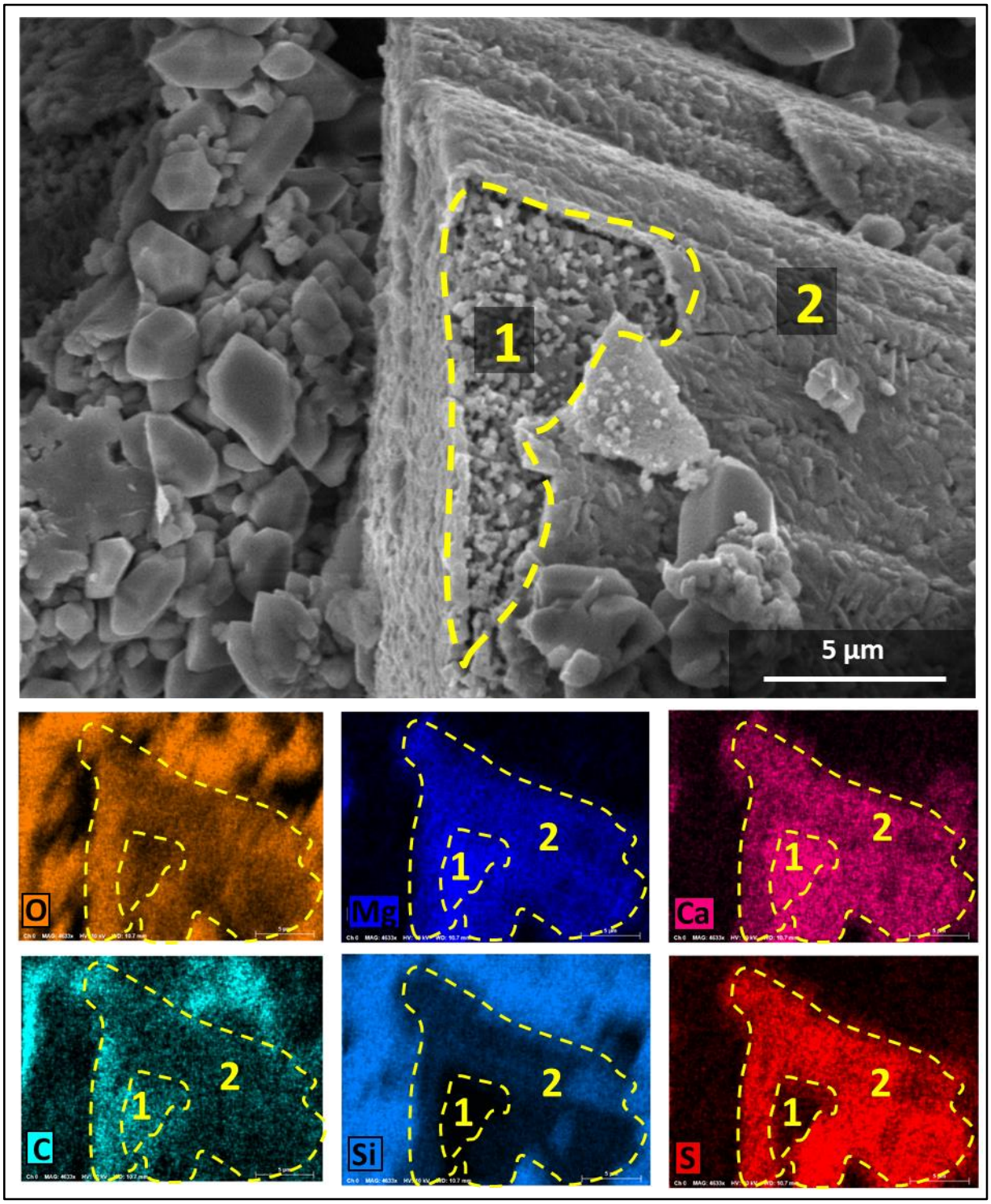

Figure 4.5.16. Results of EDS Mapping of two types microstructure patterns. Compound with the dominance of Ca, S and O (anhydrite) envelop nanocrystal aggregate, which characterized by the presence of Mg, Ca and O with some C.

Lithotype 3. Argillaceous-siliceous organic-rich mudstone

Lithotype 3 is characterized by thin laminated microstructure, caused by the distribution of clay minerals and organic matter (Figure 4.5.17). Organic matter is present in the form of wisps, thin lamellas and inclusions. OM equally fills the space between crystals, often is associated with pyrite framboids. Pyrite is presented predominantly in the form of framboids with the size 3-20 μm. Pores are rare and not exceed 0.5-1 μm in size, have elongated shape and associated with clay lamellas.

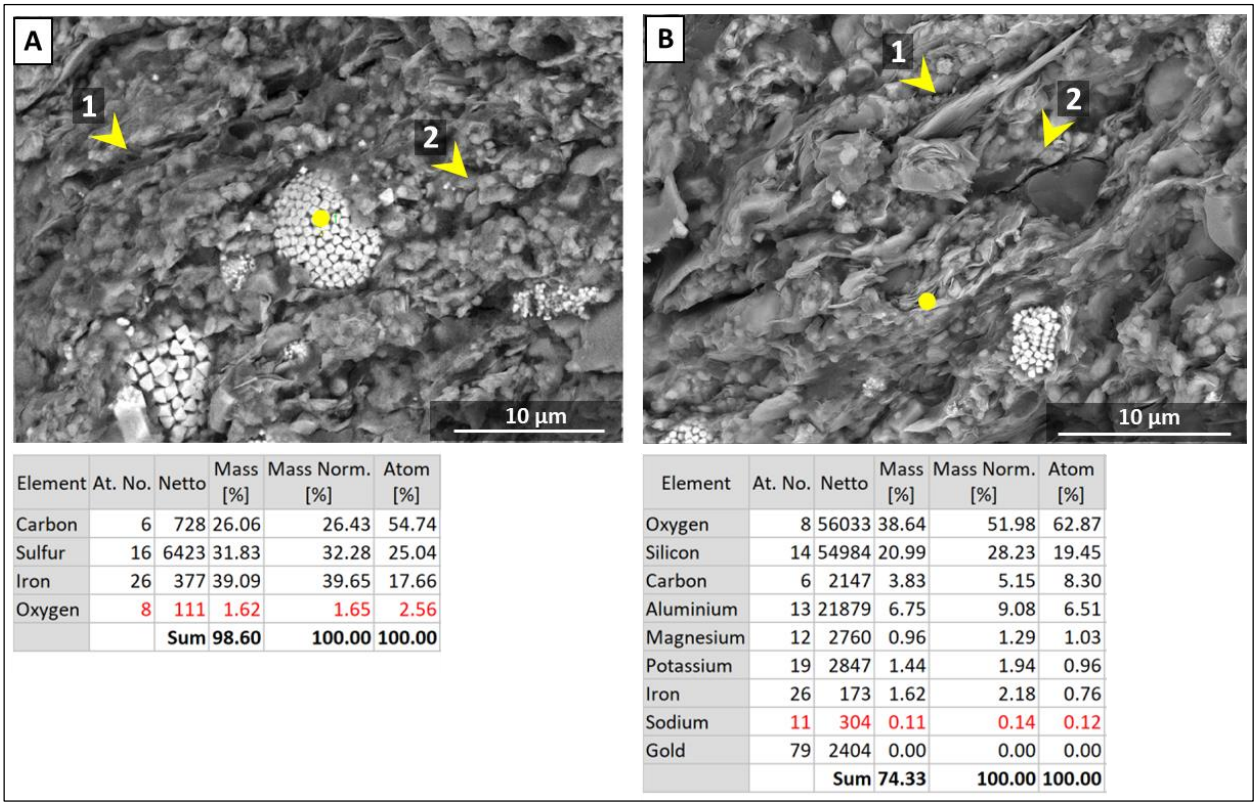

Element	At. No.	Netto	Mass [%]	Mass Norm. [%]	Atom [%]
Carbon	6	728	26.06	26.43	54.74
Sulfur	16	6423	31.83	32.28	25.04
Iron	26	377	39.09	39.65	17.66
Oxygen	8	111	1.62	1.65	2.56
		Sum	**98.60**	**100.00**	**100.00**

Element	At. No.	Netto	Mass [%]	Mass Norm. [%]	Atom [%]
Oxygen	8	56033	38.64	51.98	62.87
Silicon	14	54984	20.99	28.23	19.45
Carbon	6	2147	3.83	5.15	8.30
Aluminium	13	21879	6.75	9.08	6.51
Magnesium	12	2760	0.96	1.29	1.03
Potassium	19	2847	1.44	1.94	0.96
Iron	26	173	1.62	2.18	0.76
Sodium	11	304	0.11	0.14	0.12
Gold	79	2404	0.00	0.00	0.00
		Sum	**74.33**	**100.00**	**100.00**

Figure 4.5.17. SEM images and EDS analysis results of subsample 3O (reference sample). A. 1 – laminated OM, 2 – quartz grains, EDS analysis shows close association of OM with pyrite framboids. B. 1 – clay lamellas, 2 – OM inclusion, EDS analysis shows presence of clay minerals, quartz and organic matter. Organic matter fills the intercrystalline space.

SEM imaging of the subsample 3C (107°C) showed the rock fabric identical to the reference sample (Figure 4.5.18A), however some fractured OM inclusions were observed (Figure 4.5.18B).

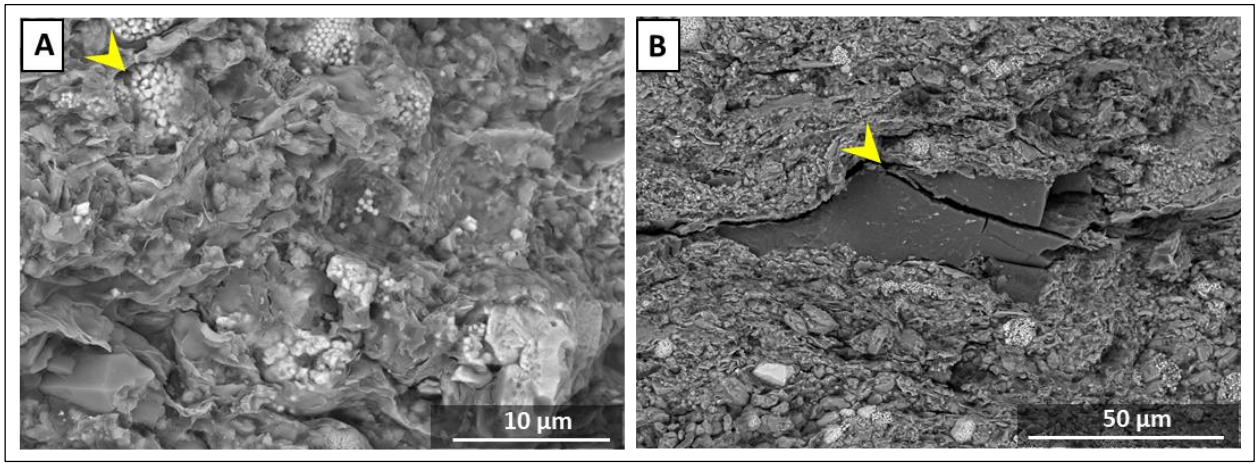

Figure 4.5.18. Lack of significant changes in the rock fabric in subsample 3C (107°C). A – some OM inclusions are fractured, B – the rock fabric is identical to its initial state.

Subsample 3B (400°C) is characterized by the reduced amount of OM – part of intercrystalline space is porous and does not filled by organic matter (Figure 4.5.19A). New pores do not exceed 3-5 µm in size, however in some cases individual 20-50 µm voids were observed, which initially were filled by OM (Figure 4.5.19B). The most part of remained OM became porous (Figure 4.5.19C). Part of remained OM is characterized by the fractures (Figure 4.5.19D).

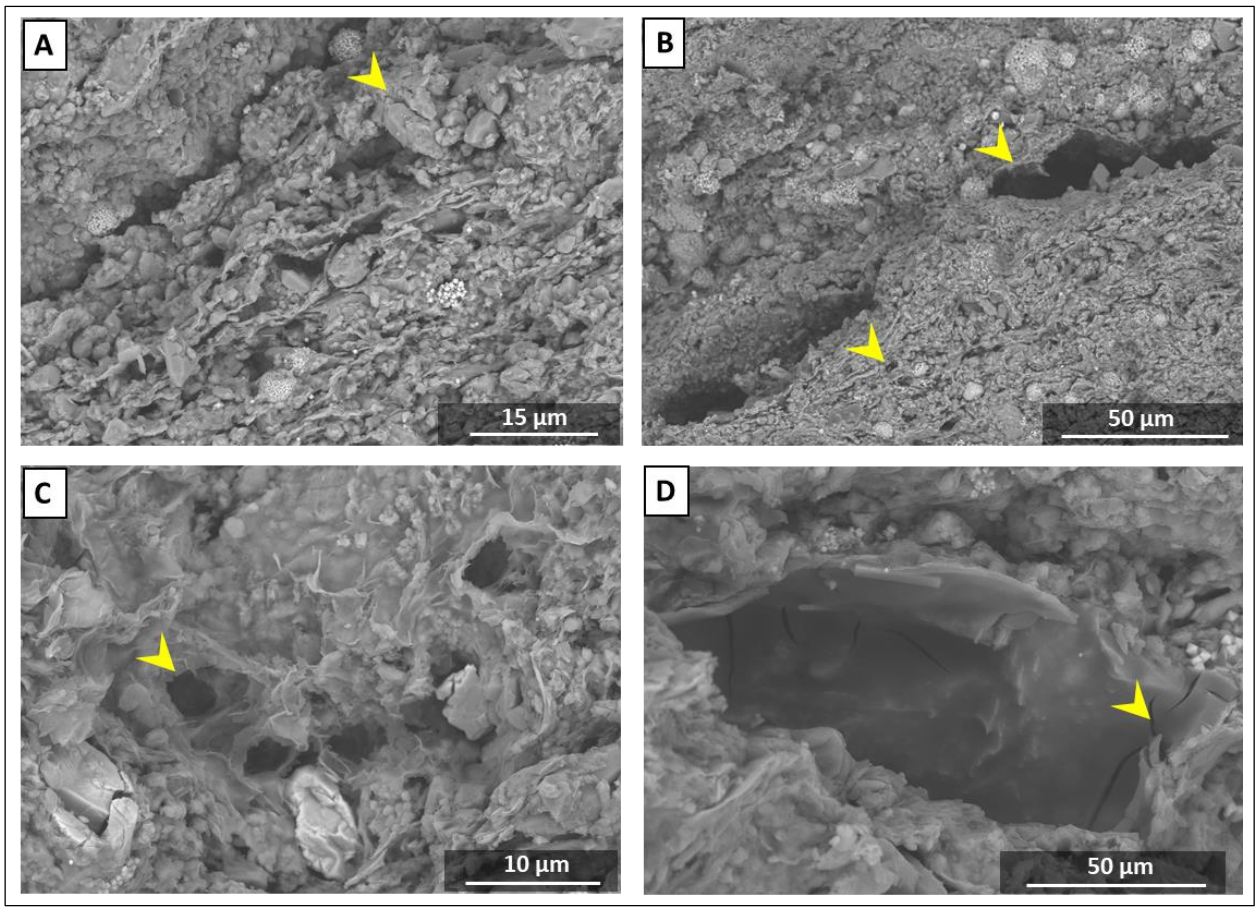

Figure 4.5.19. SEM images of subsample 3B (400°C). A – part of the intercrystalline space is free of OM. B – new pores, which initially were filled by OM. C – pores in the remained OM. D – some OM inclusions are characterized by fracturing.

Significant changes in microstructure and the composition were observed in the subsample is 3A (841°C). SEM and EDS analysis showed that structures, that resembles pyrite framboids are consist of hematite (iron oxide) (Figure 4.5.20A, Figure 4.5.21B). Clay minerals generally retained their chemical composition, however amount of oxygen has been decreased (Figure 4.5.20B). In some cases, framboidal structures are filled by anhydrite (concentration of Ca, S and O in one point) (Figure 4.5.20C). Only two cases of BaS mineral were documented (Figure 4.5.20D).

The pyrite was completely decomposed. The space initially occupied by pyrite maybe recognized by the framboidal structure (which is not framboid anymore) and the presence of iron. Two common patterns of pyrite decomposition were observed (Figure 4.5.21). The first suggests preservation of framboid geometry and the destruction of inner structure, which filled by flakes or dendritic crystals (Figure 4.5.21A,B). The second one assumes complete destruction of initial structure and formation of large Fe and O aggregates characterized by dendritic porous microustructure at micro- and nano- scales (Figure 4.5.21C,D). EDS mapping allowed to document formation of elemental iron, calcium sulfide and confirm the presence of iron oxide and anhydrite (Figure 4.5.22).

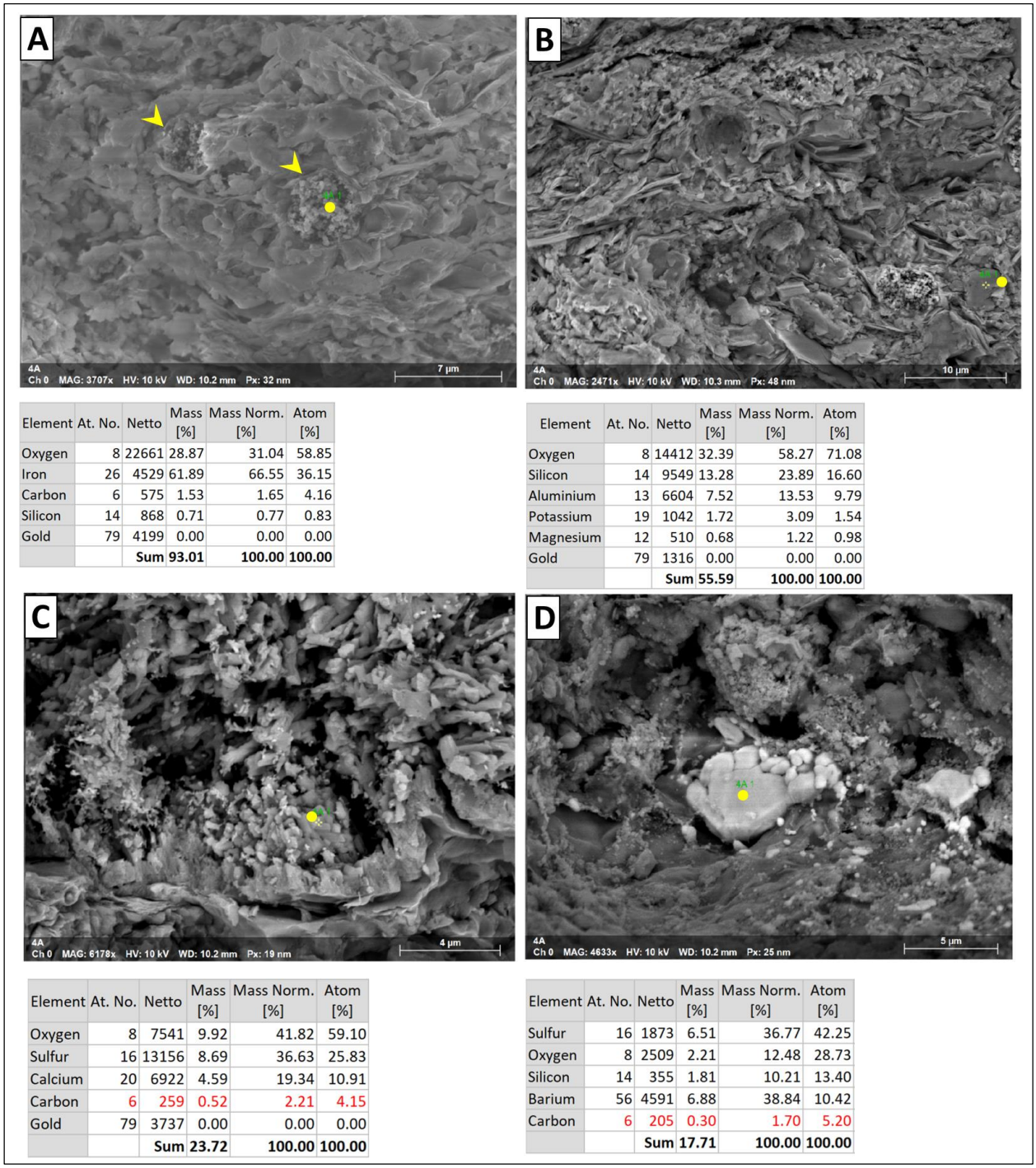

Element	At. No.	Netto	Mass [%]	Mass Norm. [%]	Atom [%]
Oxygen	8	22661	28.87	31.04	58.85
Iron	26	4529	61.89	66.55	36.15
Carbon	6	575	1.53	1.65	4.16
Silicon	14	868	0.71	0.77	0.83
Gold	79	4199	0.00	0.00	0.00
		Sum	**93.01**	**100.00**	**100.00**

Element	At. No.	Netto	Mass [%]	Mass Norm. [%]	Atom [%]
Oxygen	8	14412	32.39	58.27	71.08
Silicon	14	9549	13.28	23.89	16.60
Aluminium	13	6604	7.52	13.53	9.79
Potassium	19	1042	1.72	3.09	1.54
Magnesium	12	510	0.68	1.22	0.98
Gold	79	1316	0.00	0.00	0.00
		Sum	**55.59**	**100.00**	**100.00**

Element	At. No.	Netto	Mass [%]	Mass Norm. [%]	Atom [%]
Oxygen	8	7541	9.92	41.82	59.10
Sulfur	16	13156	8.69	36.63	25.83
Calcium	20	6922	4.59	19.34	10.91
Carbon	6	259	0.52	2.21	4.15
Gold	79	3737	0.00	0.00	0.00
		Sum	**23.72**	**100.00**	**100.00**

Element	At. No.	Netto	Mass [%]	Mass Norm. [%]	Atom [%]
Sulfur	16	1873	6.51	36.77	42.25
Oxygen	8	2509	2.21	12.48	28.73
Silicon	14	355	1.81	10.21	13.40
Barium	56	4591	6.88	38.84	10.42
Carbon	6	205	0.30	1.70	5.20
		Sum	**17.71**	**100.00**	**100.00**

Figure 4.5.20. SEM images and EDS analysis results of subsample 3A (841°C). A – inclusions, which resemble pyrite framboids are composed of iron and oxygen. B – Clay minerals (lamellas) are characterized by typical chemical composition and the microstructure. C –example of filling of framboidal structure by the anhydrite. D – crystal of BaS.

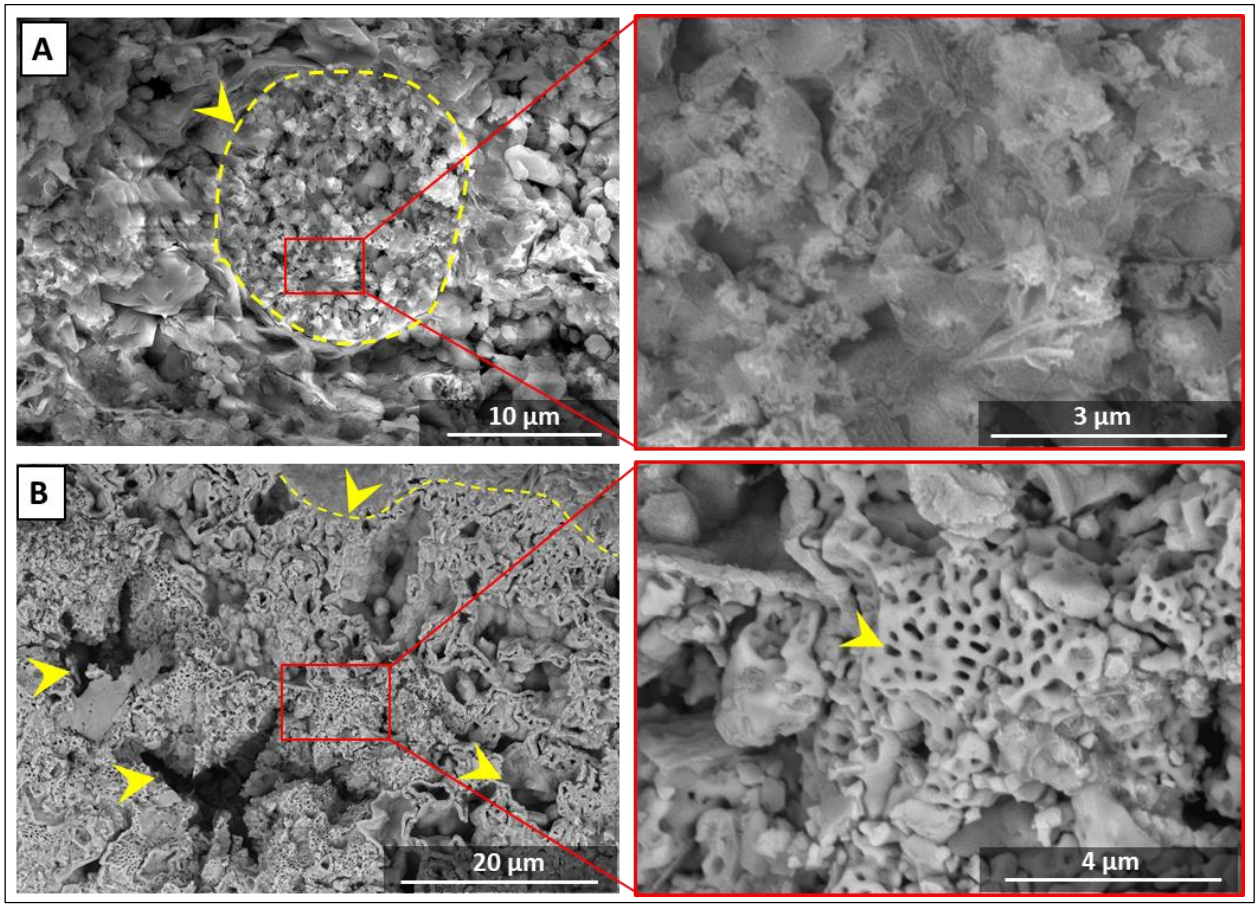

Figure 4.5.21. Two patterns of hematite formation in subsample 3A. A –framboidal structures still presence in the sample, but there no crystalline microstructure inside the framboids. B – porous hematite aggregates, pores are at micro- and nano- scales, inclusions are characterized by dendritic microustructure.

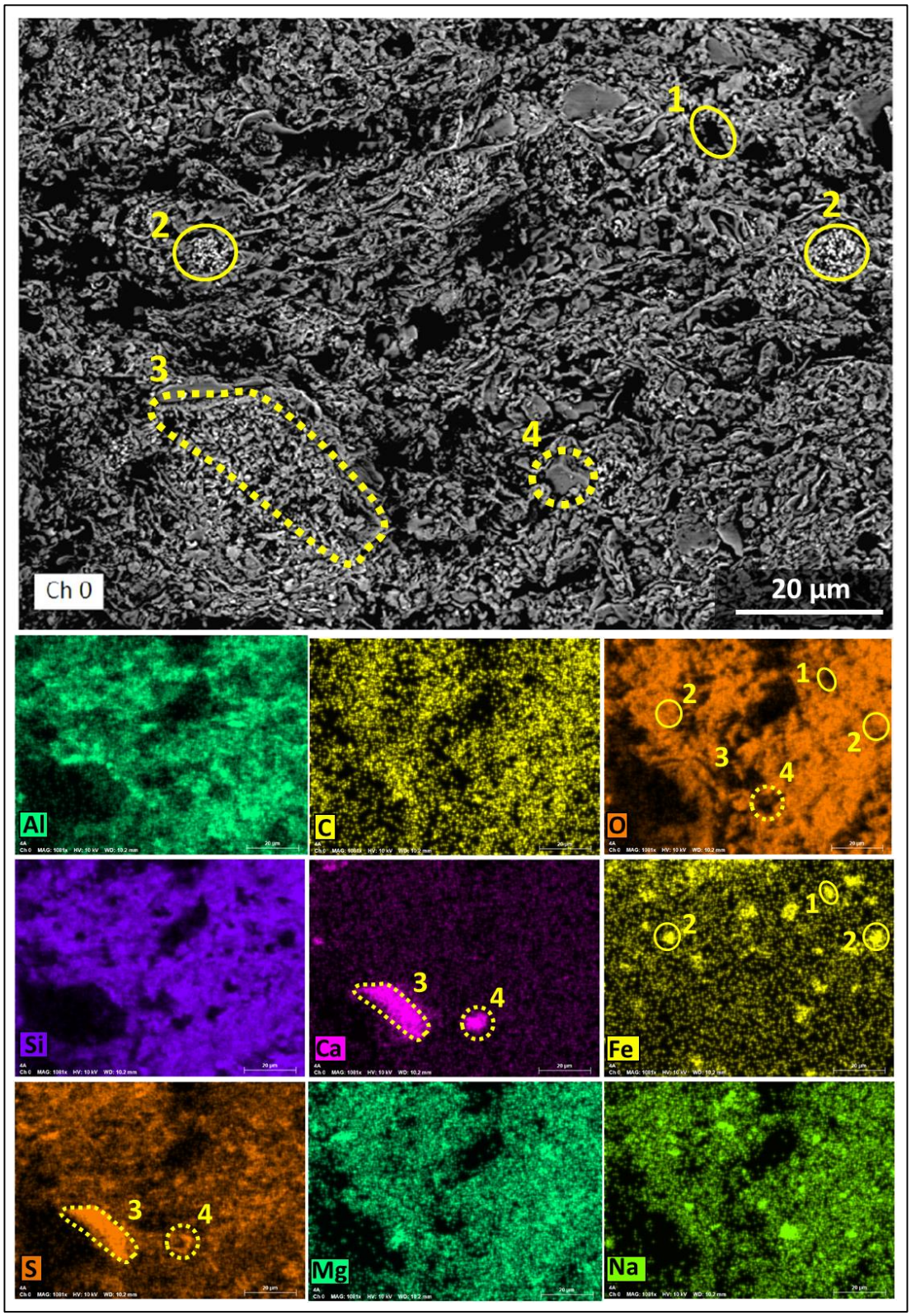

Figure 4.5.22. Results of EDS Mapping for subsample 3A. Three compounds may be identified on the maps: 1 – elemental iron, 2 – combination of iron and oxygen, 3 – combination of Ca and S, 4 – combination of Ca, S and O.

Lithotype 4. Calcareous-argillaceous organic-rich mudstone

Lithotype 4 represents a mixed siliceous, carbonate and clay mudstone. Calcite is observed in the form of individual crystals equally distributed in the rock and in the form of lenses (see thin-section optical microscopy chapter).

The lithotype at the initial state composed of a quartz, clay minerals, feldspar and calcite minerals with thin laminated structure, which caused by clay minerals and organic matter distribution (Figure 4.5.23A). Clay minerals, organic matter and pyrite framboids are in a close association (Figure 4.5.23C). Pyrite presents in the form of framboids and individual crystals (Figure 4.5.23B, D). All the crystals in the framboids are idiomorphic. OM is arranged as a wisps and inclusions with the size up to 10 μm.

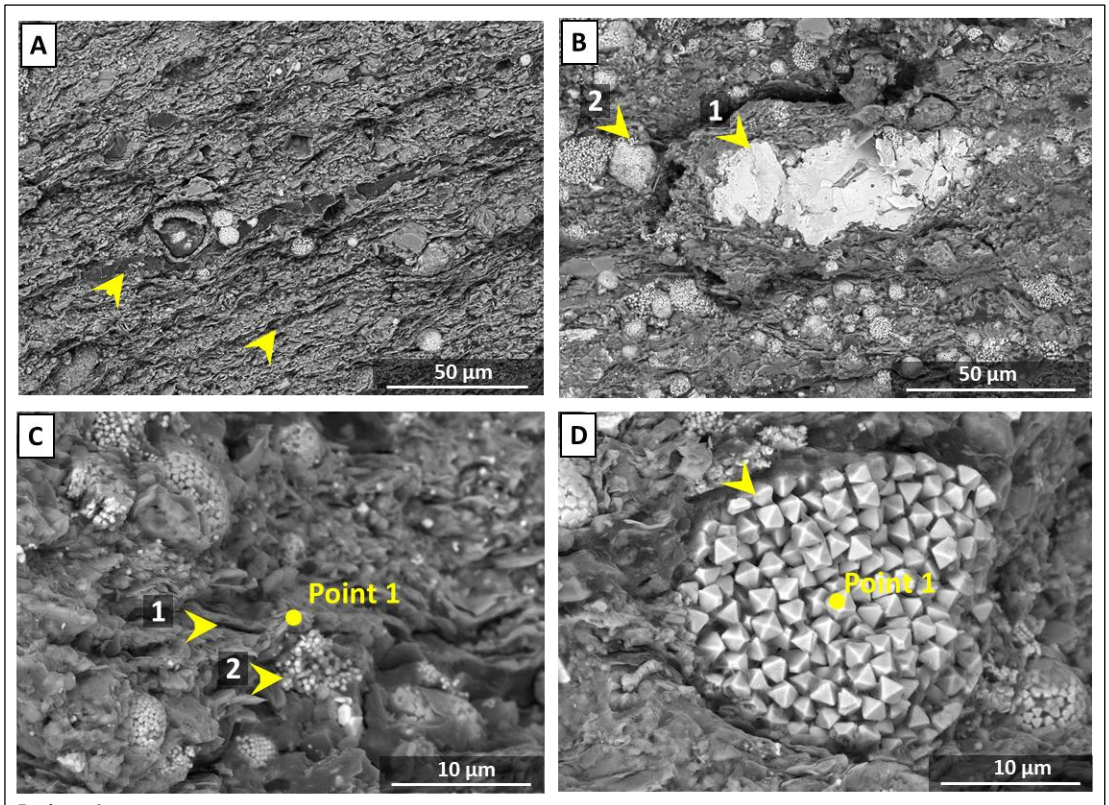

Point 1

Element	At. No.	Netto	Mass [%]	Mass Norm. [%]	Atom [%]
Oxygen	8	11550	33.56	51.53	63.43
Silicon	14	10685	17.73	27.23	19.10
Aluminium	13	6022	7.98	12.26	8.95
Carbon	6	276	2.16	3.32	5.44
Magnesium	12	648	0.96	1.48	1.20
Potassium	19	642	1.34	2.06	1.04
Iron	26	29	1.24	1.90	0.67
		Sum	**65.12**	**100.00**	**100.00**

Point 1

Element	At. No.	Netto	Mass [%]	Mass Norm. [%]	Atom [%]
Sulfur	16	15330	35.90	34.39	35.58
Carbon	6	603	12.26	11.74	32.42
Iron	26	1092	56.25	53.87	32.00
		Sum	**104.40**	**100.00**	**100.00**

Figure 4.5.23. SEM images and EDS analysis results of subsample 4O (reference sample). A – interlayering of OM (black/dark grey color) and clay minerals. B – Pyrite in two forms: pyritised fossil forms a single crystal (1), framboids (2). C – close association of clay minerals, organic matter and pyrite. 1 – elongated pores between clay lamellas, 2 – pyrite crystals embedded into organic matter. D – idiomorphic pyrite framboid forming crystals.

Subsample 4C (107°C) is characterized by sparodic porous/fractured OM, however rock fabric did not demonstrate any significant changes. The rock fabric was preserved, but some of OM inclusions became porous (Figure 4.5.24).

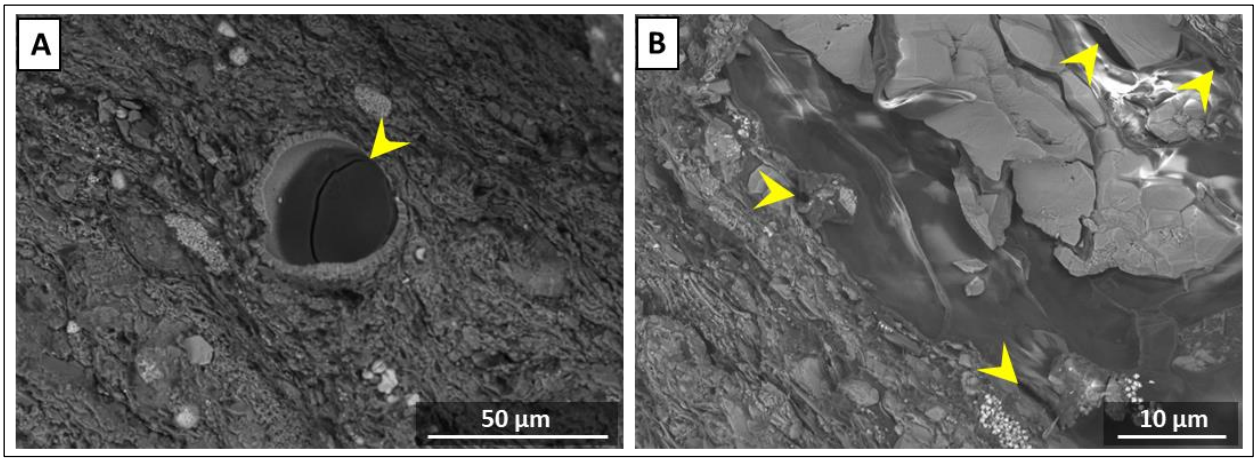

Figure 4.5.24. Formation of voids in the OM in subsample 4C (107°C), SEM images. A – fractures in OM. B – pores in OM.

The subsample 4B turned out to be special due to presence of sharp boundary of combusted area (Figure 4.5.25). In the one optical microscope image two parts were observed: light (lack of organic matter) and dark (organic matter presence) (Figure 4.5.25). The boundary between two parts may be considered as a micro- combustion front. For detailed investigation these two parts were studied in SEM separately, the results are presented below.

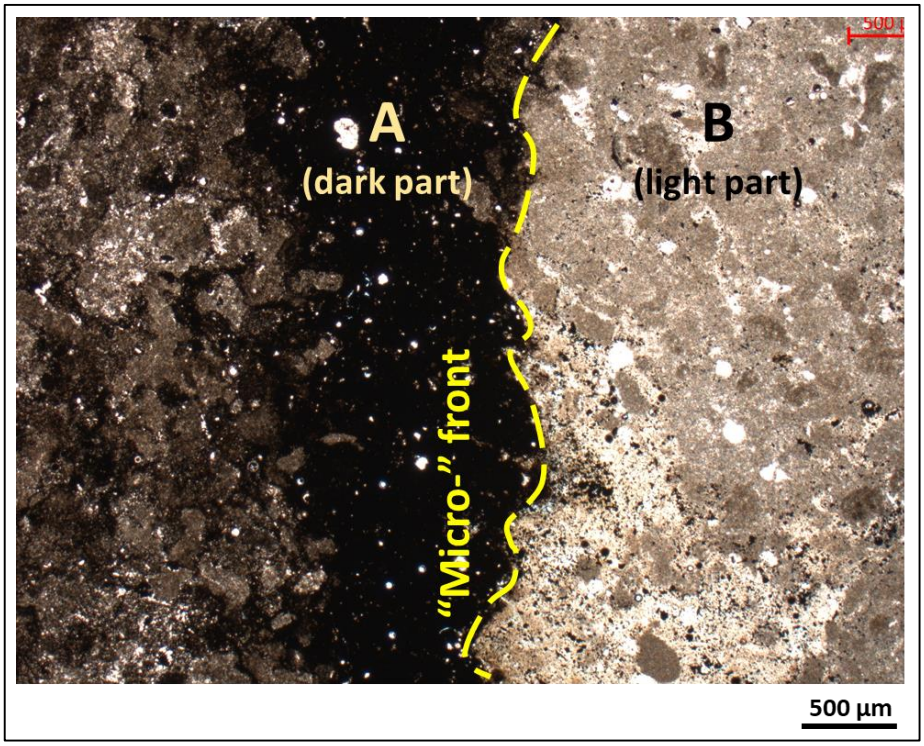

Figure 4.5.25. Two parts in a one field of view in optical microscope image. A – "dark part" is located before the combustion, dark color is due to organic matter. B – "light part" is located after the combustion front.

A. Dark part (before micro- combustion front)

The "dark" color is caused by the presence of OM (Figure 4.5.25, Figure 4.5.28). However, the amount of OM has been reduced in comparison with the reference sample, and pores are found in the intercrystalline space (Figure 4.5.28B). With the reduction of OM, calcite was partly dissolved and cavities were formed (Figure 4.5.26A) with intracrystalline nanopores (Figure 4.5.26B). Pyrite framboids retained their shape and geometry, however individual crystal habit has been altered and represents an irregular forms (Figure 4.5.26C) with reduced sulfur content (Figure 4.5.27A), which indicate formation of troilite (FeS). Single crystals of anhydrate were found (Figure 4.5.27B). The organic matter residuals form bubble like structures, which form additional porosity (Figure 4.5.28B).

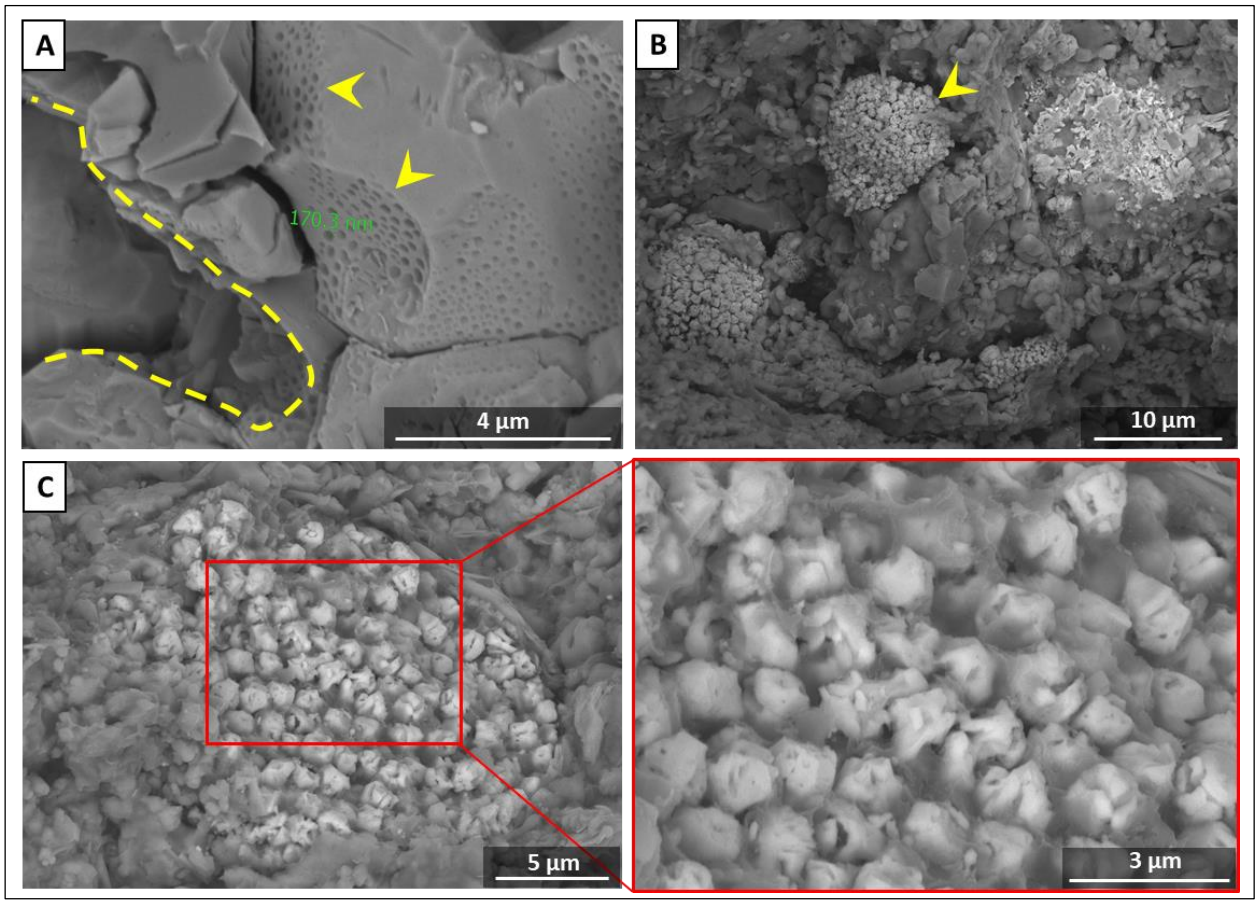

Figure 4.5.26. Microstructural alterations in subsample 4B (400°C). A – dashed line show traces of calcite dissolution, arrows indicate formation of nanopores in calcite. B – pyrite framboids retained their geometry, however individual crystals habit is altered, which is closer shown in the (C) panel.

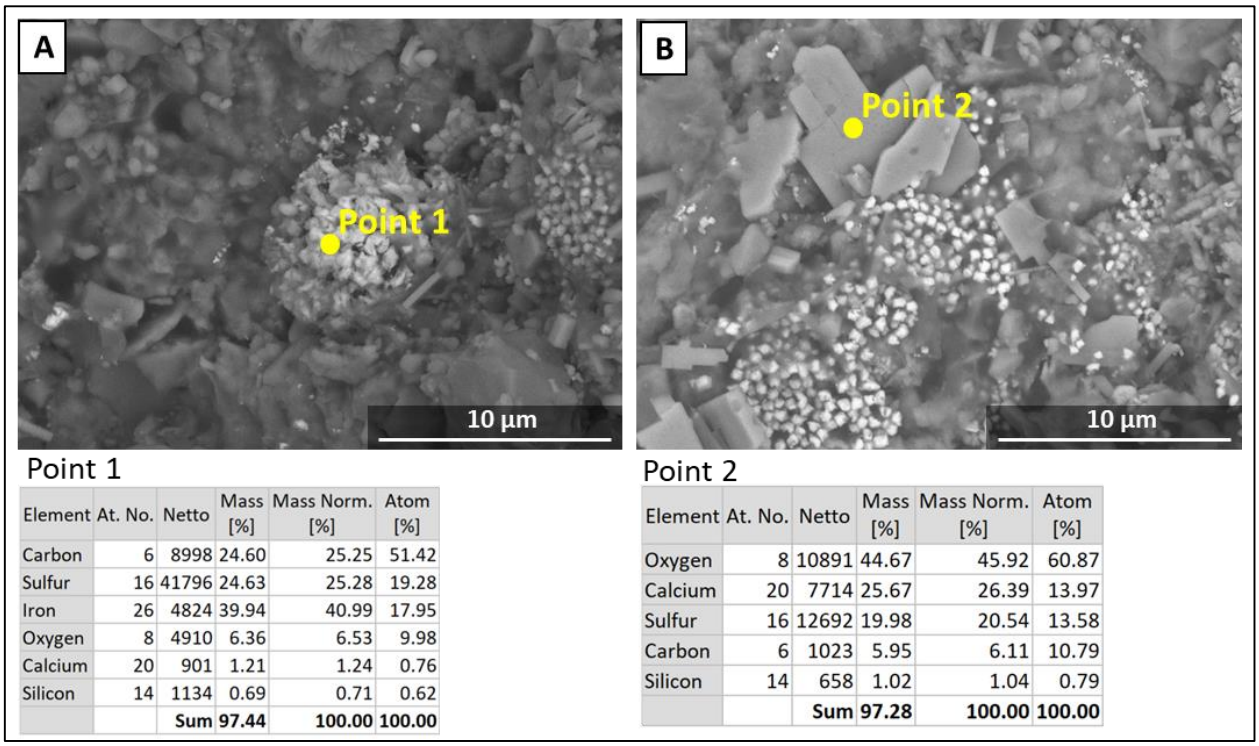

Point 1

Element	At. No.	Netto	Mass [%]	Mass Norm. [%]	Atom [%]
Carbon	6	8998	24.60	25.25	51.42
Sulfur	16	41796	24.63	25.28	19.28
Iron	26	4824	39.94	40.99	17.95
Oxygen	8	4910	6.36	6.53	9.98
Calcium	20	901	1.21	1.24	0.76
Silicon	14	1134	0.69	0.71	0.62
		Sum	**97.44**	**100.00**	**100.00**

Point 2

Element	At. No.	Netto	Mass [%]	Mass Norm. [%]	Atom [%]
Oxygen	8	10891	44.67	45.92	60.87
Calcium	20	7714	25.67	26.39	13.97
Sulfur	16	12692	19.98	20.54	13.58
Carbon	6	1023	5.95	6.11	10.79
Silicon	14	658	1.02	1.04	0.79
		Sum	**97.28**	**100.00**	**100.00**

Figure 4.5.27. Alterations of chemical composition in subsample 4B (400°C). A – pyrite (FeS_2) starts to loss sulfur and transform to FeS. B – crystal of anhydrite $CaSO_4$.

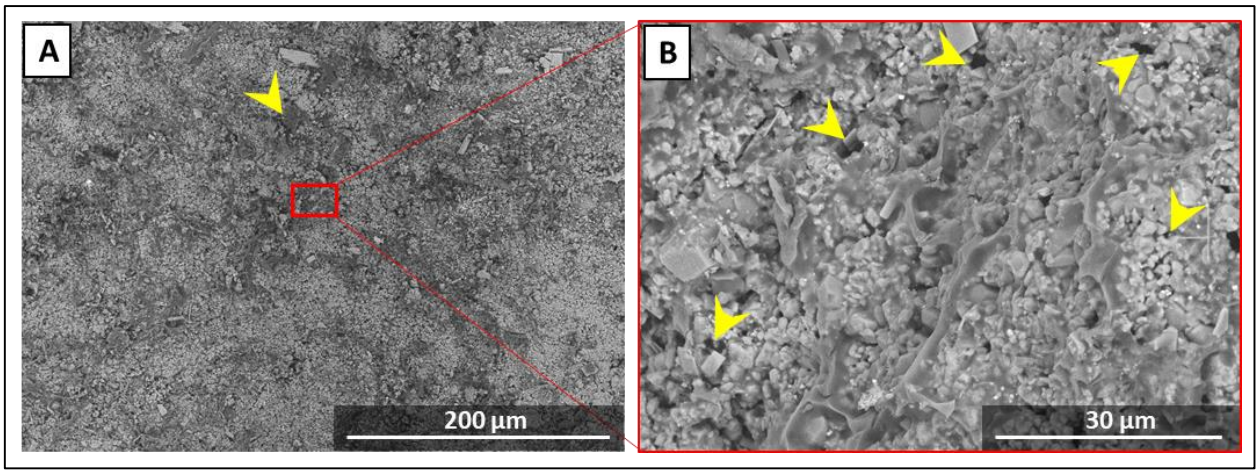

Figure 4.5.28. Organic matter (dark grey) and pore space in subsample 4B (400°C). A – sporadic distribution of OM in the sample in form of wisps and inclusions. B – pores are present in the intrercrystalline space and in the OM.

B. Light part (after micro- combustion front)

The root cause of the light color is absence of organic matter at this part (Figure 4.5.25, Figure 4.5.29A,B). Transformation and burning of OM lead to the formation of void space in the volume, initially occupied by OM (Figure 4.5.29A,B). Destruction of grain contacts with the formation of CaO occurred in the subsample (Figure 4.5.29B). The framboids still have their habitual configuration, however chemistry is changes towards decreasing of sulfur (Figure

4.5.29A) and its complete elimination with the formation of elementary iron and its gradual transformation to iron oxide with irregular shape crystals (Figure 4.5.29C).

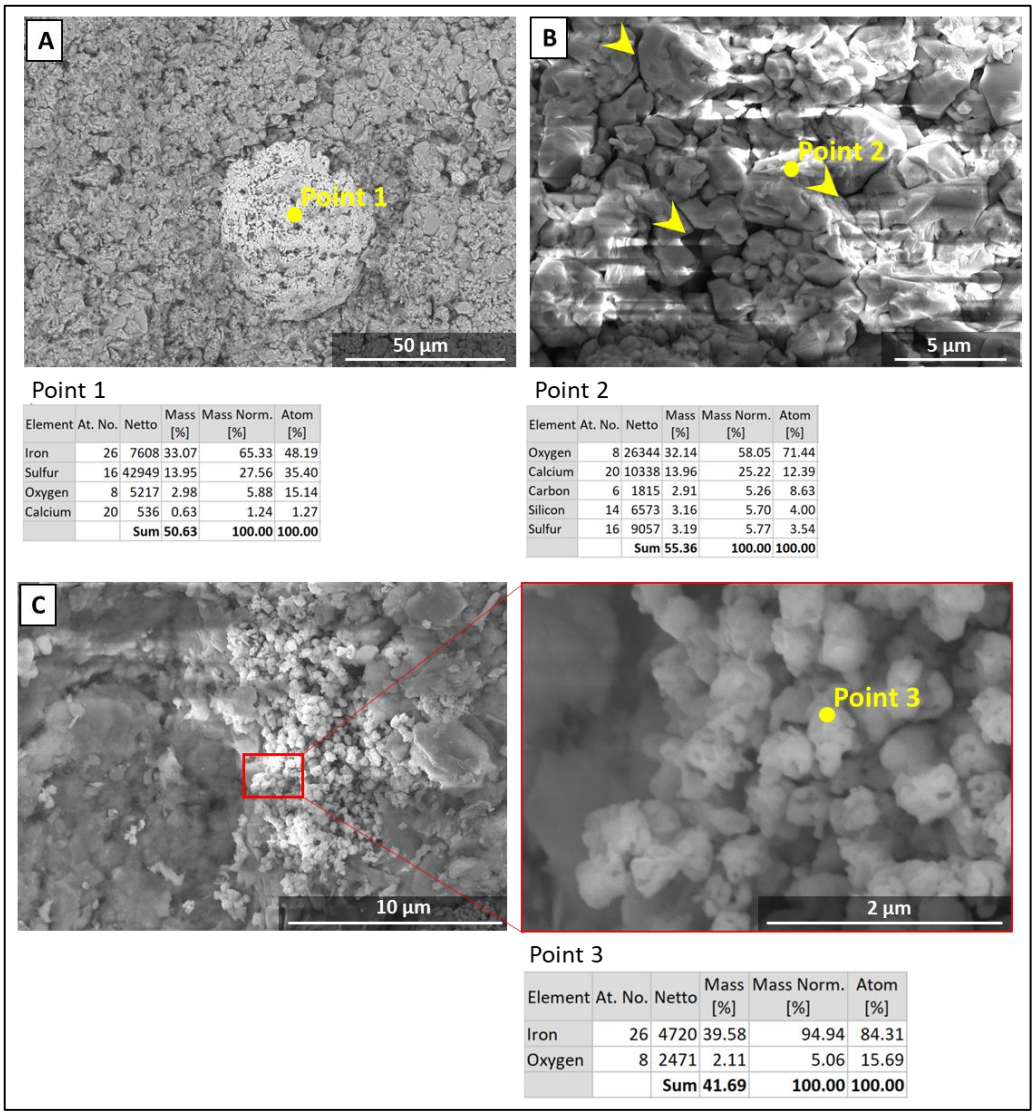

Figure 4.5.29. Microstructural and chemical alteration in the light part of subsample 5B. SEM images and EDS analysis results. A – decreasing of sulfur content in pyrite aggregates, transformation into FeS, B – destructed grain contacts, ration of Ca, C and O shows presence not only calcite, but also CaO. C – iron partly transformed to hematite (iron oxide).

The subsample 4A (841°C) is characterized by significant alteration in the phase composition and microstructure. Clay minerals (illite) is almost absent. Feldspar is presented in the form porous aggregates (Figure 4.5.31A), which is not common for the BF rocks. Calcite still present, however traces dissolution and decomposition are widespread (Figure 4.5.31B). The significant volume of the rock (30-40%) is presented Ca, Si and O dominant phase (Figure 4.5.31C, D (point 5)), which ratios are in a good correspondence with wollastonite mineral (CaSiO). Anhydrite (Figure 4.5.31D) occupies about 10-20% of the rock volume. Similarly, to other samples, hematite (iron oxide) was widely documented in the subsample (Figure 4.5.31E).

The microstructure of the rock is significantly altered (Figure 4.5.30). There are elongated voids appeared, the shape is inherited from clay minerals (Figure 4.5.30A). The size of these pores may reach 10 μm in length and 3 μm in width. The space between calcite crystals is filled by wollastonite phase, however pore space formed due to dissolution and decomposition still widely present (Figure 4.5.30B). No any framboidal structures were preserved in the rock (Figure 4.5.30C), iron and oxide (hematite) forms irregular shaped inclusions, often with porous structure. Anhydrite presented in the form needle-like tabular minerals, which fills the pore space and make it more complex (Figure 4.5.30D). Anhydrite is formed sporadically in the rock. However, in some cases it surrounds the hematite crystals, which confirm that the sulfur is came from the pyrite mineral (Figure 4.5.32, Figure 4.5.33).

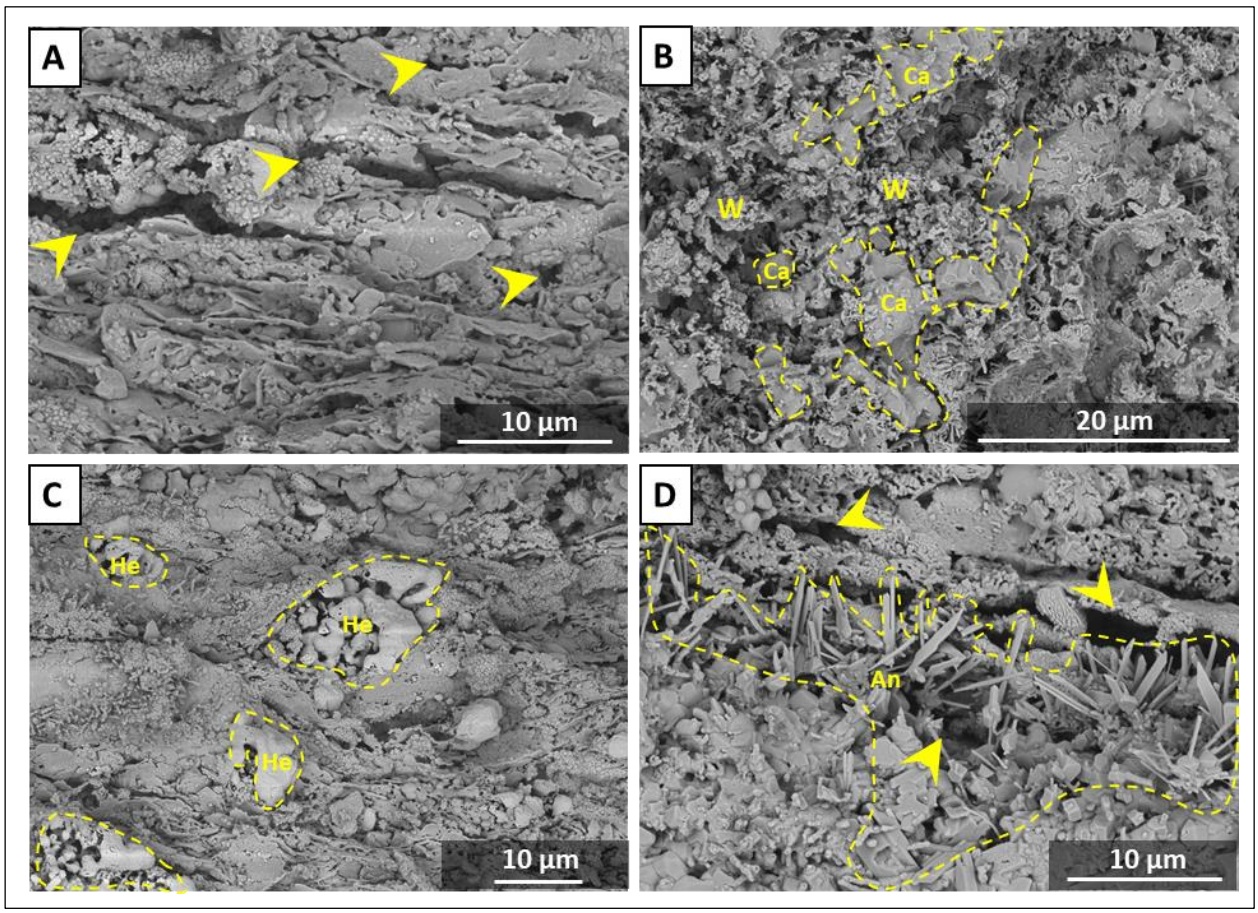

Figure 4.5.30. SEM images of subsample 4A (841°C). A – elongated voids, the shape of which is inherited from clay minerals. B – The space between calcite crystals is filled by new mineral wollastonite phase, however pore space formed due to dissolution and decomposition still widely present. C – No any framboidal structures were preserved in the rock (Figure 32C), iron and oxide (hematite) forms solid, irregularly shaped inclusions. D – Anhydrite presented in the form needle-like tabular minerals, which fills the pore space and make it more complex.

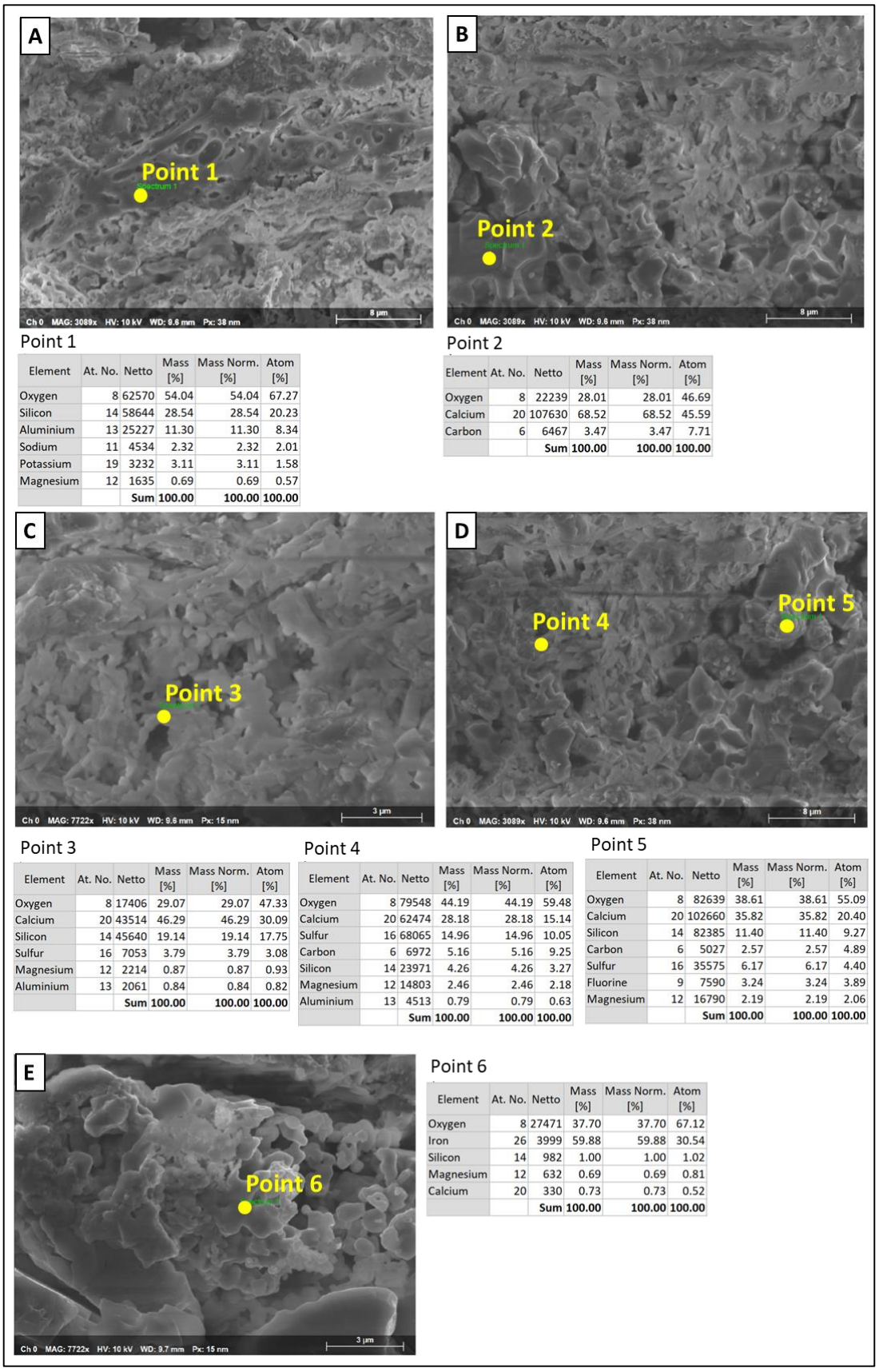

Point 1

Element	At. No.	Netto	Mass [%]	Mass Norm. [%]	Atom [%]
Oxygen	8	62570	54.04	54.04	67.27
Silicon	14	58644	28.54	28.54	20.23
Aluminium	13	25227	11.30	11.30	8.34
Sodium	11	4534	2.32	2.32	2.01
Potassium	19	3232	3.11	3.11	1.58
Magnesium	12	1635	0.69	0.69	0.57
		Sum	**100.00**	**100.00**	**100.00**

Point 2

Element	At. No.	Netto	Mass [%]	Mass Norm. [%]	Atom [%]
Oxygen	8	22239	28.01	28.01	46.69
Calcium	20	107630	68.52	68.52	45.59
Carbon	6	6467	3.47	3.47	7.71
		Sum	**100.00**	**100.00**	**100.00**

Point 3

Element	At. No.	Netto	Mass [%]	Mass Norm. [%]	Atom [%]
Oxygen	8	17406	29.07	29.07	47.33
Calcium	20	43514	46.29	46.29	30.09
Silicon	14	45640	19.14	19.14	17.75
Sulfur	16	7053	3.79	3.79	3.08
Magnesium	12	2214	0.87	0.87	0.93
Aluminium	13	2061	0.84	0.84	0.82
		Sum	**100.00**	**100.00**	**100.00**

Point 4

Element	At. No.	Netto	Mass [%]	Mass Norm. [%]	Atom [%]
Oxygen	8	79548	44.19	44.19	59.48
Calcium	20	62474	28.18	28.18	15.14
Sulfur	16	68065	14.96	14.96	10.05
Carbon	6	6972	5.16	5.16	9.25
Silicon	14	23971	4.26	4.26	3.27
Magnesium	12	14803	2.46	2.46	2.18
Aluminium	13	4513	0.79	0.79	0.63
		Sum	**100.00**	**100.00**	**100.00**

Point 5

Element	At. No.	Netto	Mass [%]	Mass Norm. [%]	Atom [%]
Oxygen	8	82639	38.61	38.61	55.09
Calcium	20	102660	35.82	35.82	20.40
Silicon	14	82385	11.40	11.40	9.27
Carbon	6	5027	2.57	2.57	4.89
Sulfur	16	35575	6.17	6.17	4.40
Fluorine	9	7590	3.24	3.24	3.89
Magnesium	12	16790	2.19	2.19	2.06
		Sum	**100.00**	**100.00**	**100.00**

Point 6

Element	At. No.	Netto	Mass [%]	Mass Norm. [%]	Atom [%]
Oxygen	8	27471	37.70	37.70	67.12
Iron	26	3999	59.88	59.88	30.54
Silicon	14	982	1.00	1.00	1.02
Magnesium	12	632	0.69	0.69	0.81
Calcium	20	330	0.73	0.73	0.52
		Sum	**100.00**	**100.00**	**100.00**

Figure 4.5.31. SEM images and EDS analysis results of subsample 4A (841°C). A – porous feldspar particle. B – Calcite. C – Ca, Si and O mineral phase (wollastonite). D – anhydrite (point 4) and wollastonite (point 5). E – hematite inclusion.

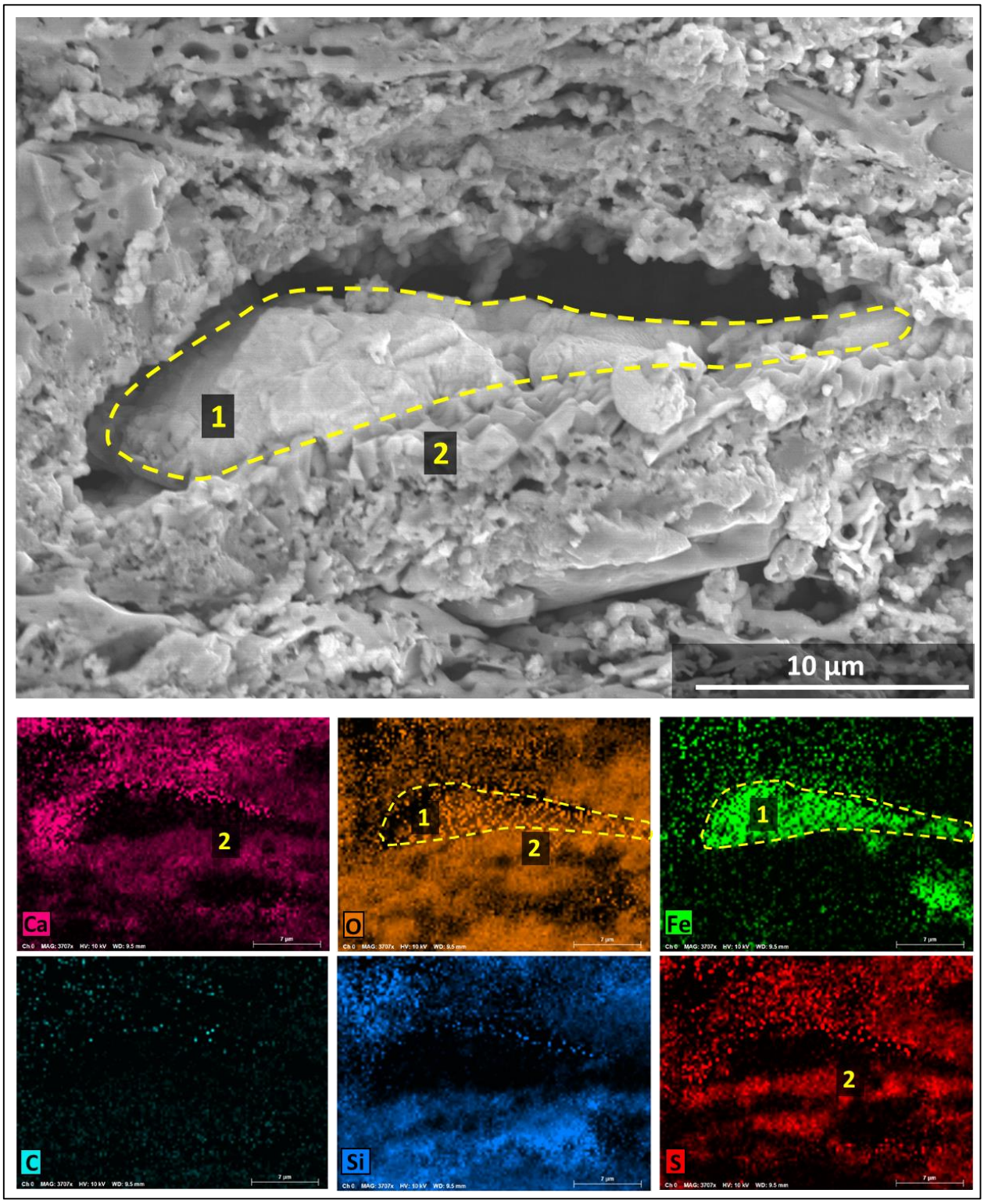

Figure 4.5.32. Results of EDS Mapping for subsample 4A (841°C). Hematite Fe_2O_3 grain (1) is surrounded by anhydrite $CaSO_4$ crystals (2).

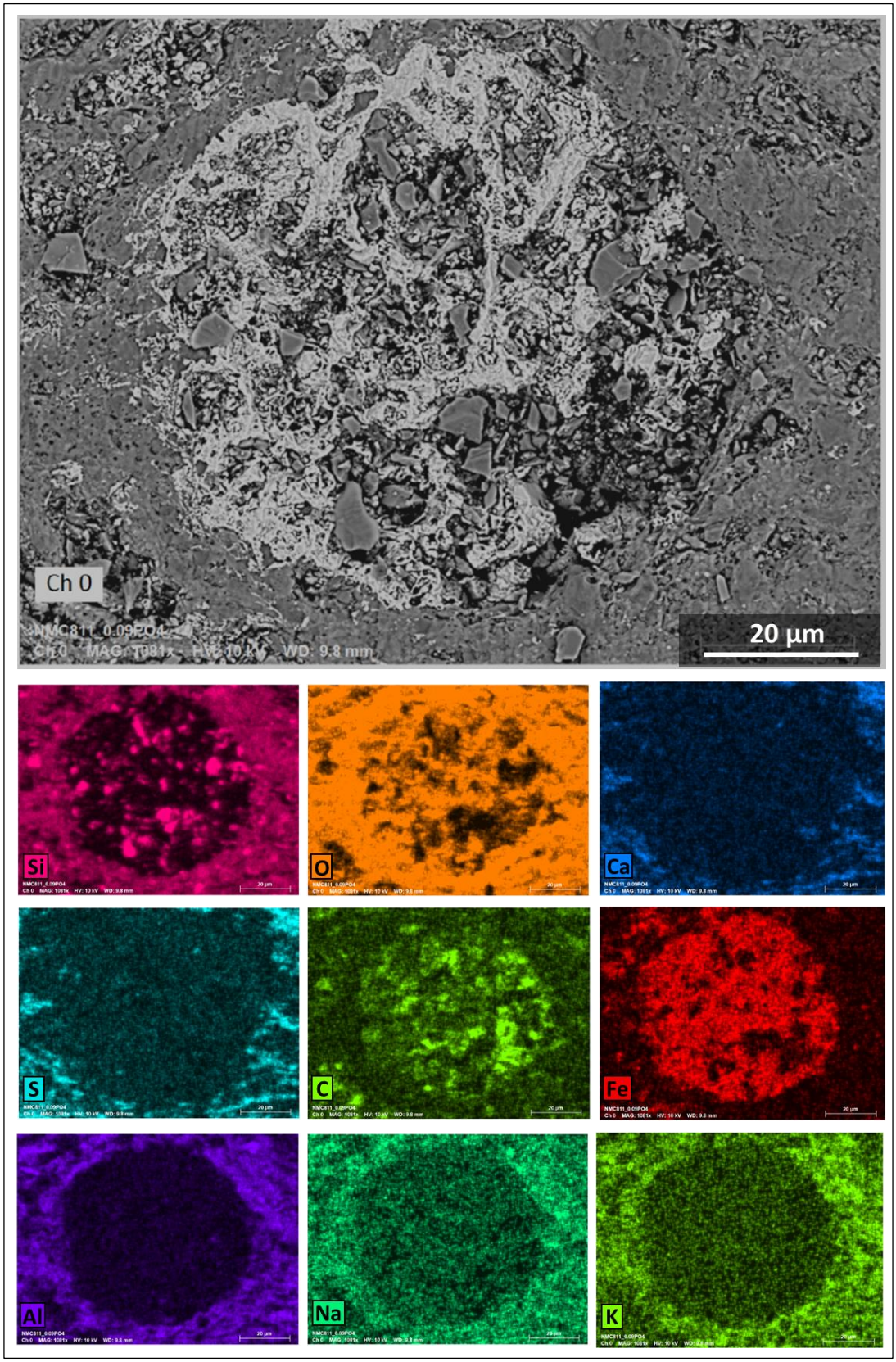

Figure 4.5.33. Results of EDS Mapping for subsample 4A (841°C). Hematite Fe_2O_3 inclusion.

4.5.4. X-ray powder diffraction

Lithotype 1. Siliceous mudstone

X-Ray powder diffraction analysis results are shown in Figure 4.5.34 and Table 4.5.1. Mineral composition of the reference sample is represented by the quartz, pyrite and small amount of dolomite (Figure 4.5.34, Table 4.5.1). The influence of 107°C on the sample (1C) did not cause any changes in the phase composition. XRD patterns of the 1O and 1C samples show that the samples are almost identical. The sample 1B (400°C) is characterized by the appearance of iron sulfide (FeS). At the highest temperature 841°C (1A) appearance of hematite and traces of anhydrite were detected, no more pyrite, iron sulfide and dolomite are in the sample. Quartz did not show any changes through the experiment.

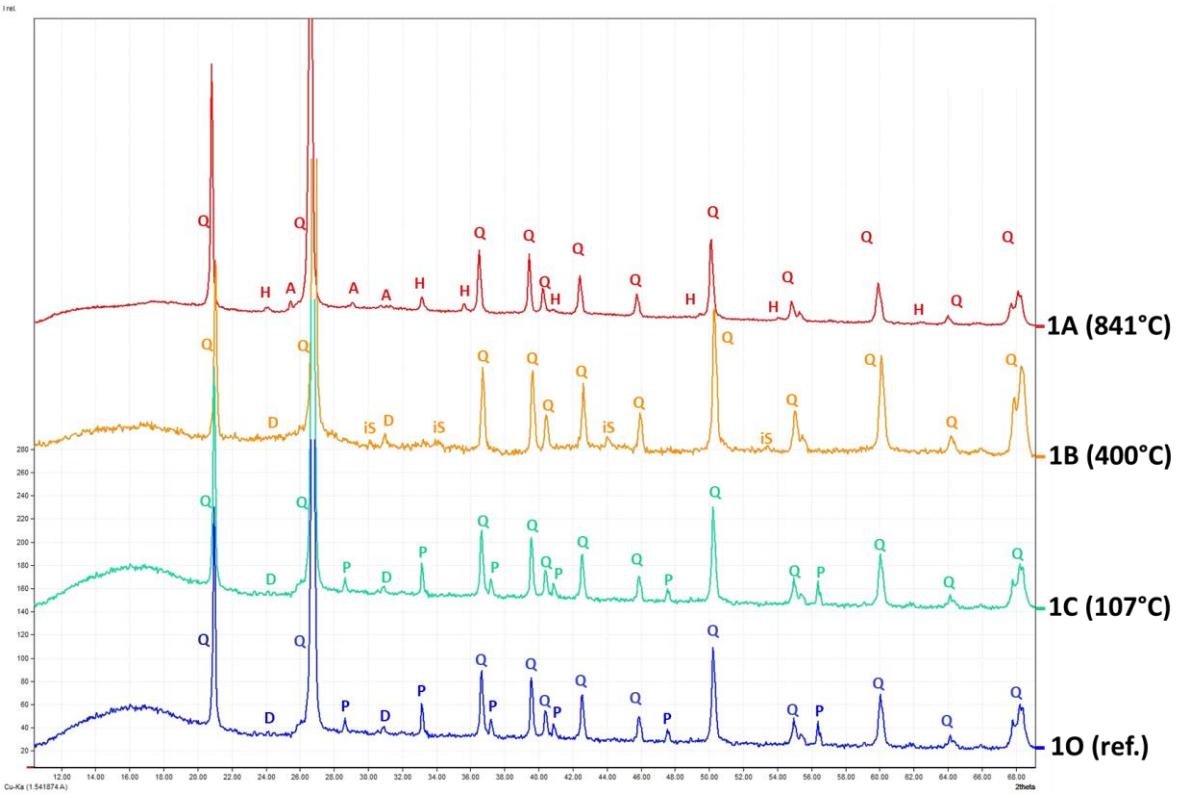

Figure 4.5.34. XRD spectra of lithotype 1 subsamples (reflection geometry, Bruker D8 ADVANCE).
Q – quartz, P – pyrite, D – dolomite, iS – iron sulfide (FeS), H –hematite (Fe_2O_3), A – anhydrite.

Table 4.5.1. Results of quantitative XRD analysis of lithotype 1 subsamples.

Sample	Quartz, %	Pyrite, %	Dolomite,%	FeS*, %	Hematite*, %	Anhydrite*, %
1O	95.2	1.9	2.9	-	-	-
1C	95.6	2.3	2.1	-	-	-
1B	95.8	-	3.1	1.1	-	-
1A	96.7	-	-	-	2.3	<1

* *newly formed minerals*

Lithotype 2. Aporadiolarian siliceous dolomite

X-Ray powder diffraction analysis results are shown in Figure 4.5.35 and Table 4.5.2. Mineral composition of the reference sample is represented predominantly by dolomite, quartz, calcite and small amount of pyrite (Figure 4.5.35, Table 4.5.2). Mineral composition stays relatively stable after the impact at temperature of 107°C and 490°C and are identical to the reference sample, only the pyrite has disappeared. After the 841°C the phase composition was significantly altered. No dolomite and pyrite were detected. At least three new mineral phase observed: periclase (MgO), anhydrite ($CaSO_4$), hematite (Fe_2O_3), some traces of CaO were found. Two peaks left not associated with particular mineral phase (due to crystal structure complexity and a very small amount), one of the possible candidate is wollastonite ($CaSiO_3$), however observed peaks not almost coincide with the database spectra. XRD experiment in transmission geometry has confirmed presence of all phases, and the peaks, which may match to wollastonite (Figure 4.5.36).

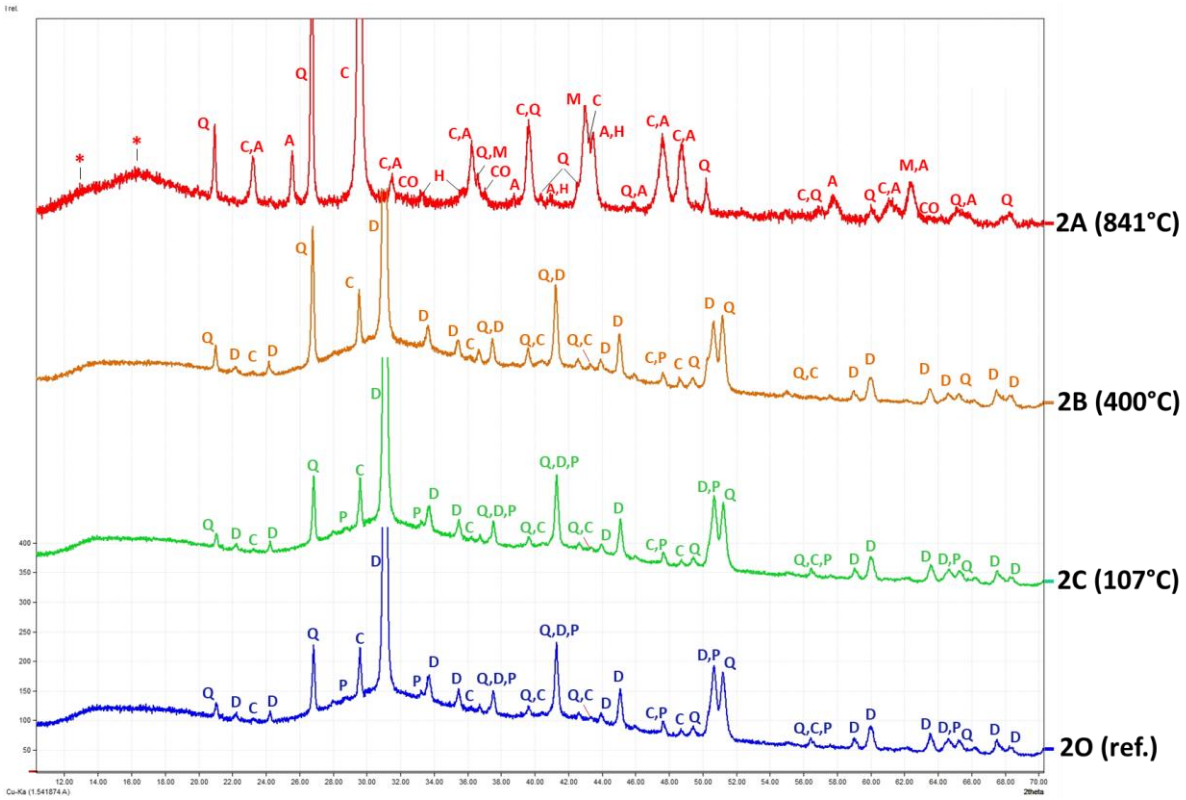

Figure 4.5.35. XRD spectra of lithotype 2 subsamples (reflection geometry, Bruker D8 ADVANCE).

Q – quartz, P – pyrite, D – dolomite, C – calcite, H – hematite (Fe_2O_3), A – anhydrite, M – periclase (MgO), CO – calcium oxide (CaO), * – unidentified phase (wollastonite?).

Table 4.5.2. Results of quantitative XRD analysis of lithotype 2 subsamples.

Sample	Dolomite, %	Calcite,%	Quartz, %	Pyrite,%	Anhydrite*, %	Fe_2O_3*, %	MgO*, %	CaO*,%
2O	78.2	8.9	11.2	1.7	-	-	-	-
2C	79.3	8.5	10.6	1.6	-	-	-	-
2B	78.3	9.1	12.6	-	-	-	-	-
2A	-	52.7	23.8	-	6.2	1.7	15.1	<0.5

** newly formed minerals*

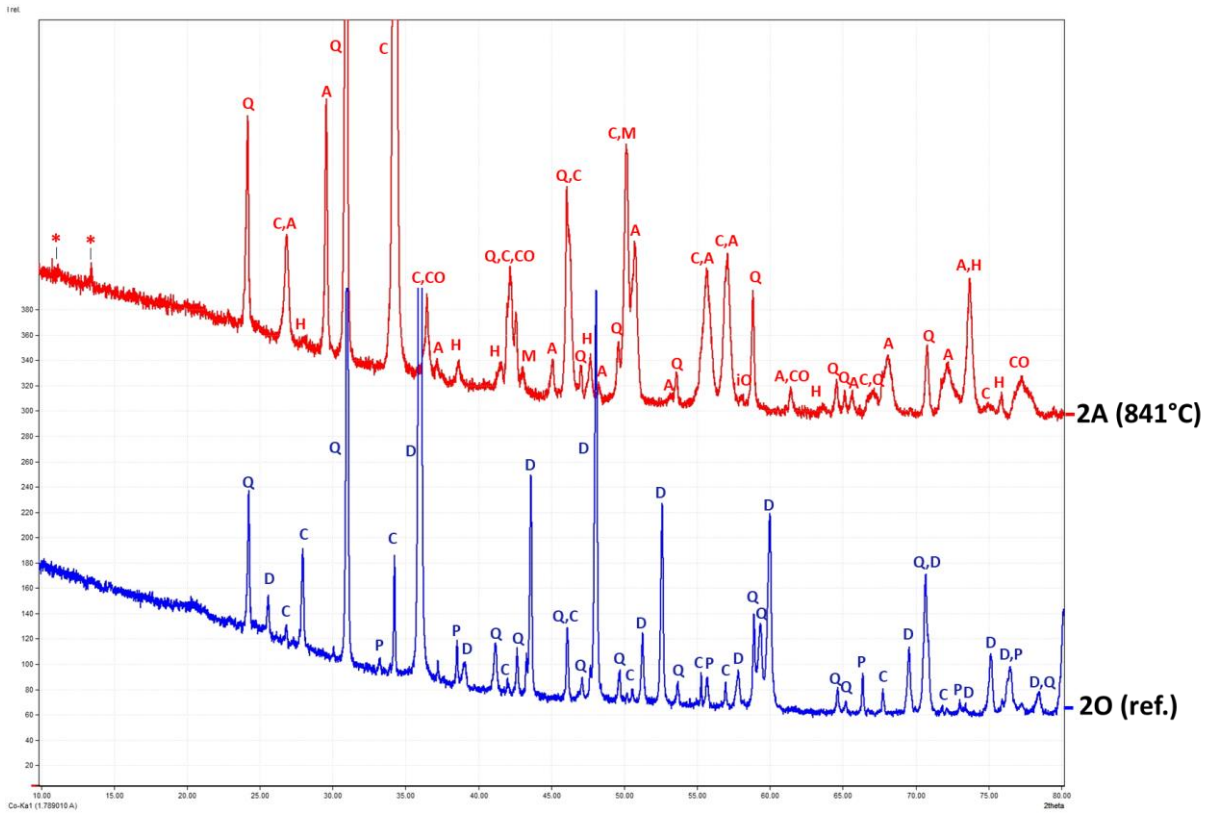

Figure 4.5.36. XRD spectra of subsamples of lithotype 2 (transmission geometry, Huber G670).

Q – quartz, P – pyrite, D – dolomite, C – calcite, H – hematite (Fe_2O_3), A – anhydrite, M – periclase (MgO), CO – calcium oxide (CaO), * – unidentified phase (wollastonite?).

Lithotype 3. Argillaceous-siliceous organic-rich mudstone

Initial composition is represented by quartz, illite, albite and pyrite (Table 4.5.3). XRD patterns of subsamples 3O, 3C and 3B (Figure 4.5.37) shows their general identity in term of composition, except of presence of iron sulfide in the 3B. 3A is characterized by disappearance of pyrite and iron sulfide, and the detection of hematite (iron oxide III, Fe_2O_3) and new phases, which cannot be cannot be reliably recognized.

To clarify new phases and confirmed already observed in reflected geometry, XRD experiment in transmission mode was performed (Figure 4.5.38). The formation of hematite was confirmed, and the new phase is mullite with a high degree of peak matching in the area of low angles. And one phase stays unrecognized due complex structure and small amounts.

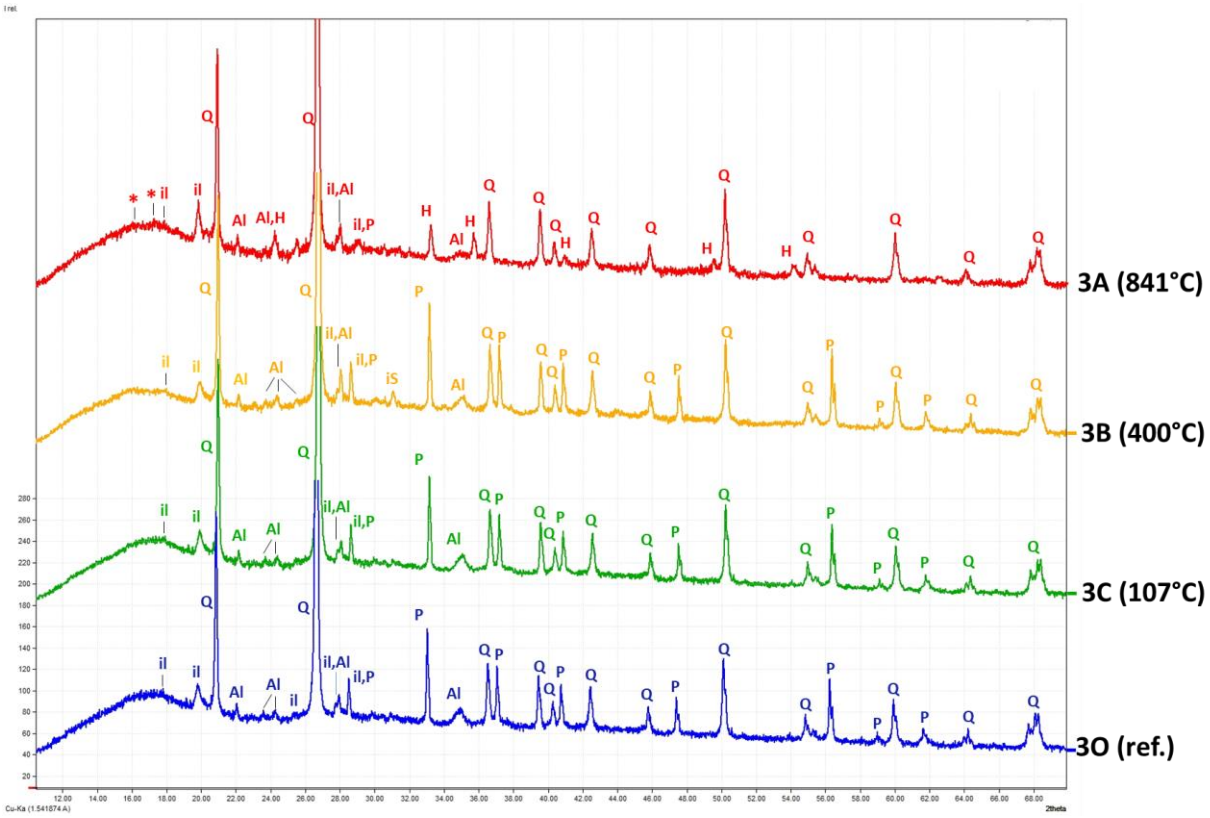

Figure 4.5.37. XRD spectra of lithotype 3 subsamples (reflection geometry, Bruker D8 ADVANCE).
Q – quartz, il – illite, P – pyrite, Al – albite, iS – iron sulfide (FeS), H – hematite (Fe_2O_3), * – unidentified phase.

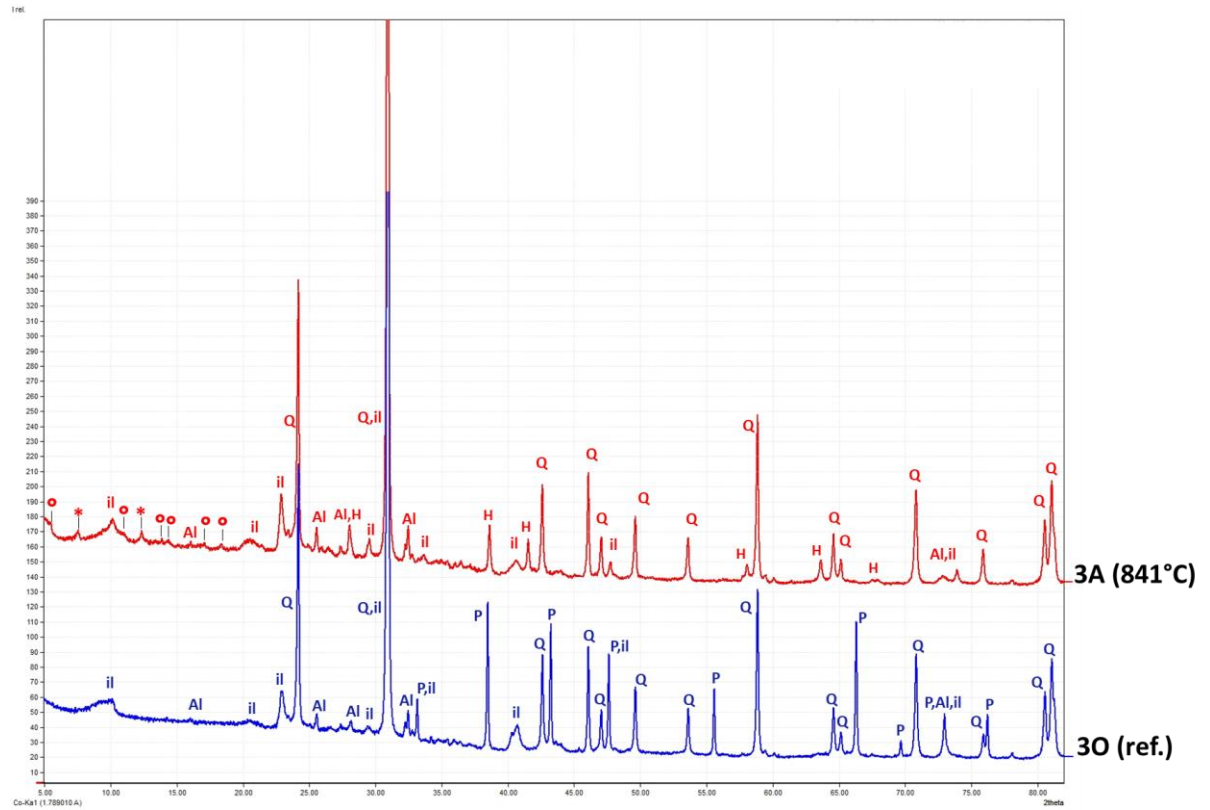

Figure 4.5.38. XRD spectra of lithotype 3 subsamples (transmission geometry, Huber G670).
Q – quartz, il – illite, P – pyrite, Al – albite, iS – iron sulfide (FeS), H – hematite (Fe_2O_3), ° – mullite, * - unidentified phase.

Table 4.5.3. Results of quantitative XRD analysis of lithotype 3 subsamples.

Sample	Quartz, %	Illite,%	Albite, %	Pyrite,%	FeS*,%	Fe_2O_3*, %	Mullite*,%
3O	65.2	21.4	8.5	4.9	-	-	-
3C	66.7	19.9	8.2	5.2	-	-	-
3B	69.5	20.1	5.2	4.2	<1	-	-
3A	63.2	9.7	6.4	-	-	4.3	16.4

** newly formed minerals*

Lithotype 4. Calcareous-argillaceous organic-rich mudstone

Mineral composition of subsamples 4O and 4C is almost identical and represented by quartz, calcite, illite, albite and pyrite (Figure 4.5.39). The subsample 4B is characterized by similar mineral composition, however appearance of iron sulfide is detected (Table 4.5.4). Variations of quantative values of mineral composition is caused by heterogeneity of samples and not related to the theramal treatment. And the sample 4A is characterized by presence of hematite and anhydrite wtih disappearance of pyrite. New peaks have been detected; however identification of phase is not possible on that XRD spectra obtained on reflected geometry.

XRD experiment with transmission geometry allowed to detect more peaks and identify newly formed minerals (Figure 4.5.40). These minerals are wollastonite ($CaSiO_3$), gehlenite ($Ca_2Al(AlSiO_7)$) and mullite ($Al_{4+2x}Si_{2-2x}O_{10-x}$). All the other phases are consistent with the reflected geometry.

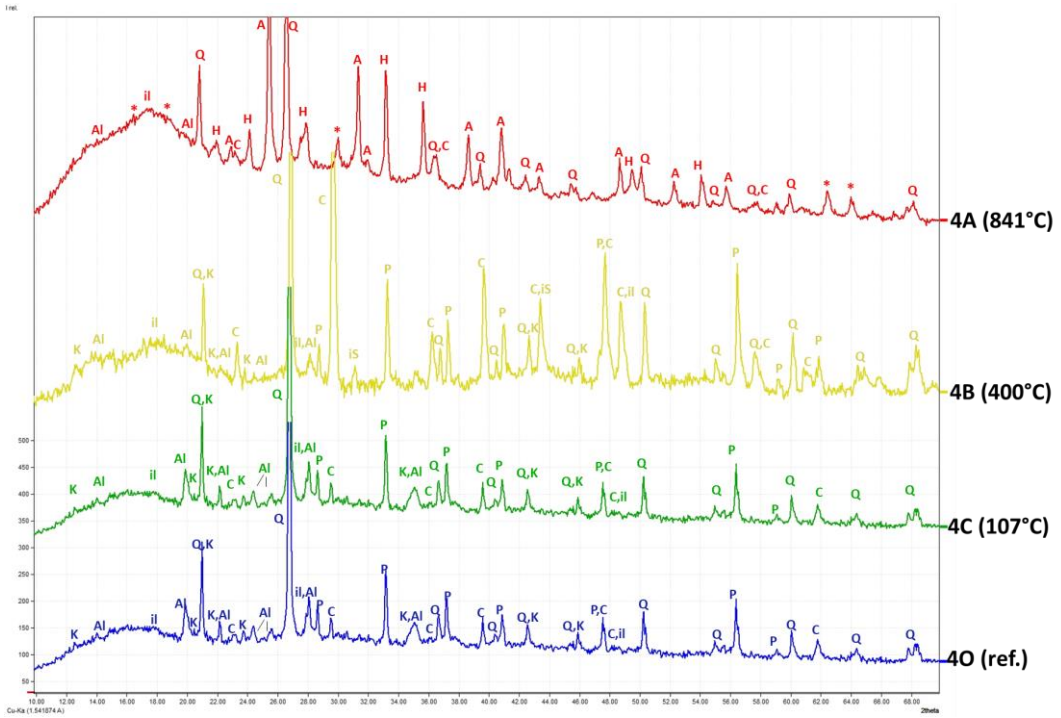

Figure 4.5.39. XRD spectra of lithotype 4 subsamples (reflection geometry, Bruker D8 ADVANCE).
Q – quartz, il – illite, P – pyrite, Al – albite, iS – iron sulfide (FeS), H – hematite (Fe_2O_3), * – peaks which cannot be related to single particular phase.

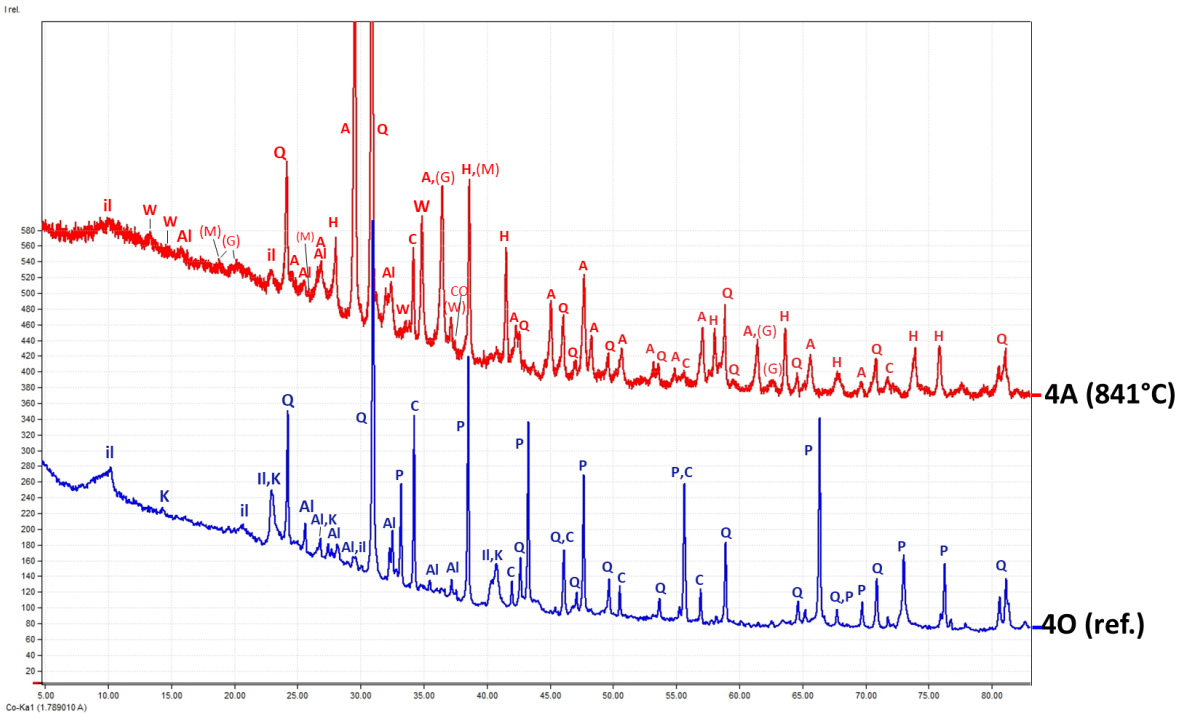

Figure 4.5.40. XRD spectra of lithotype 4 subsamples of (transmission geometry, Huber G670).

Q – quartz, il – illite, P – pyrite, Al – albite, iS – iron sulfide (FeS), H – hematite (Fe_2O_3), W – wollastonite, (M) – mullite, (G) – gehlenite.

Table 4.5.4. Results of quantitative XRD analysis of lithotype 4 subsamples.

Sample	Quartz, %	Illite,%	Calcite, %	Albite, %	Pyrite,%	Anhydrite*, %	CaO*, %	FeS*,%	Hematite*, %	Wollastonite*, %	Mullite*, %	Gehlenite*, %
4O	37.8	22.1	32.4	4.0	4.3	-	-	-	-	-	-	-
4C	29.2	29.3	35.7	2.1	3.3	-	-	-	-	-	-	-
4B	38.6	21.1	32.3	2.3	2.5	-	-	1.5	-	-	-	-
4A	34.4	2.7	4.6	5.0	-	23.5	tr.	-	7.1	12.6	9.1	<1

** newly formed minerals*
tr.- traces

4.5.5. Micro-CT imaging

Micro-CT scanning was performed for the reference subsamples ("O" series) and the subsamples after the highest temperature impact ("A" series, 841℃). Micro-CT allowed to evaluate rock fabric and porosity alterations after the experiment within the 3D volume with the 3 μm resolution. Results of porosity estimation are showed in Figure 4.5.41. Micro-CT slices and void space visualization are presented in Figure 4.5.42 and Figure 4.5.43.

Lithotype 1 (siliceous mudstone) is characterized by lack of alterations in pore space (Figure 4.5.41) and rock fabric (Figure 4.5.42) after the experiment. However, slight decrease of closed pore space with increasing of open pore space was detected. Although the lithotype is depleted in OM, that might be result of OM transformation and displacement during the experiment.

Micro-CT of lithotype 2 (aporadiolarian siliceous dolomite) showed slight increase in open porosity from 0.57% to 1.10% with no changes in closed porosity (Figure 4.5.41). Rock fabric has not been altered (Figure 4.5.42).

Lithotype 3 (argillaceous-siliceous organic-rich mudstone) is characterized by significant increase of porosity from 0.26% to 4.53% (Figure 4.5.41), open and closed porosity are in an equal proportions (2.56% and 1.97%). Micro-CT slices show that fractures and rare individual pores have been formed after the experiment (Figure 4.5.42), which are characterized by the parallel to layering orientation (Figure 4.5.43).

Lithotype 4 (calcareous-argillaceous organic-rich mudstone). Increasing of porosity from 0.24% to 3.40% has been observed after the experiment. Individual pores and fractures are equally distributed over the sample (Figure 4.5.42) with parallel to lamination orientation predominantly (Figure 4.5.43).

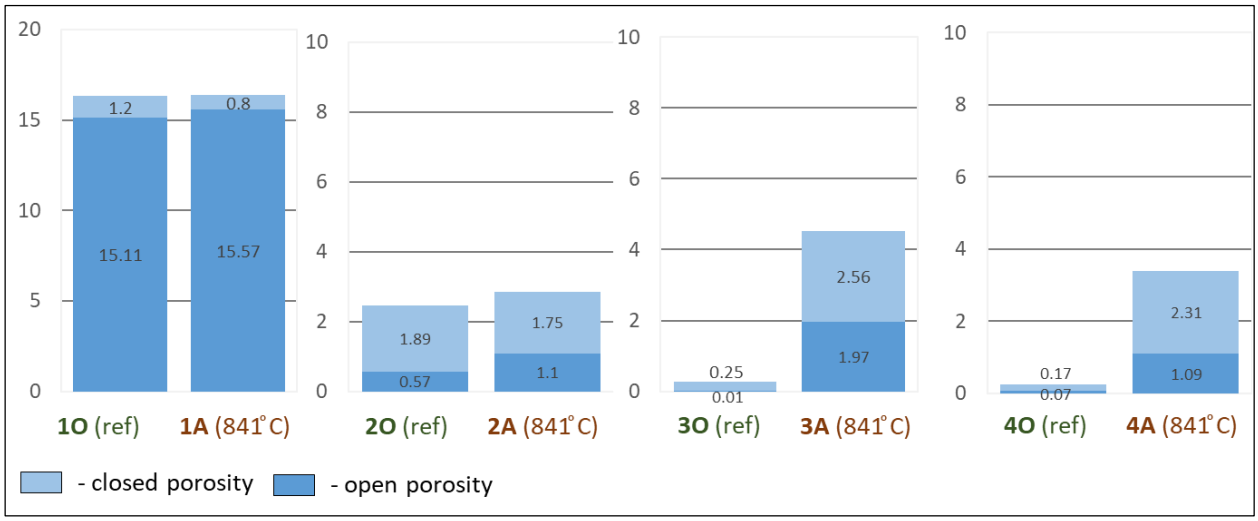

Figure 4.5.41. Porosity calculated from micro-CT.

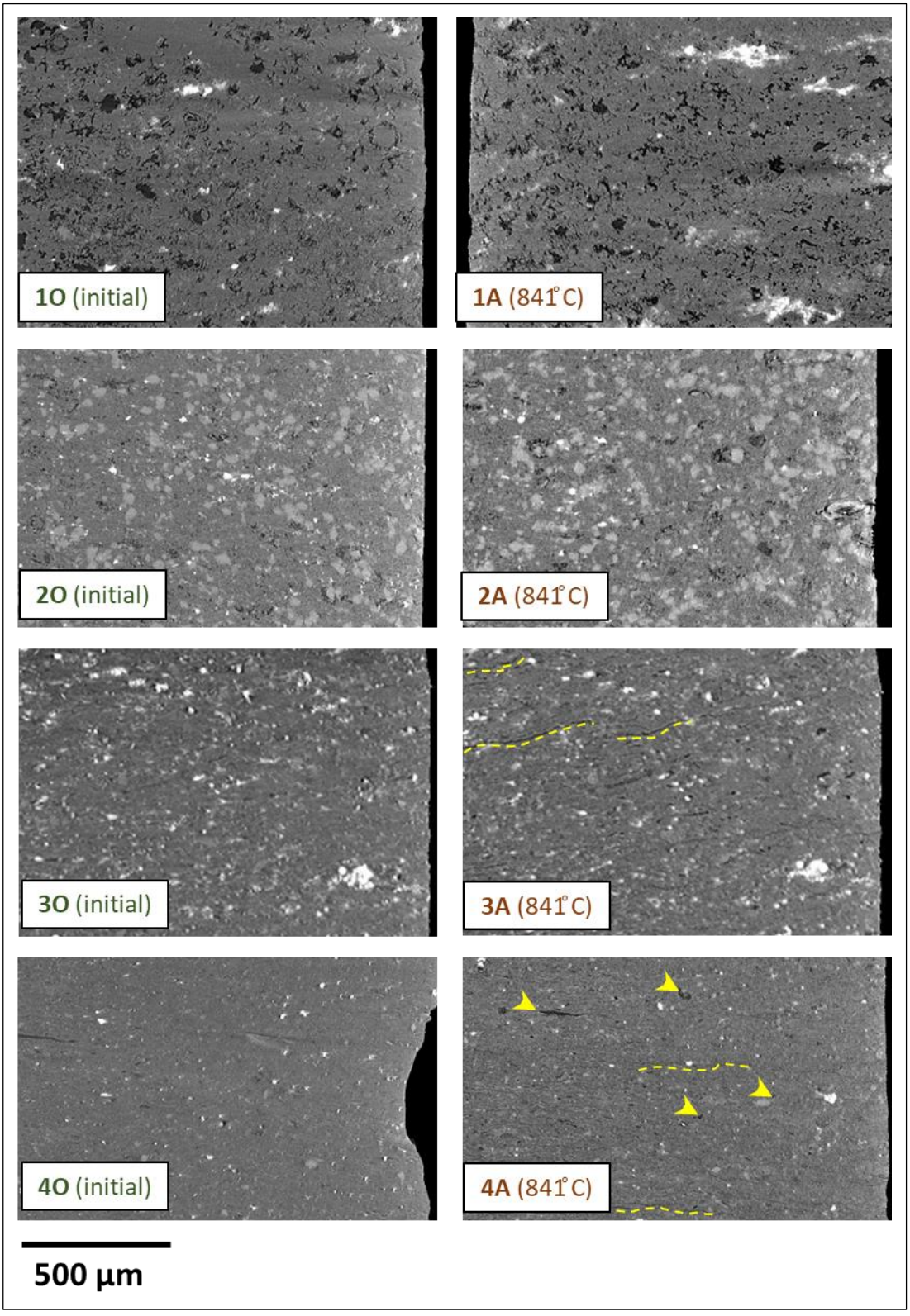

Figure 4.5.42. Micro-CT slices of scanned samples. Dashed lines show fractures, arrows indicated individual pores.

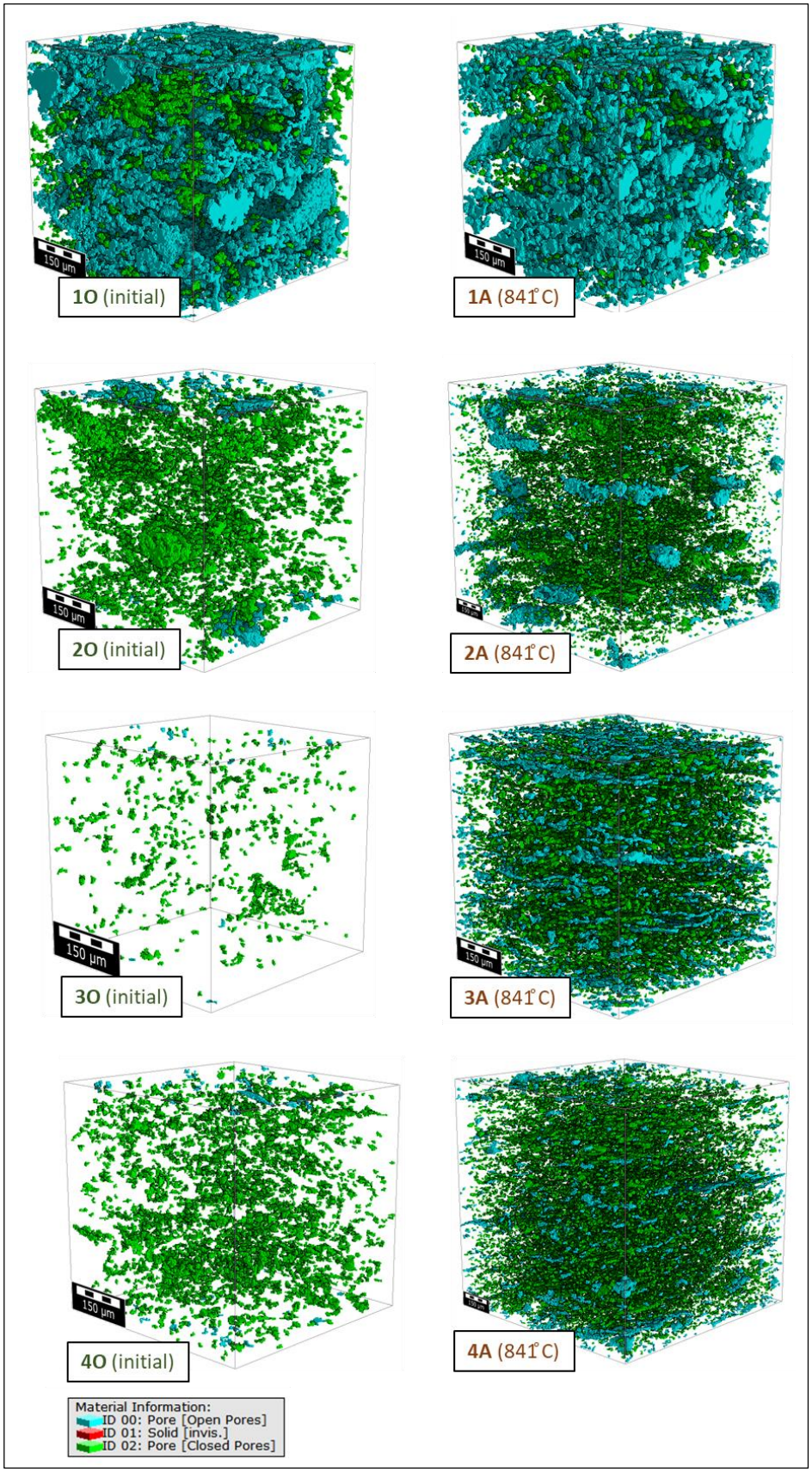

Figure 4.5.43. Void space visualization.

4.5.6. Thermal properties profiling

Thermal conductivity and heat capacity were obtained for each subsample, results are shown in Figure 4.5.44 and Figure 4.5.45.

Figure 1 illustrates thermal conductivity changing in particular lithotypes with temperature growth. Two patterns of thermal conductivity during thermal treatment are distinguished.

The first one assumes stable thermal conductivity after temperature impact – two series of lithotype 1 samples. Thermal conductivity is fluctuating around 3 W/(m*K), fluctuations do not exceed 0.17 W/(m*K) (≈5%) (Figure 4.5.44A, B), which are in line lithological heterogeneities within one lithotype (slight variations in OM distribution, porosity etc.). Stable behavior of thermal conductivity during the treatment may be explained by several factors. The lithotype 1 is characterized by relatively high initial porosity 5-8%, quartz domination in mineral composition and relatively small amount of OM (TOC=3.3 %). All these properties remain stable during the treatment: no increase of porosity due to small amount of OM, no alteration of quartz due to its stability up to thousand calcium degrees. Since thermal conductivity determined by porosity and organic matter, which do not experience significant changes – no changes in thermal conductivity.

The other pattern assumes up to 60% thermal conductivity reduction during the treatment. Lithotypes 2-4 fall under this pattern. Thermal conductivity is decreasing from the values of 1.4-2.2 W/(m*K) to 0.7-1.3 W/(m*K), or 30-60 % reduction (Figure 4.5.44A, B). Such dramatic thermal caused by number of factors for different lithotypes. For the lithotypes 3 and 4 this reduction is related to its initial state: relatively high content of OM (TOC is in the range of 11-13%) and lack of pore space. Only subsample 4C (107°C) is characterized by 10% increased thermal conductivity, which might be result of lithological heterogeneity of the sample (this lithotype is represented by carbonate lenses in clay dominated mineral matrix). Thermal treatment caused progressive transformation and displacement of OM and formation of pore space filled by air. Since the thermal conductivity of air is magnitudes lower than OM – this factor contributed to the total decline of thermal conductivity. For the lithotype 2 other factor played a crucial role – progressive decomposition of dolomite crystals during the treatment. Decomposition of large dolomite crystals into nano- and micro- crystals lead to increase of porosity inside the crystals, which in turn caused reduction of thermal conductivity. Finally, the common factor for all the lithotypes is destruction of grain contacts due to different values of thermal expansion coefficient of minerals.

Similar differentiation of lithotypes on groups are made on the basis of thermal heat capacity changing during the treatment (Figure 4.5.45). Lithotypes 1 is characterized relatively stable heat capacity on all stages (1.5-1.8 mJ/(m^3*K)), except 107°C stage, which is characterized

by 13-23 % increase. All the other lithotypes are characterized by progressive thermal heat capacity decrease up to 40%.

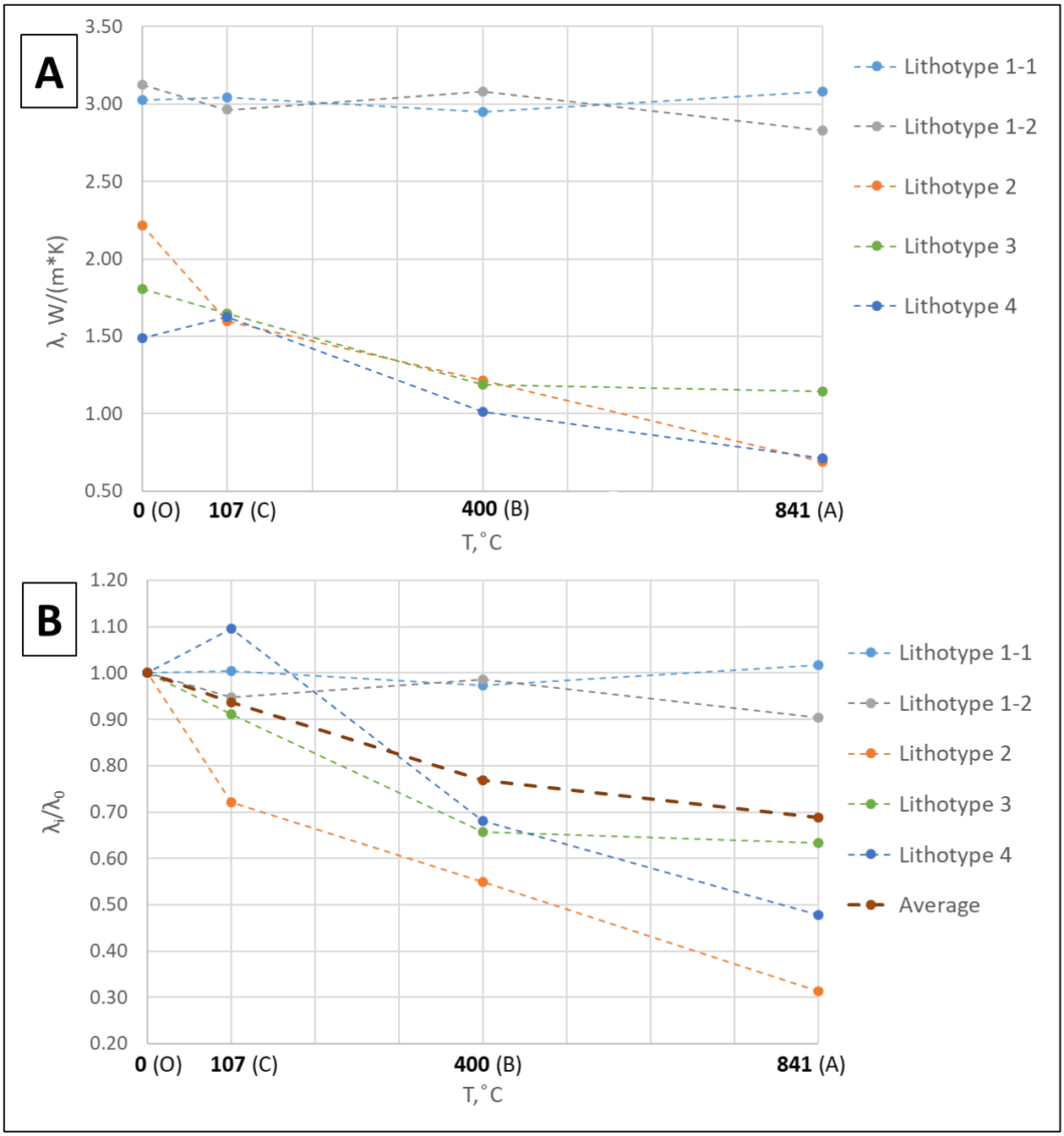

Figure 4.5.44. Thermal conductivity changing with temperature growth. A –absolute value of thermal conductivity. B – relative change of thermal conductivity. (Error bars are smaller than the point)

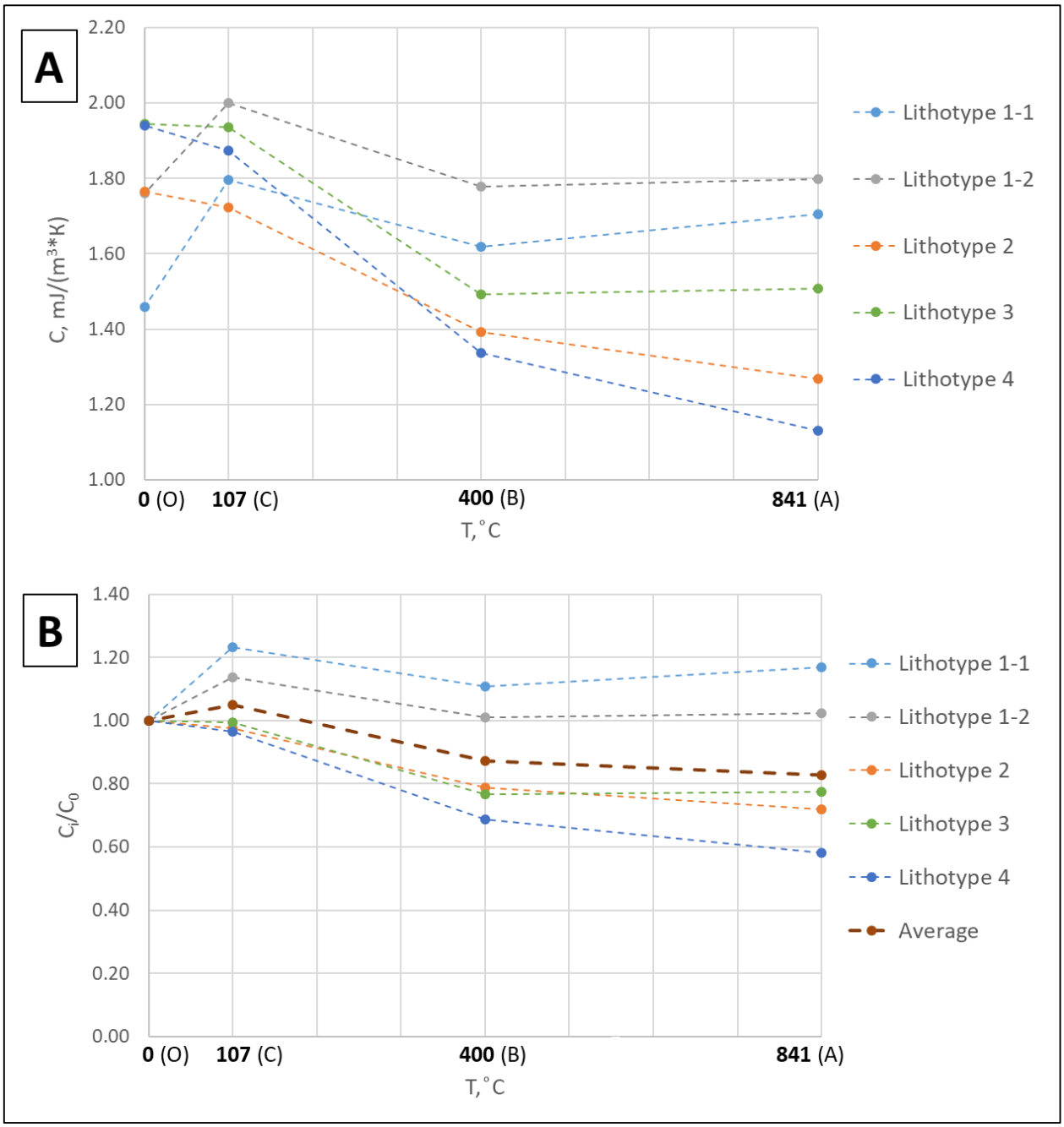

Figure 4.5.45. Thermal heat capacity changing with temperature growth. A –absolute value of thermal heat capacity. B – relative change of thermal heat capacity value. (Error bars are smaller than the point)

4.5.7. Programmed pyrolysis

Rock-Eval pyrolysis was performed for all subsamples to characterize organic matter. Results are demonstrated in Figure 4.5.46.

Results show decreasing of TOC, S1, S2 and increasing of Tmax during the temperature impact (Figure 4.5.46). According initial TOC content (Figure 4.5.46A) lithotypes may be organized into two groups. The first group is organic-rich mudstones with high TOC content, 11.5 % (lithotype 3) and 13.1 % (lithotype 4). The second group is organic lean radiolarites with the TOC content 3.3 % (lithotype 1) and 2.8 % (lithotype 2). In the same manner these two groups may be differentiated according S2 value (hydrocarbons generated through thermal cracking of nonvolatile organic matter, potential of HC producing) (Figure 4.5.46C). Organic-rich lithotypes 3 and 4 are characterized by high S2 values (lithotype 3 - 40.8 mg HC/(g rock) and lithotype 4 - 48.53 mg HC/(g rock)), whereas radiolarites are characterized by low S2 (lithotype 1 - 8.8 mg HC/(g rock) and lithotype 2 - 8.1 mg HC/(g rock)).

The temperature of 107°C did not affect the TOC content significantly. Most of the changes in TOC content and S2 value are rather associated with lithological heterogeneity than with temperature impact (Figure 4.5.46A, C). Further exposure to the temperature of 400°C leads to the noticeable TOC content decreasing (20-40 % reduction) and decline of S2 value (80-95 % reduciton) for all four lithotypes. These changes show that the most of the kerogen potential has been realized. At the temperature of 841°C TOC content and S2 value are almost zero due to combustion process.

S1 parameter (free hydrocarbons in the sample) (Figure 4.5.46B) is a very variable even within one lithotype. These variations are connected with unequal distribution of mobile fluid. Growth of the value at 107°C is associated with mobile fluid inflow in the sample during nitrogen purge. Drop of the value on a higher temperatures reveal removing of the fluids during the experiments.

T_{max} parameter (Figure 4.5.46D) show no changes at 107°C, which mean no changes in maturity of OM. Increase of T_{max} at the 400°C indicate maturation of OM accompanied with HC generation. At the 800°C OM disappears, and evaluation of T_{max} is not possible.

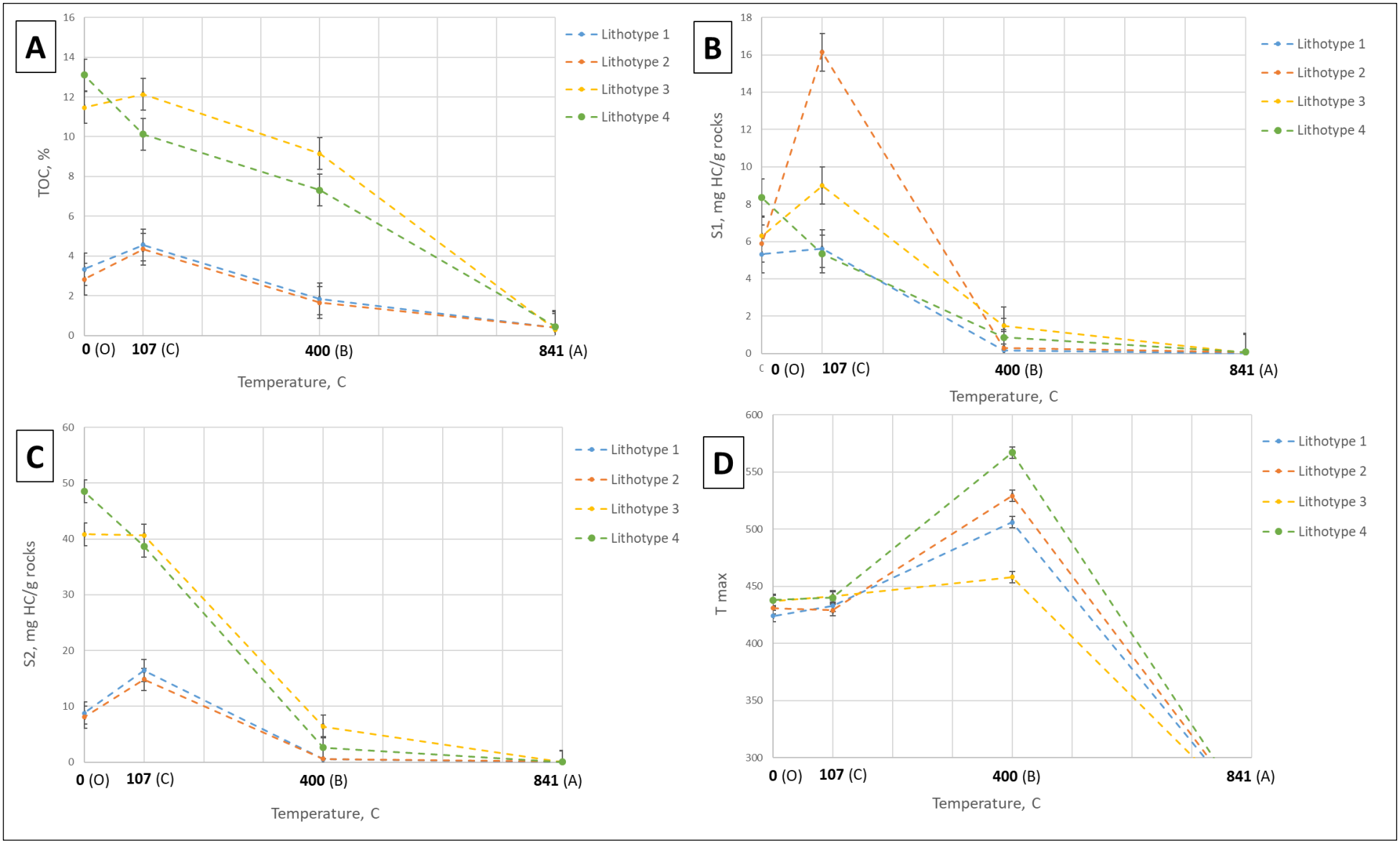

Figure 4.5.46. Evolution of key Rock-Eval pyrolysis parameters after each thermal treatment episode in subsamples. A – total organic carbon content. B – S1 parameter. C – S2 parameter. D – T max.

4.5.8. Isotope Ratio Mass Spectrometry

Isotope Ratio Mass Spectrometry analysis was performed for the initial (reference) subsamples and the subsamples exposed to the maximum temperature impact (841°C) for lithotype 1and lithotype 4 (1O, 1A, 4O, 4A). Results are given in Figure 4.5.47.

Similar effects were observed for both lithotypes. Carbon content has been reduced from 2.75 % to 0.22 % for lithotype 1 and from 8.82 % to 0.20 % for the lithotype 4 (reduction ≈95%). This reduction is a result of OM conversion to hydrocarbons at initial stages of HPAI and further burning during combustion. Carbon isotope composition was shifted towards heavier C in both cases. For the lithotype 1 shifting is 1.4 ‰ pDB, in the case of lithotype 4 shifting is more significant and is 3.9 ‰ pDB. After the combustion only residual carbon (coke) is presence in the sample, which is isotopically heavier than initial Corg. (organic carbon content). Depletion of organic matter with ^{13}C most probably is a result of kinetic effects of isotope fractionation in reactions of cracking and combustion.

Sulfur content has been also reduced for both lithotypes. The decreasing is ≈0.5 ‰ for both lithotypes (which is 30% for lithotype 1 and 10% for lithotype 4). The isotope composition is shifted towards heavier sulfur, for lithotype 1 shifting is 5.9‰, for lithotype 4 the shifting is 2.4 ‰. Sulfur content is decreasing during the combustion due to SO_2 outgassing. The most possible reason for ^{34}S depletion is a kinetics effect of isotopic fractionation in pyrite decomposition reactions with formation of anhydrite.

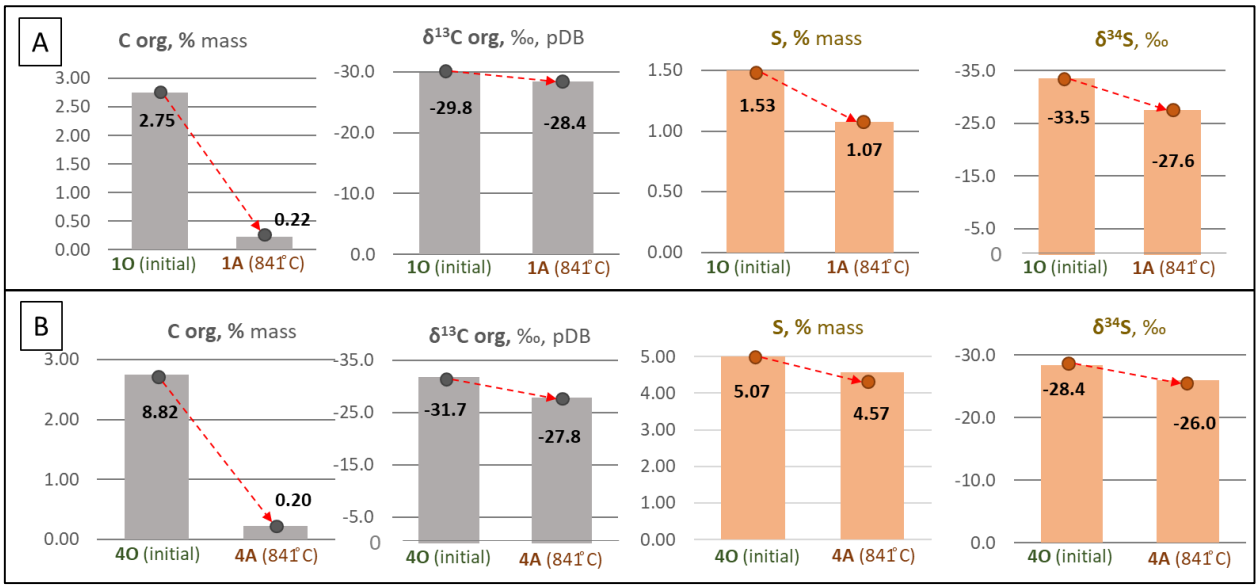

Figure 4.5.47. C and S content and isotope composition. A – lithotype 1. B – lithotype 4.

4.6. Summary

Alterations of four Bazhenov Formation lithotypes (which encompass the major lithology variations of the Bazhenov Formation shales), have been investigated during *in-situ* the high-pressure air injection experiment in the laboratory combustion tube with the temperature range of 109–919°C. Subsamples of each lithotype have been packed into specific areas of the combustion tube: behind the combustion front, ahead of the front, and approximately on the front/slightly ahead. The samples have been investigated with the set of lithological, geochemical, and petrophysical methods aimed to reveal alterations in void space, mineral matrix, and organic matter.

1. *Polarizing optical microscopy*

Optical microscopy helped to observe mineral matrix microstructural alterations and OM content decreasing during the experiment. The most altered samples are behind the combustion tube (section A, 841°C): organic matter disappeared completely, samples are characterized by reddish color, rock forming individual dolomite crystals have been destructed into smaller ones with remained initial crystal outline. The samples on the front/slightly ahead the front (400°C) are characterized by a slight decrease of OM content. No alterations are observed ahead of the front (107°C).

In the sample, located near the expected front position/slightly ahead of the front (400°C), a combustion front was directly observed on a micro-level. The width of the microfront is 3-8 mm. The area behind the front is characterized by light color, which indicates the absence of OM. The area on the other side of the front is characterized by the presence of OM. The front itself represents the darkest part, which indicates the increased concentration of OM.

2. *SEM, EDS and XRD.*

SEM was used to investigate microstructure and pore space, EDS and XRD revealed chemical and mineralogical alterations in the samples. Microstructure and composition are interrelated aspects of the rock and are considered together.

- Samples, located ahead the front (107°C), are characterized by the beginning of the formation of pore space in organic matter, which are spongy pores and fractures. Mineral matrix/rock fabric did not experience any significant changes; only rare fractures were observed.
- Closer to the front (400°C) more alterations are documented. OM is almost porous, part of OM is transformed and displaced with the formation of void space. Major components of the mineral matrix remain intact, however, clay minerals experience shrinkage resulting in elongated voids between clay lamellas and small fractures due to dehydration. Pyrite has

started to transform into FeS with concomitant microstructural alterations, expressed into losing the idiomorphic habit of individual pyrite crystals. Traces of calcite dissolution are observed.

- The most altered samples are behind the front (841°C). Organic matter is not observed, part of it is transformed and replaced (generative part) and burned (coke, non-generative part), which results in the formation of pore space throughout the sample. Mineral matrix alterations are closely associated with its initial composition (lithotype), however, there are common alterations for all the lithotypes. The common alteration is a complete transformation of pyrite and FeS into hematite (Fe_2O_3) which is confirmed by EDS and XRD. The formation of hematite is associated with pyrite framboid structures destruction and the appearance of porous dendritic structures (pores up to 5 μm), which increase the porosity.
    - Quartz-dominated lithotype (siliceous mudstone) is proved to be the most stable in terms of mineral matrix alteration. No significant changes are observed except for the hematite formation.
    - Dolomite-dominated lithotype (aporadiolarian siliceous dolomites) has been completely altered at this stage. Dolomite has decomposed into smaller nanosized (200-1000 nm) crystals of MgO, and $CaCO_3$, in some cases with anhydrite ($CaSO_4$) and wollastonite ($CaSiO_3$). The primary texture of dolomite texture is preserved. This decomposition is accompanied by the formation of two microstructural patterns: rough elongated needle-like crystals and porous clotty microstructure, which directly influence pore space. A rough surface composed of elongated needle-like crystals increases specific area, and a porous clotty microstructure of aggregates is a part of a newly formed void space.
    - Quartz and clay dominated lithotype (argillaceous-siliceous organic-rich mudstone). The main changes are associated with illite. The initial microstructure of illite has been preserved, however, lamellas are significantly shrunken and some new aggregates are observed (XRD shows the formation of mullite). This shrinkage and partial transformation of illite have an increasing effect on the void space.
    - Calcite, clay, and quartz mixed lithotype (calcareous-argillaceous organic-rich mudstone) is the most altered lithotype. The first and the most important conclusion is that no almost no initial microstructure is preserved. Calcite experienced dissolution and partial destruction with the formation of new void space (up to 3-5 μm intercrystalline pores). Only rare illite relicts are found. Feldspar crystals became porous (0.5-4 μm intracrystalline pores). Quartz crystals preserve their

structures and no alterations are observed. A number of new minerals are documented. The first one is anhydrite, which is presented in the form of needle-like tabular minerals, which fill the pore space and make it more complex. Anhydrite is often formed after the hematite (Fe_2O_3), which indicates their connection. The second new mineral, that is present throughout the sample, is wollastonite ($CaSiO_3$), which forms porous aggregates (up to 3 μm intercrystalline pores). XRD shows a possible presence of mullite ($Al_8[O(Si,Al)O_4]_4$) and gehlenite ($Ca_2Al(AlSiO_7)$). In some cases, CaO crystals are observed. Other minor compounds are CaS, MgS, BaS, Fe (elementary iron).

A detailed study of the micro- combustion front shows that before the front porous OM presence, the pyrite transformation into FeS begins. After the front no OM, pyrite continues to transform to FeS with the formation Fe_2O_3. Single CaO and anhydrite crystals observed.

The transmission XRD geometry shows much more precise results (peaks) compared to the Brag-Brentano geometry for shales. For a detailed analysis of mineral matrix alterations during thermal experiments, the transmission XRD is much more preferable.

3. Micro-CT

Micro-CT shows that the pore space after combustion front propagation is increased significantly (from initially zero up to 4-5% after the treatment) in the lithotypes characterized by initial high OM content. Whereas porosity of lithotypes with an initial relatively high porosity and low OM is not changed. Considering that the resolution of the micro-CT is limited to 3 μm, this is a rough estimation, which should be refined in future studies by BIB-SEM.

4. Rock-Eval pyrolysis

Rock-Eval pyrolysis shows a progressive depleting (transformation) of OM during the thermal impact. Behind the combustion front (841°C) no OM is detected. Within the area near the combustion front (400°C) TOC is decreased by 2.5-3% in all lithotypes (20-40 % reduction), S2 decline is 80-95 % for all four lithotypes. And on the samples ahead of the front, no significant changes are observed.

5. Isotope Ratio Mass Spectrometry

After the combustion experiment, the carbon content reduction was 95%, the sulfur content reduction was 10-30%. Isotope composition of sulfur and carbon has been shifted towards heavier isotopes in both lithotypes (carbon: ≈5% shifting for lithotype 1, and ≈12% shifting for lithotype 4; sulfur: ≈18% for lithotype 1 and ≈8% for lithotype 4). After the combustion only, residual carbon (coke) is present in the sample, which is isotopically heavier than carbon in the initial organic matter. The depletion of organic matter with ^{13}C most probably is a result of kinetic effects of isotope fractionation in reactions of cracking and combustion. The decrease in the sulfur content

is observed during the combustion due to SO_2 outgassing. The most possible reason for the ^{34}S depletion is a kinetics effect of isotopic fractionation in pyrite decomposition reactions with formation of anhydrite.

6. Thermal property profiling

Two patterns of thermal conductivity behavior during the experiment have been distinguished. The first pattern assumes stable thermal conductivity throughout the HPAI experiment. Thermal conductivity is fluctuating around 3 W/(m*K), fluctuations do not exceed 0.17 W/(m*K) (≈5%), which are in line with lithological heterogeneities within one lithotype. A stable behavior of thermal conductivity is a result of low initial OM content (TOC=3.3 %) and quartz dominated composition (quartz ≈95%). The second pattern assumes thermal conductivity reduction up to 60% during the treatment. Thermal conductivity decreases from the values of 1.4-2.2 W/(m*K) to 0.7-1.3 W/(m*K), which is a 30-60 % reduction. Such a dramatic reduction of thermal conductivity is caused by several factors: a relatively high content of OM (TOC is in the range of 11-13%), which is replaced by gas during the experiment; a lack of pore space at the initial stages; presence of clay and carbonate minerals, which are sensitive to high temperatures (dissolution, decomposition, etc.), and the destruction of grain contacts due to different values of thermal expansion coefficient of rock forming minerals. Similar patterns are observed in the thermal heat capacity behavior during the treatment. OM lean and quartz dominated lithotype is characterized by relatively stable heat capacity during the experiment (1.5-1.8 mJ/(m^3*K)), except the sample located ahead of the front (107°C), which is characterized by 13-23 % increase. All the other lithotypes are characterized by progressive thermal heat capacity decrease up to 40%.

To summarize, HPAI leads to the increase of porosity due to OM transformation and replacement, minerals matrix transformation (dolomite decomposition, calcite dissolution and partial decomposition, pyrite decomposition and clay (illite) transformations). All these processes are accompanied by the formation of new minerals such as anhydrite, hematite, periclase, wollastonite, CaO, and minor components MgS, CaS, MgS), and grain contacts destruction. These alterations are expressed in isotope composition, it was shown on the example of C and S. The formation of new void space due to displacement of OM leads to a significant drop in thermal conductivity.

Chapter 5. Detailed characterization of kerogen microstructural transformation during thermal maturation

5.1. Motivation

HPAI laboratory experiment (see Chapter 4. Experimental modeling of the mineral matrix alteration and void space evolution during high temperature treatment) showed very high sensitivity of organic matter (kerogen) microstructure to thermal exposure: formation of pores, fractures and partial or complete disappearance. Detailed step-by-step investigation of OM in combustion tube is not possible due to number of reasons (very big scale - several meter scale of the lab equipment, economical feasibility, the impact of heterogeneous combustion front propagation, number of factors which potentially might influence the porosity). Detailed, focused and small scale (millimeters, first centimeters) study of OM microstructure is needed. Organic matter porosity (kerogen porosity) is one of the most important pore type in oil shales [96,98,100]. Most of the researches show that organic pores can significantly contribute to the total porosity of shales, and in some cases it might exceed 40% within individual particles [96,98,101,102]. However, there are numerous gaps in understanding the evolution, controlling factors and origins of organic pores and their associated networks [103]. Organic pores are mainly sub-micrometer size voids hosted in the OM [44,96,98,100,104]. Usually OM pores are characterized by isolated irregular shape and bubble-like structure, these pores can be interconnected in the 3D volume and form an effective network [96,100–102,105]. It is commonly suggested that OM porosity is controlled by thermal maturation and OM type [96,98,104,106–108]. A number of authors states that increasing thermal maturity leads to increasing organic porosity [96,98,102,109]. This assumption is predominantly based on qualitative comparisons between shales in natural thermal maturity gradient samples. In contrast to the maturity-controlled porosity theory, Löhr et al. (2015a) found that OM-hosted pores also may be present in immature (pre-oil window) shales. In that case OM pores are not purely a product of thermal maturation but are controlled by OM type [106]. The study focuses on investigating the organic matter microstructure evolution during thermal maturation in different conditions: at a variety of natural maturation stages; during isothermal treatment in open system at temperature series and under the pressure with variable duration in a closed system.

5.2. Materials

To analyze organic porosity 12 samples from 10 wells located in the central and northern parts of the West Siberian petroleum basin within the Bazhenov Formation organic-rich shales interval were prepared (Figure 5.2.1). The collected samples represent the maturity level from immature to the end of the oil window. To focus the study on the effect of thermal maturity and avoid the influence of other factors (e.g., mineral composition, OM type variations) we have collected siliceous mudstone samples from the upper part of the Bazhenov Formation, which is characterized by relatively stable mineral composition and identical kerogen type II organic matter [24,27].

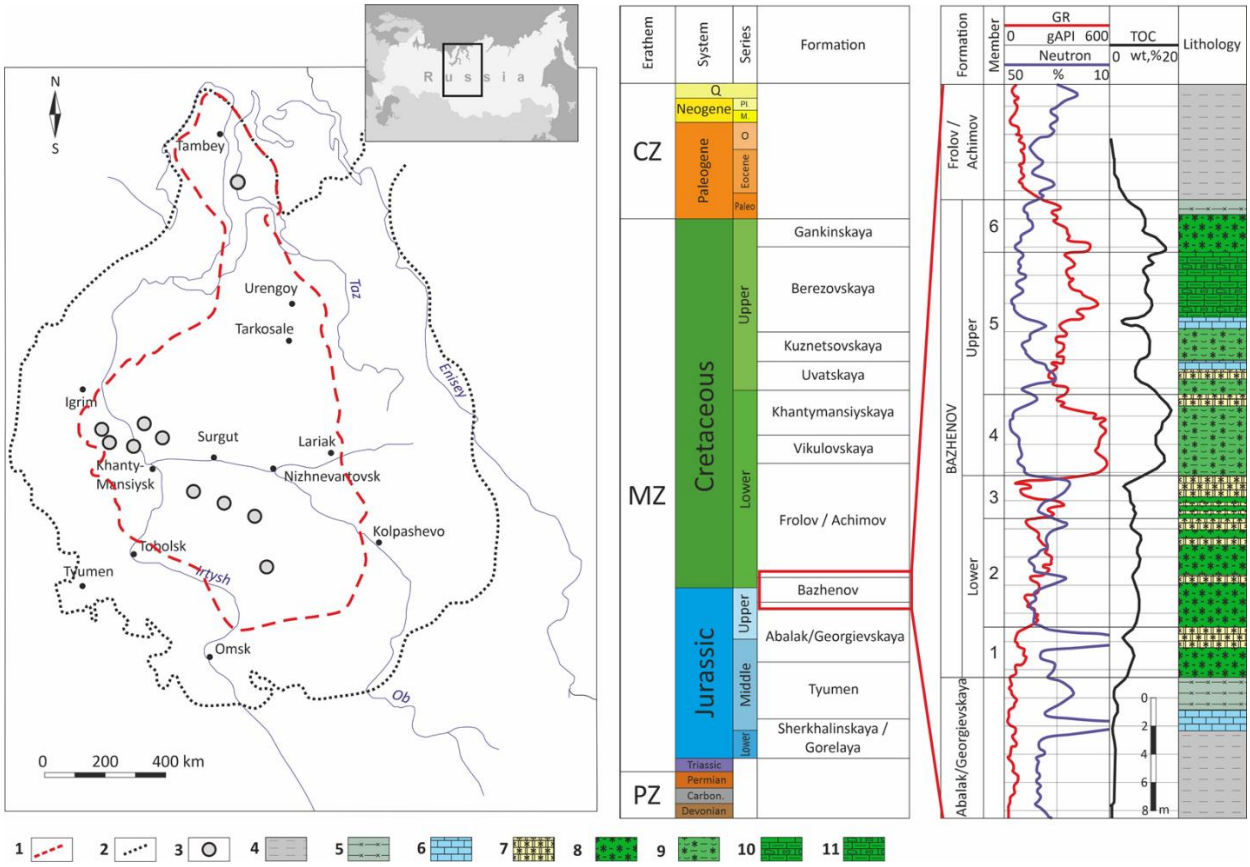

Figure 5.2.1. The location of the Bazhenov Formation organic-rich shales and investigated wells (left). Generalized lithostratigraphic column (right) (modified after Panchenko et al., 2016 and Ulmishek, 2003).

1 – boundary of Bazhenov Formation stratigraphical equivalents; 2 – boundary of Bazhenov Formation; 3 – location of the studied wells; 4 – argillaceous mudstone; 5 – siliceous-argillaceous mudstone; 6 – calcareous mudstone; 7 – siliceous radiolarite; 8 – organic-rich argillaceous-siliceous mudstone; 9 – organic-rich siliceous mudstone; 10 – organic-rich mixed mudstone; 11 – organic-rich pyritized argillaceous-siliceous mudstone.

5.3. Methods

Broad-ion-beam Scanning Electron microscopy

Broad-ion-beam cross-sectioning

Small probes with the surface approximately of 5x5 mm were prepared from all the subsamples. Probes were pre-polished using silicon paper (P2400). Then probes were polished by Broad-ion-beam (BIB) polisher (Leica RES102). The BIB produced a flat surface about 20-25 mm^2 area perpendicular to the bedding with a topography variations of ±5 nm, which is suitable for SEM investigation of pore space in shales.

SEM imaging

Scanning Electron Microscopy (SEM) is a major method that allows to effectively investigate porosity at micro- and nanoscale in organic matter [96,98]. Loucks et al. (2009) showed that for accurate evaluation of organic porosity samples should be polished not only mechanically, but also with a broad ion beam technique, otherwise overestimation of porosity may take place due to topography variations.

Prepared probes were imaged using a Thermo Fisher Scientific I Quattro S SEM instrument equipped with secondary electron (SE) detector for pore investigation (5-10 kV, working distance 9-10 mm) and backscattered electron (BSE) detector for mineralogical heterogeneity investigation based on phase density contrast. Large areas, representative for void space analysis, were acquired by mosaic scanning approach and stitching together (Image Composite Editor, Microsoft) hundreds of single images (in the range of 500-800 images for each sample) scanned with 10% area overlap. The BSE and SE mosaic images were used for pore space analysis. For quantitative analysis of organic porosity we segmented organic pores with the neural network pixel based tool "ilastic" [110] in the ImageJ software [111].

The scanned area is approximately of 1000 μ x 1000 μ with a pixel size of 25 nm on each sample. For quantitative analysis of organic porosity we segmented organic pores with the neural network pixel based tool "ilastic" [110] in the ImageJ software [111].

Programmed pyrolysis

The method is described in the "Chapter 3. Lithological characterization of the Bazhenov Formation shales"**.**

GC×GC TOFMS

To analyze products of kerogen pyrolysis GCxGC-TOFMS/FID Pegasus 4D (LECO, USA) was used. For the analysis rock sample was powdered, places into a glass vial covered by quartz

wool. To clear the sample from the existing hydrocarbons thermal extraction at the temperature of 350°C was performed. Pyrolysis was carried out at the temperature of 500°C.

X-Ray powder diffraction analysis

The method is described in the "Chapter 3. Lithological characterization of the Bazhenov Formation shales". Reflection geometry was applied using Bruker D8 ADVANCE (Germany).

5.4. Results

5.4.1. Characterization of the samples

Organic matter was characterized with programmed pyrolysis (Table 5.4.1). Results show that TOC varies in the range of 5-21 wt.%. According to T_{max} and HI, studied samples are in a wide range of thermal maturation: from immature to the end of the oil window. Kerogen corresponds to type II. HI/T_{max} diagram in Figure 5.4.1 demonstrates that samples span the main maturity interval for Bazhenov Formation [25,43]. Such diversity of thermal maturation allowed to observe the evolution of OM porosity in the natural state during thermal maturation.

Table 5.4.1. Results of Rock-Eval pyrolysis.

Sample ID	**S1, mg/g rock**	**S2, mg/g rock**	**S3, mg CO2/g rock**	**TOC, wt.%**	**HI, mg HC/g TOC**	**OI**	**T_{max}, °C**	**Maturity level**
BF #1	7.85	124.53	1.02	17.79	700	5	418	immature
BF #2	4.28	75.98	1.05	10.87	699	9	421	immature
BF #3	3.78	75.33	0.74	11.03	683	6	436	beginning of oil window
BF #4	3.65	66.72	1.35	9.84	678	13	434	beginning of oil window
BF #5-1	9.24	79.45	0.36	15.89	500	2	438	middle of oil window
BF #5-2	4.44	45.83	0.52	9.71	472	5	444	middle of oil window
BF #6	6.02	118.33	0.75	21.13	560	4	438	middle of oil window
BF #7	4.56	25.60	0.72	7.67	334	9	447	middle of oil window
BF #8-1	2.31	25.71	0.37	9.53	269	3	441	end of oil window
BF #8-2	2.77	10.69	0.30	4.60	232	6	453	end of oil window
BF #9	0.39	9.64	0.38	6.65	145	5	443	end of oil window
BF #10	4.58	34.75	0.28	9.28	423	2	438	beginning of oil window

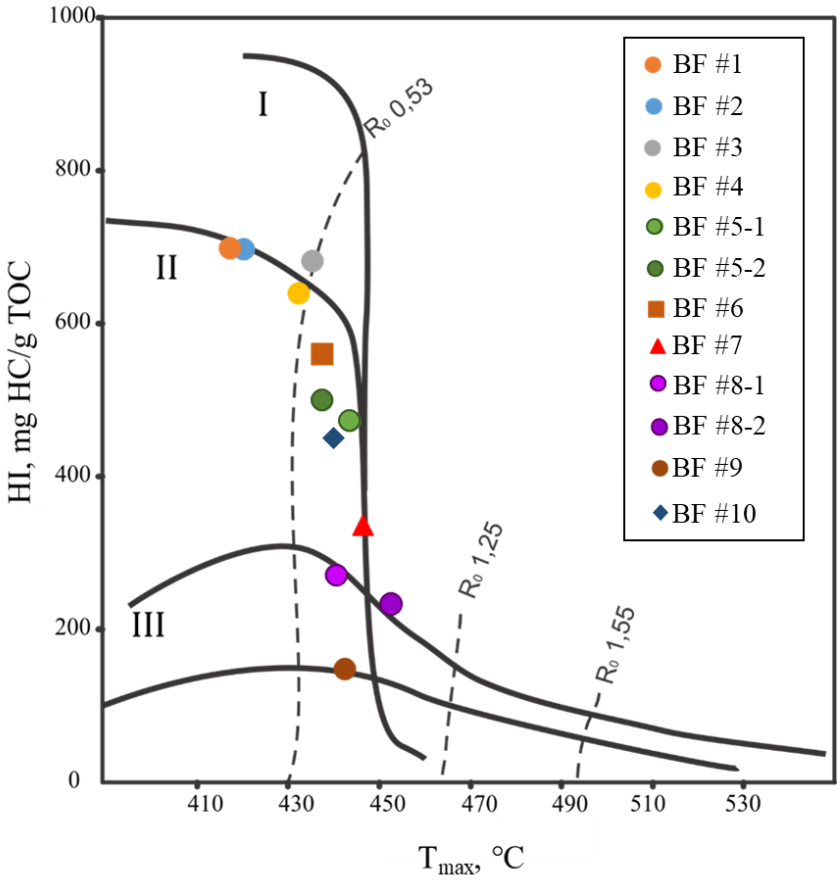

Figure 5.4.1. HI/Tmax diagram showing type and maturity for the selected samples.

X-Ray diffraction analysis showed that the selected samples are quite similar in mineral composition. All the samples are quartz dominated mudstones with variable clay, feldspar, calcite, dolomite, and pyrite content (Figure 5.4.2). Only two samples demonstrate a noticeably higher amount of clay minerals, but in general, they do not differ significantly in SEM images.

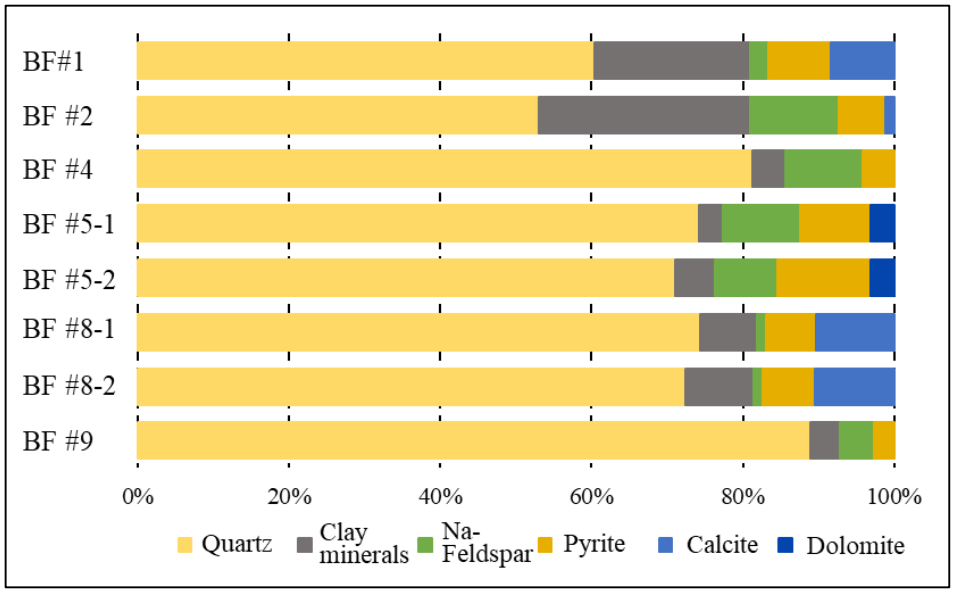

Figure 5.4.2. Mineral (inorganic) composition for the selected samples.

5.4.2. Organic porosity occurrence across natural maturity level variations

Evaluation of organic porosity was made on the basis of all prepared samples with SEM and BIB-SEM technique described above. Characterization of the samples is made by XRD and Programmed pyrolysis.

SEM investigation showed that organic porosity tends to increase with increasing thermal maturity degree for studied samples. The general observed trend is shown in Figure 5.4.3. For most of the samples, higher thermal maturation is associated with developed OM porosity. Immature samples are solid, and normally, no pores are observed. A few exceptions are possible (Figure 5.4.4). At the oil window, a significant number of the OM inclusions are porous. It seems that these pores are isolated and do not form effective pore space at this maturation stage. Pore size significantly varies even within one inclusion from 0.1 μm and up to 1 μm (Figure 5.4.3B, E, H). The shape is almost round and characterized by a bubble-like structure (Figure 5B). At the end of the oil window, OM is much more porous, almost all inclusions are characterized by both round bubble-like/spongy and elongated (crack-like) pores (Figure 5.4.3C, F, J). From a 2D view, it seems that pores are expected to form an effective pore network. Pore size varies greatly, starting from 0.1 μm and up to 3 μm and in some exceptional cases up to 8 μm due to several pores amalgamation (Figure 5.4.3J).

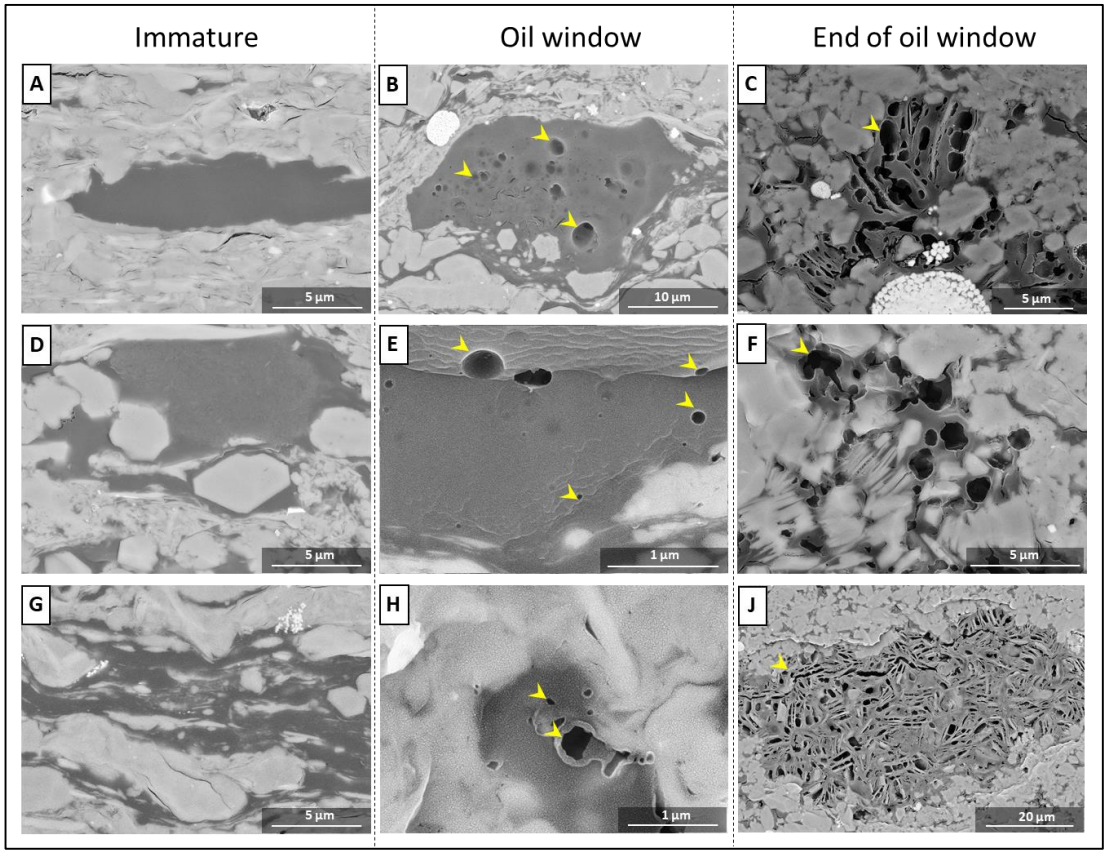

Figure 5.4.3. Increasing of organic porosity with thermal maturation level increase. (Samples: A – BF #1, B – BF #7, C – BF #9, D – BF #4, E – BF #6, F – BF #8-1, G – BF #3, H – BF #5-1, J – BF #9)

5.4.2.1. Organic porosity in immature samples

Although the general trend is that increasing thermal maturity leads to increasing organic porosity, there are few exceptions observed. The exceptions are rare for the prepared sample collection and lie apart from the thermal maturation influence, and we attribute their occurrence to the sedimentation processes.

Some immature samples are characterized by single pores in OM (Figure 5.4.4). These pores generally are rare and do not form effective pore space. Their formation is related to sedimentation and early diagenetic processes. The pore size is very small and rarely exceeds 0,5-1 μm, in some exceptional cases the size may reach 5 μm (Figure 5.4.4A).

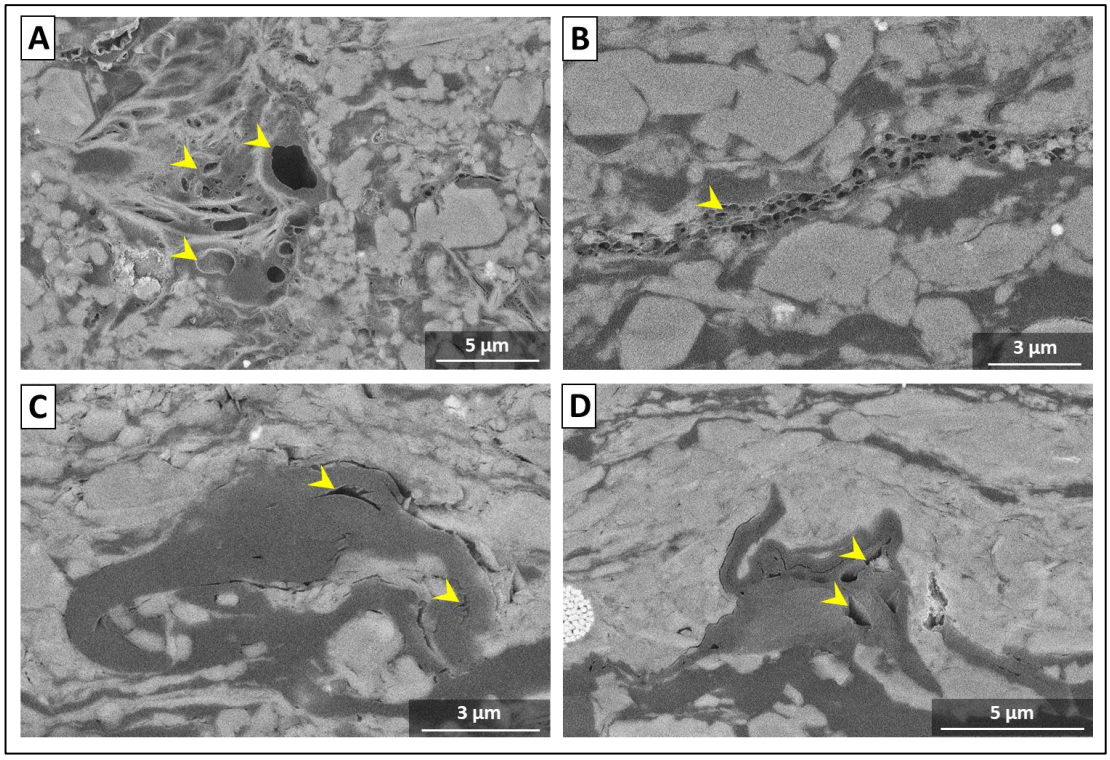

Figure 5.4.4. Porosity in OM in immature OM. A (BF #4), B (BF #6) – inherited porosity from cells initial structure, C (BF #1) – porosity due to mechanical coiling, D (BF #6) – inherited pores and convoluted pores in one OM particle.

5.4.2.2. Structure and texture of organic matter

High maturity level does not always equal the abundance of organic porosity in case of studied samples. The samples with different distributions and shapes of organic matter are characterized by different organic porosity (Figure 5.4.5). The samples with a patchy distribution of OM in form of inclusions are porous in most cases, whereas the samples with elongated lenticular OM show lack of organic porosity or are characterized by insignificant amount of voids. Two BF samples from one well are demonstrated in Figure 5.4.5. The samples are characterized by the same thermal maturation level and identical mineral composition, but the OM distribution

pattern/shape varies significantly. BF#8-1 sample has patchy OM in the form of inclusions (Figure 5.4.5A and B), most OM particles have pores from nanometers to few microns. OM in BF#8-2 sample (Figure 5.4.5C and 7) is represented by elongated lenticular shapes. In that case, the majority of OM lacks of pores and has a solid flat structure, although single voids at contact with the mineral matrix are observed (Figure 5.4.5D).

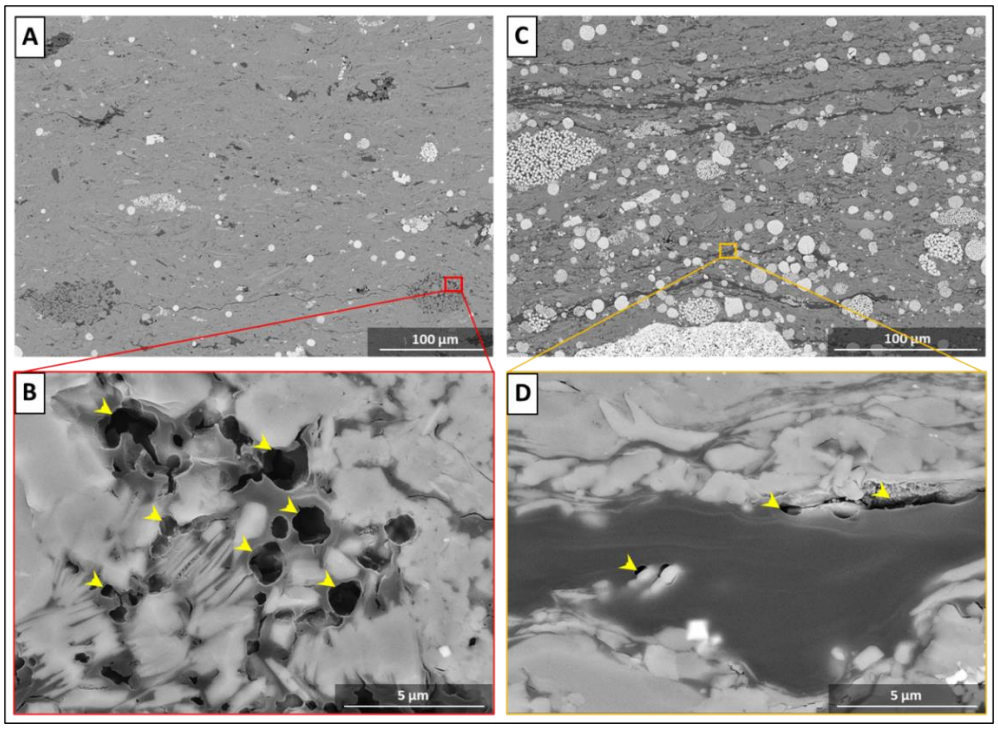

Figure 5.4.5. Organic porosity in the same well in the samples with different OM distribution. A, B – patchy distribution of OM in the sample BF #8-1, C, D – laminated distribution of OM in the sample BF #8-2.

5.4.2.3. Organic porosity classification

Organic pores were divided into several categories based on their shape, appearance, and the genesis. Organic pores categorization proposed by Ko et al. (2016) served as a prototype for the classification used in this study. We suggest distinguishing two organic porosity categories by analogy with the classical reservoir geology approach in sandstones and carbonate rocks [112]: primary organic porosity and secondary organic porosity. Primary porosity – porosity formed during the initial deposition of organic matter, secondary porosity – porosity formed due to thermal maturation. These divisions may be further categorized into several subcategories according to the shape and genesis, as it is described below and shown in Figure 5.4.6.

Primary porosity includes two categories: inherited organic pores and convoluted organic pores.

Inherited organic pores. Inherited organic pores (Figure 5.4.6A) are pores, which existed in the original organic material (cellular structure in spores, algae, leaf, wood etc.) during

sedimentation. These pores are considered as inherited and not associated with thermal maturation or mechanical compaction [73]. Inherited pores are quite common for the Bazhenov Formation immature samples, but only for the cases of patchy distributed OM. Pores of this type are characterized by regular shapes associated with detritus internal features (Figure 5.4.6A and Figure 5.4.4A,B).

Convoluted organic pores. Convoluted organic pores (Figure 8B) are the pores, which were formed due to the deformation of the organic matter particles during sedimentation or/and burial such as folding, twisting or coiling. This type of porosity is related to the OM deformation and not connected with the maturation. The size and shape of the pores are quite variable due to ductile behavior of OM and its relationships with the mineral matrix. These pores were observed in immature BF samples.

Secondary porosity includes two categories spongy and shrinkage organic pores.

Shrinkage organic pores. Shrinkage organic pores (Figure 5.4.6C) represent a discontinuity with a fracture-like elongated shape, which occur within solid OM (Figure 5.4.6C-1) or between OM and mineral grains (Figure 5.4.6C-2). Discontinuities within OM inclusions often penetrate whole inclusion and form dendritic shapes, length is usually restricted by OM inclusion size, and these discontinuities do not have any continuity in the mineral matrix. Our results show that these types of voids are common for the BF samples at the mature (end of oil window) level.

Spongy organic pores. Spongy organic pores (Figure 5.4.6D) are considered as a result of the thermal maturation process. These pores are normally at a micro- and nanometer scale, have rounded, subrounded or subangular shapes. This type is common for most of the mature samples (end of the oil window). However, we observed less abundant micro- and nanopores in the samples in the oil window (Figure 5.4.7A). These pores usually developed equally in most OM within the end oil window samples. We consider this type as a major type of secondary organic porosity in BF.

Mixed organic pores. There is possible a presence of a combination of several types of pores in matured samples. Mixed type of OM pores takes place in case of the presence of pores with different origins, for example, shrinkage OM pores and spongy organic matter pores (Figure 5.4.6E). Usually, such combinations are found in the high maturity level samples (end of oil window).

Other OM pores. We have observed pores associated with the OM located between pyrite framboid forming crystals in the few cases of immature samples. It is quite complicated to refer them to any established category due to their insignificance in terms of size and abundance (Figure 5.4.7). The size of such pores is less than 100 nm and they do not contribute to the effective pore space.

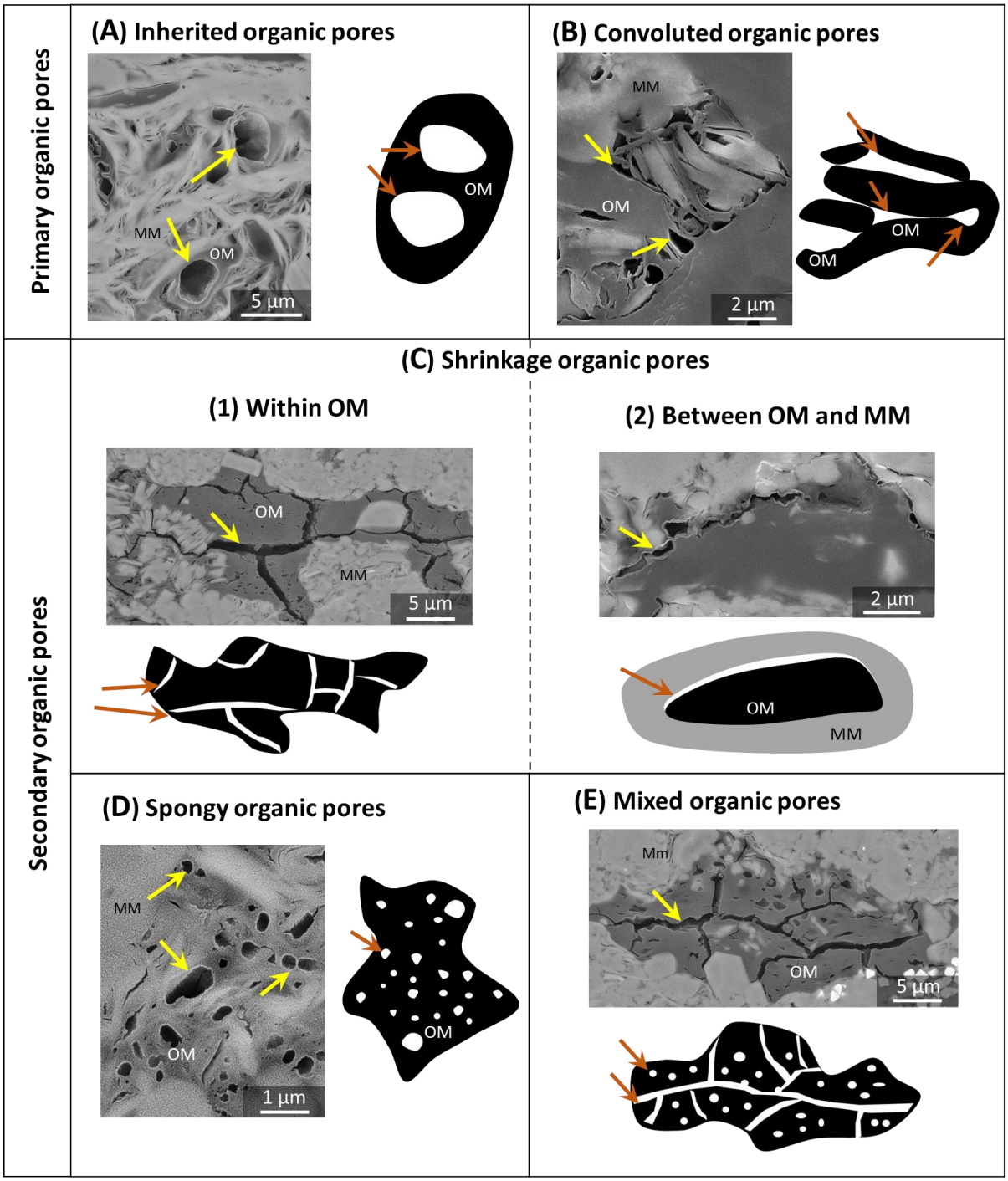

Figure 5.4.6. Organic porosity classification for the Bazhenov Formation shales. (A) Primary organic pores inherited from the original structure of OM. (B) Spongy organic pores. (C) Shrinkage organic pores: (1) pores within organic matter, (2) pores between organic matter and mineral matrix (MM). (D) Convoluted organic pores in folded OM. (E) Mixed organic pores, in that case combination of shrinkage pores and spongy organic porosity. (Samples: A – BF#4, B – BF#2, C(1) – BF#8-1, C(2) – BF#7, D – BF#9, E – BF#8-1)

However, they may influence pore forming processes during thermal EOR on shales. Their formation may be related directly to the processes occurring in the framboids during burial. Their shape and abundance do have nothing in common with inherited pores or ductile behavior of OM. Potentially genesis may be related to bacteria activity during sedimentation and early diagenesis.

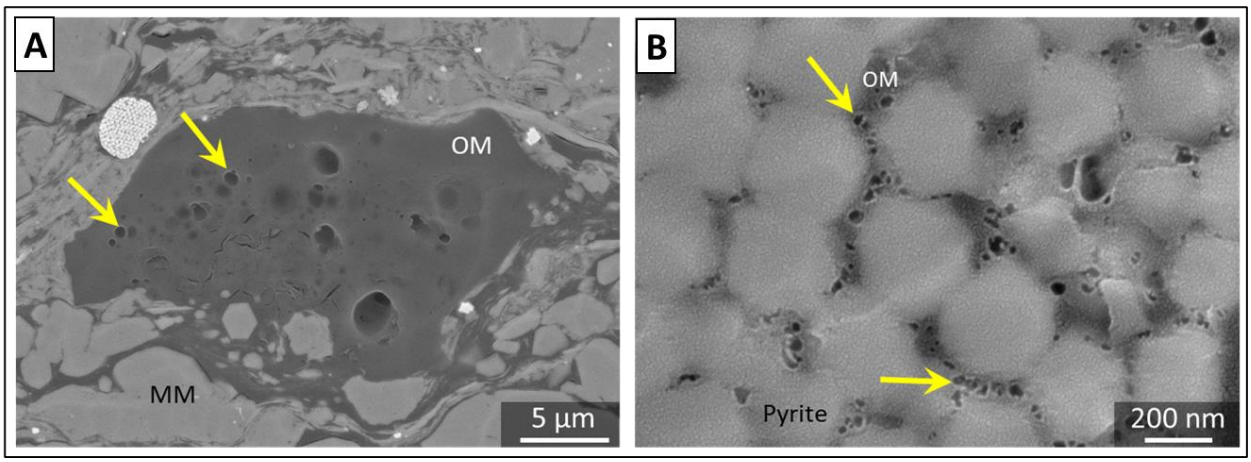

Figure 5.4.7. A – spongy organic pores in BF#7 oil window sample. Pores a less abundant and size is smaller. B – pores in OM hosted in framboids between pyrite crystals in the sample BF#3.

5.4.2.4. Size and abundance of organic pores

Porosity was determined as “area of organic pores”/”analyzed area”. For the pore size analysis, the equivalent circular diameter (ECD) was calculated, this parameter represents a diameter of a circle with the same area as that of the pore. After, mean and median equivalent diameters were determined. To reveal the role of the pores with a specific size in the organic porosity, relative porosity was calculated, which represents a relation of the area occupied by pores with a specific size to the total pores area. The results are shown in Table 5.4.2 and Figure 5.4.8.

Overall observation is that the limited pores were developed outside the organic matter, almost all pores are concentrated within the organic matter. The highest porosity value was found in the highly matured BF#9 sample - 3.5% with the strong dominance of spongy organic porosity (Figure 5.4.9A). The mixed porosity type was observed in the BF#8-1 sample (Figure 5.4.9B) with the 1.3 % value. Almost zero porosity value corresponds to the immature BF#1 sample. In that case the SEM images show solid OM without any void space with single occasional nanoscale pores. The quantitative analysis of porosity demonstrates that the mature samples are characterized by higher porosity. Only immature OM in the BF#4 sample showed relatively high porosity (1.1%), which is explained by the abundance of primary organic porosity in this sample (Figure 5.4.9C).

Organic pores vary in size and shape significantly due to the amalgamation of several pores. The observed maximum pore size is approximately 3 µm, the minimum is around 5-10 nm, even though smaller pores may be unrecognized due to resolution limitations. The majority of the pores are in the range of 100-300 nm and rarely approach 1.2 micron size (Figure 5.4.8 A,B). In some cases, the highly matured OM samples contain few organic grains with no porosity and for now it is unclear whether the lack of voids is related to different OM compositions or the local compaction. The median equivalent diameter for organic porosity is typically less than mean sizes,

which is common for all samples (Table 5.4.2). The mean equivalent diameter varies from 86 nm to 223 nm, while the median size ranges from 75 nm to 162 nm. The average equivalent diameter for investigated samples is 145 nm, the average median is 101 nm. In general, highly matured OM is associated with a larger pore size and greater porosity. The highest values were observed in the highly matured samples BF#9 and BF#8-1. Examples of equivalent diameter distribution patterns for highly matured (end of oil window) sample BF#9 and moderately matured (middle of oil window) sample BF#7 are shown in Figure 10. In case of oil window pores with the ECD less than 100 nm dominate, whereas pores with 300-400 nm ECD are present a high portion of pores.

The density of organic pores may be extremely high (Figure 5.4.9D). Organic grains may be up to 60 μm in length and contain thousands of single pores, for example, one of the largest observed OM inclusion contains approximately 3200 pores of various sizes (Figure 5.4.9D). However, according to our observations, the average organic porosity does not relate to the organic grain size.

Two samples, BF#8-1 and BF#8-2, are cored from the same well, and characterized by the identical OM maturation degree. BF#8-2 with the lenticular, parallel to bedding OM wisps, is characterized by two times lower porosity value and 30-40% smaller equivalent diameter compared to BF#8-1. Organic matter distribution patterns (patchy/lenticular) play a significant role in organic porosity development.

Table 5.4.2. Porosity values and equivalent circular diameters calculated from SEM images

	Porosity, %	Equivalent circular diameter, nm		Maturity	OM distribution
		Mean	Median		
BF#1	<0.1	-	-	immature	lenticular
BF#6	0.3	130	89	immature	lenticular
BF#4	1.1	132	85	beginning of oil window	inclusions
BF#7	0.9	86	75	oil window	lenticular
BF#8-1	1.3	181	112	end of oil window	inclusions
BF#8-2	0.6	114	80	end of oil window	lenticular
BF#9	3.5	223	162	end of oil window	inclusions

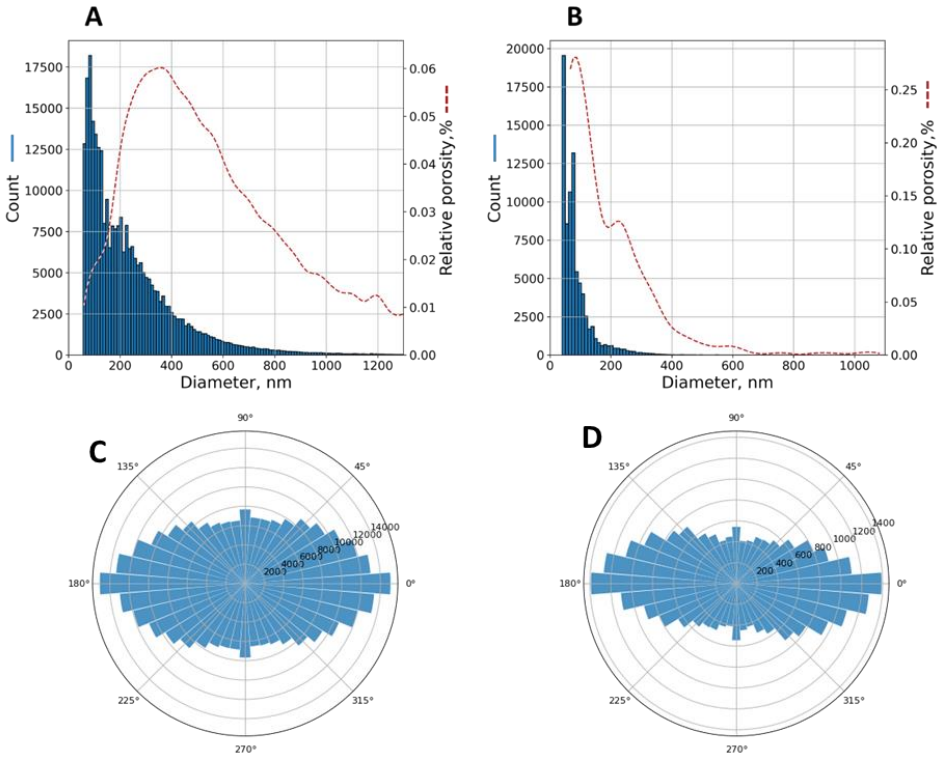

Figure 5.4.8. Histograms of equivalent circular diameter (A, B) and directional anisotropy (C, D) measured on ≈10^6µm area. A, C- highly matured sample BF#9. B, D – moderately matured sample BF#7.

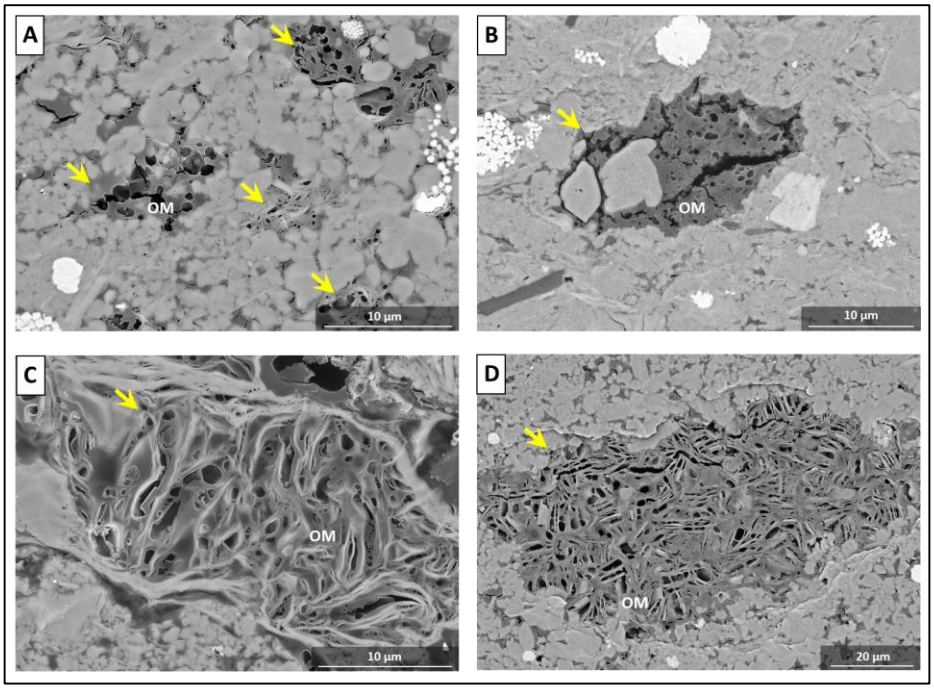

Figure 5.4.9. Different types organic pores. A – spongy pores in BF#9 sample. Organic matter is porous, which is considered as a result of thermal maturation. B – mixed type of porosity (spongy and shrinkage) in BF#8-1 sample. C – primary pores in immature BF#4 sample. Inherited pores have regular shape and unusually large size, pores are developed only within specific features. D – mixed type of pores (primary and spongy) in BF#9 sample. This huge organic grain is larger than 60 µm contain more than 3200 single organic pores.

5.4.3. Artificial thermal maturation experiment in an open system

To evaluate the thermal maturation effect on organic porosity evolution, an artificial thermal maturation experiment in an open system was performed. For the experiment, an immature sample BF#1 was prepared (initial characteristics of the sample are given in section "samples characterization") (3x5 mm cylinder with basement perpendicular to the bedding plane) to observe the organic matter texture alterations from the beginning of thermal maturation. One of the cylinder basements was both mechanically, and broad ion beam polished for correct organic porosity visualization.

Thermal treatment was performed using the HAWK Resource Workstation chamber in argon gas flow at the atmospheric pressure. The workflow of the experiment is shown in Figure 5.4.10. The experiment included ten isothermal treatment episodes with a 0.5-hour duration each at a constant temperature in the range of 350-450°C with 10°C step. A flat surface (the cylinder base) was scanned with SEM (Maps software) at the initial stage. Then, each act of the treatment was followed by an ultra-high resolution SEM (MAPS software) scanning of the same surface.

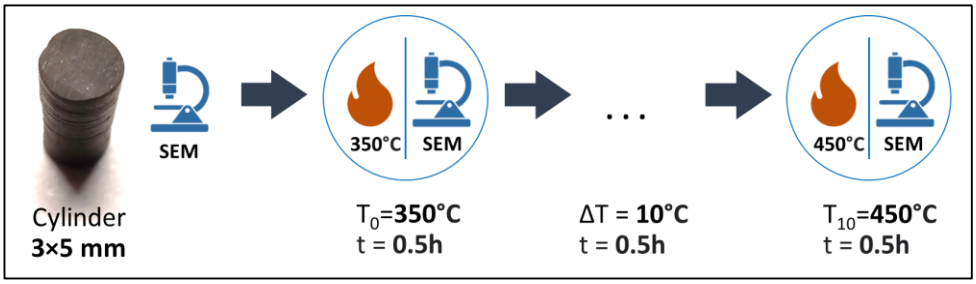

Figure 5.4.10. The workflow of the artificial thermal maturation experiment

At each stage of the experiment kerogen conversion degree was analyzed. For this purpose, powder from the same immature sample was prepared and treated using the same workflow (Figure 2). Rock-Eval analysis was carried out after following treatment episode: 350°C, 370°C, 390°C, 410°C and 450°C. Using a ratio of pyrolysis products from cracking of organic matter (S2 Rock-Eval parameter) at a specific temperature to initial pyrolysis products from OM cracking value we calculated kerogen conversion degree.

5.4.3.1. Initial structure of the organic matter

At the initial stage the sample is characterized by non-porous organic matter with only single voids in the initial state (Figure 5.4.11). Organic matter is distributed in a laminated manner (Figure 5.4.11). A few convoluted organic pores were found (Figure 5.4.11–2). Neither spongy nor shrinkage pores were identified.

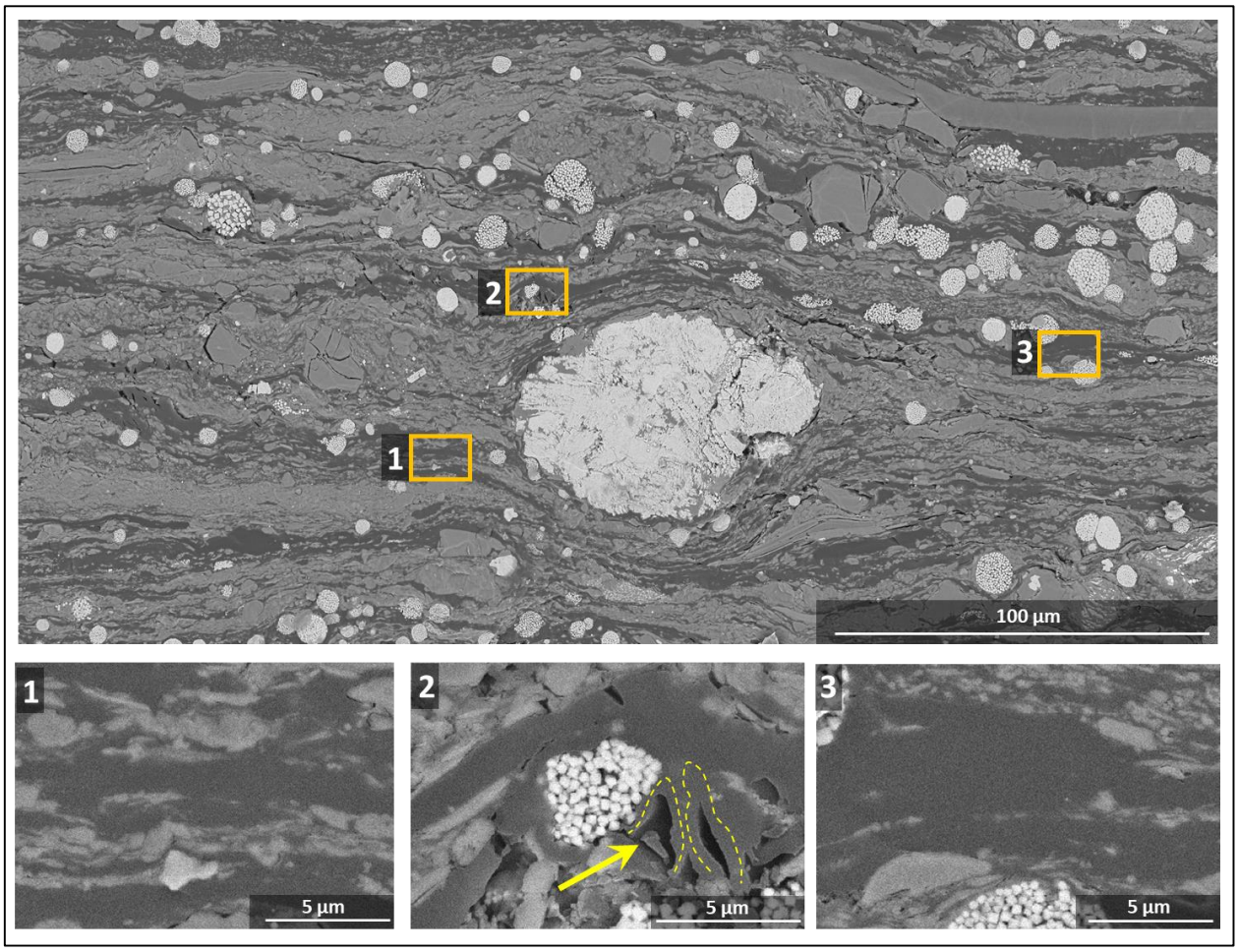

Figure 5.4.11. Initial structure of organic matter in the sample BF#1. Organic matter is solid without maturation associated porosity (1,3). Only a few convoluted pores were observed (2).

5.4.3.2. Evolution of organic matter porosity during artificial thermal maturation

SEM observations after each stage of the thermal treatment allowed to detect the formation of two pore types in OM. The first one is spongy porosity. Figure 5.4.12 demonstrates the evolution of OM within the particular area through the whole experiment. At the temperatures from 350°C to 390°C no pore occurrences were observed. At the temperature of 400°C, the first recognizable pores started to form within the 0.1-0.5 µm size range. The temperature 410°C is characterized by increasing existing pores up to 1-2 µm and the new pores formation. At 420-430°C, the amalgamation of existing pores is the dominant process, accompanied by the minor formation of new pores. And the temperatures of 440-450°C result in a minor progress in all mentioned processes. The other two examples of spongy porosity development are demonstrated in Figured 14 A and B. These examples show slight variations in the first pore appearance in OM inclusions – porosity, in some cases, starts to form at 410°C with significant further development at 420°C. Overall development of spongy porosity is continuous through the OM conversion. The

development of OM spongy porosity take place in most of OM inclusions at the temperature range 400-450°C, whereas pore development is the most active at 410-420°C.

The second type is the shrinkage organic porosity (Figure 5.4.13 C, D). The development of porosity starts at 350-370°C – elongated voids with a length of up to 20-25μm and a width up to 2-3 μm. The further treatment gradually leads to the increase of voids' width. At the temperatures of 350-400°C voids become more open, and the width is up to 2-3 μm. At 410°C, increasing voids occur due to the further shrinkage of OM and the width achieves 5-8 μm. Further treating has a minor effect on the size and occurrence of the voids. At 450°C, the formation of the internal shrinkage porosity is possible (Figure 5.4.13C - 450°C). Shrinkage voids are characterized by the elongated shape and usually occur on the mineral matrix and OM contact. The size is related to the OM particles and, in most cases, does not exceed 25μm in length and 8μm in width.

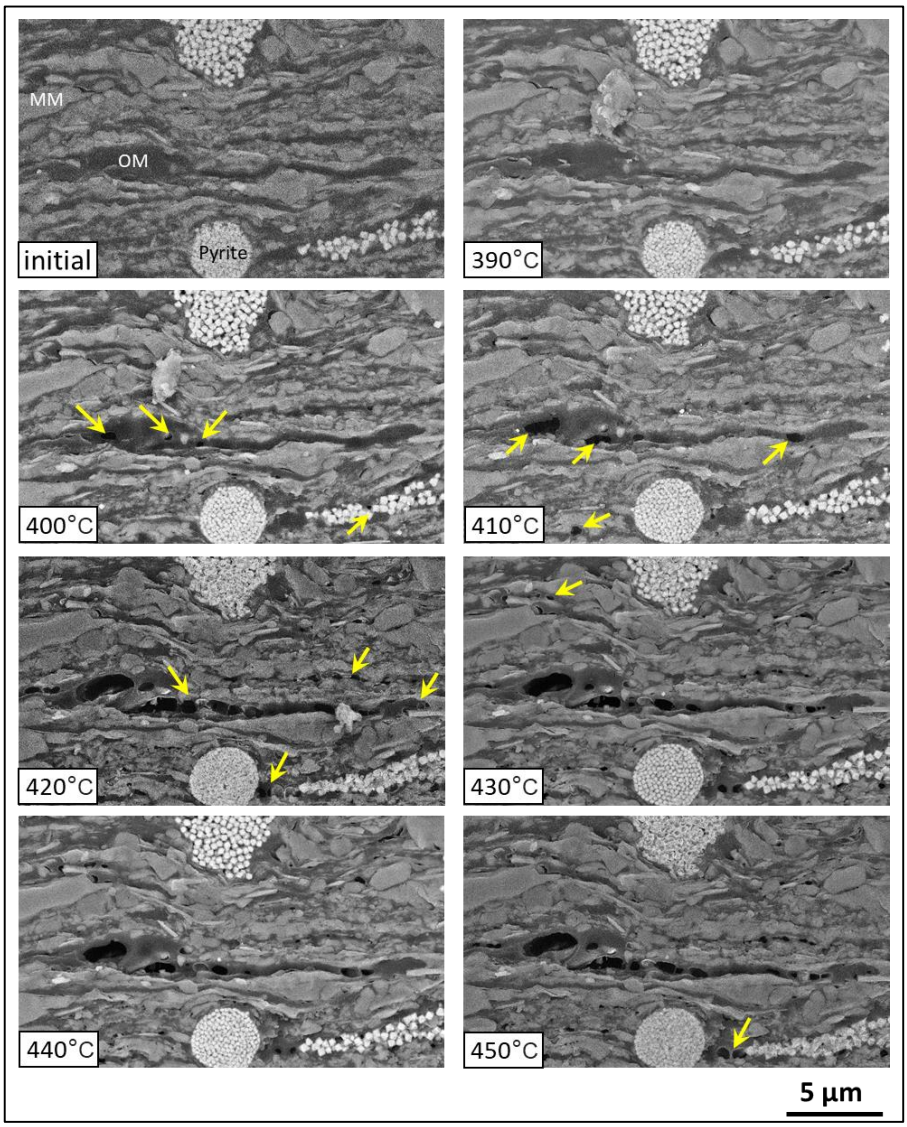

Figure 5.4.12. Evolution of pore space within specific area during artificial maturation of organic matter. Untill 400°C no changes in the micro structure of OM occur – at 390°C, OM has the same solid, not porous structure. The first significant changes occurred at the 400°C first pores were observed. Further maturation lead to the new pore formation untill 430°C, after pores become larger and more connected. The most extensive pore space formation occured at 420°C.

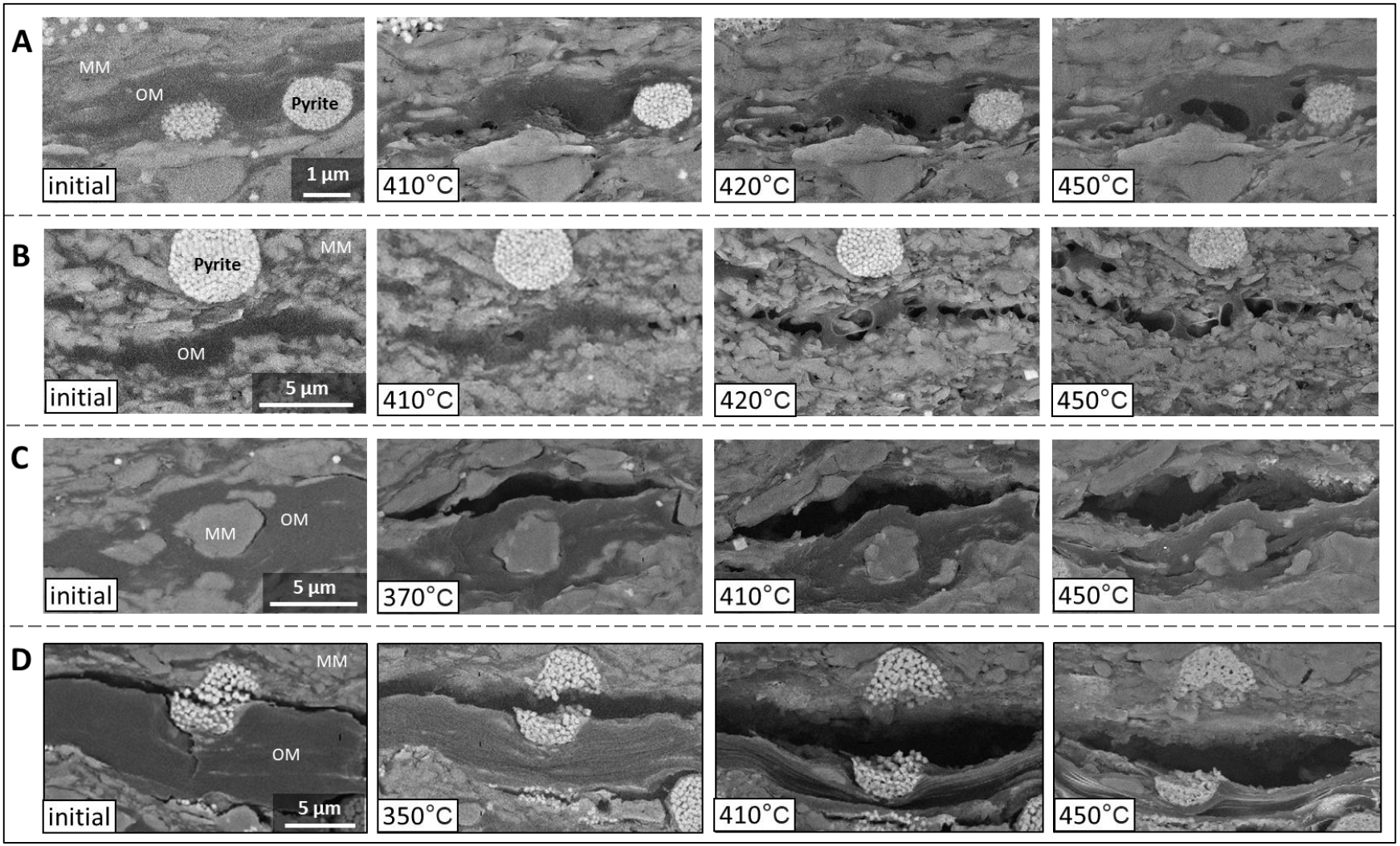

Figure 5.4.13. Evolution of the two different organic pore types during the artificial maturation experiment. A and B – spongy organic porosity development, C, D – shrinkage organic porosity development. Although the pores are quite similar to those in the subsurface there are significant differences in size and pore density. Spongy pores start to form during 410°C, whereas shrinkage pores start to develop at 410°C.

5.4.3.3. Quantitative organic pore characteristics

The results of quantitative porosity analysis of 1000×1000 μm^2, based on the gigapixel SEM images segmentation, are given in Table 5.4.3. The general trend is the increase of porosity with the treatment temperature growth. The first porosity increase was detected at the temperature 350°C – from 0.2% to 0.8%. The further treatment in the temperature range of 350-390°C resulted in a slight porosity increase from 0.8% to 1.3%. According to visual observations, the increase associates with the formation of shrinkage pores (Figure 5.4.13 C and D). Further temperature increase from 390°C to 400°C led to the porosity jump from 1.3% to 2.3%. The jump is directly related to the formation of spongy pores (Figure 5.4.13 A and B) and the progression of shrinkage porosity. The treatment at 410-450°C resulted in a slight increased porosity value up to 2.8-2.9%. The median of equivalent diameters is less than mean values, which is common for all cases (table 4). The mean equivalent diameter varies from 86 nm to 223 nm, while the median ranges from 85 nm to 128 nm. The results of the OM conversion degree are shown in Table 5.4.3. The OM conversion degree increases as the experiment progresses. The active formation of spongy porosity started at temperatures 400-410°C which in term of OM conversion is between 82-92%. The further conversion of OM had a minor impact on spongy porosity. The shrinkage porosity development started immediately after the experiment started– at 350°C, which is 21% of the conversion degree. After 92%, shrinkage porosity development was minor and consisted of size development.

The equivalent circular pore diameter analysis showed that the most abundant pores with equal 100-300 nm. At lower temperatures (350-390°C), the relative fraction of pores with an equivalent pore diameter of more than 200 μm dominates in comparison with the higher treatment temperatures (400-450°C). This effect is clearly shown in Figure 5.4.14 – at the 380°C pores with ECD >300 nm play a significant role, whereas at the 430°C we can see pure domination of pores with <200 nm size. The described effect is caused by the formation of the shrinkage pores at the treatment temperatures 350-390°C and further active formation of nanoscale spongy pores at the treatment temperatures 400-450°C. It should be mentioned that the fraction of 100-150 μm ECD is quite similar throughout the whole experiment, which may be a result of the segmentation artifacts and resolution limitations.

Table 5.4.3. Porosity values and equivalent circular diameters calculated from SEM images

Treatment temperature, °C	Porosity, %	Equivalent circular diameter, nm		Conversion, %	OM distribution
		Mean	Median		
initial	0.2	-	-	0	lenticular
350	0.8	121	103	21	
360	1.1	135	109	-	
370	1.2	190	125	44	
380	1.4	197	128	-	
390	1.3	158	105	82	
400	2.3	165	109	-	
410	2.6	142	106	92	
420	2.9	123	85	-	
430	2.8	138	98	97	
440	2.8	156	112	-	
450	2.9	160	111	99	

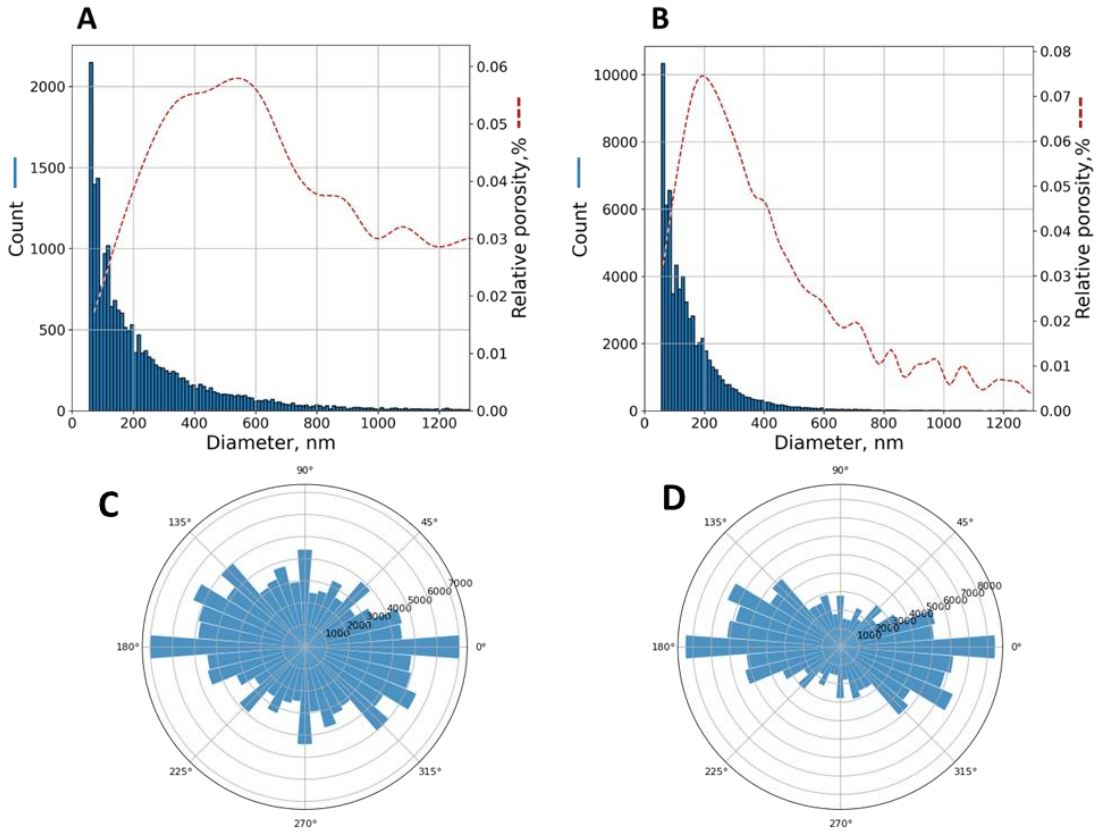

Figure 5.4.14. Histograms of equivalent circular diameter and directional anisotropy measured on ≈10^6μm area. A, C - 380°C. B, C – 430°C.

Figure 5.4.15 shows the evolution of porosity value and conversion degree over the temperature. Porosity progressively rises with temperature and conversion growth. The conversion degree (Figure 5.4.15, red line) is in a good correspondence with porosity change (Figure 5.4.15, blue bars), which indicates the direct relation of porosity evolution and kerogen transformation.

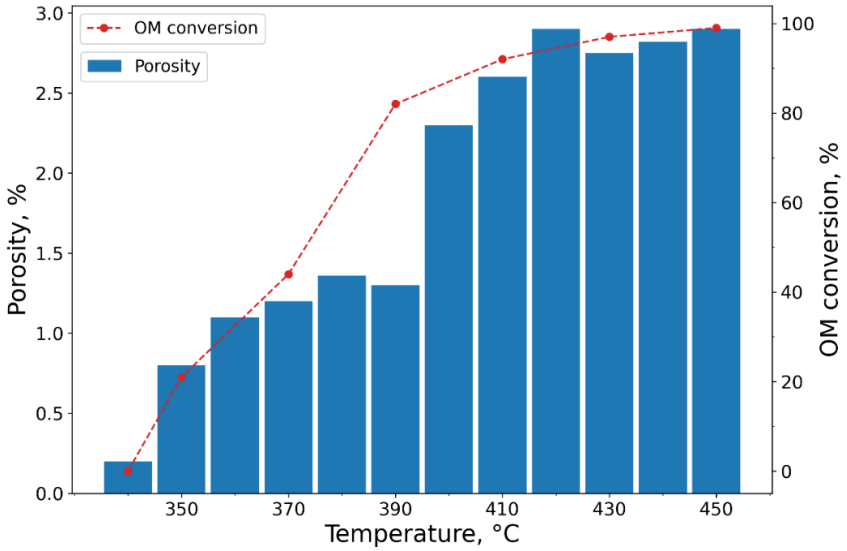

Figure 5.4.15. Porosity increasing with temperature and conversion growth.

5.4.4. Kerogen thermal decomposition products

Kerogen pyrolysis products were analyzed for BF #10 sample. Analysis was performed with GC×GC TOFMS with the sequential investigation of kerogen microstructure by SEM technique.

Results of kerogen decomposition analysis are given in Table 5.4.4. On the basis of flame ionization detector (FID) data obtained during pyro-GC analysis composition of products were calculated: gas and low-boiling liquids (C1-C7), aliphatic (alkanes, cycloalkanes, unsaturates), and aromatic components (mono-, di-, tricyclic). Kerogen may be considered as oil-prone type, it produced less than 10% of gas and oil with aliphatic/aromatic ratio higher than 30/70.

Table 5.4.4. Kerogen pyrolysis products calculated in % of total FID response.

Gas and Light HCs, %	Aliphatic Compounds, %		Aromatic Compounds, %			Aliphatic/ Aromatic Ratio
	Alkanes	Unsaturates, Cycloalkanes	Mono-Aromatics	Di-Aromatics	Tri-Aromatics	
11	10	30	16	13	20	45/55

Sample microstructure study showed voids formation during temperature increase. At the initial state organic matter is characterized by smooth and solid structure (Figure 5.4.16). After the thermal extraction at the temperature of 350°C the different (up to first nanometers) scales bubble-

like structures were documented (Figure 5.4.17). The size of the “bubble” structures is in the range of 10 nm to 300 nm. After the impact of 500°C kerogen has granular structure (Figure 5.4.18A) or represents a porous “membrane” (Figure 5.4.18B). The observed amount of organic natter has been significantly decreased.

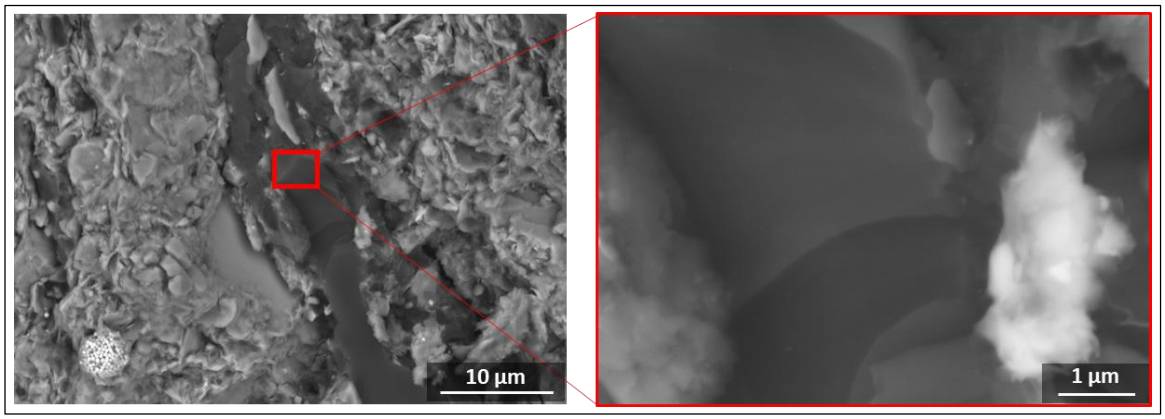

Figure 5.4.16. Non-porous, smooth microstructure of the organic matter in the sample BF #10 in the initial state.

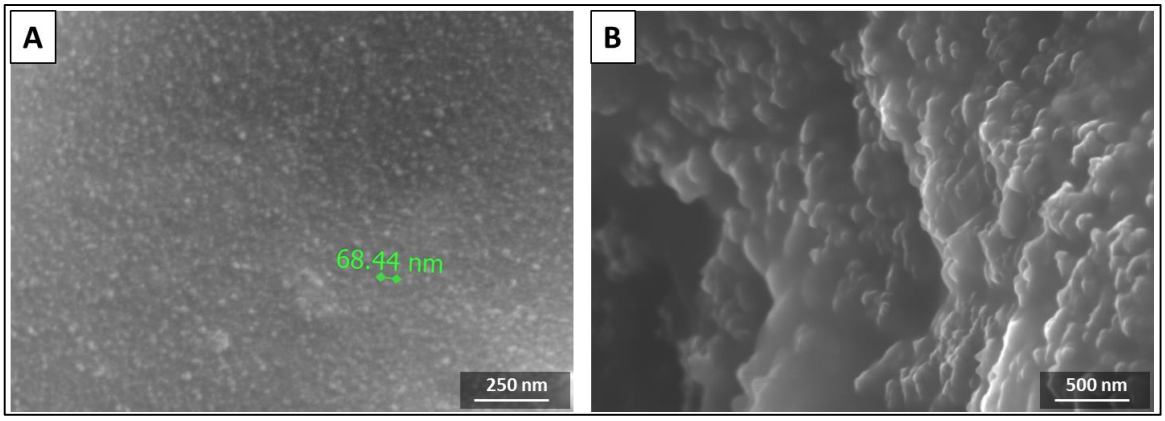

Figure 5.4.17. Bubble-like structure of organic matter in the sample BF#10 after the temperature of 350°C. A – 10-70 nm bubbles on the surface of OM. B – bubbles up to 200 nm.

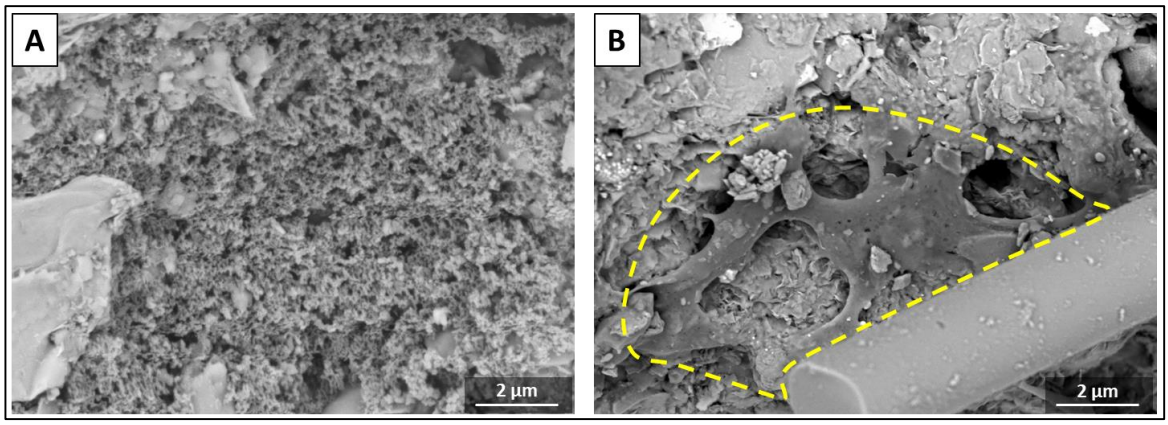

Figure 5.4.18. Porous kerogen after the temperature impact (500°C). A – example of granular microstructure. B – example of porous “membrane” of kerogen.

5.4.5. Artificial thermal maturation experiment in a closed system

For comprehensive assessment of thermal maturation impact on organic porosity evolution in a conditions close to reservoir, an artificial thermal maturation experiment in a closed system was performed. Organic matter microstructure transformations were studied by a series of experiments in a closed system in a CO_2 atmosphere at constant temperature of 350°C at the pressure of 31 MPa, the sample were exposed to three duration times 8, 30 and 72 hours.

For the experiment BF#7 subsample was disintegrated into 1-3 mm particles (no extraction). Thermal treatment was performed in the sealed 30 ml reactors (tubes) loaded in the oven (SNOL-1300) for the heating and temperature maintenance. Temperature was controlled by thermocouples (AEROPAK). The experiment consisted of three parts. The first step was CO_2 injection upto 31 MPa. The reactor was loaded into preheated oven. The reactor was kept in the oven furnace for the duration of the experiment. After the time has elapsed, the reactor is removed from the furnace, cooled, depressurized and opened.

Characterization of organic matter before and after the experiment was performed with the Rock-Eval technique. Organic matter porosity was studied with SEM method.

5.4.5.1. Organic matter transformation and porosity evolution during the experiment

Results of Rock-Eval programmed pyrolysis are given in Table 5.4.5. Figure 5.4.19 illustrates of organic matter transformation over experiment duration. S2 parameter (amount of hydrocarbons generated during pyrolysis, or remaining hydrocarbon generating potential) gradually decreases on 38%, 71% and then 77%, whereas S0 and S1 (amount of HC already presented in the sample) are increased by 1% and 13% at 8 hours, 176% and 74% at 30 hours, after the 72 hours small reduction on 30-40% was detected. Observed increasing is associated with kerogen transformation into hydrocarbons, further slight decreasing might be the result of secondary cracking with simultaneous generation of new hydrocarbons (Figure 5.4.19).

Table 5.4.5. Rock-Eval pyrolysis results

Sample ID	S0, mg/g rock	S1, mg/g rock	S2, mg/g rock	S3, mg CO2/g rock	TOC, wt.%	HI, mg HC/g TOC	OI	T_{max}, °C
before	1.39	2.63	20.42	0.91	6.94	294	13	453
8 hours	1.41	2.99	12.69	0.78	6.17	206	13	455
30 hours	3.84	4.58	5.91	0.63	5.98	99	11	463
72 hours	3.21	3.71	4.63	0.57	5.7	81	10	467

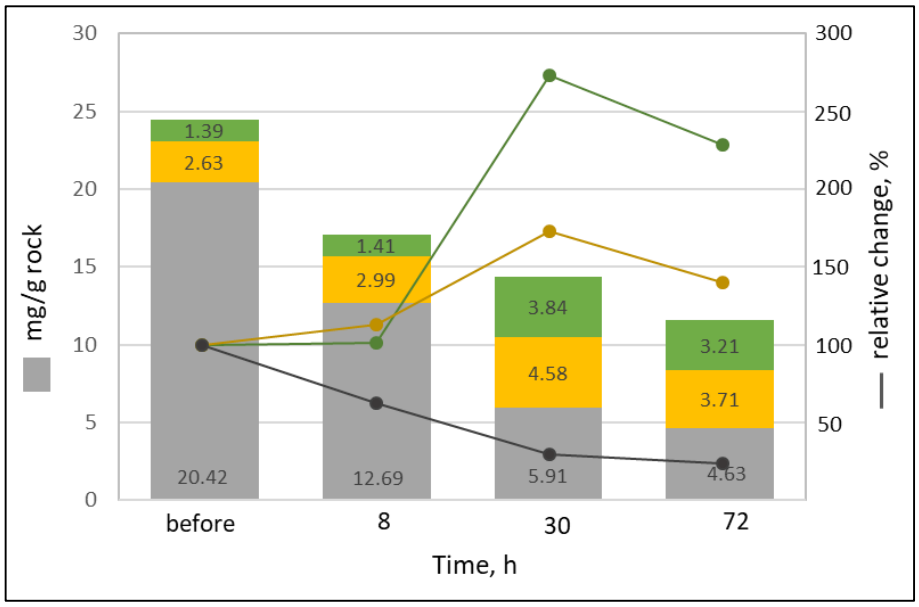

Figure 5.4.19. Rock-Eval pyrolysis parameters (absolute and relative values) evolution with time.

SEM study showed continuous development of organic porosity over the time within individual OM particles (Figure 5.4.20). Samples at the initial state are characterized by non-porous, flat, solid organic matter (Figure 5.4.20, before), however some single porous inclusions might be found. After 8 hours experiment significant number of OM particles are characterized by the presence of bubble-like structures and single pores in OM (Figure 5.4.20, 8 hours). After 30 hours episode most of the OM particles are porous (Figure 5.4.20, 30 hours). Pores are may be attributed to the spongy porosity according proposed classification. Pores are 0.1-1 μm in size. After t 72 hours experiment almost all OM particles are porous (Figure 5.4.20, 72 hours). Pores are 0.05-2 μm in size and tightly concentrated in a single OM inclusion. Spongy porosity is the dominant type, however single shrinkage pores were documented (Figure 5.4.21).

Since the polishing of the such small samples is not possible with the rigorous calculation of organic porosity on SEM images over whole sample area, amount of OM particles were calculated with the differentiation on porous and non-porous. Results are given in Table 5.4.6. Results clearly show increasing of number of porous organic particles.

Table 5.4.6. Results of OM particles counting.

	Number of OM particles			
	Before	8 hours	30 hours	72 hours
Total	27	31	26	39
Porous	9	14	17	34
Percentage of porous, %	33	45	65	87

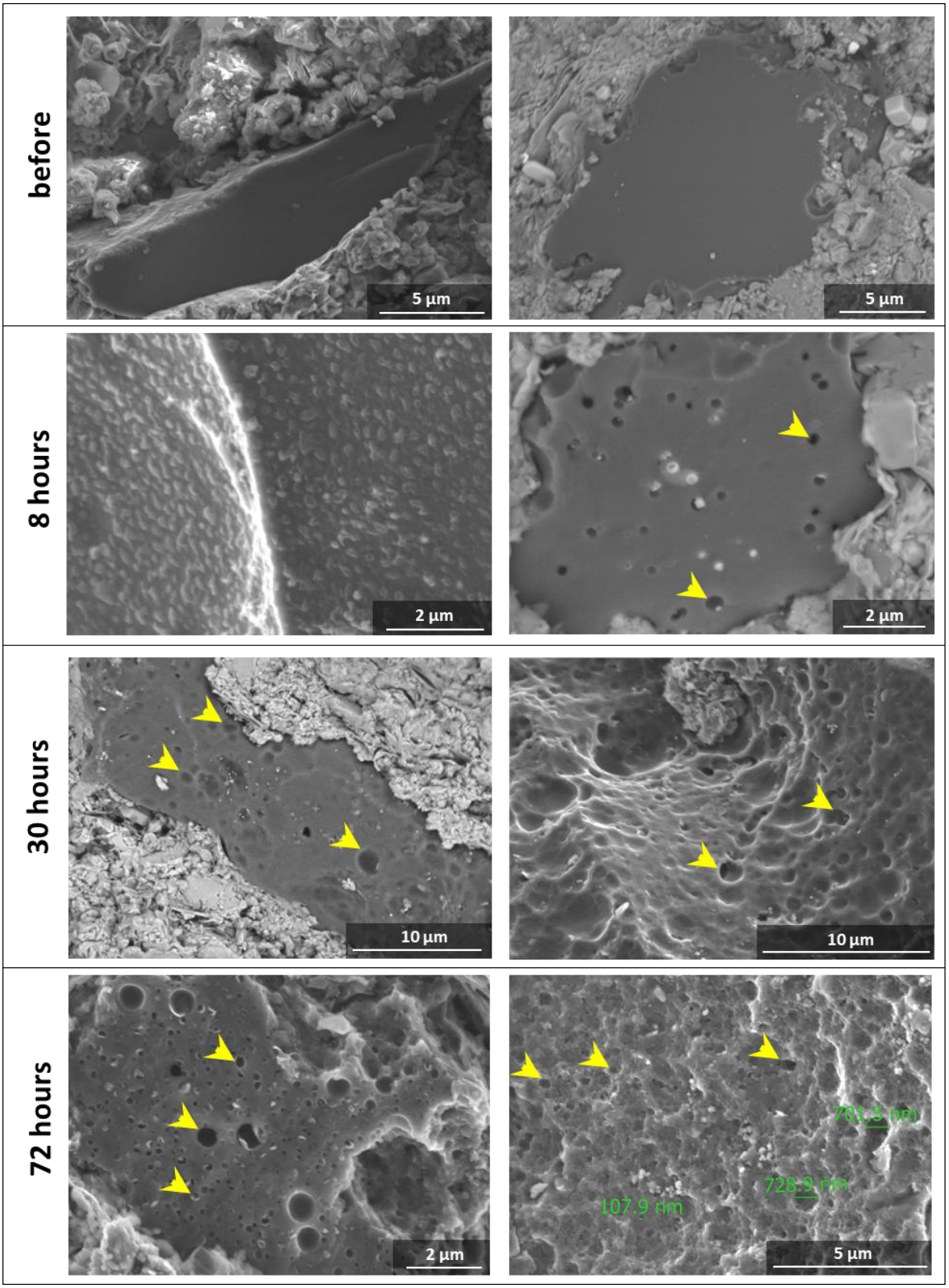

Figure 5.4.20. SEM images of samples after a specific experiment duration.

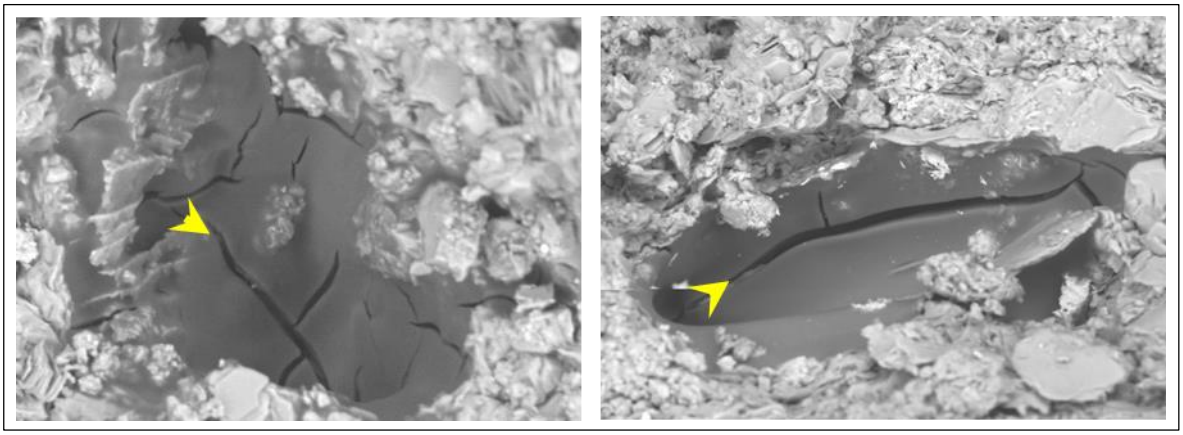

Figure 5.4.21. Shrinkage pores in the kerogen after the 72 hours thermal impact.

5.5. Summary

The study revealed on the influence of thermal maturation processes on the microstructure of organic matter (kerogen) both natural occurring porosity and resulting from artificial thermal maturation. Naturally occurring organic porosity is mainly controlled by thermal maturity; however, there are voids resulting from primary processes associated with sedimentation processes. Classification of organic pores based on the genesis has been proposed. It was shown that OM porosity is also defined by the rock fabric and OM structure. The artificial maturation experiment aided to observe the development of organic pores within individual organic inclusions in open and closed systems. In both cases, the formed organic pores are similar to those, occurred naturally. The key outcomes of the study are given below.

Organic porosity occurrence across natural maturity level variations

1. Kerogen porosity in the Bazhenov Formation shales is closely related to the thermal maturation degree. Thermal maturation is a key aspect of organic pore development.
2. The first single pores start to form within the middle of the oil window. At the end of the oil window, the majority of organic particles are porous and form an effective pore space network.
3. There are certain types of organic pores in immature Bazhenov Formation rocks, which are the result of primary processes such as sedimentation. However, these pores are quite rare and do not tend to form an effective pore space.
4. Classification of organic pores has been proposed. Organic pores in the Bazhenov Formation are classified according to the genesis into primary (sedimentation related) and secondary (thermal maturation related) pores. A further division implies structural features. Primary pores are represented by inherited and convoluted pores. Secondary pores are spongy, shrinkage, and mixed pores.
5. Rock fabric plays a vital role in organic pore development and preservation. It is shown that shales characterized by an interlayering of mineral components and organic matter lenticulars do not tend to preserve organic porosity. The reason is load-bearing organic matter without grain support affected compaction during burial. Whereas shales with organic inclusions (lenses, patchy distribution), non-load-bearing with grain support, have a good chance to preserve both primary and secondary porosity.

Artificial thermal maturation experiments

1. Artificial thermal maturation controlled experiments clearly confirmed the crucial factor of thermal maturation for organic porosity development. Thermal treatment of organic-

rich shales to the temperatures when kerogen transforms to hydrocarbons leads to the formation and further development of organic porosity.

2. The formation of organic porosity during artificial thermal maturation, apart from its fundamental significance, is a significant beneficial positive factor for the implementation of thermal enhanced oil recovery technologies in shales.
3. The experiment in the open system showed, that first pores appeared at the temperature of 350°C (conversion of OM>21%), which represents shrinkage pores, the second significant rise was detected at the 400°C (conversion of OM>82%), which occurred at the expense of spongy pores. Further temperature increase and the OM conversion lead to the pores amalgamation and pore size increase.
4. The experiment in the closed system at a constant temperature of 350°C at the pressure of 31 MPa shows the formation of bubble-like structures on the surface of OM and single OM pores after 8 hours. These bubbles are considered as a precursor of hydrocarbons, and probably contain some oil. After 30 hours experiment more than half of the OM inclusion were porous (65%), and after 72 hours most of the OM were porous (87%). Rock-Eval pyrolysis shows a decrease of S2 parameter during the experiment (realization of generation potential) up to 77%, and an increase of S0 and S1 parameters (hydrocarbons presented in the samples) up to 176%. However, a slight decrease was detected after 72 hours, which might be result of secondary cracking and simultaneous formation of hydrocarbons.

Chapter 6. Analysis of the results from the point of view of perspectivity and effectiveness of the high temperature treatment technology

The chapter is devoted to the complex analysis of the experimental results of the high-temperature treatment experiments on Bazhenov Formation shales and the fundamental reasons behind the documented alterations. The mineral matrix has undergone significant changes, which vary considerably within different lithotypes and depend on the initial mineral composition, as well as the organic matter, which also has been changed during the treatment. These changes have influenced the reservoir properties. Based on the analysis, the most suitable lithotypes were suggested for the high temperature-based technology application.

6.1. Mineral matrix alterations during the high-temperature treatment

Siliceous minerals

No changes in the siliceous (quartz) component during the experiments were observed, only minor grain contacts destructions. However, it is essential to take into account transformation of α-quartz to β -quartz at the temperature of 573°C, and conversion of β-quartz to β-tridymite at 870°C (Figure 6.1.1). The transformations are accompanied by gradual density reduction: 2.65 g/cm^3 (α-quartz), 2.53 g/cm^3 (β-quartz) and 2.25 g/cm^3 (β-tridymite) [113]. The transformation temperatures can be shifted to higher values at elevated pressures (Figure 6.1.1). The transformations are reversible; however mechanical properties can alter significantly [114].

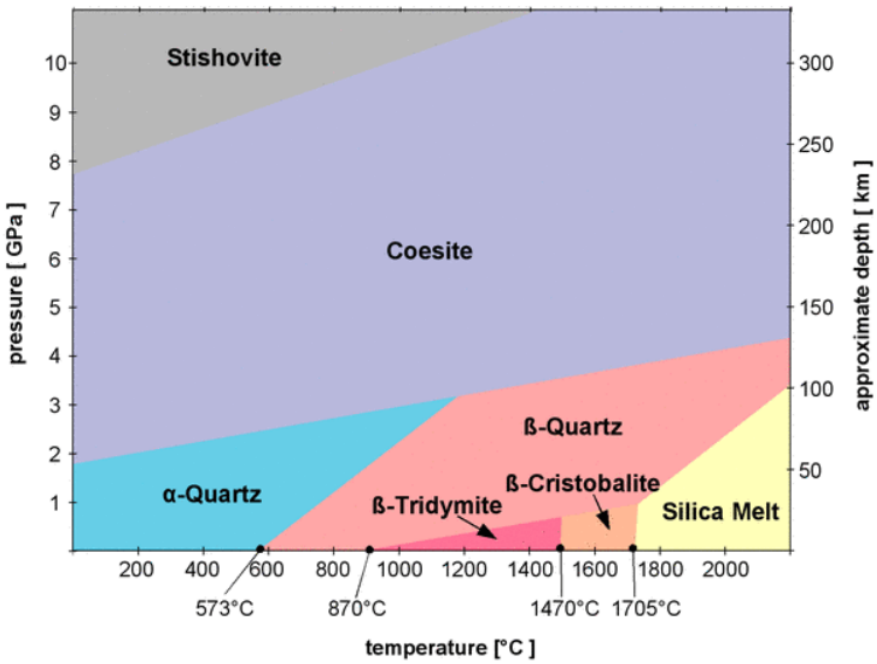

Figure 6.1.1. Phase diagram of SiO_2 [113]

Carbonate minerals.

Carbonates in the studied shales are presented by calcite and dolomite. The lithotypes behind the combustion front (841°C) rich in carbonates are characterized by numerous alterations after the experiment (see "Chapter 4. Experimental modeling of the mineral matrix alteration and void space evolution during high temperature treatment"): the destruction of dolomite with the formation of magnesium oxide (MgO), calcite ($CaCO_3$), calcium oxide (CaO) and a number of new minerals (anhydrite, wollastonite, gehlenite).

Decomposition of dolomite occurs according following reaction [115]:

$$CaMg(CO_3) \rightarrow CaCO_3 + MgO + CO_2$$

Since both $CaCO_3$ and CaO were observed in one sample, CaO and MgO are results of two simultaneous processes [115,116]:

$$CaMg(CO_3) \rightarrow CaO + MgO + CO_2$$

$$CaCO_3 \rightarrow CaO + CO_2$$

The MgO is characterized by needle-like crystals, which form a rough surface. Newly formed $CaCO_3$ is characterized by intercrystalline void space and nano-sized crystals. The resulting pore-space effect is the increase in specific surface area and porosity. CaO served as a trigger for further mineral matrix transformation and participated in a variety of reactions.

The formation of wollastonite and anhydrite is a result of joint presence and interaction with other minerals and are considered below.

Clay minerals

First alterations in clay minerals (illite) were observed at the temperature of 400°C (right ahead of the combustion front) in all clay containing lithotypes: elongated voids and fractures were observed. After the combustion front propagation (841°C) there is a clear differentiation of alterations in two clay-containing lithotypes (argillaceous-siliceous organic-rich mudstone and calcareous-argillaceous organic-rich mudstone). In the case of argillaceous-siliceous organic-rich mudstone (illite rich) only further development took place for elongated voids between lamellas and the formation of fractures. The reason behind this process is the water removal. At the 400°C physically bounded water removal occured. And at the 841°C dihydroxylations by condensation

of hydroxyl groups into water molecules took place [117]. The process is described as follows [118]:

$$KAl_3Si_3O_{10}(OH)_2 \rightarrow KAl_3Si_3O_{11} + H_2O$$

Calcareous-argillaceous organic-rich mudstone is characterized by several mineral matrix transformations, resulting in new minerals. The transformations are related to the decomposition of carbonates and the formation of CaO. CaO is combined with anhydrous illite and forms gehlenite ($Ca_2Al_2SiO_7$) with the CO_2 release, K_2O (alkalis), and amorphous silica (SiO_2) [117]. At the same time the amorphous silica is combined with the CaO and forms wollastonite ($CaSiO_3$) [119]:

$$KAl_3Si_3O_{11} + CaCO_3 \rightarrow Ca_2Al_2SiO_7 + SiO_2 + K_2O + CO_2$$

$$CaCO_3 + SiO_2 \rightarrow CaSiO_3 + CO_2$$

Wollastonite occupied the major volume of the rock replacing illite, whereas gehlenite plays a minor role – only traces were found on the XRD patterns. Amorphous silica can be formed omitting the stage of the gehlenite formation and can be directly combined with the calcium oxide. Wollastonite forms a pore space with a pore size of up to 3 μm, and a crystal size of 0.5-4.5 μm. The formation of wollastonite occurred after the combustion front propagation with a maximum temperature of 841°C at 31 MPa. According to the literature, the formation of wollastonite occurs in between 800°C and 900°C at the ambient pressure.

XRD patterns showed the presence of mullite in the sample after the 841°C. The formation of mullite is associated with the transformation of illite minerals. Available data on the mullite formation is limited. The [117] shows that no mullite was found after the series of high-temperature experiments (600 – 1000°C), Grim [118] reports 600-700°C destruction of illite lattice, formation of spinel at 850°C, amorphous silica, and the formation of mullite at 1100°C. No spinel was observed in our experiments, however, traces of mullite were found. No significant effect on pore space was observed. The following process is suggested:

$$Al_2Si_2O_7 \rightarrow Si_3Al_4O_{12} + SiO_2$$

It should be mentioned that the identification of mullite is very complicated due to its complex pattern and multi-component composition of samples.

Pyrite

First alterations of pyrite microstructure were observed at the 400°C accompanied by sulfur reduction. The combustion front propagation (841°C) leads to the formation of hematite (Fe_2O_3) and the complete microstructure change with additional pore space formation. It is important to emphasize that atmosphere ahead of the front is close to the inert, whereas the front propagation represents a high temperature oxidation process. The pyrite is very sensitive to the temperature and oxygen presence. The microstructural alterations, after the temperature of 400°C, impact the result of pyrite decomposition into pyrrhotite and sulfur in an inert environment [120]:

$$FeS_2 \rightarrow FeS_x + S_2$$

This process of decomposition continues until elemental iron formation:

$$FeS \rightarrow Fe + S_2$$

Oxidation at the temperature of 841°C induced much more complicated processes and products. XRD and EDS showed a presence of hematite (Fe_2O_3) after the experiment. Two processes occur simultaneously, oxidation of pyrite, which has been left, and the oxidation of pyrrhotite. Hematite (Fe_2O_3) and SO_3 are the main products of these two processes. Literature data suggest that both processes involve the formation of iron sulfates [120], however, it was not confirmed in the current experiment. Considering only the key reactions and products, the transformation of pyrite are generalized and described by the following reactions [120]:

$$FeS_2 + O_2 \rightarrow Fe_2(SO_4)_3 + SO_2$$

$$FeS_2 + O_2 \rightarrow FeSO_4 + SO_2$$

$$Fe_2(SO_4)_3 \rightarrow Fe_2O_3 + SO_3$$

$$FeSO_4 \rightarrow Fe_2O_3 + SO_3 + SO_2$$

$$SO_2 + O_2 \rightarrow SO_3$$

The experiment involves successive thermal decomposition of pyrite into pyrrhotite and its further oxidation:

$$FeS_2 \rightarrow FeS_x + S_2$$

$$S_2 + O_2 \rightarrow SO_2$$

$SO_2+O_2 \rightarrow SO_3$

Oxidation of pyrrhotite:

$FeS_x + O_2 \rightarrow Fe_2O_3 + SO_2$

$FeS_x + O_2 \rightarrow Fe_2(SO_4)_3 + SO_2$

$FeS_x + O_2 \rightarrow FeSO_4 + SO_2$

$FeSO_4 \rightarrow Fe_2O_3 + SO_3 + SO_2$

$Fe_2SO_4{}_3 \rightarrow Fe_2O_3 + SO_3$

$SO_2 + O_2 \rightarrow SO_3$

The transformation of pyrite with the presence of carbonates results in the formation of anhydrite ($CaSO_4$), and minor products such as MgS, CaS, BaS. Anhydrite has the greatest impact on pore space and mineral matrix (see Chapter 4. Experimental modeling of the mineral matrix alteration and void space evolution during high temperature treatment). Anhydrite makes pore space more complex due to numerous small crystals on the one hand and serves as a buffer for sulfur on the other hand, which could have a damaging effect on both generated hydrocarbons and the equipment. There are three possible pathways of the anhydrite formation.

The first process involves H_2O, which is a result of clay dehydration, described above, and CaO, which is a product of calcite decomposition:

$SO_3+H_2O \rightarrow H_2SO_4$

$CaO + H_2SO_4 \rightarrow CaSO_4 + H_2O$

The second process implies the presence of S_2, formed after pyrite decomposition. This process is considered insignificant due to oxidation of S_2 into SO_2.

$CaO + S2 \rightarrow CaS + SO2$

$CaS+O_2 \rightarrow CaSO_4$

The third process is the shortest way of formation of anhydrite and can be considered as major:

$CaO + SO_3 \rightarrow CaSO_4$

Feldspar

Porous aggregates of feldspar (solid solutions between K-feldspar ($KAlSi_3O_8$) and albite ($NaAlSi_3O_8$)) were observed in the samples after the impact of 841°C (after the combustion front propagation). It should be noted that no significant changes were observed in chemical composition, however, a significant alteration of the microstructure took place. The observation can be explained by possible melting of the feldspar during the experiment with consolidation after the temperature was dropped. The melting suggestion is supported by literature data [121]. However, there are studies which show more complex processes in feldspar at high temperatures and pressures. The sodium feldspar is transformed into an assemblage of jadeite and quartz at high pressure and temperature (700°C, 3 kbar) as follows [122]:

$$NaAlSi_3O_8 \rightarrow NaAlSi_2O_6 + SiO_2$$

And the transformation of K-feldspar in the temperature range of 400-800°C and pressure of 10-30 kbar transforms into a hexagonal phase $KAlSi_3O_8\ H_2O$ by the following chemical reaction [123]:

$$KAlSi_3O_8 + H_2O \rightarrow KAlSi_3O_8\ H_2O$$

However, in dry conditions K-feldspar is stable at 1000 and 60 kbar [123].

These alterations lead to the formation of porous structures in feldspar aggregates, which are beneficial for the reservoir properties of a rock.

6.2. Organic matter transformation during thermal maturation

6.2.1. Organic porosity occurrence across natural maturity level variations

Secondary organic porosity origin and occurrence

The analysis of the Bazhenov Formation organic matter microstructure at different stages of thermal maturation showed a direct relation of the OM porosity abundance to the thermal maturation level. The earliest pores in OM have been detected at maturity around the middle of the oil window, but at this level pores are not developed enough and perhaps do not form an effective pore space. At the end of oil window, we suggest that OM porosity can form connected porosity. The latter suggestion is based on the research performed by Vasiliev et. al [102] with the FIB-SEM technique on Bazhenov Formation samples. They analyzed a small rock volume (3.1x2.6x6.1 μm^3) of a Bazhenov Formation sample with a nanometer resolution and showed that the porosity of matured Bazhenov Formation samples could reach 6.1 % with 0.2-2 μm pore size

and 75% pore connectivity. In the current study from the qualitative analysis of 1000 μm x 1000 μm area in seven samples, we showed that porosity can reach 3.5% in matured samples with maximum 4 μm individual pore size.

The obtained trends in this study are supported by a number of works devoted to the OM porosity in the organic-rich shale formations. Loucks et al. (2009) [98] based on SEM investigation of organic matter in mudstones of the Mississippian Barnett shales concluded that the abundance of OM pores and size increase is related to thermal maturity. Modica and Lapierre (2012) [108] suggested a direct tie of organic porosity development to kerogen transformation in Mowry Shales in the Powder River Basin. Similar conclusions are given by Wu et al. (2015) [74], Kuila et al. (2014) [124] and Ko et al. (2016) [73]. Nevertheless, the actual impact of the thermal maturity on organic porosity is poorly understood, its impact is complex and can both form and destroy the pores Katz and Arango (2018) [103], Mastalerz et al. (2013) [125], Reed et al. (2014) [126], and should be investigated carefully for each formation individually.

It had been commonly observed that the formation of organic pores starts at the gas generation stage or at more advanced levels of maturation [127]. Regarding BF organic matter porosity Balushkina et al. (2014) assumed that OM pores in BF may start to form at the beginning of the gas window. However, in this study, we argue that first OM pores start to form significantly earlier – at the middle of the oil window (Figure 5). This observation is in good correspondence with the reports, which suggest that organic porosity may develop within the stage of the oil generation, for instance, Fishman et al. (2013) [128] demonstrated that organic porosity might develop in the middle of the oil window in the Eagle Ford Formation, which was later confirmed by Pommer and Milliken (2015) [129]. Reed (2017) also suggested that OM porosity starts to develop at the early oil window. Jennings and Antia (2013) [131] documented the beginning of OM porosity development at the onset of the oil window and went to a maximum at the gas window. These observations are in line with Loucks et al. (2009) [96] who showed an increase of OM porosity at the middle of the oil window. However, the question of the first OM pores development is quite wider and encompasses not only thermal maturation, but also sedimentation, diagenesis, preservation during burial and rock fabric related issues. Some researchers reported an organic porosity increase during the oil window and then its disappearance at more advanced levels of maturation [97,100].

In the discussion of organic pores, it is necessary to mention that organic pores are often considered as a result of the exsolution of hydrocarbons during secondary cracking (maturation) of OM. Loucks et al. (2009) proposed that pores are formed as a result of kerogen transformation into gases and liquids with coalescence into bubbles. A similar point of view is held by Dahl et al. (2012) [132], who noted that kerogen conversion to oil and gas with hydrocarbons migration leads

to open voids formation. Keel (2015) [133] suggested that increasing thermal maturity results in aromaticity, which leads in turn to a restructuring of OM with the formation of "aromatic islands" surrounded by space created by the release of volatiles. Fishman et al. (2012) [134] in contrast stated that organic porosity is not connected with hydrocarbon generation. In the current study, we do not have a direct conformation of mentioned theories, however, the experimental results on the artificial maturation showed the formation of spongy pores with progressive thermal maturation, which we suggest is a result of hydrocarbon formation.

It was found that the specific shape of pores is often observed in the matured samples. According to the classification developed (see section "5.4.2.3. Organic porosity classification"), these pores are spongy and shrinkage pores, sometimes, they were observed together. Similar spongy shape pores were observed by Loucks et al. (2009) in matured Barnett shales, by Chalmers et al. (2012) in Barnett, Haynesville, and Doig units, by Curtis et al. (2012a) in Woodford Shale and others [44,73,104,129,136]. Generally, all the authors agree that these pores are the result of the thermal maturation process as well as hydrocarbons exsolution [137,138]. Shrinkage pores are much less described in the literature. Ko et al. (2016) suggested that these pores are heating experimental artifacts appeared after temperature drop and may not be present in the subsurface. Nonetheless, Wood et al. (2015) support the idea that these pores may be caused by the devolatilization of bitumen, Klaver et al. (2016) in turn suggested that crack like pores in OM may be a result of hydraulic fracturing of OM due to volume changes due to hydrocarbon generation. We found shrinkage pores across several samples in two variations: within OM itself and at the OM-MM boundary. Shrinkage voids within OM are typical for matured OM (late oil window), whereas shrinkage voids at the OM-MM boundary were found at oil window samples.

Although thermal maturity is an incredibly important factor for OM porosity appearance, it is not only the factor controlling OM porosity development in shales [103]. OM pores also were described by a number of authors in immature samples [129,140–143]. In some other cases, OM pores were not present in the mature samples. The authors of such reports consider thermal maturation as a minor factor [104,107], or as a factor that leads to individual pore size decreasing [74] or organic porosity decline [144].

Primary organic porosity in immature rocks

Apart from the thermal maturation induced organic porosity, we have observed OM pores in immature samples. We have identified two primary pore types. The first ones are inherited pores, which are considered to be inherited from the original deposited organic matter (cellular structure in spores, algae, leaf, etc.). The second ones are convoluted OM pores, the formation of these pores is related to the deformation of the organic matter particles during sedimentation or/and

burial such as folding, twisting, or coiling. These pores are considered as not connected with the maturation process and described in Boquillas Formation [73] and Mediterranean sapropels [141].

Despite some reports suggesting organic porosity is an exclusive product of thermal maturation and is nearly absent in immature shales [124], there is well-documented evidence of organic porosity in the originally deposited and immature organic matter [129,140–143]. Pommer and Milliken (2015) reported the appearance in the immature Mediterranean sapropels both preserved primary inherited algal OM cell porosity and pores formed after algal OM deformation. Mastalerz et al. (2013) showed the appearance of inherited pores in alginates reaching 1 μm in size. Löhr et al. (2015b) demonstrated the presence of organic pores in immature Monterey shales. They suggested that OM is inherently porous - voids between the cells of colonial algae and membranes of individual cells. Although OM porosity in immature mudstones is not common, there is enough evidence to state that voids may be inherited from the original deposited organic matter. It should be mentioned that in most cases low matured OM in shales are not porous [140] or porosity is too low to form effective pore space. However, it was shown in the current study through the quantitative analysis of SEM images that primary pores may exceed 1% with the size of individual pores up to 1-2 μm and mean equivalent diameter 132 nm, which is comparable to samples at oil window maturation level.

Rock fabric, mineral composition, and compaction

Another factor that we suggest significantly affects OM porosity is a rock fabric. We found at the same level of thermal maturation that OM may be either porous or not porous depending on the organic matter distribution pattern in the rock. Two principal cases are possible: a) rock is grain supported and OM is non-load-bearing or b) there are no rigid grain supports and OM is a load-bearing component. In the first case, grain support protects the OM from continuous compaction during the thermal maturation process, so organic pores have a good chance to be preserved. In the second case, organic matter is not supported, which results in compaction during maturation and OM pores are not formed or immediately closed as they appeared. The effect is confirmed by the data on the OM distribution pattern given in Table 2, particularly the organic porosity of the samples characterized by the OM in the form of inclusions systematically higher. A similar idea was proposed by Curtis et al. (2012a), who tried to explain porosity development and lack of pores in a single field of view in Woodford Shale by the absence/presence of grain support.

A number of studies [103,136,143] consider OM porosity development and preservation as a function of the mineral composition, which in turn determines the compaction process. According to the research presented by İnan et al. (2018) clay enriched mineral matrix tends to be affected by compaction and hydrocarbon expulsion with no formation of OM porosity, whereas silica-rich mudstones are considered as stable rocks with good OM preservation abilities. In the

current study, samples are characterized with similar mineral composition, although two samples slightly differ from others by relatively high (≈20 wt.%) amount of clay minerals. Two samples from one well, demonstrated in Figure 7, have almost identical mineral compositions, but OM porosity differs significantly. We completely agree that mineral composition may play a significant role as it was proposed by İnan et al. (2018), especially regarding the compaction process, however, our study shows that the critical role is played by exactly rock fabric or, in other words, by the presence/absence of grain support and finally load on organic matter.

6.2.2. Organic porosity formation during artificial thermal maturation

There is a number of authors that state that thermal maturation is one of the most important factors [74,96,108,124], as well there are researchers who suggest that thermal maturation plays a minor role [104,107]. The results of the artificial thermal maturation experiment allow observing the evolution of organic porosity within specific OM particles during thermal maturation, which confirms the idea that thermal maturation is one of the key factors controlling organic porosity development in shales.

Two types of pores were detected, shrinkage and spongy pores. We suggest that the formation of shrinkage pores is associated with the elimination of hydrocarbons (extractable organic matter) from the rock, and the formation of spongy pores is related to the transformation of kerogen into hydrocarbons.

Analysis of the porosity during the experiment showed that there are two sparks in porosity value. We suggest that the first spark is associated with the formation of shrinkage pores. Normally, shrinkage organic pores are larger than any other type and form in the range of 350-370°C. The second spark is detected at 400°C, which is associated with the formation of spongy pores, nanometer scale, they are significantly smaller than shrinkage pores. Figure 15 demonstrates, that at 380°C most of the porosity is represented with pores characterized by 400-600 nm. And at a higher temperature, 430°C, a major part of porosity is composed of pores with equivalent cicular diameter (ECD) of approximately 200 nm.

The comparison of organic pores in the artificially matured samples and samples with varying maturity from the subsurface show both similarities and differences. The observed spongy and shrinkage pores are quite similar in terms of shape and size in both cases. The porosity range of the treated sample consists of the values of untreated samples. The matured untreated subsurface sample BF#9 is characterized by a higher value of mean and median equivalent diameter in comparison with the treated sample. That can be a result of the primary pore presence in the rock with the grain support and completely different pressure conditions.

The results of this experiment directly show that spongy and shrinkage organic pores develop as a result of the thermal maturation of organic matter. Moreover, additional organic matter hosted pore space could be created in the organic-rich shales with the use of elevated temperatures artificially.

Significance of OM porosity

There are two aspects of the significance of the organic porosity in the Bazhenov Formation. The first one is the presence of unconventional reservoirs in organic-rich shales. It implies that generated hydrocarbons might stay in the formed pores without migration, and in that case, the source rock will be a reservoir for oil and gas. The second aspect is related to EOR application in shales, particularly the possibility of artificial reservoir creation filled by generated hydrocarbons. These processes are associated with converting solid kerogen into liquid hydrocarbons through thermal methods, described by Sun et al. (2015) and Kokorev et al. (2014) [58], which convert solid OM into liquid hydrocarbons, and there is a crucial aspect of pore space development during thermal treatment. An exact understanding of pore formation processes helps to control them and direct them in the right direction, as well as choose suitable intervals for thermal EOR technologies.

6.3. Mineral matrix related pore space evolution and organic matter transformation during high-temperature treatment

A detailed analysis of alterations in shales during high-temperature experiments showed the direct influence of mineral matrix alterations and organic matter microstructural transformations on void space. The evolution of pore space varies in different lithotypes. However, there are common sequences of main components transformation: transformations start with an organic matter porosity formation, and, after the complete transformation of organic matter, alterations of mineral matrix take place.

Initial stages of thermal impact on shales lead to the formation of pore space in organic matter (inert atmosphere). The development of organic matter porosity is a result of kerogen conversion into hydrocarbons. Most of the organic matter transformations occur approximately up to 450°C. Different duration experiments in a closed system showed the great impact of exposure time on the organic matter microstructure: evolution of organic porosity continuous at a constant temperature with the organic matter transformation. The conversion of kerogen into hydrocarbons continues until the generative part is depleted. Further replacement of the non-generative part of kerogen (coke) can take place during oxidation. The burning of coke leads to a complete replacement of organic matter. All the space occupied by OM may be considered as pore space. These processes are described by the following formula.

$$V_{initial\ OM} + V_{OM\ porosity} = V_{residual\ OM} + V_{OM\ porosity\ 1} = V_{MM\ porosity}$$

Initial state — Thermal impact in inert conditions — Oxidation

where:
- $V_{initial\ OM}$ – volume of organic matter in a shale before the treatment
- $V_{OM\ porosity}$ – volume of pore space in organic matter. $V_{OM\ porosity}$ is close to 0 for non-matured shales, however exceptions are possible due to presence of primary porosity.
- $V_{residual\ OM}$ – residual volume of organic matter after the thermal impact at inert conditions ($V_{residual\ OM} < V_{initial\ OM}$).
- $V_{OM\ porosity\ 1}$ – volume of pore space in organic matter after the thermal impact at inert conditions ($V_{OM\ porosity\ 1} > V_{OM\ porosity}$)
- $V_{MM\ porosity}$ – volume of pore space formed instead of oxidized organic matter.

The volume of organic porosity may be considered as a function of temperature, time, and probably pressure – these aspects of future studies. Using the equation, it is possible to estimate the effectiveness of the pore space formation due to organic matter transformation (V_{OM}) on a well scale using porosity coefficient $k = \frac{V_{OM}}{V_{rock}}$, which implies that $V_{OM} = kV_{rock}$. V_{rock} might be calculated simply from thickness and area.

At temperatures above 400-450°C, alterations of mineral matrix begin. The absolute majority of alterations are accompanied by changes in a void space. The conceptual scheme in Figure 6.3.1 encompasses all the main alterations in shales, Table 6.3.1 provides a short description of key processes that influence pore space. All the alterations are classified by the influence on the porosity into favorable, not favorable, and those processes that can play dual role depending on the mineral's composition of a rock. There are numerous lithotypes distinguished in the BF by many researchers [20], only the main characteristics of the mineral composition are determined, which will serve as a basis for the reasonable lithotype selection for the high-temperature treatment (Figure 6.3.1). The lithotypes enriched by pyrite with low carbonate composition should be avoided for high-temperature treatment because pyrite is a source of sulfur, which contaminates hydrocarbons and has a damaging effect on the equipment. The lithotypes with low OM content and absence of initial porosity are also not suitable for the technology implication. Dolomite-rich shales should be carefully analyzed before participation in the high-temperature treatment due to the dolomite decomposition and decreasing of void space, especially in the case of pyrite presence and low porosity. The lithotypes are favorable for the high-temperature treatment and characterized by high OM content (TOC>5%), with small amount or absence of pyrite (in case of high pyrite content, presence carbonates are needed, which will serve as a buffer for sulfur). Mixed illite and calcite lithotypes will have the largest increase in porosity due to the transformation of

illite and quartz into wollastonite. Whereas illite rich, or quartz rich lithotypes are characterized by the formation of elongated voids or microfractures. Quartz dominated (radiolarites) shale lithotypes with initial high porosity (up to 15%) should be used as a local conventional reservoir for hydrocarbon accumulation during thermal technologies application due to its rock fabric stability.

Four lithotypes in the study are divided into 2 groups according to porosity, organic matter content, and rock fabric. The first group includes lithotypes 1 and 2, which are characterized by relatively high initial porosity (up to 15%) and low content of OM (TOC<3%). The second group is represented by lithotypes 3 and 4. The lithotypes are characterized by low initial porosity (<1%) and high organic matter content (TOC>10%). Two groups differ in the pore space evolution process (Figure 6.3.2) by the relative rock component contribution to porosity. There is a common pathway of void space formation during thermal impact. The first stages of the thermal impact (300-450°C) involve organic matter (generative part of kerogen) transformation into hydrocarbons with the organic porosity development. Non-generative part of kerogen is removed ("burnt") in case of oxidative atmosphere. The oxidation leads to the formation of porosity in the space initially occupied by organic matter (or coke (non-generative part of kerogen) if the oxidation follows inert impact). Further temperature increase results in sequential mineral matrix transformations, which are generally associated with porosity increase. Group 1 is characterized by a slight increase of porosity due to the transformation of both organic matter and mineral matrix. Group 2 shows porosity increase mainly due to the organic matter transformation at the initial stages, and mineral matrix related porosity development at temperatures above 400-450°C. The conceptual schemes of porosity evolution for the two groups are shown in Figure 6.3.2. This is a first approximation of relationship between evolution of pore space within different lithotypes, mineral composition, organic matter content, and initial porosity. Detailed correlations should be constructed on the basis of quantitative data obtained by high resolution techniques such as BIB-SEM and FIB-SEM, which is a matter of future research. Mineral matrix transformations can be critical for many aspects of high-temperature treatment application in the case of particular mineral composition (Figure 6.3.1, Table 6.3.1).

All the documented alterations significantly influence the physical properties of shales. It is shown that thermal conductivity was reduced up to 70%, which is crucial for the thermal based EOR methods planning and application. Ignoring such a great reduction of thermal conductivity might lead to dramatic errors in modeling of EOR modeling, especially concerned with high temperatures, such as high-pressure air injection, in-situ combustion, and others. On the other hand, changes in thermal properties may be used as an express method for alteration degree assessment.

Alterations of the mineral matrix also resulted in the isotope composition of some chemical elements, it was shown in the example of sulfur. This effect might be used for robust monitoring of high-temperature based technologies.

Table 6.3.1. Short description of alterations accompanied with pore space during high-temperature treatment demonstrated in Figure 6.3.1.

Component/Process	Effect
Illite transformations	Void space increase due to the formation of elongated pores and microfractures. Illite turns into wollastonite in the presence of carbonates.
Quartz transformations	Destruction of grain contacts does not lead to significant alterations in pore space. However, the mechanical properties of rock may be influenced by the transformations (weakening the rock which is good for further fracturing).
Dolomite decomposition	The process leads to the formation of MgO, which increases the complexity of void space filling existing pore space and increasing specific surface area. Not favorable.
Calcite decomposition	Calcite decomposes into CO_2 and CaO, CaO helps to retain the sulfur formed from pyrite in the rock preventing its combining with HC and equipment. However, calcite decomposition leads to the increase of pore space complexity and the formation of a number of new minerals with Ca.
Pyrite decomposition	Process results in the formation of different sulfur compounds (SO_2, SO_3, S_2), which has a very negative effect on hydrocarbons quality and the equipment.
Feldspar transformations	No significant chemical alterations. Melting and other transformation resulted in additional pore space. Positive effect on pore space.
New minerals formation	Anhydrite Anhydrite is a result of calcite and pyrite decomposition products interaction, and, at the same time it is a result of sulfur retention. Retention of sulfur prevents contamination of hydrocarbons and damaging of equipment. However, anhydrite significantly increase complexity of the pore space.

	Wollastonite Wollastonite aggregates form very porous chemically stable media. It is the result of illite and calcite decomposition. Positive effect on porosity. MgS, CaS, BaS Fill existing pore space, negative effect on pore space.
Transformations of organic matter	Development of organic porosity during thermal impact. Pyrolysis of kerogen leads to the formation of pore space in kerogen. Oxidation results in a replacement of the organic matter (including the non-generative part of kerogen) and the formation of pore space.

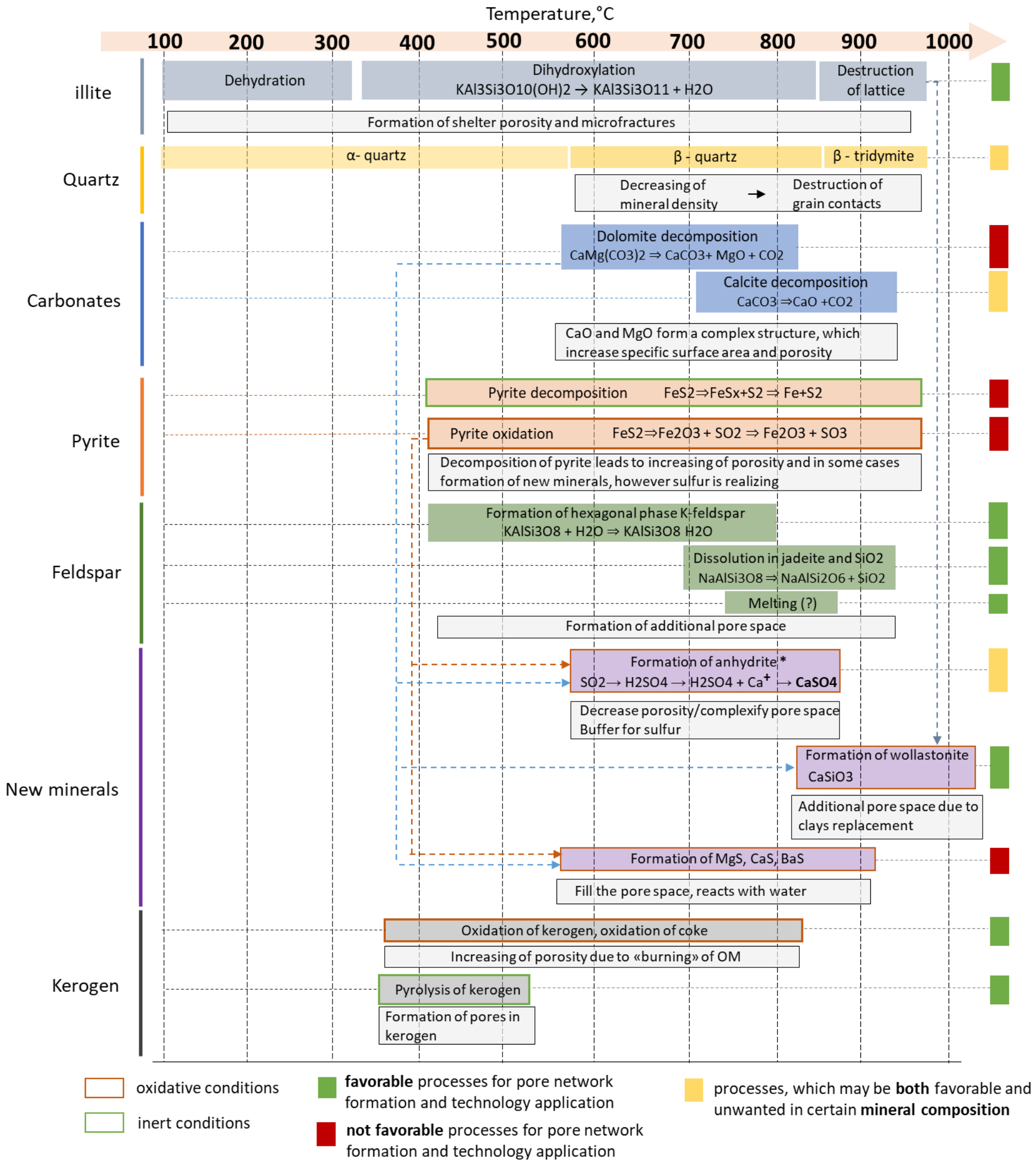

Figure 6.3.1. Conceptual scheme of alterations in shales during high-temperature treatment. Description is given in Table 6.3.1.

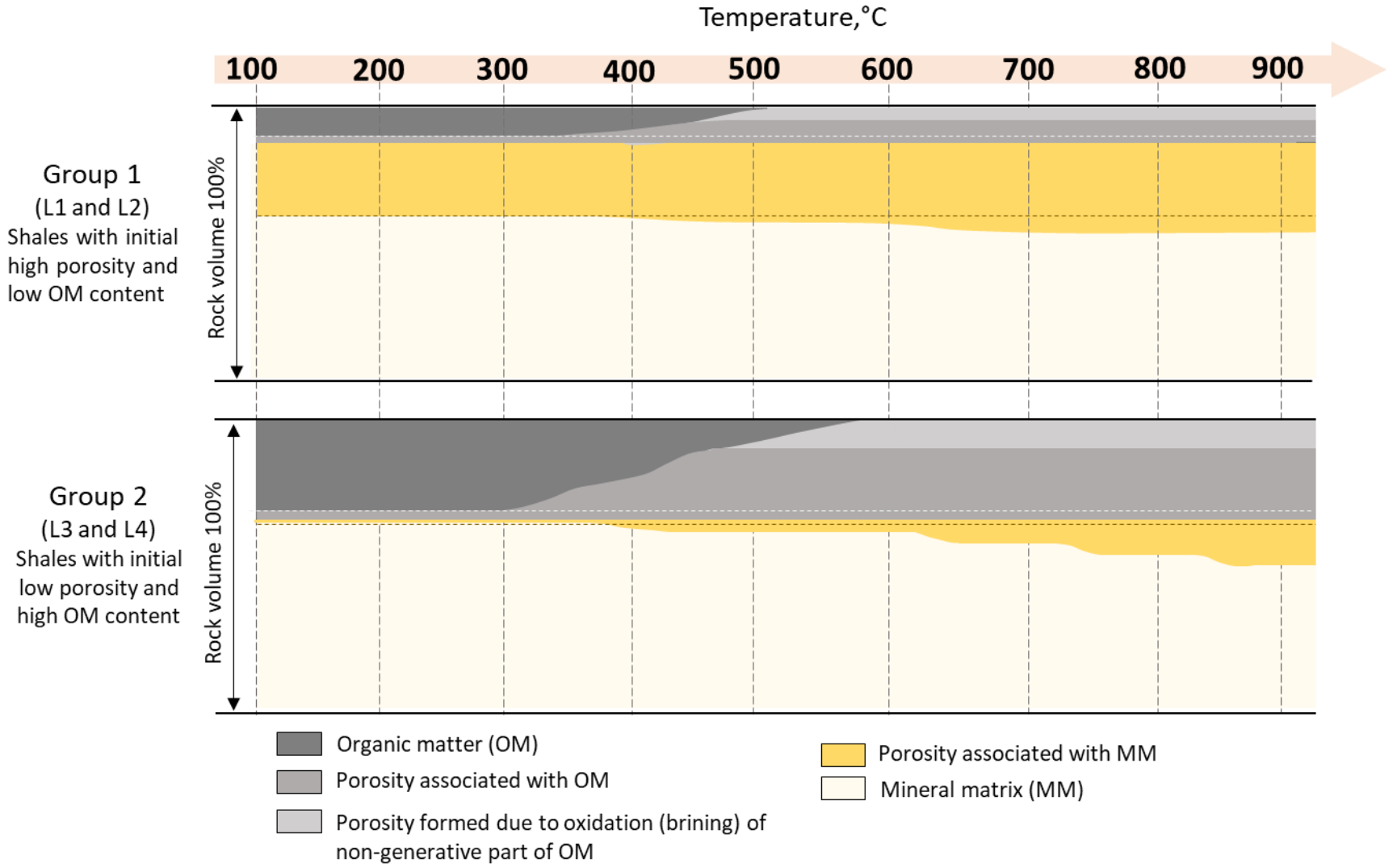

Figure 6.3.2. Conceptual schemes of pore space evolution in two groups of lithotypes during high-temperature treatment. Group 1 is characterized by only slight increase of porosity due to both OM and MM transformations, group 2 is characterized by increasing of porosity due to OM transformations and further MM transformations. The degree and the volume of porosity in MM depends on the mineral composition.

6.4. Summary

Mineral matrix alterations during the high-temperature treatment

High-temperature treatment exposed mineral matrix to the significant chemical and mineralogical alterations accompanied by microstructural transformations. The changes have affected every component of the BF shales. Fundamental processes behind observed alterations have been analyzed and summarized in the conceptual schemes of shale alterations.

Siliceous component (Quartz). Reversible transformations of α-quartz to β -quartz (573°C), β-tridymite (870°C). The process is accompanied by gradual density reduction.

Carbonate minerals (calcite, dolomite). Decomposition of calcite and dolomite occurs at the temperatures of ~570°C and ~700°C respectively with the formation of CaO and MgO. CaO serves as a material for the formation of new minerals (anhydrite, wollastonite, and other minor compounds such as CaS).

Clay minerals (illite). The thermal treatment leads to dehydration (until 320°C) with the following dihydroxylation and with the formation of elongated voids and microfractures. Approximately after 840°C destruction of lattice starts with the formation of additional pore space and new minerals (wollastonite, mullite).

Pyrite. The high-temperature impact causes pyrite decomposition accompanied by significant microstructural alterations. Inert atmosphere involves removing sulfur from pyrite (FeS_2) with the formation of S_2 (gas) and pyrrhotite (FeS_x). Oxidation provokes a series of complex processes. Which results in the formation of hematite (Fe_2O_3) and a series of sulfur compounds (SO_2, SO_3, and S_2). Sulfur can have serious negative effects on hydrocarbon quality and equipment. However, CaO retains sulfur with by the anhydrite ($CaSO_4$) precipitation.

Feldspar. Feldspar (solid solutions between K-feldspar (KAlSi3O8) and albite (NaAlSi3O8)) has porous microstructure after the experiment. It suggested that the porous structure is caused by the formation of hexagonal phase KAlSi3O8 H_2O, sodium feldspar transformation into an assemblage of jadeite and quartz and melting.

Organic matter transformation during thermal maturation

Organic porosity in the Bazhenov Formation shales is closely related to the thermal maturation level. Thermal maturation is a crucial factor behind secondary organic pore development. The first single pores start to form in the middle of the oil window. At the end of the oil window, the majority of organic particles are porous and form an effective pore space network. There are certain types of organic pores in immature Bazhenov Formation rocks, which are the result of primary processes such as sedimentation. However, these pores are quite rare and do not tend to form an effective pore space. Rock fabric plays a vital role in organic pore development

and preservation. We suggest that mudrocks with an interlayering of mineral components and elongated particles/lenticulars of organic matter do not tend to preserve organic porosity. The reason is load-bearing organic matter without grain support affected compaction during burial. Whereas mudrocks with organic inclusions (lenses, patchy distribution), non-load-bearing with grain support, have a good chance to preserve both primary and secondary porosity.

The artificial thermal maturation experiment confirmed that maturity is the crucial factor for organic porosity development. Thermal treatment of organic-rich shales to the temperatures when kerogen transforms to hydrocarbons may lead to the formation or further development of organic porosity. The development of organic porosity continues until the kerogen generative part is depleted. Further replacement of the non-generative part of kerogen (coke) may take place during oxidation. The burning of coke leads to a complete replacement of organic matter. All the space occupied by OM may be considered as pore space. The volume of organic porosity may be considered as a function of temperature, time, and probably pressure – these aspects of future studies.

Pore space evolution and organic matter transformation during high-temperature treatment

Conceptual schemes of the shale alteration and pore space evolution were proposed. The schemes encompass all the chemical and accompanied microstructural alterations for key shale components. The evolution of pore space varies in different lithotypes depending on mineral composition, organic matter content, and initial porosity. However, there is a common evolution pathway for all lithotypes: transformation starts with an organic matter porosity formation and development; after the organic matter is almost converted, alterations of mineral matrix take place.

Lithotypes, which are not suitable for high-temperature treatment: shales enriched by pyrite and low carbonates composition should be avoided for high-temperature treatment (pyrite is a source of sulfur, which contaminates hydrocarbons and has a damaging effect on equipment). The lithotypes with low OM content and absence of initial porosity also should be avoided. Dolomite-rich mudstones should be carefully analyzed before technology implication: dolomite decomposition leads to the void space decreasing, especially in pyrite presence and low porosity. The lithotypes, which are favorable for the high-temperature treatment: high OM content (TOC>5%), absence, or a small amount of pyrite (in case of high pyrite content, presence carbonates are needed, which will serve as a buffer for sulfur). Mixed illite and calcite lithotypes have the largest increase of porosity after the treatment due to illite and silica transformation into wollastonite. Mono-mineralogical illite or quartz dominated lithotypes are relatively stable and might be recommended for the technology implication. Quartz dominated lithotypes with initial high porosity (>5%) can be used as a conventional local reservoir for hydrocarbon accumulation due to its rock fabric stability.

Chapter 7. Summary, conclusions and recommendations

In the thesis systematic study of void space evolution and organic matter microstructural transformation during high-temperature treatment has been performed on the example of Bazhenov Formation shales. The study is based on a series of laboratory high-temperature experiments and complex analysis with a set of advanced lithological, geochemical, and petrophysical methods. The first step was a reasonable selection of lithotypes for the experiments. The four lithotypes, which encompass major mineral component variations in the Bazhenov Formation shales, were selected on the basis of detailed lithological studies (siliceous mudstone, aporadiolarian siliceous dolomite, argillaceous-siliceous organic-rich mudstone, and calcareous-argillaceous organic-rich mudstone). A new approach of kerogen thermal properties determination on rock cuttings was developed and patented during investigations. The approach is based on the thermal property profiling technique, it made possible continuous TOC determination in shales on the core. The central experiment of the study is an *in-situ* high-pressure air injection laboratory experiment in a combustion tube. The experiment aided to analyze the alterations of shales at different positions of the combustion front: behind, ahead, and approximately at the combustion front (temperature range was 107-841°C). All the samples were studied by a complex of lithological, geochemical, and petrophysical methods. As a result, numerous alterations related to the mineral matrix and organic matter were revealed. Micro-combustion front was observed and introduced in the subsample, packed in the area near the combustion front. Since organic matter is very sensitive to thermal treatment, its microstructural transformations were investigated in a series of special experiments, which include treatment in open and closed systems. The experiments showed crucial role of thermal maturity in organic porosity evolution. The detailed study of organic matter made possible to classify organic pores according to their genesis and structural features. Essential factors for organic pore space evolution and preservation were revealed. A special part of the thesis is devoted to the analysis of all the alterations and processes during high-temperature treatment in organic-rich shales. A comprehensive analysis helped to construct a complex conceptual scheme of shale components alterations and pore space evolution for different lithotypes and provide recommendations.

The outcomes of the study imply a prediction accuracy increase of high-temperature based technology simulations and technologies application efficiency enhancement due to providing the whole complex shale alterations associated with high-temperature treatment (pore space evolution, chemical reactions, thermal conductivity changing). The results make possibel to reasonably choose the most appropriate intervals/lithotypes for technology application. Understanding the full range of chemical processes associated with mineral matrix will facilitate the correct equipment material choice for both agent injection and hydrocarbons extraction. The observed effects in the

mineral matrix might be used for control and monitoring of the high-temperature treatment processes in shales. Moreover, the results of the PhD study might be applicable in numerous high-temperature procedures associated with non-shales rock treatments such as in-situ combustion procedures in conventional or heavy oil carbonate/clastic reservoirs, which implies similar technology in similar condition. Other areas where results might be useful are nuclear waste storage, geothermal energy and deep resource extraction, and underground coal gasification. We believe that the obtained knowledge brings the creation an effective technology for effective hydrocarbon recovery technology from organic-rich shales closer.

The main conclusions of the study are given below.

1. Mineral matrix of Bazhenov Formation shales significantly alters during high-temperature treatment. Each component of the mineral matrix undergoes chemical and physical changes. The key alterations for the main shale mineral components are given below.

- *Siliceous component (Quartz).* Reversible transformations of α-quartz to β -quartz (573°C), β-tridymite (870°C). The process is accompanied by gradual density reduction.
- *Carbonate minerals (calcite, dolomite).* Complete decomposition of dolomite into MgO and calcite with further partial decomposition into CaO (~570°C and ~700°C respectively). The formation of CaO led to the precipitation of new minerals (anhydrite, wollastonite, and other minor compounds such as CaS).
- *Clay minerals (illite).* Dehydration (until 320°C) with the following dihydroxylation with the formation of voids and microfractures. Destruction of lattice (after 840°C) starts with the formation of additional pore space and new minerals (wollastonite, mullite).
- *Pyrite.* Decomposition of pyrite (from ~400°C). Inert atmosphere: removing sulfur from pyrite (FeS_2) with the formation of S_2 (gas) and pyrrhotite (FeS_x). Oxidative atmosphere: a series of complex processes, which resulted in the formation of hematite (Fe_2O_3) and sulfur compounds (SO_2, SO_3, and S_2). The sulfur can have had a serious negative effect on hydrocarbon quality and equipment. However, CaO retained sulfur with the anhydrite ($CaSO_4$) precipitation.
- *Feldspar.* Formation of the porous structure. The porous structure was caused by three interconnected processes: formation of hexagonal phase $KAlSi_3O_8$ H_2O, sodium feldspar transformation into an assemblage of jadeite, and quartz, and melting.

The knowledge about mineral matrix alterations should serve as a basis for lithotype/interval selection during high-temperature EOR technology implications in shales.

2. Alterations of mineral matrix reflected into isotope ratio of specific chemical elements. The effect was shown with the sulfur and carbon example: isotope composition of sulfur and carbon had been shifted towards heavier isotopes (carbon: ≈5-12% sulfur: ≈8-18%).

The established effect makes this method a promising tool for monitoring high temperature EOR applications.

3. Microstructure of solid organic matter (kerogen) of Bazhenov Formation shales continuously transforms during natural thermal maturation and high-temperature treatment. The transformation starts with the formation of bubble-like structures, which further evolve into organic pores. The key conclusions regarding the organic matter are given below.

- Kerogen porosity in the Bazhenov Formation shales is closely related to the thermal maturation degree. Thermal maturation is a key aspect of organic pore development. The role of thermal maturation is confirmed by the observation of the samples across natural maturation levels variations and by artificial thermal maturation experiments.
- Organic pores are preceded by nano-bubble microstructure formation. The first single pores start to form within the middle of the oil window. At the end of the oil window, the majority of organic particles are porous and form an effective pore space network.
- Organic pores in Bazhenov Formation shales differ in their geometry, shape, abundance, and relationship with the organic matter, which reflect their genesis. The proposed classification of organic pores makes possible effectively distinguish the genesis of the organic porosity and its perspectivity in terms of shale reservoir properties. Organic pores in Bazhenov Formation are classified according to the genesis into primary (sedimentation related) and secondary (thermal maturation related) pores. Further division implies structural features. Primary pores are represented by inherited and convoluted pores. Secondary pores are spongy, shrinkage, and mixed pores.
- Rock fabric plays a vital role in organic pore development and preservation. It is shown that those organic-rich shales, which are characterized by interlayering of mineral components and organic matter lenticulars do not tend to preserve organic porosity. Whereas shales with patchy distributed organic matter (inclusions, lenses) demonstrate good preservation of both primary and secondary porosity.
- High-temperature treatment leads to the porosity formation in kerogen. Inert atmosphere treatment produces porosity until the generative part of kerogen is converted. The further oxidation leads to the burning of kerogen non-generative parts and the formation of pore space, which is equal to the initial OM volume.
- Treatment time (duration) plays an important role in organic porosity development. Increasing a treatment duration at a specific temperature (>350) leads to the development of organic porosity.

Microstructural transformations in organic matter during high-temperature treatment have two aspects. The first one is related to the hydrocarbons generation from the kerogen and their first

migration, it is the fundamental side of the question. The second one is practical, which is related to the pore space formation during thermal EOR technology application. The porosity change in organic matter during the treatment should be considered during EOR processes simulations, planning and interval selection.

4. Pore space of Bazhenov Formation shales continuously evolves during high-temperature treatment, which is caused by mineral matrix alterations and organic matter transformations. The pore space evolution differs in the different lithotypes.

- The evolution of pore space varies within different lithotypes depending on mineral composition, organic matter content, and initial porosity. However, there are common evolution pathways for all lithotypes: transformation starts with an organic matter transformation (organic porosity development) with minor mineral matrix engagement (<350-450°C). After the organic matter is almost converted (>350-450°C), alterations of mineral the matrix take place.
- The highest porosity increase (up to 4% total porosity) after the combustion front propagation (841°C) is in the high initial organic matter content (TOC>5%) lithotypes.
- The lithotypes with relatively low organic-matter content (TOC<5%) are characterized by minor porosity increase (<1%) after combustion front propagation (841°C).

The quantitative data was obtained with the micro-CT method, which is limited in spatial resolution by 2 μm. The results should be considered as a minimum increase of porosity because SEM showed an abundance of pores with a size of <2 μm in all samples. SEM showed, that the largest pores are formed after the organic matter replacement, whereas pores resulting from the mineral matrix transformation are small (<2 μm).)

- Organic matter transformation (conversion ~99%) in the inert atmosphere leads to the porosity increase, which is equal to the value of the generative part of kerogen. Whereas, porosity increase after the oxidation (removing the non-generative part of kerogen) is equal to the initial organic matter volume.

The evolution of pore space both in the mineral matrix and organic matter during high-temperature treatment is a crucial process for the fluid flow, which in turn determines hydrocarbons production. This evolution is closely related to lithology. Results must be considered during EOR processes simulations, planning and interval/lithotypes selection.

5. One more significant result of the study is connected to the thermal conductivity after the combustion front propagation. Rock thermal conductivity reduction was 70% in the lithotypes with high organic matter content. The reduction occurred due to the destruction of grain contacts, replacement of organic matter by void space and decomposition of minerals. No thermal

conductivity reduction was observed for the lithotypes lean in organic matter, which is a result of absence of significant alterations in the mineral matrix due to quartz stability.

Thermal conductivity decrease is crucial for the preparation and application of EOR techniques in shales. Ignoring such a great thermal conductivity reduction can lead to dramatic errors in EOR modeling, especially related to heat mass transfer simulations, such as high-pressure air injection, in-situ combustion, and others.

Recommendations

The recommendations for the technology implications have been developed for different lithotypes. The lithotypes features, which are favorable for the high-temperature treatment: high OM content (TOC>5%), absence, or a small amount of pyrite (in case of high pyrite content, carbonates presence is needed, which will serve as a buffer for sulfur). Mixed illite and calcite lithotypes have the largest porosity increase after the treatment due to illite and silica transformation into wollastonite. Dolomite-rich mudstones should be carefully analyzed before technology implication: dolomite decomposition leads to the void space decreasing, especially in pyrite presence and low porosity. Lithotypes, which are not suitable for high-temperature treatment: shales enriched by pyrite and low carbonates composition should be avoided for high-temperature treatment (pyrite is a source of sulfur, which contaminates hydrocarbons and has a damaging effect on equipment), or lower temperatures should be used (<400°C) excluding pyrite decomposition. The lithotypes with low OM content and absence of initial porosity also should be avoided. Mono-mineralogical illite or quartz dominated lithotypes are relatively stable and might be recommended for the technology implication. Quartz dominated lithotypes with initial high porosity (>5%) can be used as a conventional local reservoir for hydrocarbon accumulation due to their rock fabric stability.

Also, the obtained results are recommended to use for thermal EOR simulation and sensitivity studies. The changing porosity and thermal conductivity in the mineral matrix and OM potentially will significantly influence the results of the simulations.

Bibliography

[1] IEA. World Energy Outlook 2019. 2019.

[2] Ahmed U, Meehan DN. Unconventional Oil and Gas Resources. CRC Press; 2016. https://doi.org/10.1201/b20059.

[3] Taciuk W. Does oil shale have a significant future? Oil Shale 2013;30:1–5. https://doi.org/10.3176/oil.2013.1.01.

[4] Statistics I. Technically Recoverable Shale Oil and Shale Gas Resources : An Assessment of 137 Shale Formations in 41 Countries Outside the United States. vol. 2013. 2013.

[5] Sun Y-H, Bai F-T, Lü X-S, Li Q, Liu Y-M, Guo M-Y, et al. A Novel Energy-Efficient Pyrolysis Process: Self-pyrolysis of Oil Shale Triggered by Topochemical Heat in a Horizontal Fixed Bed. Sci Rep 2015;5. https://doi.org/10.1038/srep08290.

[6] Yakovleva-Ustinova T. Russian companies investing more in shale projects. Oil Gas JournalRussia 2014;June/July.

[7] Tiwari P, Deo M, Lin CL, Miller JD. Characterization of oil shale pore structure before and after pyrolysis by using X-ray micro CT. Fuel 2013;107:547–54. https://doi.org/10.1016/j.fuel.2013.01.006.

[8] Zou C, Zhai G, Zhang G, Wang H, Zhang G, Li J, et al. Formation, distribution, potential and prediction of global conventional and unconventional hydrocarbon resources. Pet Explor Dev 2015;42:14–28. https://doi.org/10.1016/S1876-3804(15)60002-7.

[9] Speight JG. Shale Oil Production Processes. 2012. https://doi.org/10.1016/C2012-0-00597-2.

[10] Kar T, Hascakir B. In-situ kerogen extraction via combustion and pyrolysis. J Pet Sci Eng 2017;154:502–12. https://doi.org/10.1016/j.petrol.2017.01.051.

[11] Saif T, Lin Q, Bijeljic B, Blunt MJ. Microstructural imaging and characterization of oil shale before and after pyrolysis. Fuel 2017;197:562–74. https://doi.org/10.1016/J.FUEL.2017.02.030.

[12] Saif T, Lin Q, Gao Y, Al-Khulaifi Y, Marone F, Hollis D, et al. 4D in situ synchrotron X-ray tomographic microscopy and laser-based heating study of oil shale pyrolysis. Appl Energy 2019;235:1468–75. https://doi.org/10.1016/j.apenergy.2018.11.044.

[13] Saif T, Lin Q, Butcher AR, Bijeljic B, Blunt MJ. Multi-scale multi-dimensional microstructure imaging of oil shale pyrolysis using X-ray micro-tomography, automated ultra-high resolution SEM, MAPS Mineralogy and FIB-SEM. Appl Energy 2017;202:628–47. https://doi.org/10.1016/j.apenergy.2017.05.039.

[14] Saif T, Lin Q, Singh K, Bijeljic B, Blunt MJ. Dynamic imaging of oil shale pyrolysis using synchrotron X-ray microtomography. Geophys Res Lett 2016;43:6799–807. https://doi.org/10.1002/2016GL069279.

[15] Kobchenko M, Panahi H, Renard F, Dysthe DK, Malthe-Srenssen A, Mazzini A, et al. 4D imaging of fracturing in organic-rich shales during heating. J Geophys Res Solid Earth 2011;116. https://doi.org/10.1029/2011JB008565.

[16] Panahi H, Kobchenko M, Renard F, Mazzini A, Scheibert J, Dysthe D, et al. A 4D synchrotron x-ray-tomography study of the formation of hydrocarbon-migration pathways in heated organic-rich shale. SPE J 2013;18:366–77. https://doi.org/10.2118/162939-PA.

[17] Henderson J. Tight Oil Developments in Russia October 2013. Wpm52 2013.

[18] Ulmishek GF. Petroleum Geology and Resources of the West Siberian Basin, Russia. 2003. https://doi.org/https://doi.org/10.3133/b2201G.

[19] EIA. World Shale Resource Assessments. Eia 2015:1. http://www.eia.gov/analysis/studies/worldshalegas/.

[20] Kontorovich AE, Yan PA, Zamirailova AG, Kostyreva EA, Eder VG. Classification of rocks of the Bazhenov Formation. Russ Geol Geophys 2016;57:1606–12. https://doi.org/10.1016/j.rgg.2016.10.006.

[21] Lazar OR, Bohacs KM, Macquaker JHS, Schieber J, Demko TM. Capturing key attributes of fine-grained sedimentary rocks in outcrops, cores, and thin sections: Nomenclature and description guidelines. J Sediment Res 2015;85:230–46. https://doi.org/10.2110/jsr.2015.11.

[22] Kontorovich AE, Moskvin VI, Bostrikov OI, Danilova VP, Fomin AN, Fomichev AS, et al. Main oil source formations of the West Siberian Basin. Pet Geosci 1997;3:343–58. https://doi.org/10.1144/petgeo.3.4.343.

[23] Kontorovich AE, Ponomareva E V., Burshtein LM, Glinskikh VN, Kim NS, Kostyreva EA, et al. Distribution of organic matter in rocks of the Bazhenov horizon (West Siberia). Russ Geol Geophys 2018;59:285–98. https://doi.org/10.1016/j.rgg.2018.03.007.

[24] Topchii MS, Pronina N V., Kalmykov AG, Kalmykov GA, Fomina MM, Karpov YA, et al. The Distribution of Organic Matter in the Rocks of the Bazhenov High-Carbon Formation. Moscow Univ Geol Bull 2019;74:274–84. https://doi.org/10.3103/S0145875219030128.

[25] Kozlova E V., Bulatov TD, Leushina EA, Spasennykh MY, Gutman IS, Potemkin GN, et al. Estimation of the organic matter maturity level in the Bazhenov formation deposits. GEOMODEL 2019 - 21st Conf. Oil Gas Geol. Explor. Dev., 2019. https://doi.org/10.3997/2214-4609.201950155.

[26] Aleksin GA, Durdiev ZZ, Rostovtsev VN. Oil and gas potential of Jurassic rocks of the Yamal and Gydan Peninsulas. Geol Neft i Gaza 1983;2:1– 6.

[27] Panchenko I, Nemova VD, Smirnova ME, Ilyina MV, Baraboshkin EY, Ilyin VS. Stratification and detailed correlation of Bazhenov horizon in the central part of the Western Siberia according to lithological and paleontological core analysis and well logging. Oil Gas Geol 2016:22–34.

[28] Decision of the 6th interdepartmental stratigraphic meeting on consideration and adoption of refined stratigraphic schemes Mesozoic deposits of western Siberia. 2004.

[29] Zonenshayn LP, Kuzmin MI, Natapov LM. Tectonics of lithospheric plates of the USSR (Tektonika litosfernykh plit territorii SSSR). 1990.

[30] Kontorovich AE, Peters KE, Moldowan JM, Andrusevich VE, Demaison GJ. Hydrocarbon biomarkers in oils of the Middle Ob region. Geol i Geofiz 1991;32:3–34.

[31] Ryabukhin GE, Zinin VA. Petroleum potential of Triassic rocks of the Russian Arctic shelf. Geol Neft i Gaza 1992;12:2–5.

[32] Surkov VS. Riftogenesis and petroleum basins of Siberia. Geol Neft i Gaza 1998:33–6.

[33] Vyshemirsky VS. Bazhenov Horizon of West Siberia (Bazhenovskiy gorizont Zapadnoy Sibiri). Novosibirsk: 1986.

[34] Rudkevich MY, Ozeranskaya LS, Chistyakova NF, Kornev VA, Maksimov EM. Petroleum-productive complexes of the West Siberian basin (Neftegazonosnye kompleksy Zapadno-Sibirskogo basseyna). Moscow: Nedra; n.d.

[35] Surkov VS, Smirnov LV. Cenozoic tectonic events and phase differentiation of hydrocarbons in the Hauterivian–Cenomanian complex of the West Siberian basin. Geol Neft i Gaza 1994:3–6.

[36] Melnikova EG. Structural and genetic factors to form the Bovanenkovo deposit (West Siberia). Moscow Univ Geol Bull 1992;47:77–9.

[37] Postnikov A V., Gutman IS, Postnikova O V., Olenova KY, Khasanov II, Kuznetsov AS, et al. Different-scale investigations of geological heterogeneity of Bazhenov formation in terms of hydrocarbon potential evaluation. Neft Khozyaystvo - Oil Ind 2017:8–11. https://doi.org/10.24887/0028-2448-2017-3-8-11.

[38] Postnikov A V., Postnikova O V., Olenova KY, Sivalneva O V., Hasanov II, Osintseva NA, et al. New methodological aspects of lithological research of rocks Bazhenov formation. Neft Khozyaystvo - Oil Ind 2015:23–7.

[39] Nemova VD. Multi-level lithological typization of rocks of the Bazhenov formation. Neft Khozyaystvo - Oil Ind 2019;2019:13–7. https://doi.org/10.24887/0028-2448-2019-8-13-17.

[40] Gavrilov AE, Zhukovskaya EA, Tugarova MA, Ostapchuk MA. Objective Bazhenov rocks classification (the case of the Western Siberia central part fields). Neft Khozyaystvo - Oil Ind 2015:38–40.

[41] Eder VG. Application of cluster analysis to distinguish the types of Bazhenov Formation rocks according to the content of main rock-forming oxides (Primenenie klasternogo analiza dlya vydeleniya tipov porod bazhenovskoj svity po soderzhaniyu osnovnyh porodoobrazuy. Geokhimiya 2002:233–8.

[42] Kozlova EV, Bogdanovich NN, Stenin VP, Leushina EA, Karamov TI, Bulatov TD, et al. The organic matter in subsalt deposits from the Astrakhan arch: Analysis of molecular composition and assessment of the residual oil generation potential | Оценка остаточного нефтегенерационного потенциала и состав битумоидов подсолевых отложений Астрахан. 3rd Int. Conf. Geol. Casp. Sea Adjac. Areas 2019, 2019.

[43] Spasennykh M, Maglevannaia P, Kozlova E, Bulatov T, Leushina E, Morozov N. Geochemical trends reflecting hydrocarbon generation, migration and accumulation in unconventional reservoirs based on pyrolysis data (On the example of the bazhenov formation). Geosci 2021;11. https://doi.org/10.3390/geosciences11080307.

[44] Loucks RG, Reed RM. Scanning-electron-microscope petrographic evidence for distinguishing organic-matter pores associated with depositional organic matter versus migrated organic matter in mudrocks. GCAGS J 2014;3:51–60.

[45] Nemova VD, Pogodaeva AM, Kim OO, Matyukhina TA. Petrophysical characteristics of the Late Jurassic - Early Cretaceous productive levels of the Sredne-Nazym field. Neftegazov Geol Teor I Prakt 2020;15. https://doi.org/10.17353/2070-5379/12_2020.

[46] Chen W, Lei Y, Ma L, Yang L. Experimental Study of High Temperature Combustion for Enhanced Shale Gas Recovery. Energy and Fuels 2017;31:10003–10. https://doi.org/10.1021/acs.energyfuels.7b00762.

[47] Chapiro G, Bruining J. Combustion enhance recovery of shale gas. J Pet Sci Eng 2015;127:179–89. https://doi.org/10.1016/j.petrol.2015.01.036.

[48] Ross DJK, Marc Bustin R. The importance of shale composition and pore structure upon gas storage potential of shale gas reservoirs. Mar Pet Geol 2009;26:916–27. https://doi.org/10.1016/j.marpetgeo.2008.06.004.

[49] INTEK I. Profiles of companies engaged in domestic oil shale and tar sands resource and technology development. Secur Fuels from Domest Resour 2011.

[50] Symington WA, Kaminsky RD, Meurer WP, Otten GA, Thomas MM, Yeakel JD. ExxonMobil's Electrofrac^{TM} process for in situ oil shale conversion. ACS Symp Ser 2010;1032:185–216. https://doi.org/10.1021/bk-2010-1032.ch010.

[51] Symington WA, Burns JS, El-Raba AM, Otten GA, Pokutylowicz N, Spiecker PM, et al. Field Testing of Electrofrac Process Elements at ExxonMobil's Colony mine. 29th Oil Shale Symp 2009:13.

[52] Allix P, Bumham A, Fowler T, Herron M, Kleinberg R, Symington B. Coaxing Oil from Shale. Oilf Rev 2010;22:4–15.

[53] Pan Y, Xiao L, Chen C, Yang S. Development of Radio Frequency Heating Technology for Shale Oil Extraction. Open J Appl Sci 2012;02:66–9. https://doi.org/10.4236/ojapps.2012.22008.

[54] Fowler TD, Vinegar HJ. Oil shale ICP - Colorado field pilots. SPE West Reg Meet 2009 - Proc 2009:270–84. https://doi.org/10.2118/121164-ms.

[55] Crawford PM, Biglarbigi K, Dammer AR, Knaus E. Advances in world oil shale production technologies. Proc - SPE Annu Tech Conf Exhib 2008;6:4101–11. https://doi.org/10.2118/116570-ms.

[56] Environmental assessment. Chevron Oil Shale Research, Development & Demonstration. 2006.

[57] Darischev VI, Delia SV, Karpov VB, Shadchnev AN. RITEK - 25 Years of Innovation, Volume 2 2017:200.

[58] Kokorev VI, Darishchev VI, Akhmadeishin IA, Shchekoldin KA, Boksernam AA. The results of the field tests and prospects of termogas development of Bazhenov formation in OJSC RITEK. Soc Pet Eng - SPE Russ Oil Gas Explor Prod Tech Conf Exhib 2014, RO G 2014 - Sustain Optimising Prod Challenging Limits with Technol 2014;1:268–79. https://doi.org/10.2118/171172-ms.

[59] Moore RG, Mehta SA, Ursenbach MG. A Guide to High Pressure Air Injection (HPAI) Based Oil Recovery 2007. https://doi.org/10.2523/75207-ms.

[60] Johnson HR, Crawford PM, Bunger JW. Strategic Significance of America's Oil Shale Resource. Oil Shale Resour Technol Econ 2004;II:1–33.

[61] Somerton WH. Thermal properties and temperature-related behavior of rock/fluid systems. 1992. https://doi.org/10.1016/0377-0273(93)90059-z.

[62] Prats M, O'Brien SM. Thermal Conductivity and Diffusivity of Green River Oil Shales. JPT, J Pet Technol 1975;27:97–106. https://doi.org/10.2118/4884-PA.

[63] Tisot PR. Alterations in Structure and Physical Properties of Green River Oil Shale by Thermal Treatment. vol. 12. 1967. https://doi.org/10.1021/je60034a031.

[64] Zhao J, Yang D, Kang Z, Feng Z. A micro-CT study of changes in the internal structure of Daqing and Yan'an oil shales at high temperatures. Oil Shale 2012;29:357–67. https://doi.org/10.3176/oil.2012.4.06.

[65] Popov EY, Bondarenko TM, Dobrovolskaya SA, Kalmykov AG, Morozov N V., Erofeev AA. The potential of tertiary methods application for unconventional hydrocarbon systems exposure on the example of Bazhenov formation. Neft Khozyaystvo - Oil Ind 2017:54–7. https://doi.org/10.24887/0028-2448-2017-3-54-57.

[66] Bondarenko TM, Mukhametdinova AZ, Popov EY, Cheremisin AN, Kalmykov AG, Karpov IA. Analysis of changes in Bazhenov formation rock properties as a result of high-pressure air injection based on laboratory modelling data. Neft Khozyaystvo - Oil Ind 2017:40–4. https://doi.org/10.24887/0028-2448-2017-3-40-44.

[67] Mukhametdinova A, Mikhailova P, Kozlova E, Karamov T, Baluev A, Cheremisin A. Effect of thermal exposure on oil shale saturation and reservoir properties. Appl Sci 2020;10:1–24. https://doi.org/10.3390/app10249065.

[68] Chen Q, Kang Y, You L, Yang P, Zhang X, Cheng Q. Change in composition and pore structure of Longmaxi black shale during oxidative dissolution. Int J Coal Geol 2017;172:95–111. https://doi.org/10.1016/j.coal.2017.01.011.

[69] Chen W, Zhou Y, Yu W, Yang L. Experimental study of low-temperature shale combustion and pyrolysis under inert and noninert environments. SPE Prod Oper 2019;35:178–87. https://doi.org/10.2118/194507-PA.

[70] Sun Y, Bai F, Liu B, Liu Y, Guo M, Guo W, et al. Characterization of the oil shale products derived via topochemical reaction method. Fuel 2014;115:338–46. https://doi.org/10.1016/j.fuel.2013.07.029.

[71] Sun Y, Bai F, Liu B, Liu Y, Guo M, Guo W, et al. Characterization of the oil shale products derived via topochemical reaction method. Fuel 2014;115:338–46. https://doi.org/10.1016/J.FUEL.2013.07.029.

[72] Cavelan A, Boussafir M, Le Milbeau C, Laggoun-Défarge F. Impact of Oil-Prone Sedimentary Organic Matter Quality and Hydrocarbon Generation on Source Rock Porosity: Artificial Thermal Maturation Approach. ACS Omega 2020;5. https://doi.org/10.1021/acsomega.0c01432.

[73] Ko LT, Loucks RG, Zhang T, Ruppel SC, Shao D. Pore and pore network evolution of Upper Cretaceous Boquillas (Eagle Ford-equivalent) mudrocks: Results from gold tube pyrolysis experiments. Am Assoc Pet Geol Bull 2016;100:1693–722. https://doi.org/10.1306/04151615092.

[74] Wu S, Zhu R, Cui J, Cui J, Bai B, Zhang X, et al. Characteristics of lacustrine shale porosity evolution, Triassic Chang 7 Member, Ordos Basin, NW China. Pet Explor Dev 2015;42:185–95. https://doi.org/10.1016/S1876-3804(15)30005-7.

[75] Sun C, Ling S, Wu X, Li X, Chen J, Jiang W. Oxidation of black shale and its deterioration mechanism in the slip zone of the Xujiaping landslide in Sichuan Province, Southwestern China. Catena 2021;200. https://doi.org/10.1016/j.catena.2020.105139.

[76] Kaldas K, Preegel G, Muldma K, Lopp M. Wet air oxidation of oil shales: Kerogen dissolution and dicarboxylic acid formation. ACS Omega 2020;5:22021–30. https://doi.org/10.1021/acsomega.0c01466.

[77] Basu S, Verchovsky AB, Bogush A, Jones AP, Jourdan AL. Stability of Organic Carbon Components in Shale: Implications for Carbon Cycle. Front Earth Sci 2019;7. https://doi.org/10.3389/feart.2019.00297.

[78] Chen W, Zhou Y, Yang L, Zhao N, Lei Y. Experimental study of low-temperature combustion characteristics of shale rocks. Combust Flame 2018;194:285–95.

https://doi.org/10.1016/j.combustflame.2018.04.033.

[79] Khakimova L, Bondarenko T, Cheremisin A, Myasnikov A, Varfolomeev M. High pressure air injection kinetic model for Bazhenov Shale Formation based on a set of oxidation studies. J Pet Sci Eng 2019;172:1120–32. https://doi.org/10.1016/j.petrol.2018.09.021.

[80] Kislukhin IV. Peculiar features of geological structure and oil and gas presence of the Jurassic-Neocomian deposits of the Yamal Peninsula. Tymen: TyumGNGU; 2012.

[81] Skorobogatov VA, Stroganov LV. Gydan: geological structure, hydrocarbon resources, future. Moscow: Nedra-biznecscentr; 2006.

[82] Zakharov VA. Conditions of formation of the Volgian-Berriasian high-carbonaceous Bazhenov formation of West Siberia by data of paleoecology. Evolution of the biosphere and biodiversity. Evol Biosph Biodivers 2006;1:552–69.

[83] Zlobina ON, Rodchenko AP. Lithological-geochemical characteristic of the Golchikha formation in the section of the Payakhskaya-4 well (the Gydan facies region. North of Middle Siberia). Interexpo GEO-Siberia 2015.

[84] Nikitenko BL, Devyatov VP, Rodchenko AP. The Gol'chikha formation (Upper Bathonian-Lower Boreal berriasian) of the Yenisei-Khatanga depression (west of the North Siberian lowland). Geol i Geofiz 2020.

[85] Ryzhkova SV, Burshtein LM, Yershov SV, Kazanenkov EV. the Bazhenov Horizon of West Siberia: Structure, Correlation, and Thickness. Geol i Geofiz 2018:1053–74. https://doi.org/10.15372/gig20180709.

[86] Balushkina NS, Kalmykov GA, Khamidullin RA, Korost D V., Shyshkov V, Fadeeva NP. Secondary reservoirs of the Bazhenov and Abalak formations and the structure of the pore space. Search Discov 2014:1–26.

[87] Lazar OR, Schieber J, Macquaker JHS, Demko TM, Bohacs KM. Mudstone Primer: Lithofacies variations, diagnostic criteria, and sedimentologic–stratigraphic implications at lamina to bedset scale. SEPM Concepts Sedimentol Paleontol #12 2015:205.

[88] Espitalié J, Laporte JL, Madec M, Marquis F, Leplat P, Paulet J, et al. Méthode rapide de caractérisation des roches mètres, de leur potentiel pétrolier et de leur degré d'évolution. Rev l'Institut Français Du Pétrole 1977;32:23–42. https://doi.org/10.2516/ogst:1977002.

[89] Espitalie J, Deroo G, Marquis F. La pyrolyse Rock-Eval et ses applications. Rev - Inst Fr Du Pet 1985;40:563–79.

[90] Popov Y, Beardsmore G, Clauser C, Roy S. ISRM Suggested Methods for Determining Thermal Properties of Rocks from Laboratory Tests at Atmospheric Pressure. Rock Mech Rock Eng 2016;49:4179–207. https://doi.org/10.1007/s00603-016-1070-5.

[91] Popov E, Karamov T, Popov Y, Spasennykh M, Kozlova E. Method for determining total content of organic matter in rocks of shale strata enriched with hydrocarbons (versions), 2020.

[92] Kontorovich AE, Kontorovich VA, Ryzhkova S V., Shurygin BN, Vakulenko LG, Gaideburova EA, et al. Jurassic paleogeography of the West Siberian sedimentary basin. Russ Geol Geophys 2013;54:747–79. https://doi.org/10.1016/j.rgg.2013.07.002.

[93] Leushina E, Bulatov T, Kozlova E, Panchenko I, Voropaev A, Karamov T, et al. Upper jurassic–lower cretaceous source rocks in the north of western siberia: Comprehensive geochemical characterization and reconstruction of paleo-sedimentation conditions. Geosci 2021;11. https://doi.org/10.3390/geosciences11080320.

[94] Idrisova E, Gabitov R, Karamov T, Voropaev A, Liu MC, Bogdanovich N, et al. Pyrite morphology and δ34S as indicators of deposition environment in organic-rich shales. Geosci 2021;11. https://doi.org/10.3390/geosciences11090355.

[95] Eder VG, Zamiraylova AG, Kalmykov GA. Evidence of carbonate rocks formation on geochemical barriers in black shale on the example of the bazhenov formation of the Western Siberia. Georesursy 2019;21:143–52. https://doi.org/10.18599/grs.2019.2.143-152.

[96] Loucks RG, Reed RM, Ruppel SC, Jarvie DM. Morphology, genesis, and distribution of nanometer-scale pores in siliceous mudstones of the mississippian barnett shale. J Sediment Res 2009;79:848–61. https://doi.org/10.2110/jsr.2009.092.

[97] Chen J, Xiao X. Evolution of nanoporosity in organic-rich shales during thermal maturation. Fuel 2014;129:173–81. https://doi.org/10.1016/j.fuel.2014.03.058.

[98] Loucks RG, Reed RM, Ruppel SC, Hammes U. Spectrum of pore types and networks in mudrocks and a descriptive classification for matrix-related mudrock pores. Am Assoc Pet Geol Bull 2012;96:1071–98. https://doi.org/10.1306/08171111061.

[99] Bondarenko T. Evaluation of high-pressure air injection potential for in situ synthetic oil generation from oil shale: Bazhenov Formation. 2018.

[100] Curtis ME, Cardott BJ, Sondergeld CH, Rai CS. Development of organic porosity in the Woodford Shale with increasing thermal maturity. Int J Coal Geol 2012;103. https://doi.org/10.1016/j.coal.2012.08.004.

[101] Sondergeld CH, Ambrose ; R J, Energy D, Rai CS, Moncrieff J. SPE 131771 Micro-Structural Studies of Gas Shales. 2010.

[102] Vasiliev AL, Pichkur EB, Mikhutkin AA, Spasennykh MY, Bogdanovich NN, Balushkina NS, et al. The study of pore space morphology in kerogen from Bazhenov Formation. Oil Gas Ind 2015;10:28–31.

[103] Katz BJ, Arango I. Organic porosity: A geochemist's view of the current state of understanding. Org Geochem 2018;123:1–16. https://doi.org/10.1016/j.orggeochem.2018.05.015.

[104] Milliken KL, Rudnicki M, Awwiller DN, Zhang T. Organic matter-hosted pore system, Marcellus Formation (Devonian), Pennsylvania. Am Assoc Pet Geol Bull 2013;97:177–200. https://doi.org/10.1306/07231212048.

[105] Ambrose RJ, Hartman RC, Diaz-Campos M, Akkutlu IY, Sondergeld CH. New pore-scale considerations for shale gas in place calculations. SPE Unconv Gas Conf 2010 2010:167–83. https://doi.org/10.2118/131772-ms.

[106] Löhr SC, Baruch ET, Hall PA, Kennedy MJ. Is organic pore development in gas shales influenced by the primary porosity and structure of thermally immature organic matter? Org Geochem 2015;87:119–32. https://doi.org/10.1016/j.orggeochem.2015.07.010.

[107] Lu J, Ruppel SC, Rowe HD. Organic matter pores and oil generation in the Tuscaloosa marine shale. Am Assoc Pet Geol Bull 2015;99:333–57. https://doi.org/10.1306/08201414055.

[108] Modica CJ, Lapierre SG. Estimation of kerogen porosity in source rocks as a function of thermal transformation: Example from the Mowry Shale in the Powder River Basin of Wyoming. Am Assoc Pet Geol Bull 2012;96:87–108. https://doi.org/10.1306/04111110201.

[109] Curtis ME, Sondergeld CH, Ambrose RJ, Rai CS. Microstructural investigation of gas shales in two and three dimensions using nanometer-scale resolution imaging. Am Assoc Pet Geol Bull 2012;96:665–77. https://doi.org/10.1306/08151110188.

[110] Berg S, Kutra D, Kroeger T, Straehle CN, Kausler BX, Haubold C, et al. Ilastik: Interactive Machine Learning for (Bio)Image Analysis. Nat Methods 2019;16:1226–32. https://doi.org/10.1038/s41592-019-0582-9.

[111] Schneider CA, Rasband WS, Eliceiri KW. NIH Image to ImageJ. Nat Methods 2012;9:671–5.

[112] Oyeneyin B. Introduction to the Hydrocarbon Composite Production System. Dev. Pet. Sci., vol. 63, 2015, p. 11–128. https://doi.org/10.1016/B978-0-444-62637-0.00002-6.

[113] Wenk, H. R., & Bulakh A. Minerals: their constitution and origin. Cambridge Univ Press 2016.

[114] Johnson SE, Song WJ, Cook AC, Vel SS, Gerbi CC. The quartz α↔β phase transition: Does it drive damage and reaction in continental crust? Earth Planet Sci Lett 2021;553. https://doi.org/10.1016/j.epsl.2020.116622.

[115] Olszak-Humienik M, Jablonski M. Thermal behavior of natural dolomite. J Therm Anal Calorim 2015;119:2239–48. https://doi.org/10.1007/s10973-014-4301-6.

[116] Karunadasa KSP, Manoratne CH, Pitawala HMTGA, Rajapakse RMG. Thermal decomposition of calcium carbonate (calcite polymorph) as examined by in-situ high-temperature X-ray powder diffraction. J Phys Chem Solids 2019;134:21–8. https://doi.org/10.1016/j.jpcs.2019.05.023.

[117] Nigay PM, Cutard T, Nzihou A. The impact of heat treatment on the microstructure of a clay ceramic and its thermal and mechanical properties. Ceram Int 2017;43:1747–54. https://doi.org/10.1016/j.ceramint.2016.10.084.

[118] Grim RE, Bradley WF. Investigation of the Effect of Heat on the Clay Minerals Illite and Montmorillonite. J Am Ceram Soc 1940;23:242–8. https://doi.org/10.1111/j.1151-2916.1940.tb14263.x.

[119] Obradović N, Filipović S, Rusmirović J, Postole G, Marinković A, Radić D, et al. Formation of porous wollastonite-based ceramics after sintering with yeast as the pore-forming agent. Sci Sinter 2017;49:235–46. https://doi.org/10.2298/SOS1703235O.

[120] Hu G, Dam-Johansen K, Wedel S, Hansen JP. Decomposition and oxidation of pyrite. Prog Energy Combust Sci 2006;32:295–314. https://doi.org/10.1016/j.pecs.2005.11.004.

[121] Peterson JW, Newton RC. Reversed experiments on biotite-quartz-feldspar melting in the system KMASH: implications for crustal anatexis. J Geol 1989;97:465–85. https://doi.org/10.1086/629323.

[122] Birch AF, LeComte P. Temperature-pressure plane for albite composition. Am J Sci 1960;258:209–17. https://doi.org/10.2475/ajs.258.3.209.

[123] Seki Y, Kennedy KC. The Breakdown of Potassium Feldspar KAlSiO3O8 at high temperatures and high pressures. Am Mineral 1964;49.

[124] Kuila U, McCarty DK, Derkowski A, Fischer TB, Topór T, Prasad M. Nano-scale texture and porosity of organic matter and clay minerals in organic-rich mudrocks. Fuel 2014;135:359–73. https://doi.org/10.1016/j.fuel.2014.06.036.

[125] Mastalerz M, Schimmelmann A, Drobniak A, Chen Y. Porosity of Devonian and

Mississippian New Albany Shale across a maturation gradient: Insights from organic petrology', gas adsorption, and mercury intrusion. Am Assoc Pet Geol Bull 2013;97:1621–43. https://doi.org/10.1306/04011312194.

[126] Reed RM, Loucks RG, Ruppel SC. Comment on "Formation of nanoporous pyrobitumen residues during maturation of the Barnett Shale (Fort Worth Basin)" by Bernard et al. (2012). Int J Coal Geol 2014;127:111–3. https://doi.org/10.1016/j.coal.2013.11.012.

[127] Wei L, Mastalerz M, Schimmelmann A, Chen Y. Influence of Soxhlet-extractable bitumen and oil on porosity in thermally maturing organic-rich shales. Int J Coal Geol 2014;132:38–50. https://doi.org/10.1016/j.coal.2014.08.003.

[128] Fishman N, Guthrie J, Honarpour M. The stratigraphic distribution of hydrocarbon storage and its effect on producible hydrocarbons in the Eagle ford Formation, South Texas. Unconv Resour Technol Conf 2013, URTC 2013 2013. https://doi.org/10.1190/urtec2013-157.

[129] Pommer M, Milliken K. Pore types and pore-size distributions across thermal maturity, Eagle Ford Formation, southern Texas. Am Assoc Pet Geol Bull 2015;99:1713–44. https://doi.org/10.1306/03051514151.

[130] Reed RM. Organic-matter pores: new findings from lower-thermal-maturity mudrocks. GCAGS J 2017;6:99–110.

[131] Jennings DS, Antia J. Petrographic characterization of the eagle ford shale, south Texas: Mineralogy, common constituents, and distribution of nanometer-scale pore types. AAPG Mem 2013:101–13. https://doi.org/10.1306/13391708M1023586.

[132] Dahl J, Moldowan JM, Walls J, Nur A, Devito J. Creation of porosity in tight shales during organic matter maturation. Search Discov 2012;40979:36pp.

[133] Keel MB. Organic Porosity Distribution: A Function of Aromaticity in Organic-Rich Mudrocks. 2015.

[134] Fishman NS, Hackley PC, Lowers HA, Hill RJ, Egenhoff SO, Eberl DD, et al. The nature of porosity in organic-rich mudstones of the Upper Jurassic Kimmeridge Clay Formation, North Sea, offshore United Kingdom. Int J Coal Geol 2012;103:32–50. https://doi.org/10.1016/j.coal.2012.07.012.

[135] Chalmers GR, Bustin RM, Power IM. Characterization of gas shale pore systems by porosimetry, pycnometry,surfacearea,andfield emission scanning electron microscopy/ transmission electron microscopy image analyses: Examples from the Barnett, Woodford, Haynesville, Marcellus,andDoig units. Am Assoc Pet Geol Bull 2012;96:1099–119. https://doi.org/10.1306/10171111052.

[136] İnan S, Al Badairy H, İnan T, Al Zahrani A. Formation and occurrence of organic matter-hosted porosity in shales. Int J Coal Geol 2018;199:39–51. https://doi.org/10.1016/j.coal.2018.09.021.

[137] Yang R, He S, Yi J, Hu Q. Nano-scale pore structure and fractal dimension of organic-rich Wufeng-Longmaxi shale from Jiaoshiba area, Sichuan Basin: Investigations using FE-SEM, gas adsorption and helium pycnometry. Mar Pet Geol 2016;70:27–45. https://doi.org/10.1016/j.marpetgeo.2015.11.019.

[138] Klaver J, Desbois G, Littke R, Urai JL. BIB-SEM pore characterization of mature and post mature Posidonia Shale samples from the Hils area, Germany. Int J Coal Geol 2016;158:78–89. https://doi.org/10.1016/j.coal.2016.03.003.

[139] Wood JM, Sanei H, Curtis ME, Clarkson CR. Solid bitumen as a determinant of reservoir quality in an unconventional tight gas siltstone play. Int J Coal Geol 2015;150–151:287–95. https://doi.org/10.1016/j.coal.2015.03.015.

[140] Curtis ME, Sondergeld CH, Rai CS. Investigation of the microstructure of shales in the oil window. Unconv Resour Technol Conf 2013, URTC 2013 2013. https://doi.org/10.1190/urtec2013-162.

[141] Milliken KL, Ko LT, Pommer M, Marsaglia KM. Sem petrography of Eastern Mediterranean sapropels: Analogue data for assessing organic matter in oil and gas shales. J Sediment Res 2014;84:961–74. https://doi.org/10.2110/jsr.2014.75.

[142] Zargari S, Canter KL, Prasad M. Porosity evolution in oil-prone source rocks. Fuel 2015;153:110–7. https://doi.org/10.1016/j.fuel.2015.02.072.

[143] Löhr SC, Baruch ET, Hall PA, Kennedy MJ. Is organic pore development in gas shales influenced by the primary porosity and structure of thermally immature organic matter? Org Geochem 2015;87:119–32. https://doi.org/10.1016/j.orggeochem.2015.07.010.

[144] Valenza JJ, Drenzek N, Marques F, Pagels M, Mastalerz M. Geochemical controls on shale microstructure. Geology 2013;41:611–4. https://doi.org/10.1130/G33639.1.